

# รายงานวิจัยฉบับสมบูรณ์

การศึกษาเชิงทดลองการเผาไหม้แบบขั้นและการเผาไหม้ซ้ำเพื่อการลดการ ปลดปล่อยก๊าซไนโตรเจนออกไซด์จากเตาเผาฟลูอิไดซ์เบดที่ใช้เชื้อเพลิงชีวมวล

Experimental Studies on Fuel Staging and Reburning Technology for Reducing NO<sub>x</sub>

Emissions of a Fluidized-Bed Combustor Co-Firing Biomass Fuels

Prof. Dr. Vladimir Kuprianov และคณะ

กุมภาพันธ์ 2562

# รายงานวิจัยฉบับสมบูรณ์

### โครงการ

การศึกษาเชิงทดลองการเผาไหม้แบบขั้นและการเผาไหม้ซ้ำเพื่อการลดการ ปลดปล่อยก๊าซไนโตรเจนออกไซด์จากเตาเผาฟลูอิไดซ์เบดที่ใช้เชื้อเพลิงชีวมวล

Experimental Studies on Fuel Staging and Reburning Technology for Reducing  $NO_x$  Emissions of a Fluidized-Bed Combustor Co-Firing Biomass Fuels

คณะผู้วิจัย	สังกัด
1. ศ.ดร. Vladimir Kuprianov	ภาควิชาวิศวกรรมเครื่องกลและระบบการผลิต สถาบันเทคโนโลยีนานาชาติสิรินธร
2. ผศ.ดร. พิเชฐ นิลดวงดี	มหาวิทยาลัยธรรมศาสตร์ สาขาวิชาวิศวกรรมเครื่องกล
3. Mr. Chhaina Se	คณะวิศวกรรมศาสตร์และเทคโนโลยีอุตสาหกรรม มหาวิทยาลัยราชภัฏเพชรบุรี ภาควิชาวิศวกรรมเครื่องกลและระบบการผลิต
	สถาบันเทคโนโลยีนานาชาติสิรินธร มหาวิทยาลัยธรรมศาสตร์

สนับสนุนโดยสำนักงานกองทุนสนับสนุนการวิจัย (ความเห็นในรายงานนี้เป็นของผู้วิจัย สกว.ไม่จำเป็นต้องเห็นด้วยเสมอไป)

### Acknowledgement

The Authors wish to acknowledge sincerely the financial support from the Thailand Research Fund and Thammasat University (Contract No. BRG 5980005).

Deep appreciation and thanks are given to undergraduate students from Mechanical Engineering Program, Sirindhorn International Institute of Technology, Thammasat University for the effective assistance in conducting experiments.

#### **Abstract**

This Project is aimed at studying the potential of fuel staging and the reburning technology for reducing NO<sub>x</sub> emissions of a fluidized-bed combustor co-firing biomass fuels. Palm kernel shell (PKS), pelletized rice husk (PRH), and pelletized cassava rhizome (PCR) with elevated fuel-N were selected as base (primary) fuel, whereas high moisture/low-calorific biomasses, oil palm empty fruit bunch (EFB), moisturized rice husk (MRH), and eucalyptus bark (EB), were used as reburn (secondary) fuel. Four groups of experiments, for (i) individual (conventional) combustion of the selected fuels, (ii) co-combustion of the pre-mixed fuels (with conventional air supply), (iii) co-combustion of the selected biomasses using fuel staging (with conventional air supply), and (iv) co-combustion of the selected biomass fuels using reburning technology, were performed on a cone-shaped bed (referred to as "conical FBC) fluidized-bed combustor using silica sand/alumina sand/silica sand and alumina sand mixture as bed material. The experimental tests for (co-)firing/reburning tests conducted at similar heat input (200 kW<sub>th</sub>) to the reactor, while ranging mass/energy fraction of the fuels, excess air and secondary-to-total air ratio (the latter being applied during reburning).

Prior to the (co-)combustion studies, "cold-state" hydrodynamic tests were performed to determine the possible hydrodynamic characteristics and regimes used for the following-up co-firing experiments. From the cold state hydrodynamic study, the static bed height of 30 cm can be recommended for the co-firing experiments, as ensuring stable fluidization of the bed (at reasonable  $u_{\rm mff}$ ) at a sufficient amount of the bed material, high enough to sustain ignition and combustion of biomasses in the combustor.

In the main co-combustion study, three case studies with different objectives were performed including (i) co-firing of PKS and EFB, (ii) co-firing of PRH and MRH, and (iii) co-firing of PCR and EB.

In the first case study, PKS and EFB was co-fired in a fuel staged fluidized-bed combustor using mixtures of alumina sand (AS) and silica sand. This case study aimed at (i) to assess the optimal mass/energy fraction of the co-fired fuels in the total fuel supply and the optimal amount of excess air for the PKS/EFB co-firing, (ii) to study the effects of fuel staging, excess air, and bed material type on the combustion and emission characteristics of the conical FBC, and (iii) to investigate the influence of the AS/SS ratio on the physiochemical conditions of the selected bed mixtures at different operating times. As revealed in this study, energy fraction of empty fruit bunch of ~0.15 and excess air value of 55% were optimal for co-firing PKS and EFB reducing 25–35% NO emission compared to individual firing of palm kernel shell. By using AS/SS bed mixtures with a prevailing proportion of rather expensive AS, bed agglomeration can be prevented for a relatively long operating time. However, the AS/SS beds exhibited time related

alterations in physiochemical characteristics. With a higher SS content in the AS/SS mixture, the NO emission somewhat increased, mainly because of the lowered catalytic activity of the bed for the NO–CO reaction, whereas the bed material showed a diminished capability to withstand bed agglomeration.

The second case study was fluidized bed co-combustion of PRH and MRH, focusing on the effects of co-combustion methods on combustion and emission performance of the combustor. An optimization analysis was performed to determine the optimal EF2, EA, and SA/TA, leading to minimal emission costs of the applied co-firing techniques. EF2=0.15 and EA=45% was optimal for co-combustion of the pre-mixed fuels, as well as for their co-firing using fuel staging, while EF2=0.15, EA=50%, and SA/TA=0.25 are most appropriate when co-firing the fuels using a reburning method. Under optimal operating conditions, the combustor ensures high (~99%) combustion efficiency and reduced NO emission: by about 13% when co-firing pre-mixed fuels, by 37% for the fuel-staged co-combustion, and by 53% when using reburning, as compared to burning the base fuel alone. However, some increase in the CO and CxHy emissions was observed when using the proposed co-firing techniques.

The third case study was aimed at studying the combustion efficiency and emissions of a fluidized-bed combustor co-fired with PCR and EB, using: (i) fuel staging (at bottom air injection) and (ii) a reburning technique, to reduce NO emission from the combustor. Silica sand (SS), alumina sand (AS), and a mixture of both were employed as the bed material in this combustor to investigate the potential of the bed materials in preventing bed agglomeration for a relatively long time. With fuel staging and reburning, the combustor operated under optimal conditions can decrease the NO emission by ~20% and ~50%, respectively. However, when using silica sand as the bed material, a small proportion of agglomerates is formed in the bed during 8 h of combustor operation for both co-firing methods. With alumina sand and alumina-silica sand mixture (alternative bed materials), bed agglomeration can be prevented in the combustor for a relatively long operational time. However, both alternative bed materials show time-domain changes in their physiochemical characteristics, pointing at a gradual decrease of the bed capability to withstand agglomeration, mainly due to continuous carryover of fine alumina-rich particles (generated in the fluidized bed in collisions and attrition of the AS grains) from the combustor.

**Keywords:** Biomass, Fluidized-bed combustion, Co-firing techniques, NO emission reduction, Bed agglomeration prevention.

### **Executive Summary**

**Project Title:** Experimental Studies on Fuel Staging and Reburning Technology for Reducing NO<sub>x</sub> Emissions of a Fluidized-Bed Combustor Co-Firing Biomass Fuels

**Principal Investigator:** Prof. Vladimir Kuprianov (D. Eng.) School of Manufacturing Systems and Mechanical Engineering (ME Program), Sirindhorn International Institute of Technology, Thammasat University

Email. ivlaanov@siit.tu.ac.th

Project budget: 1,500,000 Baht

**Duration:** 2 years (from May, 31, 2016 to May 31, 2018)

Objective: This research Project (study) was aimed at investigating the potential and benefits of the fuel-staged and reburning technologies for reduction of highly-hazardous NO<sub>x</sub> emissions when burning biomass with elevated fuel-N (as main fuel) in a fluidized-bed combustion system at maximum possible fuel conversion into energy. Developing recommendations on the optimal operating parameters, ensuring the highest combustion efficiency of the combustor and maximum NO emission reduction when using the fuel-staged and reburning technologies, was among the main objective of the study. The effects of (i) the combustion method, (ii) fuel properties (e.g., moisture, fuel-N, and volatile matter of both fuels), and (iii) operating conditions (excess air, proportion of primary and secondary/reburning fuel, and air staging when reburning) on formation and oxidation/reduction of major gaseous pollutants (CO, CxHy, and NO) in distinct reactor regions, as well as on the emissions and combustion efficiency of the biomassfueled combustor was investigated. Special attention was given to the effects of the selected co-firing methods on physiochemical conditions of the bed material at different operating times.

**Methods:** A "cold-state" hydrodynamic study was conducted on a special experimental rig with cone-shaped bed to determine the possible hydrodynamic characteristics and regimes used for the following-up co-firing experiments. The total

pressure drop across a distributor-bed system was measured for variable superficial air velocity by using U-tube manometer with two static pressure probes.

In the co-firing experiments, palm kernel shell (PKS), pelletized rice husk (PRH), and pelletized cassava rhizome (PCR) with elevated fuel-N were selected as base (primary) fuel, whereas high moisture/low-calorific biomasses, oil palm empty fruit bunch (EFB), moisturized rice husk (MRH), and eucalyptus bark (EB), were used as reburn (secondary) fuel. Four groups of experiments, for (i) individual (conventional) combustion of the selected fuels, (ii) co-combustion of the pre-mixed fuels (with conventional air supply), (iii) co-combustion of the selected biomasses using fuel staging (with conventional air supply), and (iv) co-combustion of the selected biomass fuels using reburning technology, were performed on a cone-shaped bed (referred to as "conical FBC) fluidized-bed combustor using silica sand/alumina sand/silica sand and alumina sand mixture as bed material. The experimental tests for (co-)firing/reburning tests conducted at similar heat input (200 kW<sub>th</sub>) to the reactor, while ranging mass/energy fraction of the fuels, excess air and secondary-to-total air ratio (the latter being applied during reburning). To study the effects of excess air on the combustion and emission characteristics, each Case Study includes test groups for four percentages of excess air: 20%, 40%, 60%, and 80%. In the reburning tests, the secondary-to-total air ratio (SA/TA) is another important parameter. at each (fixed) EA, the reburning tests were performed for four secondary-to-total air (SA/TA) ratios: 0.1, 0.2, 0.3, and 0.4.

During the tests, temperature was recorded at different points along the reactor centerline and at stack, using eight stationary Chromel-Alumel thermocouples. In each trial at fixed operating conditions, O<sub>2</sub>, CO, C<sub>x</sub>H<sub>y</sub> as CH<sub>4</sub>, and NO are measured along the combustor height and at stack using a new model "Testo-350" gas analyzer.

To determine the optimal operating variables, ensuring minimal "external" costs of the combustor for the selected co-firing options, a cost-based optimization method was applied in this work.

To understand the interaction mechanism between the selected bed material and fuel ash during long term co-firing tests, a SEM-EDS: JEOL, JSM-6610LV scanning

electron microscope (SEM), integrated with an energy dispersive X-ray spectrometer (EDS), was used to examine the physiochemical characteristics of individual grains sampled from the bed at the end of co-firing testing with different bed materials. The objectives of the SEM-EDS test were to investigate the distribution of coatings (or that of binding materials in agglomerates, if any) over the bed particle surface, and determine the elemental composition of the coating at some selected spots on a bed particle. An X-ray fluorescence (XRF) system was employed to observe the time-related variation in the chemical composition of the used/reused bed materials (AS and AS/SS mixture), as well as that of PM.

**Results and Outputs:** The static bed height of 30 cm can be recommended for the co-firing experiments, as ensuring stable fluidization of the bed (at reasonable  $u_{\rm mff}$ ) at a sufficient amount of the bed material, high enough to sustain ignition and combustion of biomasses in the combustor.

The findings revealed that, the effects of operating parameters, such as the energy fraction of secondary/reburn fuel in the total fuel supply (EF<sub>2</sub>), excess air (EA), and the secondary-to-total air ratio (SA/TA) in the reburning tests, on the combustion and emission characteristics of the combustor were noticeable. The selected co-firing techniques create reducing conditions for NO (due to substantial CO and C<sub>x</sub>H<sub>y</sub>) in the primary and secondary/reburn zones. Under optimal operating condition, NO emission reduction by 50% was achievable. With alumina sand and alumina–silica sand mixture (alternative bed materials), bed agglomeration can be prevented in the combustor for a relatively long operational time. However, both alternative bed materials show time-domain changes in their physiochemical characteristics, pointing at a gradual decrease of the bed capability to withstand agglomeration, mainly due to continuous carryover of fine alumina-rich particles (generated in the fluidized bed in collisions and attrition of the AS grains) from the combustor.

The main finding from this Project have been published in (or presented at): *International Journals* 

- 1. Kuprianov, V.I., Ninduangdee, P., and Suheri, P. (2018). Co-firing of oil palm residues in a fuel staged fluidized-bed combustor using mixtures of alumina and silica sand as the bed material, *Applied Thermal Engineering*, Vol. 144, 5 November 2018, pp. 371-382. ISI Q1, Impact factor = 3.771
- 2. Ninduangdee, P. and Kuprianov, V.I. (2018). Experimental investigation and empirical modeling of flow regimes and hydrodynamic characteristics of a cone-shaped bed using sand-biomass binary mixtures, *Chemical Engineering and Processing Process Intensification*, Vol. 131, September 2018, pp. 1-11. ISI Q1, Impact factor = 2.826
- 3. Ninduangdee, P. and Kuprianov, V.I. (2018). Fluidized bed co-combustion of rice husk pellets and moisturized rice husk: The effects of co-combustion methods on gaseous emissions, *Biomass and Bioenergy*, Vol. 112, May 2018, pp. 73-84. ISI Q1, Impact factor = 3.358
- 4. Ninduangdee, P. and Kuprianov, V.I. (2018). Co-combustion of rice husk pellets and moisturized rice husk in a fluidized-bed combustor using fuel staging at a conventional air supply, *Songklanakarin Journal of Science and Technology*, Vol. 40, No. 5, September-October 2018, pp. 1081-1089. ISI Q2

#### International conferences

- 1. Se, C., Kuprianov, V.I., Ninduangdee, P. (2018). Co-firing cassava rhizome and eucalyptus bark in a fluidized-bed combustor using reburning: combustor performance and time-related bed behavior, *Proceedings of the International Conference on Green Energy for Sustainable Development*, 24-26 October 2018, Phuket, Thailand, 8 p.
- 2. Ninduangdee, P., Se, C., Kuprianov, V.I. (2018). Time-related bed behavior in a fluidized-bed combustor co-firing pelletized cassava rhizome and eucalyptus bark: a comparative study between conventional and alternative bed materials, *Proceedings of the 6th Asian Conference on Innovative Energy and Environmental Chemical Engineering*, 4-7 November 2018, Sun Moon Lake, Taiwan, pp. 277-282.

- 3. Se, C., Kuprianov, V.I., Ninduangdee, P. (2018). Co-combustion of pelletized cassava rhizome and eucalyptus bark for reducing NOx in a fluidized-bed combustor, *Proceedings of the 6th Asian Conference on Innovative Energy and Environmental Chemical Engineering*, 4-7 November 2018, Sun Moon Lake, Taiwan, pp. 271-276.
- 4. Siricharuanun, T., Rerkpisut, N., Boonsai, P., Ninduangdee, P., and Kuprianov, V.I. (2018). Co-combustion characteristics of pelletized cassava rhizome and eucalyptus bark: thermogravimetric analysis and kinetic modeling, *Proceedings of the 6th Asian Conference on Innovative Energy and Environmental Chemical Engineering*, 4-7 November 2018, Sun Moon Lake, Taiwan, pp. 425-430.
- 5. Se, C., Ninduangdee, P., and Kuprianov, V.I. (2018). Co-firing of pelletized cassava rhizome and eucalyptus bark in a fluidized bed: studies on the effects of co-firing methods and bed material type on the combustor performance and time-related bed behavior, *Proceedings of the 26th European Biomass Conference and Exhibition*, 14-17 May 2018, Copenhagen, Denmark, pp. 378-389.
- 6. Kuprianov, V. I. and Ninduangdee, P. (2017). Experimental study on the biomass–biomass co-combustion for reducing NOx in a fluidized-bed combustor: a comparison between the co-firing techniques, *Proceedings of the 25th European Biomass Conference and Exhibition*, 12-15 June 2017, Stockholm, Sweden, p. 384-392.
- 7. Ninduangdee, P. and Kuprianov, V.I. (2016). Study on co-combustion of pelletized and moisturized rice husks in a cone-shaped fluidized-bed combuster using fuel staging for reducing NOx emissions: optimization of operating variables, *Proceedings of the 7th TSME International Conference on Mechanical Engineering* (TSME-ICoME 2016), 13-16 December 2016, Chiang Mai, Thailand, 8 p.
- 8. Kuprianov, V. I. and Ninduangdee, P. (2016). Interaction between biomass ash and bed material during combustion of oil palm residues in a fluidized bed of alumina sand, *Proceedings of the 5th Asian Conference on Innovative Energy and Environmental Chemical Engineering (ASCON-IEEChE 2016)*, 13-16 November 2016, Yokohama, Japan, pp. 126-131.

- 9. Ninduangdee, P. and Kuprianov, V.I. (2016). Co-combustion of pelletized and moisturized rice husks in a fluidized-bed combustor using fuel staging and reburning for reducing NOx emissions, *Proceedings of the 5th Asian Conference on Innovative Energy and Environmental Chemical Engineering (ASCON-IEEChE 2016)*, 13-16 November 2016, Yokohama, Japan, pp. 615-620.
- 10. Kuprianov, V. I., Ninduangdee, P., and Suheri, P. (2016). Fuel-staged co-combustion of high-alkali oil palm residues in a fluidized-bed combustor using mixtures of alumina and silica sand to prevent bed agglomeration, *The 24th European Biomass Conference and Exhibition (EUBCE 2016)*, 6-9 June 2016, Amsterdam, The Netherlands, pp. 420-428.

### **Table of Contents**

Chapter	Title	Page
	Acknowledgement	i
	Abstract	ii
	Executive Summary	iv
	Table of Contents	X
	List of Figures	XV
	List of Tables	xxi
1	Introduction	1
	1.1 Rationale of the study	1
	1.2 Objectives of the project	4
	1.3 Scope of the study	5
2	Literature Review	7
	2.1 Hydrodynamic regimes and characteristics of tapered and	
	conical fluidized-bed reactor using a single bed material	7
	2.2 Hydrodynamic characteristics of a conical fluidized bed	
	using binary mixtures	13
	2.3 Conventional fluidized-bed combustion of biomass fuels	15
	2.4 Combustion techniques with alternative design and	
	hydrodynamics	17
	2.5 Staged combustion technologies	18
	2.6 Co-firing biomass fuels in a fluidized bed	21
	2.7 Reburning technology	21
	2.8 Ash-related problems in biomass-fueled fluidized-bed	
	combustion systems	26
	2.9 The alternative bed materials to extend bed agglomeration	
	tendency	27

# **Table of Contents (cont'd)**

Chapter	Title	Page
3	Materials and Methods	32
	3.1 The selected fuels and bed materials	32
	3.2 Experimental facilities	34
	3.2.1 Experimental set up for the cold-state hydrodynamic	
	study	34
	3.2.2 Experimental set up for the (co-)combustion study	36
	3.3 Experimental planning	39
	3.4 Methods for determining operating parameters	39
	3.5 Methods for determination of heat losses and combustion	
	efficiency of the conical FBC	40
	3.6 Methods for optimization of operating variables	41
	3.7 Study of time-related characteristics of the bed materials	
	and PM during co-firing tests	42
4	Hydrodynamic Regimes and Characteristics of a Cone-Shaped	
	Bed with a Sand-Biomass Binary Mixture	43
	4.1 Flow regimes of a cone-shaped bed	43
	4.2 Hydrodynamics of a cone-shaped bed using monodispersed	
	particles	46
	4.3 Hydrodynamics of a cone-shaped bed with a sand-biomass	
	binary mixture	49
	4.3.1 Behavior of a cone-shaped bed using a sand-PKS	
	binary mixture	49
	4.3.2 Behavior of a cone-shaped bed with a sand-EFB	
	binary mixture	50
	4.4 Relative hydrodynamic characteristics of a cone-shaped	
	bed with sand-biomass binary mixtures	53

	4.5 Empirical models for predicting major hydrodynamic	
	characteristics of a cone-shaped bed with a binary mixture	
	of the bed material mixed with palm kernel shell	55
5	Co-firing of Oil Palm Residues in a Fuel Staged Fluidized-bed	
	Combustor using Mixtures of Alumina and Silica Sand as the	
	Bed Material	58
	5.1 Optimizing operating parameters for co-firing PKS and	
	EFB using pure alumina sand as the bed material	58
	5.2 Effects of operating variables on the heat losses and	
	combustion efficiency of the combustor (co-)fired with	
	PKS and EFB	60
	5.3 Radial profiles temperature and gas concentrations inside	
	the conical FBC combustor co-fired with PKS and EFB at	
	the optimal energy fraction of EFB	62
	5.4 Effects of excess air on combustion characteristics and	
	pollutant behaviors inside the reactor using a mixture of	
	alumina and silica sand as the bed material	63
	5.5 Effects of excess air and bed material type on the emissions	
	and combustion efficiency	65
	5.6 Physical condition and particle size distribution of the bed	
	material at different operating times	67
	5.7 SEM-EDS analysis of the used/reused bed materials	68
	5.8 Time-related changes in compositions of the bed materials	
	and particulate matter	72
6	Fluidized Bed Co-combustion of Rice Husk Pellets and	
	Moisturized Rice Husk: The Effects of Co-combustion	
	Methods on Gaseous Emissions	74
	6.1. Distribution of temperature and Ω2 in the conical FBC	74

# **Table of Contents (cont'd)**

Chapter	Title	Page
	6.2. Formation and oxidation of CO and CxHy inside the	
	conical FBC	76
	6.3. Formation and reduction of NO inside the reactor	78
	6.4. Effects of the co-firing options on gaseous emissions	81
	6.5. Combustion efficiency	82
	6.6. Optimal operating conditions	84
7	Co-firing of Pelletized Cassava Rhizome and Eucalyptus Bark	
	in a Fluidized Bed: Studies on the Effects of Co-firing Methods	
	and Bed Material Type on the Combustor Performance and	
	Time-Related Bed Behavior	87
	7.1 Combustion and emission characteristics inside the conical	
	FBC using silica sand as the bed material	87
	7.2 Effects of (co-)combustion techniques on the emissions and	
	combustion efficiency	92
	7.3 Optimal operating parameters for the co-combustion	
	techniques with fuel staging and reburning	96
	7.4 SEM-EDS analysis of the bed materials	97
	7.5 Time-related changes in compositions of the bed materials	
	and particulate matter	99
8	Conclusions and Recommendations	101
	8.1 Conclusions	101
	8.2 Recommendations for the future work	103
	References	104
	Project Outputs	111
	Appendices: Paper Reprints	114

# **List of Figures**

Figures	S	Page
2.1	Flow regimes in a tapered fluidized bed: (a) fixed-bed regime, (b)	
	partially fluidized-bed regime, (c) fully fluidized-bed regime, (d)	
	transition regime, and (e) turbulent fluidized-bed regime	8
2.2	Net pressure drop as a function of the superficial fluid velocity (u)	
	at the inlet of the tapered bed	10
2.3	The $\Delta p$ - $u$ diagram for a gas-solid conical bed	11
2.4	Pressure drop across the air distributor versus operating air	
	velocity and the $\Delta p$ - $u$ diagram of the alumina conical bed for	
	different static bed heights	12
2.5	The $\Delta p$ - $u$ diagram of a conical bed of alumina mixed with peanut	
	shells (PNS) for variable weight percentage of biomass in the	
	binary mixture for different static bed	14
2.6	Schematic of reburning technology in coal-fired boiler	22
3.1	Schematic diagram of the experimental set up for the cold-state	
	hydrodynamic study	35
3.2	Schematic diagram of the experimental setup for co-combustion	
	tests with fuel staging and reburning	37
4.1	A typical $\Delta p$ - $u$ diagram of a cone-shaped bed when using	
	alumina/dolomite/limestone as bed material for	
	fluidization/defluidization procedures	43
4.2	Appearance of the cone-shaped bed in different hydrodynamic	
	regimes: (a) fixed (stationary) bed, (b) partially fluidized bed, (c)	
	fully fluidized bed, and (d) turbulent fluidized bed	44

Figure	S	Page
4.3	Pressure drop across the air distributor versus superficial velocity,	
	and the $\Delta p$ - $u$ diagram of the bed (including effects of AD) using	
	pure bed materials: (a) alumina sand, (b) dolomite, and (c)	
	limestone for different static bed heights	47
4.4	Pressure drop across the bed (including effects of AD) using	
	alumina sand (upper), dolomite (middle), and limestone (lower) as	
	the bed material mixed with PKS of 3-6 mm particle sizes in	
	different proportions: (a) 2.5 wt.% and (b) 10 wt.%	48
4.5	Effects of the static bed height and biomass particle size on the $\Delta p$ -	
	u diagram of alumina sand mixed with PKS (including effects of	
	AD) in different proportions: (a) 2.5 wt.% and (b) 10 wt.%	50
4.6	Pressure drop across the bed (including effects of AD) using	
	alumina sand (upper), dolomite (middle), and limestone (lower) as	
	the bed material mixed with EFB in different proportions: (a) 1	
	wt.% and (b) 5 wt.%	51
4.7	Relative pressure drop (including effects of AD) versus the relative	
	superficial air velocity of the cone-shaped bed using alumina sand	
	(upper graphs), dolomite (middle graphs), and limestone (lower	
	graphs) mixed with (a) 3-6 mm PKS particles size and (b) 6-9 mm	
	PKS particles in various proportions at different static bed heights	52
4.8	Relative pressure drop (including effects of AD) versus the relative	
	superficial air velocity of the cone-shaped bed using (a) alumina	
	sand, (b) dolomite, and (c) limestone mixed with EFB in various	
	proportions at different static bed heights	53

54 56
56
56
56
57
58
59
62
64

Page
+ 25% SS)
(50% AS +
67
the original
0% SS) bed
68
SS particles
sing a (75%
6 AS + 50%
nder optimal
69
gglomerates,
sing a (25%
al operating
70
BC co-fired
ring options
on with the
75
cal FBC co-
ent co-firing
parison with
76

Figures		Page
6.3	Axial profiles NO in the conical FBC co-fired with PRH and MRH	
	at EA $\approx$ 40%, using different co-firing options for (a) EF <sub>2</sub> = 0.15	
	and (b) $EF_2 = 0.25$ , in comparison with the conventional	
	combustion of PRH	79
6.4	Emissions of CO (upper), C <sub>x</sub> H <sub>y</sub> as CH <sub>4</sub> (middle), and NO (lower)	
	from the conical FBC when co-firing PRH/MRH under variable	
	operating conditions using: (a) pre-mixed fuels, (b) fuel staging	
	with bottom air injection, and (c) reburning	82
6.5	Emission ("external") costs of the conical FBC co-fired with PRH	
	and MRH under variable operating conditions using: (a) a	
	feedstock of the pre-mixed fuels, (b) fuel staging at bottom air	
	injection, and (c) reburning at $EF_2 = 0.15$	85
7.1	Axial profiles of temperature and O2 in the conical FBC co-fired	
	with PCR and EB at (a) $EF_2 = 0.15$ and (b) $EF_2 = 0.25$ , using fuel	
	staging and reburning at excess air of about 40%, compared to	
	conventional combustion of PCR	88
7.2	Axial profiles of CO and $C_xH_y$ (as $CH_4$ ) in the conical FBC (co-	
	)fired with PCR and EB at (a) $EF_2 = 0.15$ and (b) $EF_2 = 0.25$ , using	
	fuel staging and reburning at excess air of about 40%, compared to	
	conventional combustion of PCR	89
7.3	Axial profiles NO in the conical FBC (co-)fired with PCR and EB	
	at (a) $EF_2 = 0.15$ and (b) $EF_2 = 0.25$ , using fuel staging and	
	reburning at excess air of about 40%, compared to conventional	
	combustion of PCR	91
7.4	Emissions of CO, C <sub>x</sub> H <sub>y</sub> as CH <sub>4</sub> , and NO from the conical FBC co-	
	fired with PCR and EB under variable operating conditions, using	

	(a) fuel staging and (b) reburning, compared to conventional	
	combustion of PCR	93
7.5	Emission costs of the conical FBC co-fired with PCR and EB	
	under variable operating conditions using: (a) fuel staging with	
	bottom air injection and (b) reburning at $EF_2 = 0.15$ (bed material:	
	silica sand)	96
7.6	SEM-EDS spot analyses of the bed agglomerates sampled after 8-h	
	co-firing tests on the conical using (a) fuel staging and (b)	
	reburning (bed material: silica sand)	97
7.7	SEM-EDS spot analyses of the bed particles sampled after 30-h	
	reburning tests on the conical FBC using (a) alumina sand and (b)	
	AS/SS mixture as the bed material	98

### **List of Tables**

<b>Tables</b>		Page
1.1	Energy potential of major biomasses of Thailand in 2017	2
2.1	Demonstration projects for NO <sub>x</sub> emission reduction by reburning	
	technology	23
3.1	Properties of the selected biomasses used in co-combustion	
	experiments	32
3.2	Ash composition of the selected biomasses used in co-combustion	
	experiments	33
3.3	Composition of the alumina sand and silica sand used in co-	
	combustion experiments	34
3.4	Operating parameters maintained or varied in the (co-)combustion	
	tests	38
5.1	Emissions and the combustion efficiency of the conical FBC using	
	alumina sand as bed material when co-firing PKS and EFB at	
	different operating conditions	61
5.2	Emissions, heat losses, and combustion efficiency of the conical	
	FBC, co-fired with PKS and EFB at a constant energy fraction of	
	EFB (EF $_2$ = 0.15) and variable excess air when using selected	
	AS/SS mixtures as bed material	66
5.3	Composition of the bed materials used/reused in the conical FBC	
	during co-firing of PKS and EFB under optimal operating	
	conditions at different time instants of combustor operation	72
5.4	Composition of particulate matter originating from the co-firing of	
	PKS and EFB in the conical FBC under optimal operating	
	conditions when using selected AS/SS mixtures as the bed material	
	for different operating times	73

# List of Tables (cont'd)

Tables		Page
6.1	Combustion heat losses and efficiency of the conical FBC (co-)fired with PRH and MRH using selected (co-)firing techniques at	00
6.2	variable operating parameters  Major gaseous emissions from the conical FBC co-fired with PRH  and MRH at optimal operating parameters when using the selected  co-combustion methods, as compared with burning pure PRH at	83
	similar excess air	86
7.1	Heat losses and combustion efficiency of the conical FBC co-fired with PCR and EB, using fuel staging and reburning techniques at variable operating parameters, compared to burning pure PCR (bed	
	material: silica sand)	94
7.2	Composition of the bed materials used/reused in the conical FBC and that of PM generated during co-combustion of PCR and EB using a reburning technique, for different time instants of	
	combustor operation	100

### Chapter 1

#### Introduction

#### 1.1 Rationale of the study

In Thailand, over 60% of the primary energy demand is covered by energy imports. Since local fossil fuels and hydropower resources are limited, the country has developed a roadmap entitled as the "Renewable and Alternative Energy Development Plan (AEDP 2012–2021)" aiming at a substantial (by 25%) increase of energy production from domestic alternative energy resources within the nearest ten years. According to this plan, the total installed capacity of biomass-fuelled power generating facilities is expected to increase up to 3600 MWe by the year 2021 (DEDE, 2015).

Biomass is the main renewable energy resource in Thailand because of the agricultural foundation of this country. Annually, the Thai agricultural and forest-related sectors generate a tremendous amount of various biomass residues and wastes showing great potential as a fuel in direct combustion systems, or, alternatively, as raw material for production of biofuels. Table 1.1 summarizes the energy potential of the biomass available in Thailand for the year 2017. It can be seen in Table 1.1 that the total annual energy potential of Thai biomass residues and wastes is high, accounting for 38,367.9 ktoe (equivalent to 1606 PJ) (DEDE, 2017). Thus, effective utilization of various types of biomass for energy production in this country can promote the energy security and diversification of energy sources in the domestic energy-related sectors.

As known, biomass as fuel for heat and power generation offers a number of advantages compared to fossil fuels from both technological and environmental points of view. Sustainable agricultural biomass residues produced by the Thai agricultural sectors on a large scale can be treated as CO<sub>2</sub>-neutral with regard to their combustion, i.e., reducing the CO<sub>2</sub> net emission from the domestic power generation. Another apparent benefit of biomass utilization through combustion is a quite low emission of SO<sub>2</sub>, usually due to insignificant sulphur content in biomass (Werther et al., 2000).

**Table 1.1** Energy potential of major biomasses of Thailand in 2017.

Source	Biomass residues and	Biomass energ	y potential
	wastes	ktoe	PJ
Industrial sugarcane	Top and trashier	7251.6	303.6
	Bagasse	5021.9	210.3
Rice	Paddy husk	2364.5	99.0
	Straw	11931.5	499.5
Maize	Stalk, top, and leaves	1588.9	66.5
	Cob maize	352.9	14.8
Cassava	Stalk	1361.6	57.0
	Root	1058.2	44.3
Oil palm	Frond	1167.9	48.9
	Fiber	1250.7	52.4
	Shell	1343.5	56.3
	Empty fruit bunch	1183.3	49.5
Coconuts	Shell	88.9	3.7
	Husk	182.8	7.7
	Frond, empty bunch	171.3	7.2
Soybeans	Stalk, leaves, shell	17.2	0.7
Para rubber	Char coal	914.7	38.3
	Fuel wood	422.9	17.7
	Frond and leaves	136.6	5.7
	Sawdust	39.5	1.7
Pineapple	Stalk	477.0	20.0
Total		38367.9	1606.4

Source: DEDE. (2017)

For effective and environmental-friendly utilization of biomass, highly efficient energy conversion technologies are required. Among proven combustion technologies (such as grate-fried, suspension-fired and fluidized bed systems), fluidized-bed combustion systems (combustors and boiler furnaces) have been considered as most

appropriate for converting biomass into energy, mainly due to some important advantages over great firing and pulverized-fuel firing systems, such as fuel flexibility, excellent mixing characteristics, relatively low temperature, thermal homogeneity, low pollutant emissions, and high combustion efficiency (Chyang et al., 2008; Permchart and Kouprianov, 2004; Werther et al., 2000). However, combustion of some agricultural wastes, particularly with elevated fuel-N, is often accompanied by elevated NO emission (Akpulat et al., 2010; Madhiyanon et al., 2006; Qian et al., 2011; Vamvuka et al., 2012).

Co-firing (or co-combustion) of two or more fuels with different properties is one of the most effective ways of improving emission performance of a combustion system, while maintaining its combustion efficiency at a relatively high level. Some related studies on grate-firing, pulverized fuel-firing, and cyclone-firing systems, as well as with fluidized-bed combustion techniques, revealed that co-firing is flexible for fuel type (coal, biomass, RDF, combustible wastes, etc.) and combustion method (Nussbaumer, 2003; Salzmann and Nussbaumer, 2001), but was affected by the technique of fuel injection into a combustor (or furnace).

A large number of studies on the co-firing of coal and biomass, commonly burned as a blended feedstock in modified pulverized coal-fired boilers, have reported a reduced (net) production of CO<sub>2</sub>, as well as a noticeable reduction in NOx and SO<sub>2</sub> emissions, compared to burning coal on its own (Sahu et al., 2014; Sami et al., 2001; Turn et al., 2006). Quite limited information regarding the co-firing of biomass with another biomass in a single fluidized-bed combustion system is reported in the literature. However, some pilot studies revealed that biomass—biomass co-firing systems can effectively utilize problematic fuels (e.g., with unacceptable emission characteristics and/or very low calorific value) with lower emissions of NO<sub>x</sub>, compared to firing a base fuel (Chakritthakul and Kuprianov, 2011; Kuprianov et al., 2006).

The fuel-staged combustion methods, such as fuel biasing and reburning, have been proposed to reduce  $NO_x$  in various combustion systems (co-)fired with coal/biomass. When using fuel biasing (a type of fuel staging), a base fuel is injected into the main combustion zone, whereas the rest of the fuel (or another fuel) is added

downstream of the primary zone with no air supply (Baukal, 2001). As a result, chemical reactions occurring in the secondary zone generate precursors (radicals) to participate in the reduction of NO<sub>x</sub> previously formed in the primary zone. A recent study on the cofiring of palm kernel shell (primary fuel) and high-moisture empty fruit bunch (secondary fuel) in a fluidized-bed combustor has revealed a 35% NO emission reduction that can be achieved via the use of fuel-staged combustion with bottom air injection. However, the NO<sub>x</sub> reduction level depends on the mass/energy share of the secondary fuel and excess air (Suheri and Kuprianov, 2015).

A reburning method has been suggested as one of the most effective solutions to reduce NOx emissions from different combustion systems. This method is, in effect, a combination of fuel staging and air staging (Nussbaumer, 2003). The relevant processes basically occur within three sequent zones of the reactor: (i) primary zone where primary (main) fuel burns, (ii) reburn zone where the reburn (secondary) fuel is injected into the reactor to create a fuel-rich conditions resulting in a reduction of NOx formed in the preceding zone, and (iii) burnout zone, where the burnout (secondary) air is introduced for achieving complete combustion (Smoot et al., 1998). The reburning method has been extensively studied on large-scale pulverized coal-fired boilers and grate-fired biomassfueled systems, with different types of reburn fuel. Some pioneering studies have reported up to 70% NOx reduction that can be achieved with this method, with no adverse effects on the operation of a combustion system (Harding and Adams, 2000; Salzmann and Nussbaumer, 2001; Smoot et al., 1998).

As follows from the literature review, there remains a lack of knowledge regarding to the fuel staging and reburning in fluidized-bed combustion systems using biomass as primary and secondary/reburn fuels. Research studies on application of these combustion technologies for effective and low-NO<sub>x</sub> utilization of domestic biomasses are therefore required.

#### 1.2 Objectives of the project

The main goal of this research project is to investigate the potential and benefits of the fuel-staged and reburning technologies for reduction of highly-hazardous  $NO_x$ 

emissions when burning biomass with elevated fuel-N (as main fuel) in a fluidized-bed combustion system at maximum possible fuel conversion into energy.

The objectives pursued in this research project are as follows:

- to modify the fluidized-bed combustor for the co-firing two (primary and secondary/reburning) biomass fuels using the fuel-staged and reburning combustion methods;
- to perform four experimental test series on the combustor for: (i) conventional fluidized-bed combustion of individual (primary/secondary/reburning) biomass fuels, (ii) co-combustion of the pre-mixed fuels using conventional air supply (iii) co-combustion of the fuels using fuel staging (i.e., injection of these fuels into the combustor at different levels) and conventional (bottom) air supply, and (iv) co-combustion of the fuels using reburning technology (integrating fuel staging and air staging);
- to investigate the effects of (i) the combustion method, (ii) fuel properties (e.g., moisture, fuel-N, and volatile matter of both fuels) and (iii) operating conditions (excess air, proportion of primary and secondary/reburning fuel, and air staging when reburning) on formation and oxidation/reduction of major gaseous pollutants (CO, C<sub>x</sub>H<sub>y</sub>, and NO) in distinct reactor regions, as well as on the emissions and combustion efficiency of the biomass-fueled combustor;
- to investigate the effects of fuel staging and reburning on physiochemical conditions of the bed material at different operating times;
- to quantify and compare the NO reduction efficiency between the fuel-staged and reburning combustion methods for specified ranges of operating conditions;
- to provide recommendations on the optimal operating parameters ensuring the highest combustion efficiency of the combustor and maximum NO emission reduction when using the fuel-staged and reburning technologies;
- to provide a state-of-the-art on recent and ongoing achievements in developing/improvement of the NO emission reduction technologies.

#### 1.3 Scope of the study

The limitations of the study are as follows:

- a fluidized-bed combustion technique (the conical FBC) is solely used to achieve the work objectives;
- an experimental part of the Project includes four test series (i) conventional fluidized-bed combustion of individual biomass fuels, (ii) co-combustion of the premixed fuels using conventional air supply, (iii) co-combustion of the fuels using fuel staging (i.e., injection of these fuels into the combustor at different levels) with conventional (bottom) air supply, and (iv) co-combustion of the fuels using reburning technology (integrating fuel staging and air staging). For comparability, all test series were performed at a constant heat input to the conical FBC, 200 kW<sub>th</sub>;
- palm kernel shell, pelletized rice husk, and pelletized cassava rhizome were used as primary fuel, while oil palm empty fruit bunch, moisturized rice husk, and eucalyptus bark were used as secondary/reburn fuel;
- bed materials (silica sand/alumina sand) of the 300–500  $\mu$ m particle size were used as inert bed material in the conical FBC;
- different analytical/measuring techniques, such as a thermogravimetric analysis (TGA) system, a scanning electron microscope integrated with an energy dispersive X-ray spectrometer (SEM–EDS), an X-ray fluorescence (XRF) technique, and a heat flux meter (sensor) are employed in this research.

### Chapter 2

#### **Literature Review**

# 2.1 Hydrodynamic regimes and characteristics of tapered and conical fluidized-bed reactor using a single bed material

Hydrodynamic characteristics of a gas-solid fluidized bed are important input data for optimal design and operation of a fluidized-bed combustion system. These characteristics are basically used: (i) to determine the best configuration, (ii) to select proper auxiliary equipment for a combustion system, and (iii) to quantify a possible range of operating conditions of the system (Kaewklum and Kuprianov, 2008).

A large number of studies on modeling of hydrodynamic characteristics of gas—solid fluidized bed (such as the minimum fluidization velocity and the pressure drop across the bed) have been devoted to columnar (cylindrical and prismatic) reactors/devices operated under "cold" (ambient) conditions. Depending on properties and characteristics of the bed material and those of a fluidizing agent, the behavior of a columnar fluidized bed is represented by different fluidization types, the major of them being bubbling, slugging, channeling and jetting (Geldart, 1973; Kunii and Levenspiel, 1991).

Though the conventional (i.e., columnar) fluidized-bed systems have been widely used in various industrial applications, there are some inherent drawbacks, such as channeling/slugging behavior (especially, at high superficial gas velocity) deteriorating the gas-solid mixing quality of a fluidized bed. In cylindrical/prismatic fluidized beds with significant diameter and height, pressure at the bed bottom plane is much greater than that at the bed top. So, fluidizing gas tends to expand when rising through the bed. As a result, the gas velocity increases continuously along the bed height and reaches its maximum at the bed top, leading eventually to a pressure fluctuation in the bed (Shi et al., 1984).

Compared to conventional fluidized beds, the hydrodynamic characteristics of non-cylindrical (tapered and conical) fluidized beds are reported to be quite different. In a

tapered/conical fluidized bed, the cross-sectional area of the bed increases along the bed height. This bed geometry results in a reduction of the gas velocity along the axial distance in the bed, and consequently, an insignificant pressure drop across the bed and therefore smooth bed behavior (Shi et al., 1984; Peng and Fan, 1997; Li et al., 2003).

Peng and Fan (1997) investigated the fluidization regimes and characteristics of spherical glass beads of 1.2 mm diameter fluidized by water in a tapered bed. Fig. 2.1 depicts the flow regimes and the appearance at different stages of the bed behaviors. With increasing fluidizing velocity (*u*) related to the bottom plane of the bed, five sequent hydrodynamic regimes were observed in this liquid-solid bed: (1) the fixed-bed regime (when all bed particles were unmoved), (2) the partially fluidized-bed regime (when the

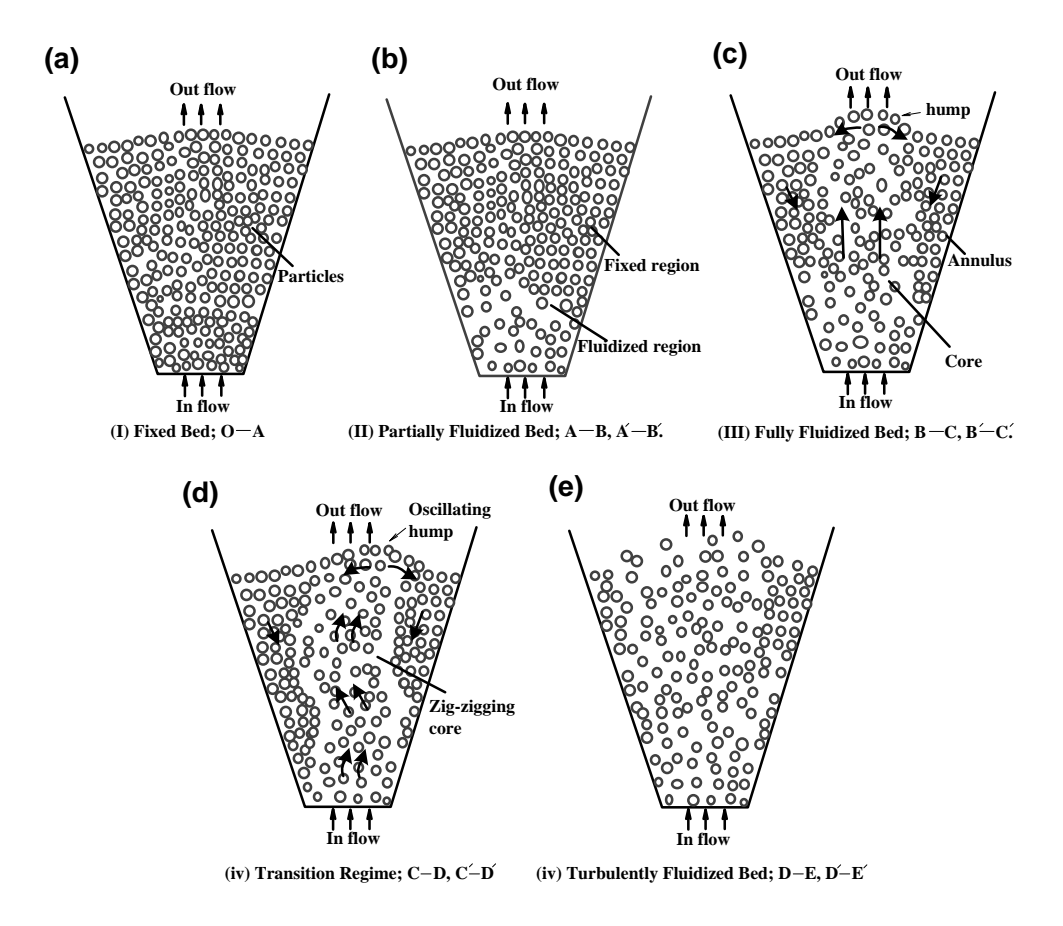


**Fig. 2.1** Flow regimes in a tapered fluidized bed: (a) fixed-bed regime, (b) partially fluidized-bed regime, (c) fully fluidized-bed regime, (d) transition regime, and (e) turbulent fluidized-bed regime (Peng and Fan, 1997).

bed particles close to the air distributor were fluidized, while the particles in upper bed layers were still unmoved), (3) the fully fluidized-bed regime (when the bed particles were fluidized in all bed layers), (4) the transition regime (showing a gradual change to the turbulent bed behavior), and (5) the turbulent fluidized-bed regime. The magnitude of the net pressure drop  $(-\Delta P_N)$  as a function of the superficial fluid velocity (u) at the bed inlet is shown in Fig. 2.2, along with the hydrodynamic characteristics for two experimental procedures: (1) for bed fluidization and (2) bed defluidization.

In the test for bed fluidization, with increasing u within the fixed-bed regime  $(O \rightarrow A)$ , the net pressure drop across the bed increased until its maximum value,  $\Delta P_{max}$ , was attained. However, in this regime, the bed was characterized by constant voidage across the bed volume and unchanged height, as illustrated in Fig. 2.1a. At critical Point A, the lowest layer of the bed began to fluidize (see Fig. 2.1b). The superficial fluid velocity, starting to the partially fluidized bed regime, was termed the minimum velocity of partial fluidization  $(u_{mpf})$ . In the partially fluidized-bed regime  $(A \rightarrow B)$ , the bed particles moved freely in the bottom bed region, where the bed voidage was greater than that in the upper (fixed-bed) region. With increasing u, the pressure drop reduced from –  $\Delta P_{max}$  to  $-\Delta P_b$  at Point B (as illustrated in Fig. 2.2), where the fully fluidized-bed regime started its occurrence. The corresponding superficial fluid velocity at Point B was termed the minimum velocity of full fluidization ( $u_{\rm mff}$ ). At this point, the entire bed was involved in fluidization, exhibiting a random appearance of small-size bubbles (splashes) on the bed surface. In the fully fluidization regime (path  $B \rightarrow C$ ), with increasing u in the range greater than  $u_{\rm mff}$ , the net pressure drop stayed (almost) constant. At this stage, the fluidizing fluid released from the bed through the hump, formed on the top surface of the bed. When this occurred, the particles in the central zone of the bed accelerated in the upward direction, thus forming a core region with a relatively large voidage, while the particles in the peripheral zone moved downward at a rather low speed, forming the annulus of a lower voidage compared to the central zone, as shown in Fig. 2.1c. As observed during the transition regime of the bed (C $\rightarrow$ D), when u reached Point C, the hump started oscillating in the horizontal direction, forming a zig-zagging core, as seen in

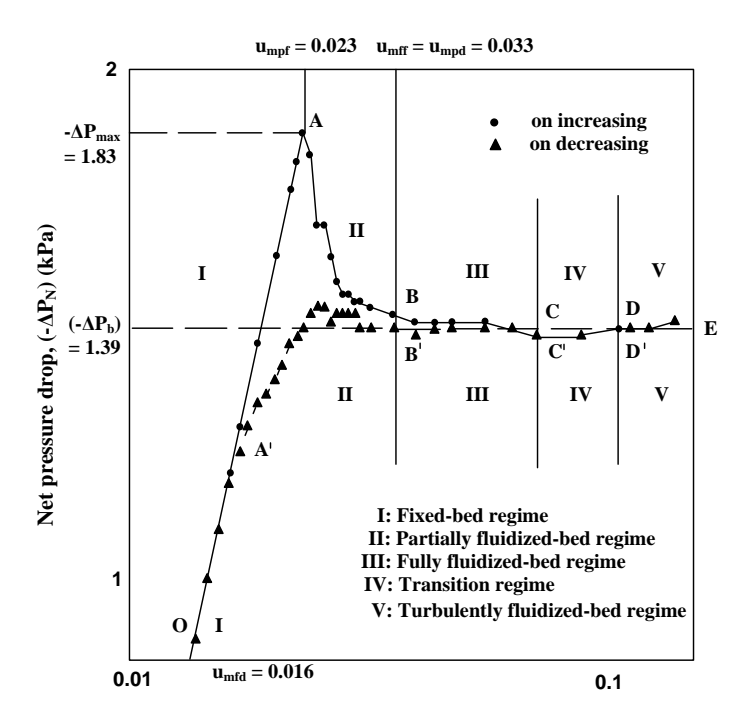


**Fig. 2.2** Net pressure drop as a function of the superficial fluid velocity (*u*) at the inlet of the tapered bed (Peng and Fan, 1997).

Fig. 2.1d. However, the pressure drop fluctuated insignificantly in this transition regime. At Point D, when u was sufficiently high, the bed entered into the turbulent fluidized-bed regime, whereas the net pressure drop still remained at nearly the same level as in the proceeded regime. However, the bed turbulency in this regime was extremely high. As seen in Fig. 2.1e, the bed particles in this turbulent fluidized-bed regime moved randomly, showing however, no zig-zagging core.

In the test for bed defluidization, the pressure drop as a function of decreasing u was represented by the path  $E \rightarrow D' \rightarrow C' \rightarrow B' \rightarrow A' \rightarrow O$ , as seen in Fig. 2.2. At Point B', where the superficial velocity was equal to the maximum velocity of partial defluidization ( $u_{mpd}$ ), the bed regime was "switched" from the fully fluidized bed to the partially fluidized bed. When u was reduced to the maximum velocity of full defluidization ( $u_{mfd}$ ), the fluidization stopped at all the bed layers.

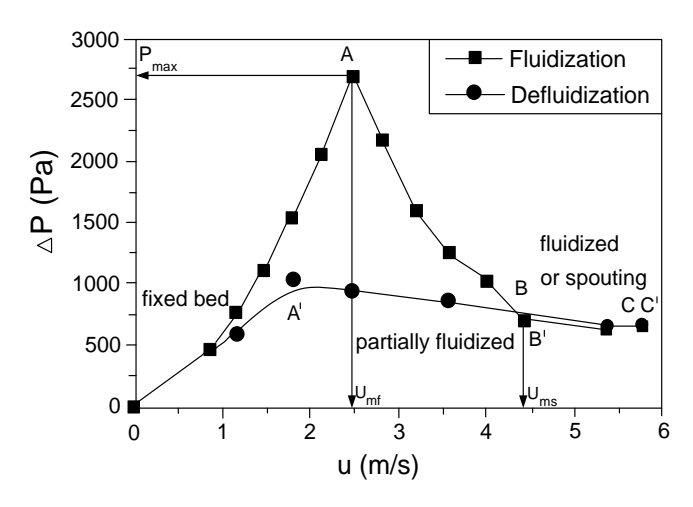


**Fig. 2.3** The  $\Delta p$ -u diagram for a gas-solid conical bed (Jing et al., 2000).

Studies on conical fluidized beds with various bed materials and fluidizing agents revealed bed behavior and characteristics quite similar to those of the tapered fluidized beds regimes (Kwauk, 1992; Jing et al., 2000; Li et al., 2003).

Jing et al. (2000) studied the hydrodynamic behavior of the Geldard-D ceramic spheres in a conical test rig, using air as a fluidizing agent. Fig. 2.3 depicts the  $\Delta p$ -u diagram for the bed during fluidization and defluidization processes investigated in this study. For the limited range of superficial air velocity (u), the bed exhibited three flow regimes: (i) the fixed-bed regime, (ii) the partially fluidized-bed regime, and (iii) the fully fluidized-bed regime. In the fixed-bed regime, the dependence of the pressure drop across the bed ( $\Delta P$ ) on the superficial air velocity (u) from the fluidization test was represented by a non-linear (parabolic-like) profile. However, this conical bed showed behavior similar to the above tapered bed. At (critical) Point A, when u reached the minimum velocity of partial fluidization, the pressure drop attained a significant level ( $\Delta P_{max}$ ). With a further increase of u, the bed went through the partially fluidized-bed regime, showing a substantial reduction in  $\Delta P$ . At Point B, when u was sufficiently high, the fluidized bed turned into one of the fluidization regimes: (1) slugging (at the cone angle of 20°), (2) bubbling fluidization (at the cone angle of 40°), or (3) spouting (at the cone angle of 60°), as reported by Jing et al. (2000) and Olazar et al. (1992).

The effects of the bed particle size and bed geometry have been reported to be important. When using Geldart-B particles (typical for biomass-fueled fluidized-bed combustion systems using inert bed materials), the bubbling fluidization regime likely occurs in a gas-solid bed of  $30\text{--}45^{\circ}$  cone angle and 20--40 cm static bed height, as revealed by experimental results from some studies (Jing et al., 2000; Permchart and Kouprianov, 2004; Kaewklum and Kuprianov, 2008; Arromdee and Kuprianov, 2012a). However, the Geldart-D and even Geldart-B particles may be in the spouting fluidization regime, especially, in beds with a relatively high cone angle (e.g.,  $60^{\circ}$ ), when the pressure drop across the bed gradually decreases with higher u. Besides, an undesirable slugging fluidization regime may occur in beds of groups of B/D particles when using small (less than  $30^{\circ}$ ) cone angles (Olazar et al., 1992; Jing et al., 2000).

Arrondee and Kuprianov (2012a) studied the hydrodynamic characteristics of a conical bed of a 40° cone angle and 0.25 m inner diameter of the bed bottom plane. Alumina sand of 300–500  $\mu$ m particle sizes was used as the bed material in the experiments, while air was the fluidizing agent. The tests were performed at three different static bed heights (BHs): 20 cm, 30 cm, and 40 cm. Fig. 2.4 shows the  $\Delta p$ -u diagram of the conical bed using alumina sand for three selected BHs (solid dots), as well as the contribution of the pressure drop across the air distributor to the total pressure drop

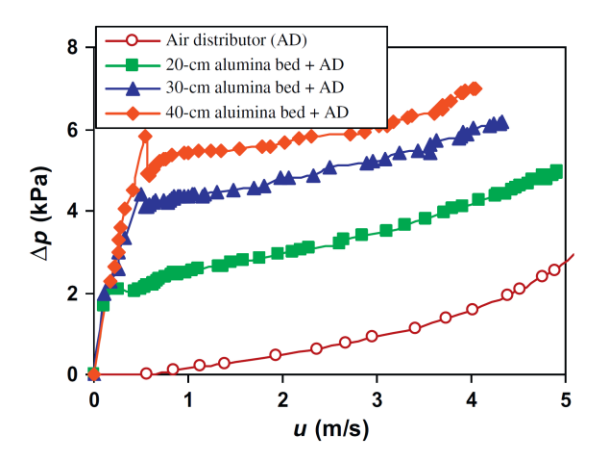


Fig. 2.4 Pressure drop across the air distributor versus operating air velocity and the  $\Delta p$ — u diagram of the alumina conical bed for different static bed heights

(Arromdee and Kuprianov, 2012a).

 $\Delta p$  for variable u (open dots). The authors found that, for each BH, the bed exhibited three sequent flow regimes when varying u from 0 to 4–5 m/s: (1) the fixed-bed regime, (2) the partially fluidized-bed regime, and (3) the full bubbling fluidized-bed regime. From Fig. 2.4, BH affected on the hydrodynamic characteristics ( $u_{\rm mpf}$  and  $u_{\rm mff}$ ) of the bed, showing some increase of these characteristics (a feature typical for conical gas—solid beds, as reported by Jing et al. (2000) and Kaewklum and Kuprianov (2008), which resulted in an increase of the corresponding maximum pressure drop across the bed.

As revealed in Fig. 2.4, with increasing the superficial air velocity (u) in the bubbling fluidized-bed regime,  $\Delta p$  was found to gradually increase. This fact was mainly due to the contribution of the pressure drop across the air distributor. Therefore, if the pressure drop across the air distributor were subtracted from  $\Delta p$ , the pressure drop across only the fluidized bed,  $\Delta p_{\text{bed}}$ , would be then represented by an invariant characteristic (i.e.,  $\Delta p_{\text{bed}} \approx \text{constant}$ ), showing trends similar to those in the above-mentioned literature sources.

#### 2.2 Hydrodynamic characteristics of a conical fluidized bed using binary mixtures

In a real fluidized-bed combustion system, the fluidized bed consists of the particles of material, as well as the fuel-char and fuel-ash particles. According to Basu (2006), the fuel particles account for from 1% to 3% (by wt.) of all solid matter in the bed of a typical fluidized-bed boiler. To investigate the effects of biomass presence in a fluidized bed of inert material, a cold-state hydrodynamic study of a binary (sand-biomass) mixture fluidized in conical beds has been performed and reported (Arromdee and Kuprianov, 2012a). As revealed by this study, the hydrodynamic behaviors of the bed with the binary mixture are influenced by the properties of both bed material and biomass, the major effects being produced by the density and particle size of the two components of a binary mixture.

The fluidization characteristics of binary mixtures were studied in a cone-shaped bed of 40° cone angle using alumina sand as the bed material by Arromdee and Kuprianov (2012a). Prior to cold-state tests, alumina sand was premixed with shredded peanut shells in different proportions (2.5–10 wt.%) of the biomass in the binary mixture.

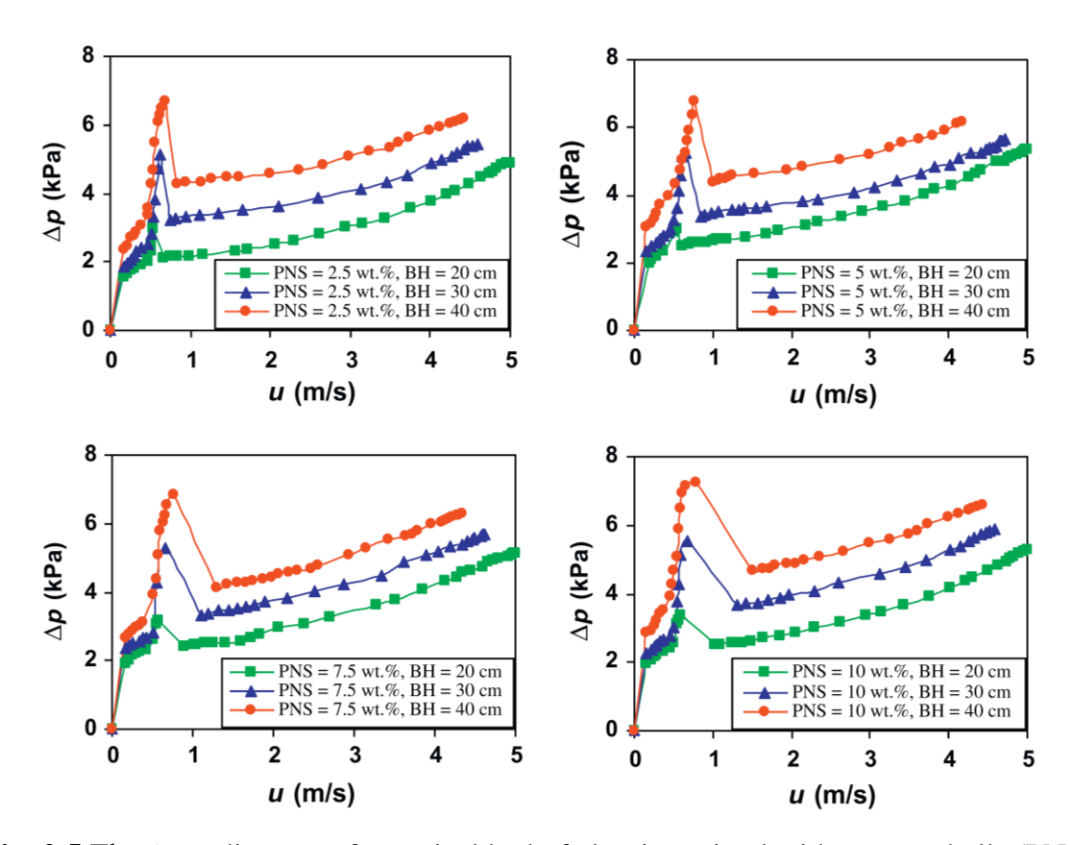


Fig. 2.5 The  $\Delta p$ -u diagram of a conical bed of alumina mixed with peanut shells (PNS) for variable weight percentage of biomass in the binary mixture for different static bed heights (Arromdee and Kuprianov, 2012a).

Fig. 2.5 compares the  $\Delta p$ -u diagram of the conical bed with different biomass-sand mixtures between the static bed heights of 20 cm, 30 cm, and 40 cm, presented in individual graphs for distinct biomass fractions in the mixture. Like in the previous-discussed study with pure alumina, four fluidization regimes were observed in the bed with a binary mixture. However, the gradient  $d(\Delta p)/du$  for the binary mixtures, especially in the fixed-bed regime, was not as smooth as that for pure alumina sand. This result was explained by presence of peanut shells in the binary mixture, which likely led to the higher friction force between the particles of alumina sand and biomass compared to the pure bed material, resulting in a greater momentum of airflow required to overcome the friction force.

With increasing wt.% of biomass in the binary mixture at a fixed bed height, both  $u_{\rm mpf}$  and  $u_{\rm mff}$  somewhat increased, and the effect from static bed height strengthened with the higher static bed. For a bed of 30 cm height, with increasing the percentage (weight fraction) of biomass in the binary mixture from 2.5 to 5 wt.%, the  $u_{\rm mff}$  increased from 0.7 to 0.9 m/s, whereas the corresponding total pressure drop (at  $u_{\rm mff}$ ) was nearly the same, i.e., irrespective of the biomass fraction. The difference between  $u_{\rm mff}$  and  $u_{\rm mpf}$  in Fig. 2.5 increased with a higher percentage of biomass.

#### 2.3 Conventional fluidized-bed combustion of biomass fuels

A number of combustion technologies, including grate-fired, suspension-fired, and fluidized-bed combustion systems, have been used for burning biomass (Werther et al., 2000). However, as outlined in Section 3, the fluidized-bed combustion technology has been recognized to be the best option for energy conversion from biomass.

A large pool of research publications have been devoted to individual firing of various biomasses in conventional fluidized-bed combustion systems (furnaces/combustors), typically of a prismatic shape with a single (bottom) air supply. In most biomass-fueled fluidized-bed systems, inert bed material (e.g., silica/quartz sand) fluidized by combustion air is used to sustain biomass ignition and combustion at the furnace/combustor bottom region.

The major gaseous emissions from a conventional fluidized-bed combustion system, NO<sub>x</sub> and CO, are reported to depend on fuel properties (contents of N, S, moisture and ash), as well as on the combustor load and excess air, affecting the bed temperature (Kuprianov et al., 2006; Permchart and Kouprianov, 2004; Werther et al., 2000). Excess air and bed temperature are the most important operating variables (parameters) of a fluidized-bed combustion. Typically, the bed temperature is ranged from 750 °C to 950 °C, while excess air is adjusted within the range from 20% to 60% when firing various biomass fuels. As revealed by a large number of research works, there is an opposite trend in behavior of NO<sub>x</sub> and CO emissions when varying combustion conditions. With increasing both excess air and combustion (bed) temperature, the NO<sub>x</sub> emissions increase, basically following the fuel-NO formation

mechanism, while the CO emission from the combustion system decreases at a rate strongly depending on the levels of excess air and temperature (Kouprianov and Permchart, 2003; Kuprianov et al., 2005). It should be noted that high levels of CO and hydrocarbons in the region of biomass devolatilization leads to a substantial mitigation of NO formation in the vicinity of fuel injection (Arromdee and Kuprianov, 2012; Kuprianov and Arromdee, 2013), and, consequently, to a reduction of the  $NO_x$  emissions, thus affecting the emission performance of a combustion system.

However, a number of research studies have reported unacceptably high emissions of  $NO_x$  and CO, particularly when burning some biomasses with elevated fuel-N in conventional fluidized-bed combustion systems.

Akpulat et al. (2010) studied the fluidized-bed combustion of olive cake. As revealed by this study, burning this biomass with elevated fuel-N resulted in the extremely high NO emission (up to 1400 mg/Nm<sup>3</sup>, at 6% O<sub>2</sub> and on a dry gas basis), particularly at higher excess air values.

Kaynak et al. (2005) investigated the combustion of peach and apricot stones in a bubbling fluidized-bed combustor using quartz sand as the inert bed material. The fuel feedrate in the tests on this combustor was ranged from 5 g/min to 20 g/min. The combustion efficiency (including effects of heat losses due to both CO and C<sub>x</sub>H<sub>y</sub> emissions) was reported to be in the range of 96–97% for peach stones and 93–96% for the apricot stones, when excess air was ranged from 40% to 100% during the tests with both fuels. An increase in excess air had a weak effect on the CO emission for firing apricot stones, which fluctuated around 1500 mg/Nm<sup>3</sup>. However, in the case with peach stones, the CO emissions increased from 6500 mg/Nm<sup>3</sup> to 13,500 mg/Nm<sup>3</sup> with increasing excess air. The C<sub>x</sub>H<sub>y</sub> emissions for the two biomasses increased (in almost linear relationship with excess air), remaining in the range of 340–460 mg/Nm<sup>3</sup>, i.e., at a substantial level. When burning these stones, the NO emission slightly increased as excess air was higher. The average NO emission was found to be 280 mg/Nm<sup>3</sup> and 250 mg/Nm<sup>3</sup> for apricot and peach stones, respectively, despite the high levels of CO and C<sub>x</sub>H<sub>y</sub> in flue gas. Higher NO emissions from firing apricot stones can be attributed to the

higher fuel-N compared to peach stones. Due to insignificant fuel-S, the SO<sub>2</sub> emission for the two biomass fuels was negligible.

#### 2.4 Combustion techniques with alternative design and hydrodynamics

A number of research studies have been recently performed on a fluidized-bed combustor with cone-shaped bed (referred to as 'conical FBC') for firing some Thai biomasses, such as rice husk, sugar cane bagasse, various shells, and oil palm residues (Kuprianov and Arromdee, 2013; Kuprianov et al., 2006; Kuprianov et al., 2005). Compared to a columnar fluidized-bed combustion system (combustor/furnace), the conical FBC exhibits some apparent benefits, such as: (i) a relatively small amount of inert bed material, (ii) shorter start-up time of the combustor, and (iii) lower pressure drop across the fluidized bed (for identical bed material and static bed height), leading to the reduced operating costs of the combustor (Ninduangdee and Kuprianov, 2014; Ninduangdee and Kuprianov, 2013).

The studies revealed that these biomasses can be burned in the proposed combustor of the 200–350 kW<sub>th</sub> heat input (depending on biomass type) with high combustion efficiency and good environmental performance. Fuel properties (fuel-moisture, fuel-N, biomass chemical structure and particle size) and operating conditions (combustor load and excess air) have apparent effects on the combustion and emission performance of the reactor. At optimum operating conditions, the combustor can be operated with the combustion efficiency of up to 99.5%, ensuring an acceptable level of the CO and NO emissions (meeting the corresponding domestic emission standards for environmental protection).

Madhiyanon et al. (2006) performed a study on firing Thai rice husk in a novel cyclonic fluidized-bed combustor ( $\psi$ -FBC) of the 100 kW<sub>th</sub> heat input. High (98.4–99.6%) combustion efficiency at a rather low CO emission, 50–400 ppm (at 6% O<sub>2</sub>), were achieved when firing rice husk at excess air of 67–130%. However, the NO emission from this combustor was high, at a level of 350–425 ppm (at 6% O<sub>2</sub>), mainly due to high bed temperature (>1000 °C) and excess air, exceeding the NO emission limit established in this country for local biomass-fuelled industrial applications.

A short-combustion-chamber fluidized-bed combustor (SFBC) has been recently proposed and studied by Madhiyanon et al. (2010) for firing rice husk at the heat input of 250 kW<sub>th</sub> and excess air of 76%. Quite low CO emission, 15–130 ppm (at 6%  $O_2$ ), leading to the rather high combustion efficiency (> 97%) were achieved under these operating conditions, whereas the NO emission was high, 230–350 ppm (at 6%  $O_2$ ), exceeding the national NO emission limit.

The conical fluidized-bed combustor, as well as  $\psi$ -FBC and SFBC techniques, have been tested for co-firing biomass and/or biomass/coal (as addressed below).

#### 2.5 Staged combustion technologies

Staged combustion technologies (using air staging or/and fuel staging) have been developed and implemented on various combustion techniques with the aim to minimize NO<sub>x</sub> emissions (Nussbaumer, 2003; Salzmann and Nussbaumer, 2001).

In air-staged combustion, primary air is supplied into the bed region with a deficiency of air, while secondary air is injected into the combustion chamber with a certain excessive amount (Nussbaumer, 2003; Okasha, 2007). The combustibles, such as CH<sub>4</sub>, H<sub>2</sub>, and CO, formed in the bottom region at a (primary) air deficiency are characterized by their high concentrations, mitigating NO formation in this region (as mentioned above). However, in the second stage (upper level), some part of NO can be formed by secondary air (Leckner et al., 2004), thus lowering the NO reduction efficiency of this method.

Okasha (2007) burned rice straw in an atmospheric bubbling fluidized-bed combustor of 0.3 m inner diameter and 3.3 m height. Silica sand of 0.25–0.5 mm in diameter and 30 cm bed height was used as bed material. Prior to experiments, the biomass was pelletized. In all experiments, total excess air was constant, about 20%, whereas the proportion of secondary air was varied from 0% to 40% (of total air) at distinct values of bed temperature: 750 °C, 800 °C and 850 °C.

For each bed temperature, the CO emission increased with the higher percentage of secondary air, mainly due to (i) a greater carryover of gaseous combustibles (volatiles) from the combustor bottom to the freeboard, and (ii) rather low intensity of mixing

between the combustion products from the bed zone and the secondary air. The CO emission was found to increase with lowering bed temperature, likely due to the diminishing of the combustibles oxidation rate (despite increased residence time of gases in the bed region). However, an increase in the amount of secondary air resulted in the lower NO<sub>x</sub> emissions, mainly due to the reduced temperature and increased concentrations of CO and light hydrocarbons in the fluidized bed. In addition, an increase in secondary air led to the higher heat loss with unburned carbon, resulting in the diminishing of the combustion efficiency. As shown in this study, the bed temperature of 850 °C and secondary air of 30% ensured the highest combustion efficiency (nearly 98%) at quite low NO<sub>x</sub> emissions (about 120 ppm), whereas the CO emission was high (about 1500 ppm).

Youssef et al. (2009) studied the effects of excess air ratio and air staging on the combustion characteristics of four types of biomass fuels (wheat straw, sawdust-wood, cottonseed burs, and corncobs) in a circulating fluidized-bed combustor. In this work, the feed rate of the biomass fuels was varied from 8.5 kg/h to 11.85 kg/h to maintain bed temperature at a fixed level, while varying the excess air ratio from 1.08 to 1.4. As the fuels were burned using air staging, secondary air pipes were installed at levels of 0.3 m and 0.8 m above the combustor bottom. During the experiments, the primary-to-total air ratio was controlled at a constant value of 0.5, whereas the secondary-to-total air ratio was maintained at about 0.15 at the first level and 0.25 at the second one. The ratio of carrier air to total air was about 0.1. As reported in this study, at (total) excess air of 24%, the emissions from the combustor can be adjusted at minimized levels for the selected proportions of primary and secondary air. However, a relatively low density of biomass causes an elevated carryover of fuel from the combustor bottom, leading to deterioration in the fuel burnout and, consequently, higher CO emissions, whereas the NO<sub>x</sub> emissions for all the fuels were at an acceptable level (below 300 mg/m<sup>3</sup> at 7% O<sub>2</sub>). For this reason, sawdust and straw with their light particles cannot be recommended for their utilization in circulating fluidized-bed combustors/furnaces, while the high-density burs and corncob

are suitable for high-efficiency and low-emission combustion in the proposed system with air staging.

The effects of air staging were also studied for firing cotton stalk in two combustion techniques: the 0.2 MW<sub>th</sub> bubbling fluidized-bed combustor (Sun et al., 2008) and the 0.5 MW<sub>th</sub> circulating fluidized-bed combustor (Sun et al., 2010) at relatively high secondary-to-total air ratio (SA/TA), when maintaining total excess air in the two combustors at a constant value: 37% and 32%, respectively. The NO emission of both combustors (at 6% O<sub>2</sub>) decreased: from 183 ppm to 120 ppm, when changing SA/TA from 0.37 to 0.58 in the bubbling fluidized-bed combustor, and from 141 ppm to 127 ppm, when switching SA/TA from 0.40 to 0.47 in the swirling fluidized-bed combustor. However, the CO emission of the combustors did not show a single trend: with increasing SA/TA, this emission was roughly the same and relatively low (190–270 ppm) for the former combustor, but exhibited a substantial reduction, from 940 ppm to 320 ppm, for the latter one.

In the fuel-staged combustion, a primary fuel is fed into a bed region and therefore fired at excess air. Meantime, the rest part of fuel (or different, secondary fuel) is supplied into the above zone (with no air supply) to establish preferable conditions for NO reduction (high concentrations of CO and  $C_xH_y$  in the vicinity of the secondary air injection). This leads to the fuel biasing in the axial direction inside the combustor. Suheri and Kuprianov (2015) reported the results from the co-firing of two oil biomasses, palm kernel shell (primary fuel) and empty fruit bunch (secondary fuel), in a conical fluidized-bed combustor using fuel-staging at conventional (bottom) air supply into the reactor. Under optimal conditions (0.15 energy fraction of secondary fuel and 50% excess air), the combustor can be operated with high (about 99%) combustion efficiency, while reducing the NO emission by about 50% compared to firing pure palm kernel shell at similar heat input.

However, the combustion method, involving the fuel staging at conventional air supply, needs further studies with the aims to determine (i) the most effective biomass-

biomass couples, ensuring an essential NO reduction, and (ii) a general potential of this low-cost method.

#### 2.6 Co-firing biomass fuels in a fluidized bed

Kuprianov et al. (2006) studied on the co-firing of premixed 'as-received' sugar cane bagasse and rice husk in a conical fluidized bed combustor with the aim of achieving more effective utilization of these biomasses. It was found that the co-firing at the rice husk energy fraction greater than 0.6 resulted in the sustainable combustion, with the 95–96% combustion efficiency, and lower NO emissions compared to firing pure rice husk. Through the co-firing with rice husk, an effective use of 'as-received' sugar cane bagasse becomes feasible for energy conversion in fluidized-bed combustion systems, whereas the attempts to burn raw bagasse were unsuccessful (Kuprianov et al., 2005).

Coal was co-fired with rice husk using the  $\psi$ -FBC and SFBC techniques (reviewed above). As in the discussed cases of firing pure rice husk, the CO emission and the combustion efficiency were quite acceptable, whereas the NOx emissions was elevated (Madhiyanon et al., 2009), exceeding the national emission limit for this pollutant.

#### 2.7 Reburning technology

Reburning has been suggested as the most effective solution to reduce the  $NO_x$  emissions from different combustion systems. Fig. 2.6 depicts the schematic of a coal-fired boiler using reburning. It can be seen in Fig. 2.6 that this combustion method involves fuel staging with: (1) the primary combustion zone where primary (main) fuel burns; and (2) the reburn zone where the reburn fuel (typically, natural gas) injected into the combustion chamber creates the fuel-rich conditions (with high concentration of H, CH, CH<sub>2</sub> and radicals), causing some of  $NO_x$  produced in the primary combustion zone to react with these radicals, thus converting  $NO_x$  to molecular nitrogen ( $N_2$ ) and other nitrogenous species with the overall  $NO_x$  reduction effect. The  $CH_i$  radicals react with the  $NO_x$  entering the reburning zone through the following reactions (Adams and Harding, 1998; Casaca and Costa, 2009; Salzmann and Nussbaumer, 2001):

$$CH_i + NO = HCN + O (2.1)$$

$$NO + NH_i = N_2 + H_2O$$
 (2.2)

Hydrogen cyanide produced in (R1) is converted to  $N_2$  via the following reactions:

$$O + HCN = NCO (2.3)$$

$$NCO + H = NH + CO (2.4)$$

$$NH + H = N + H_2$$
 (2.5)

$$N + NO = N_2 + O \tag{2.6}$$

Overfire air must be added in the region above the reburn zone (as seen in Fig. 2.7) to ensure complete combustion. The key process design parameters of the reburning are: stoichiometric ratio (SR) at the primary zone, total excess air, energy fraction of reburn fuel, and residence time ( $\tau$ ). By using reburning, up to 70% NO<sub>x</sub> reduction is

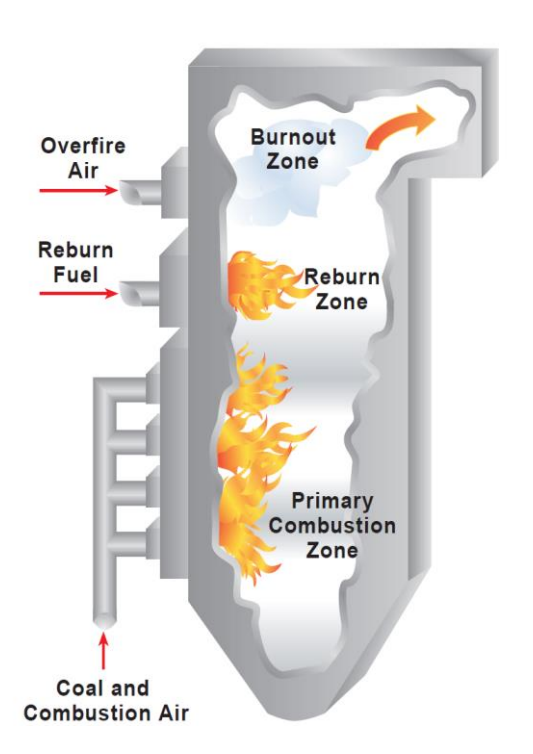


Fig. 2.6 Schematic of reburning technology in coal-fired boiler (DOE, 2015).

achievable with no adverse effects on boiler operation (Harding and Adams, 2000; Salzmann and Nussbaumer, 2001; Smoot et al., 1998).

Many fuels have been investigated as a reburn fuel, e.g., natural gas, liquid and solid fuels (Ballester et al., 2008; Kicherer et al., 1994). Table 2.1 summarizes the results from a demonstration project on the reburning technology using different reburn fuels (DOE, 2015). As seen in Table 2.1, the percentage of NOx reduction varied from 30% to over 70%, depending on (i) furnace type and scale, (ii) reburning fuel and (iii) simultaneous use of low-NOx burners.

Compared with other fuels, biomass as a reburning fuel has several advantages: (i) biomass fuels contain lower levels of sulfur and nitrogen, suggesting their lower SO<sub>2</sub> and NOx emissions, (ii) they are renewable and nearly CO<sub>2</sub>-neutral fuels, and (iii) they have a higher content of volatile matter, leading to a greater reduction of NOx (Ballester et al., 2008; Harding and Adams, 2000).

Harding and Adams (2000) conducted experiments using hardwood and softwood as a reburning fuel in a pilot-scale test rig to determine the feasibility of reburning with wood, and compare the effectiveness of wood as a reburning fuel to coal and natural gas. In addition, effects of wood properties (moisture content, molecular composition, particle size) on the  $NO_x$  reduction was also investigated in this study. Experimental results

**Table 2.1** Demonstration projects for NO<sub>x</sub> emissions reduction by reburning technology.

Boiler	Reburning fuel	NO and SO <sub>2</sub> reduction
60–110 MW <sub>e</sub> cyclone, coal-fired	Coal	36–52%, w/bituminous
40–75 MW <sub>e</sub> , tangential	Natural gas 15–25%	NO <sub>x</sub> : 67%
		SO <sub>2</sub> : 52–80%
20–33 MW <sub>e</sub> , cyclone	Natural gas 22–33%	NO <sub>x</sub> : 60–66%
		SO <sub>2</sub> : 32–63%
172 MW <sub>e</sub> , wall-fired	Natural gas 5–20%	NO <sub>x</sub> : 30% (using low-NO <sub>x</sub> burners)
		NO <sub>x</sub> : 60-73% (using gas reburning
		coupled with low-NO <sub>x</sub> burners)

Source: The U.S. Department of Energy (DOE, 2015).

showed the NO<sub>x</sub> reduction of about 70% at 10–15% wood heat input. The stoichiometric ratio in the reburning zone was the most important variable affecting the NO<sub>x</sub> reduction. The highest reduction was at a reburn stoichiometric ratio of 0.85. The NO<sub>x</sub> reduction efficiency decreased to about 40-50% at higher stoichiometric ratios (0.9 < SR < 0.95) and to 30% at the stoichiometric ratio of approximately 1.0. The NO<sub>x</sub> reduction was strongly dependent on the initial NO<sub>x</sub> concentration and only slightly dependent on temperature: the temperature increased the NO<sub>x</sub> reduction efficiency. The wood properties including fuel-moisture and particle size exhibited insignificant effects on the NO<sub>x</sub> reduction. However, fuel-N in wood had important effects on the NO<sub>x</sub> emissions level. The findings also revealed that the CO emission was quite high, reaching maximum value of about 1600 ppm, when using coal as a reburn fuel. However, when using wood as the reburn fuel, CO emission was found to be at quite low level (e.g., typically below 40 ppm), but, higher than the CO emission obtained for natural gas as reburn fuel (less than 20 ppm). The authors therefore suggested wood can be effectively used as a reburning fuel which is capable to reduce NO<sub>x</sub> emission as compare to natural gas or coal.

Kicherer et al. (1994) examined the  $NO_x$  reduction during the combustion of pulverized fuel using different reburn fuels. Among them, light fuel oil (almost 100% volatiles), natural gas (100% volatiles) and straw (75% volatiles) led to the higher  $NO_x$  reduction compared to coal (with 32% volatiles). When using light fuel oil, natural gas, and straw, substantial burnout efficiency was observed even at extremely high fuel-rich conditions in the reburn zone. Temperature had important effects, since a slow release of volatiles likely delayed the reactions between  $CH_i$  radicals and NO.

Casaca and Costa (2005) investigated the effectiveness of the reburning process using rice husk, natural gas, and ethylene as reburn fuels in a large-scale laboratory furnace. As found in this study, the reburn zone residence time had an important effect on the  $NO_x$  reduction efficiency. With increasing this operating parameter (from 0.31 s to 0.93 s), the NO reduction was greater. The findings revealed that at the residence time of

about 0.7 s, the reburning performance of rice husk was comparable to that of natural gas, showing about 60% NO<sub>x</sub> reduction at the reburn fuel fraction of 25-30%.

Ballester et al. (2008) performed an extensive experimental investigation of biomass (oak sawdust), used as reburn fuel, in a semi-industrial-scale furnace for the specified ranges of residence time (0.41–1.44 s) and stoichiometric ratio (0.85–1.05) at the reburn zone. For validation of experimental results, parallel testing with natural gas (NG) as reburn fuel was also conducted at similar operating conditions. As found in this study, oak sawdust significantly reduced NO<sub>x</sub> emissions. As compared to NG reburning, the NO<sub>x</sub> reduction was 4–10%; however, higher HCN concentrations were in the reburn zone, mainly, due to fuel-N in oak sawdust, and HCN was higher with increasing the proportion of biomass. Meanwhile, biomass generated CO and some hydrocarbon compounds responsible for the NO reduction in the reburn zone. Also, the presence of biomass char and ash particles contributed to the NO<sub>x</sub> reductions, however at a small extent.

Casaca and Costa (2009) investigated the effects of reburn fuel (rice husk) particle size on the  $NO_x$  reduction. As revealed by the experimental results, an increase in the biomass particle size resulted in lowered burnout efficiency, but more significant  $NO_x$  reduction. This fact can be explained by a high level of hydrocarbon compounds, such as  $CH_i$  and HCCO in the reburn zone, which were preferable for the  $NO_x$  reduction.

The reburning experiments with six types of biomasses (including rice straw, wheat straw, maize stalk, cotton stalk, rice husk and baggase), and wheat straw char were carried out in an entrained flow reactor by Lu et al. (2013). In this study, the effects of (i) biomass type, (ii) stoichiometric ratio (SR<sub>2</sub>) and reaction temperature ( $T_2$ ) in the reburn zone, (iii) biomass particle size ( $d_p$ ), and (iv) reburning fuel fraction ( $R_{\rm ff}$ ) on the NO reduction were investigated. The higher NO reduction efficiency (50–70%) was achieved at the range of SR<sub>2</sub> = 0.7–0.8, when controlling  $R_{\rm ff}$  within 20–25% during reburning of all the biomasses. Compared to other selected reburn fuels, cotton stalk with higher volatiles and alkali metals (K, Na) exhibited better performance in the NO reduction. In the

meantime, with increasing  $d_p$ , the NO reduction efficiency somewhat deteriorated insignificantly.

Shu et al. (2015) investigated the potential of NO reduction through reburning three biomasses (rice husk, sawdust and corncob) in a horizontal fixed-bed quartz reactor. The effects of (i)  $O_2$  entering the reburning zone, (ii) particle size of the biomass, and (iii) the initial NO concentration on the reduction efficiency were the focus of this study. The findings indicated that the biomass type had a significant influence on the NO reduction efficiency. The maximum NO reduction (55  $\pm$  2.4%) was found when using sawdust as reburn fuel, followed by corncob (44  $\pm$  2.1%) and rice husk (43  $\pm$  1.8%). Finer biomass particles promoted easier biomass devolatilization, which was beneficial for the NO reduction. The authors recommended that hydrocarbons in the fuel (mainly CH<sub>4</sub>) were mainly responsible for the reduction of NO emission, whereas CO and H<sub>2</sub> had little effects on this result.

From many literature sources, the reburning technology has been proven to have a great potential for the NO emission reduction from the combustion of various types of fossil fuels in boilers with burners. This technology is also flexible to the type of reburn fuel. However, information on the reburning technology in fluidized-bed combustion systems, especially in those fueled with biomass, is currently not available. Therefore, research study in this area is needed, particularly on the systems burning local biomasses.

#### 2.8 Ash-related problems in biomass-fueled fluidized-bed combustion systems

Much research have been recently addressed ash-related problems of biomass combustion, such as bed agglomeration, as well as slagging and fouling, which may likely occur in a fluidized-bed combustion system when firing biomass with elevated content of alkali-based compounds in fuel ash and using silica/quartz sand as inert bed material. Severe agglomeration is reported to result in bed defluidization, even at rela tively low bed temperatures (typical for biomass combustion), which eventually leads to complete shutdown of the system (Chaivatamaset and Tia, 2015; Khan et al., 2009; Werther et al., 2000). An important contribution to investigation of the agglomeration mechanisms has been recently made by Thai researchers.

During fluidized-bed combustion of corncobs and palm shells, a risk of intensive bed agglomeration and fast bed defluidization is found to be high, as revealed by the study of Chaivatamaset et al. (2011). In this study, palm shells and corncobs with the potassium content in ashes of 5.8 wt.% and 33 wt.% (as oxides), respectively, were fired in a laboratory-scale fluidized-bed combustor using quartz sand as the bed material. In all experiments, palm shells and corncobs were tested at identical operating conditions. As reported by the authors, bed agglomeration occurred within few hours of combustion tests. The agglomerate samples were collected and then analyzed for their physical and chemical prosperities through a SEM–EDS analysis. The findings indicated that inorganic materials in biomass ash, especially alkali metals, play a significant role in bed agglomeration. Corncobs, as compared to palm shells, showed a higher tendency to bed agglomeration mainly due to the greater potassium content in fuel ash, which likely form a large amount of potassium silicate melts.

Chaivatamaset et al. (2014) has reported the results from the combustion study of palm fruit bunch and rice straw with a substantial amount of  $K_2O$  (21.4% for palm fruit bunch and 10.6% for rice straw) in fuel ash. It was found that, within only an hour of combustor operation, the complete defluidization occurred. The study revealed that the presence of potassium silicates liquid phase, generated by the melting and chemical reaction, was responsible for the agglomeration. Collisions between the sand particles and the burning fuel particles were the dominant mechanism of the inorganic migration. The condensation/deposition of alkali salts on the bed particle surface was another mechanism, especially important in the case of firing palm bunch with substantially high potassium content.

Thus, when selecting biomass fuels for their use in the reburning combustion systems, special actions must be undertaken to prevent bed agglomeration (Khan et al., 2009; Nussbaumer, 2003).

#### 2.9 The alternative bed materials to extend bed agglomeration tendency

During the recent decade, a number of research studies have been performed on fluidized-bed combustion of K-rich biomasses using alumina sand and porous alumina as bed material. Some of these studies have been devoted to combustion efficiency and emission performance of fluidized-bed combustion techniques when burning cotton stalk, cedar pellets, and, peanut and tamarind shells (Shimizu et al., 2006; Sun et al., 2008a; Kuprianov and Arromdee, 2013). The studies revealed high (about 99%) combustion efficiency and acceptable gaseous emissions, whereas no features of bed agglomeration were found in these studies.

Shimizu et al. (2006) observed fast defluidization (within 1 h) when burning cedar pellets in a laboratory-scale bubbling fluidized-bed combustor using silica sand as bed material. However, these pellets were successfully burned in this combustor at relatively high (about 950 °C) bed temperature by using porous alumina as the bed material, which prevented bed agglomeration during all experiments.

Sun et al. (2008) used silica sand and alumina sand ( $Al_2O_3 = 79.2$  wt.%,  $SiO_2 = 13.1$  wt.%) as bed material in a 0.2 MW<sub>th</sub> bubbling fluidized-bed combustor firing cotton stalk with a substantial content of potassium ( $K_2O = 33\%$  in fuel ash). The combustor was operated at the bed temperature of 880 °C. The study showed a significant decrease in the bed agglomeration tendency after switching the bed material from silica sand to alumina sand.

Arromdee and Kuprianov (2012a) performed experiments for burning peanut shells, with an elevated content of  $SiO_2$  (13.9 wt.%) and  $K_2O$  (11.3 wt.%) in fuel ash, in the conical FBC using alumina sand ( $Al_2O_3 = 92\%$ ,  $SiO_2 = 3.5\%$ ) as the bed material. In this study, the time-related behavior of particle size and changes in the composition of the bed material during biomass combustion were investigated. Neither bed agglomeration nor significant ash deposit on the combustor walls was observed during the 30-h experimental tests, though the bed temperature in some test runs was about 930 °C. However, the contents of  $SiO_2$  and  $K_2O$  in the reused alumina significantly increased with operating time, indicating an intensive interaction between fuel ash and bed material fluidized in the bottom (conical) section of the combustor. As revealed by this study, the ash-sand interaction occurred likely via sequential formation of a coating on the surface of bed material particles, mainly due to the substantial proportions of Si and K in the fuel

ash. As a result, the (mean) particle size of the reused bed material showed some increase in volumetric diameter of the particles compared to the original (unused) alumina sand. Although no evidence of bed agglomeration was observed in this study, a substantial reduction of  $Al_2O_3$  (about 39%) in the reused bed material pointed at weakening capability to withstand bed agglomeration with operating time.

In spite of the gradual accumulation of the ash-related elements, causing a reduction of  $Al_2O_3$  in the bed, alumina sand and porous alumina have been proven as effective bed materials, which can prevent agglomeration for a relatively long operating time (Liu et al., 2007; Arromdee and Kuprianov, 2012a; Kuprianov and Arromdee, 2013).

Although the aforementioned studies have proven that alumina sand can effectively mitigate bed agglomeration, particularly through the "melt-induced" mechanism, Ergudenler and Ghaly (1993) reported an occurrence of bed agglomeration during gasification of wheat straw, with significant contents of potassium ( $K_2O = 36.2\%$ ), silica ( $SiO_2 = 27.3\%$ ), and calcium (CaO = 10.8%), in a fluidized bed of alumina sand. As reported by the authors, the agglomeration was observed at the bed temperatures over 920 °C, likely due to unfavorable proportion of the ash-forming elements (K, Si, and Ca), responsible for the formation of low-melting K and K–Ca silicates in ash, which resulted in the "melt-induced agglomeration" of the alumina sand bed.

Another bed material that can be alternatively employed in a fluidized bed is limestone (CaCO3). The use of limestone as a measure for bed agglomeration was proposed by Arvelakis et al. (2001). In this study, limestone of 0.5–1 mm particle sizes was used as a bed material in a lab-scale bubbling fluidized-bed combustor firing olive ( $K_2O = 12.55$  wt.%) and Danish straw residue ( $K_2O = 23.99$  wt.%). The experimental results revealed the capability of limestone to prolong the bed defluidization.

Fernández et al. (2006) used limestone with 0.25–2 mm particle sizes as bed material in a pilot plant (1 MW<sub>th</sub>) bubbling fluidized-bed combustor fired with almond shell and thistle, both rich in alkali metals and Ca, and containing a small amount of Si and P. Along with the high-efficiency capturing of fuel S, limestone effectively prevented

bed agglomeration during the entire experimental time. This fact can be attributed to an intensive interaction of Ca-rich fine particles (from attrition of calcined limestone) and char/ash melts, which resulted in an increased melting point of the ash eutectics and, therefore, decreased adhesiveness of the char/ash particles.

Dolomite (CaCO<sub>3</sub>· MgCO<sub>3</sub>) has been proposed as an alternative bed material, less prone to agglomeration. However, up to date, limited information on its applicability in fluidized-bed combustion systems has been presented. In light of the beneficial effects of Mg and Ca as additives, leading to the decreased agglomeration tendency (Fernández et al., 2008; Vamvuka et al., 2008), dolomite is expected to be a suitable bed material for biomass combustion. In addition, Bartels et al. (2008) reported in a review article the use of pre-calcined dolomite (CaO·MgO) as bed material in a heated batch fluidized bed (simulating a combustion system) with the addition alkali salts or alkali carbonates into the bed. The dolomite bed showed a great capability to fluidize at high operating temperatures, up to 1100 °C.

Nuutinen et al. (2004) performed a study on fluidized-bed combustion of plywood and wood residues using GR Granule (SiO<sub>2</sub> free) as a newly proposed alternative bed material. No bed agglomeration was observed during the tests, although a coating with two superimposed layers was found on the surface of the GR Granules by SEM–EDS analysis. The innermost coating layer was found to contain 40–65% calcium and 15–20% silicon, while a relatively thin outermost layer was rich in magnesium (up to 70%). Magnesium in the outer layer of the coating, originated from the attrition of the bed particles during biomass combustion. Due to the extremely high melting point of pure magnesium (2825 °C), this magnesium-rich outermost layer likely enhanced a bed capability to withstand bed agglomeration, whereas calcium inside the inner coating delayed and weakened the severity of bed agglomeration.

As reported by Bartels et al. (2008), the GR Granules were appropriate as the bed material when firing plywood (33% Na<sub>2</sub>O in the fuel ash) in four bubbling fluidized-bed boilers (5–25 MW) with the aim to prevent bed agglomeration. During 9-month operation, there was no bed agglomeration observed in all the boilers.

Olivine (49% MgO, 41% SiO<sub>2</sub>, and 8.4% Fe<sub>2</sub>O<sub>3</sub>) and blast-furnace slag (34% SiO<sub>2</sub>, 32% CaO, and 18% MgO) have been used as counter measures for bed agglomeration during fluidized-bed combustion of woody and olive residues, as well as wheat straw (Burs et al., 2004; De Geyter et al., 2007; Davidsson et al., 2008; Grimm et al., 2012). The combustion experiments for burning the residues revealed a significant decrease in the bed agglomeration tendency after switching the bed material from quartz sand to olivine or blast furnace slag. This result was basically due to the lower reactivity of ash-forming K and Ca to both olivine and blast-furnace slag, compared to quartz/silica sand. Fine solids, which were originated from the attrition of bed particles of the two bed materials with a substantial content of Mg, facilitated the formation of a Mg-rich outer layer on the surface of bed particles, protecting them from agglomeration. However, like with an alumina sand bed (Ergudenler and Ghaly, 1993), in the tests for burning wheat straw, both olivine and blast-furnace slag was subject to severe agglomeration.

However, as follows from the above overview, alternative bed materials can only prevent "coating-induced" agglomeration, while a risk of "melt-induced" agglomeration may still exist. In addition, there is a lack of information regarding: (i) the impact of the (alternative) bed material type on combustion and emission characteristics of a biomassfueled fluidized-bed combustor, (ii) the role of attrition of the bed particles in mitigating bed agglomeration, and (iii) the long-term (time-related) behavior of alternative bed materials and particulate matter (emitted from a reactor) during the combustion of high-alkali biomass.

## Chapter 3

#### **Materials and Methods**

#### 3.1 The selected fuels and bed materials

A selection of primary and secondary fuels for co-firing tests with fuel staging and reburning was done based on recommendations in by Sirisomboon and Kuprianov (2017). To achieve a sensible reduction in NO emission from the conical FBC, the co-fired fuels should have substantially different calorific values. While a primary fuel with a relatively high calorific value assures a stable and high-efficiency combustion in the primary combustion zone, the high-moisture (i.e., low-calorific) secondary/reburn fuel prevents a high temperature peak in the combustor and generates elevated/high concentrations of CO and  $C_xH_y$  (a source of light hydrocarbon radicals) responsible for NOx reduction in a secondary/reburn zone (Salzmann and Nussbaumer, 2001; Scala and Chirone, 2008; Werther et al., 2000). It is desirable (but not compulsory) to use a secondary fuel with fuel-N lower than in the base fuel to prevent intensive formation of NO in the vicinity of secondary/reburn fuel injection (Sirisomboon and Kuprianov, 2017; Suheri and Kuprianov, 2015).

**Table 3.1** Properties of the selected biomasses used in co-combustion experiments.

Biomass fuel	Ultimat	e analysis	s, mass	fraction	(%) <sup>a</sup>	Proximate analysis, mass fraction (%) <sup>b</sup>				$LHV^b$
Diomass ruci	С	Н	N	О	S	W	VM	FC	A	(MJ/kg)
Base fuels										
PKS	51.66	7.32	0.14	40.87	0.01	9.9	60.4	27.3	2.4	16.4
PRH	53.89	6.28	38.83	0.98	0.02	9.8	65.0	15.4	10.0	15.1
PCR	50.51	5.94	1.16	42.32	0.07	10.6	68.3	16.0	5.0	15.5
Secondary/reburn fuels										
EFB	23.87	9.45	0.43	29.68	0.08	41.1	44.9	10.8	2.9	5.8
MRH	53.25	5.35	40.70	0.68	0.02	29.6	41.9	14.3	14.2	10.6
EB	58.53	6.88	0.82	33.74	0.03	52.7	27.8	6.5	13.1	6.2

<sup>&</sup>lt;sup>a</sup>On dry and ash free basis

<sup>&</sup>lt;sup>b</sup> On "as-fired" basis

**Table 3.2**Ash composition of the selected biomasses used in co-combustion experiments.

Tish composition of the selected biomasses used in co-combustion experiments.										
Biomass ash	Composition (as oxides, wt.%):									
	$SiO_2$	$Al_2O_3$	$K_2O$	CaO	Na <sub>2</sub> O	MgO	Fe <sub>2</sub> O <sub>3</sub>	$P_2O_5$	$SO_3$	Cl
PKS	23.1	5.2	7.0	42.5	5.5	3.0	1.3	8.5	2.4	0.7
PCR	9.6	1.9	26.2	37.6	0.3	12.9	1.6	4.6	3.8	1.1
EFB	15.1	2.8	42.2	19.5	1	4.2	3.4	5.3	2.5	3.7
EB	22.5	6.3	11.4	44.6	0.5	3.7	2.7	2.7	0.8	2.2

In this project, palm kernel shell (PKS), pelletized rice husk (PRH), and pelletized casava rhizome (PCR) were selected as the base (or primary) fuel. Oil palm empty fruit bunch (EFB), moisturized rice husk (MRH), and eulyptus bark (EB) were choosen to be the secondary/reburn fuels.

The proximate and ultimate analyses and the lower heating value of the selected fuels are shown in Table 3.1. From data in Table 3.1, the EFB, MRH and EB had a substantially higher fuel-moisture content led to a lower calorific value of these secondary fuels compared to the base fuels, complying with the above recommendation for selection of primary and secondary fuels for co-firing tests. Because of insignificant fuel-S in both fuels, this work disregarded all issues related to the formation and emission of SO<sub>2</sub> during all test series.

Table 3.2 shows the fuel-ash analyses of the base fuels and reburn fuels, determined using a wavelength dispersive X-ray fluorescence (XRF) spectrometer. Note that the fuel ash analysis of PRH and MRH is not included in Table 3.2. However, PRH and MRH ash typically includes 85–95% SiO<sub>2</sub> and 1.5–2.5% K<sub>2</sub>O with negligible amounts of other ash-related elements, and therefore, was not reactive to all types of bed material, indicating a low propensity of rice husk for bed agglomeration. From the data in Table 3.2, a relatively high content of potassium in PKS, PCR, EFB, and EB indicates a tendency for bed agglomeration if these biomasses were burned in a fluidized bed of quartz/silica sand.

As stated above, three bed materials: (1) silica sand (SS), (2) alumina sand (AS), and (3) AS and mixed with SS, were used in two case studies: (i) co-firing PKS and EFB

**Table 3.3** Composition of the alumina sand and silica sand used in co-combustion experiments.

Composition (wt.%, as oxides):							
Bed Material	$Al_2O_3$	$SiO_2$	CaO	MgO	K <sub>2</sub> O	Na <sub>2</sub> O	$Fe_2O_3$
Alumina sand	79.09	19.53	0.09	_	0.63	0.53	0.06
Silica sand	6.59	87.82	0.06	0.13	4.24	0.27	0.55

using fuel staging and (ii) co-firing PCR and EB using fuel staging and reburning to inhibit bed agglomeration. The compositions of silica sand (SS) and alumina sand (AS), quantified with the abovementioned XRF system are shown in Table 3.3. The mean particle size (volumetric diameter) of SS and AS was 0.49 mm and 0.47 mm, while the solid density of these bed materials was 2500 kg/m<sup>3</sup> and 3500 kg/m<sup>3</sup>, respectively. In all tests, the static bed height was 30 cm. Note that, in the case study for co-firing PRH and MRH, only silica sand was used as the bed material.

#### 3.2 Experimental facilities

#### 3.2.1 Experimental set up for the cold-state hydrodynamic study

The specific objective of the cold-state hydrodynamic study was to determine the major hydrodynamic regimes and characteristics of the bed, as well as the possible range of superficial air velocity ensuring safe and stable fluidization of a conical bed when firing the selected biomasses in scheduled combustion tests.

A cold-state hydrodynamic study was performed on a special experimental model, which was constructed to reproduce the bottom part of the conical FBC (to be discussed in Subsection 3.2.2), as depicted in Fig. 3.1. The experimental rig was made of galvanized steel 1 mm in thickness and consisted of two sections: (1) a cone-shaped section with a 40° cone angle and 250 mm inner diameter at the bottom base, and (2) a cylindrical section of 2000 mm height and 1000 mm inner diameter. A transparent Plexiglas window, installed on the conical module of the apparatus, was used to monitor the bed behavior during the tests. In addition, the apparatus was equipped with measuring devices and instruments and a data acquisition system.

A 25-hp air blower was used to supply fluidizing air to the test rig through an air pipe of 100 mm inner diameter. Air was injected into the bed through an air distributor. The air distributor consisted of nineteen bubble-cap stand pipes arranged in a staggered order on a

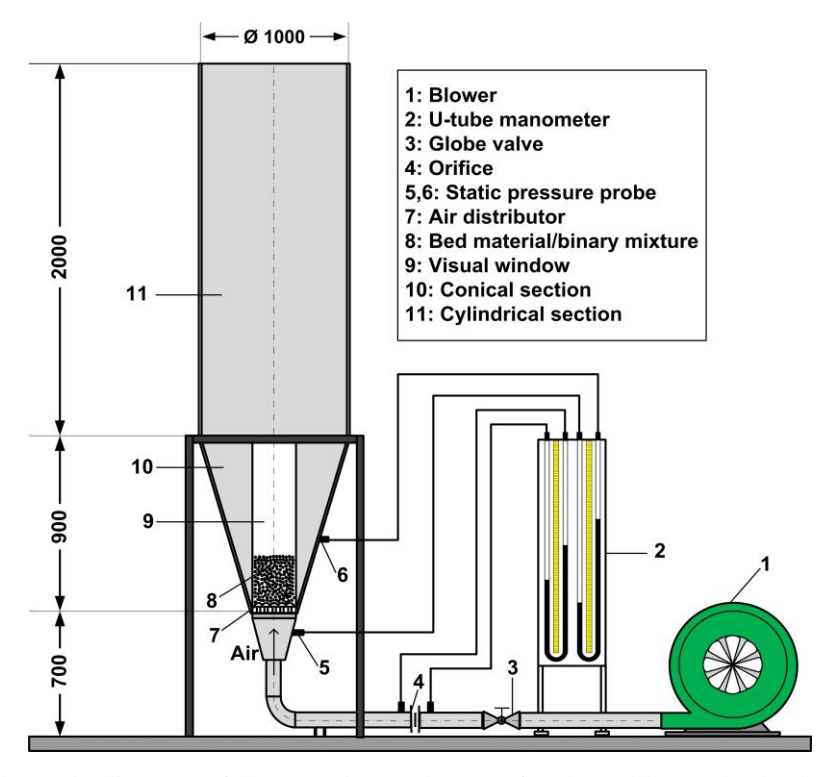


**Fig. 3.1** Schematic diagram of the experimental set up for the cold-state hydrodynamic study.

steel plate of the 250-mm-diameter distributor plate. An individual stand pipe had sixty four holes each 2 mm in diameter, distributed evenly over the pipe surface, and also six rectangular slots 3 mm in width and 15 mm in height, located under the cap of 47 mm diameter. Airflow from each individual stand pipe penetrated into the space between the pipes (through the hole and slots) in a radial direction, facilitating a quasi-uniform distribution of airflow over the air distributor plate, and thus, preventing the occurrence of the spouting fluidization regime of the gas—solid bed. The net cross-sectional area of airflow at the distributor exit (calculated as the difference between the area of the 250-mm-diameter plate and the total area occupied by the caps) was  $A_{air} = 0.016 \text{ m}^2$ .

The total pressure drop across a distributor–bed system ( $\Delta p$ ), comprising the gas–solid bed and the air distributor (AD), was measured for variable superficial air velocity (u) by using an another U-tube manometer with two static pressure probes: one was arranged in the air duct below the air distributor, while the another one was fixed over the bed, as shown in Fig 3.1.

#### 3.2.2 Experimental set up for the (co-)combustion study

A fluidized-bed combustor with a cone-shaped bed (referred to as a 'conical FBC') was used in this study. The experimental setup, including the conical FBC and auxiliary equipment (two air blowers, two screw-type fuel feeders, a cyclone for collecting particulate matter, and a diesel-fired start up burner), is shown in Fig. 3.2. During the test runs for individual firing fuel and co-firing pre-mixed fuels, the base fuel and biomass mixtures were supplied into the reactor by using a single fuel feeder located at level Z = 0.6 m above the air distributor, while the combustion air was injected into the bottom (conical) section of the conical FBC by a 25-hp air blower through the bubble-cap air distributor at the reactor bottom plane.

However, to perform co-firing tests for fuel staging and reburning methods, the combustor was additionally equipped with a secondary fuel feeder and secondary air system (the latter was used in reburning tests). During the tests of these two groups, primary and secondary fuels were delivered separately into the reactor by the two screwtype fuel feeders, as shown in Fig. 3.2. The primary fuel was injected into the fluidized bed at Z = 0.6 m above the air distributor, whereas the secondary fuel was introduced into the cylindrical section (0.5 m higher) by a secondary fuel feeder. Primary (or fluidizing) air was injected into the bed by the above-mentioned 25-hp air blower through the air distributor, whereas in reburning tests, the secondary air (SA) was tangentially introduced into the reactor at Z = 1.65 m by a secondary (5-hp) blower.

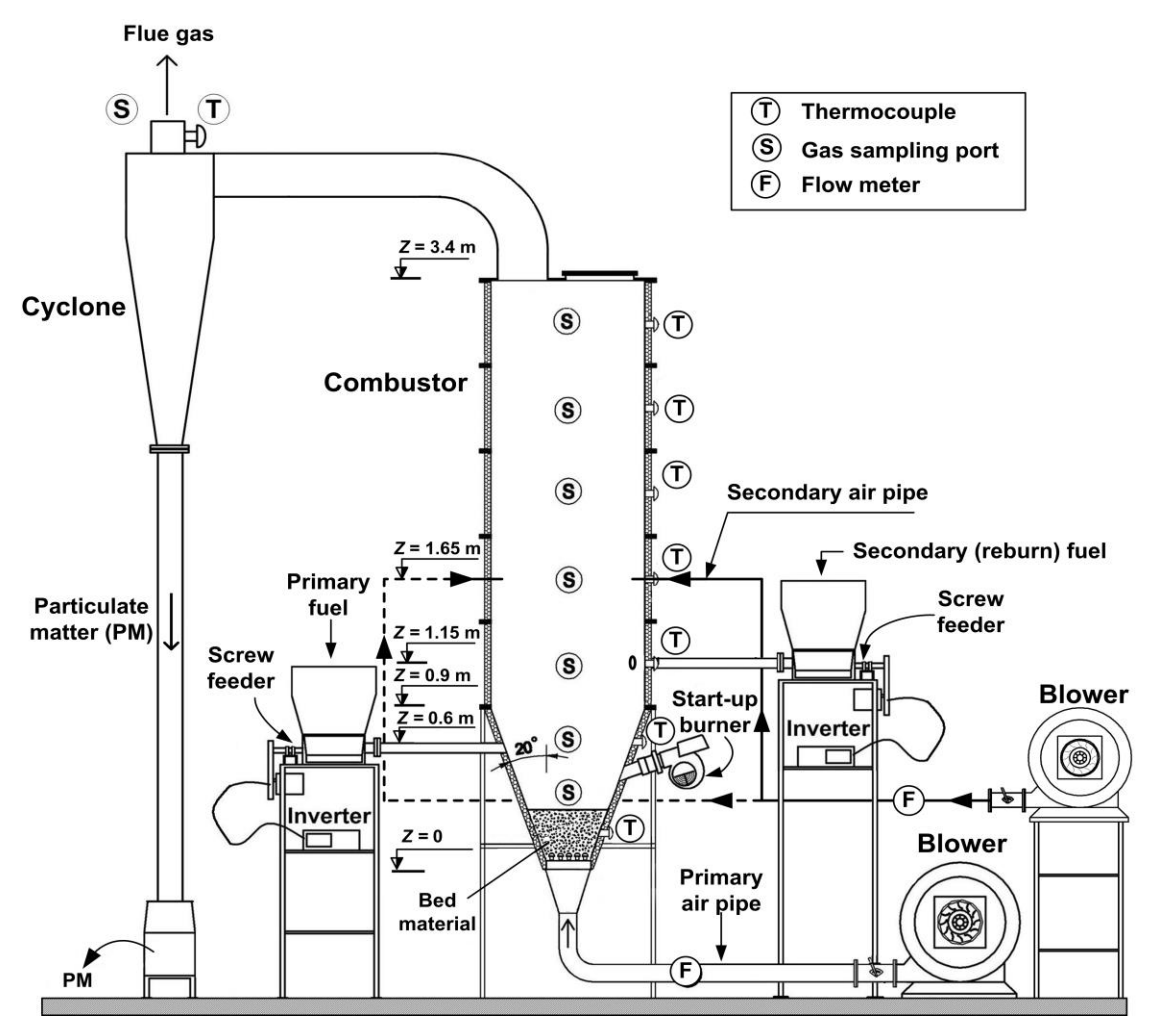


**Fig. 3.2.** Schematic diagram of the experimental setup for co-combustion tests with fuel staging and reburning.

During the combustor start up, the bed material (fluidized by primary air) is preheated using a diesel oil-fired burner from the Riello Burners Co. (model "Press G24"), fixed at a 0.5 m level above the air distributor, until the bed temperature rises to a level of about 700 °C. At this instant, the start-up burner is turned off, and the combustor starts its normal operation using (primary) fuel. In tests for fuel staging and reburning, secondary/reburning fuel is injected at the specified rate.

**Table 3.4**Operating parameters maintained or varied in the (co-)combustion tests

Test series	Parameters	Specified value or range
Case Study 1: Conventional fluidized- bed combustion of individual biomass	-	$200~\mathrm{kW_{th}}$
fuels	Excess air (EA)	20–80%
suppry	-	$200~\mathrm{kW_{th}}$
		0.1–0.25
	Excess air (EA)	20–80%
Case Study 3: Co-combustion of the selected biomass fuels using fuel staging (injection of individual fuels into the combustor at different levels)	-	$200~\mathrm{kW_{th}}$
	Excess air (EA)	20–80%
into the combustor at different levels) and conventional air supply	Energy fraction (EF <sub>2</sub> ) of secondary fuel in total fuel supply	0.1–0.25
Case Study 4: Co-combustion of the selected biomass fuels using reburning	-	$200~\mathrm{kW_{th}}$
technology (integrating fuel staging and air staging)	Excess air (EA)	20–80%
and an staging)	$(EF_2)$	0.1–0.25
	Secondary-to-total air ratio (SA/TA)	0.1 - 0.4

During the tests, temperature is recorded at different points along the reactor centerline and at stack, using eight stationary Chromel-Alumel thermocouples. In each trial at fixed operating conditions, O<sub>2</sub>, CO, C<sub>x</sub>H<sub>y</sub> as CH<sub>4</sub>, and NO are measured along the combustor height and at stack using a new model "Testo-350" gas analyzer.

A cyclone-type ash collector located downstream from the combustor is used to arrest predominant part of particulate matter (PM) originated from biomass (co-)combustion, which is then analyzed for the unburned carbon content (required for assessing the heat loss due to unburned carbon).

#### 3.3 Experimental planning

During a test series (or Case Study with the selected combustion method), the value/range of operating parameters is maintained as given in Table 3.4.

For comparability of the experimental results, all the tests are conducted at the identical (total) heat input to the combustor,  $200 \text{ kW}_{th}$ . This allows using the energy fraction of secondary/reburn fuel (EF<sub>2</sub>) as a single operating variable for characterizing an individual test run for fuel staging/reburning. To study the effects of excess air on the combustion and emission characteristics, each Case Study includes test groups for four percentages of excess air: 20%, 40%, 60%, and 80%. In the reburning tests, the secondary-to-total air ratio (SA/TA) is another important parameter. at each (fixed) EA, the reburning tests were performed for four secondary-to-total air (SA/TA) ratios: 0.1, 0.2, 0.3, and 0.4.

#### 3.4 Methods for determining operating parameters

In this work, energy fraction of a secondary fuel (EF<sub>2</sub>) and excess air (EA) were selected as independent operating parameters, while the total heat input to the reactor was constant ( $\sim$ 200 kW<sub>th</sub>) in all experimental tests.

It appears that EF<sub>2</sub> is dependent on the mass fraction of secondary fuel (MF<sub>2</sub>) in total fuel supply, which is calculated using the feed rate of primary fuel ( $\dot{m}_{\rm f1}$ ) and secondary fuel ( $\dot{m}_{\rm f2}$ ) as:

$$MF_{f2} = \frac{\dot{m}_{f2}}{\dot{m}_{f1} + \dot{m}_{f2}} \tag{3.1}$$

The  $EF_2$  is then determined by taking into account the lower heating value of primary fuel (LHV<sub>f1</sub>) and secondary/reburn fuel (LHV<sub>f2</sub>) as:

$$EF_{f2} = \frac{MF_{f2}LHV_{f2}}{(1 - MF_{f2})LHV_{f1} + MF_{f2}LHV_{f2}}$$
(3.2)

In this work, the tests in Case Studies 1-4 are performed at EF<sub>2</sub> ranged from 0.1 to 0.25. For fixed EF<sub>2</sub>, the proportion, or mass fraction of secondary/reburn fuel, is calculated from Eq. (3.2) by taking into account the heat input to the reactor and Eq. (3.1).

Another independent operating parameter used in this work was the percentage of excess air (EA) determined according to Basu et al. (2000). Prior to determining EA for a test run, the excess air ratio ( $\alpha$ ) was predicted using the actual volume fractions of O2, CO, and CxHy (as CH<sub>4</sub>) measured at stack using a Testo 350 (all represented as the percentages on a dry gas basis), by neglecting H<sub>2</sub> and assuming 79% N2 in the "dry" flue gas, as:

$$\alpha = \frac{21}{21 - (O_2 - 0.5CO - 2CH_4)}$$
 (3.3)

The percentage of EA at stack was then determined as:

$$EA = 100(\alpha - 1) \tag{3.4}$$

# 3.5 Methods for determination of heat losses and combustion efficiency of the conical FBC

For each co-firing test, the heat loss due to unburned carbon and that due to incomplete combustion of the combustor were predicted according to Basu et al. (2000) using a concept of 'equivalent fuel', whose properties were determined as the weighted averages by taking into account the corresponding properties and mass fractions (as the weight factors) of a base and secondary/reburn fuel (Sirisomboon and Kuprianov, 2017).

The heat loss due to unburned carbon ( $q_{uc,cf}$ , %LHV<sub>cf</sub>) was predicted by using the carbon content in particulate matter (PM) emitted from the combustor ( $C_{PM}$ , wt.%) and the properties of the 'equivalent fuel', such as ash content ( $A_{cf}$ , wt.%) and lower heating value (LHV<sub>cf</sub>, kJ/kg), as:

$$q_{\text{uc,cf}} = \frac{32,866C_{\text{PM}}}{(100 - C_{\text{PM}})} \frac{A_{\text{cf}}}{LHV_{\text{cf}}}$$
(3.5)

Afterwards, the heat loss due to incomplete combustion ( $q_{uc,cf}$ , %LHV<sub>cf</sub>) was quantified based on the CO and C<sub>x</sub>H<sub>y</sub> (as CH<sub>4</sub>) emission concentrations at stack (both in ppm, at 6% O<sub>2</sub> and on a dry gas basis) and by taking into account the volume of dry combustion products originated from the combustion of the 'equivalent fuel' ( $V_{dg,cf}$ ), as well as the LHV<sub>cf</sub> (kJ/kg) and the above-calculated  $q_{uc,cf}$  (%LHV<sub>cf</sub>), as:

$$q_{\text{ic,cf}} = (126.4\text{CO} + 358.2\text{C}_{\text{x}}\text{H}_{\text{y}})_{@6\%\text{O}_2} \cdot 10^{-4}V_{\text{dg,cf}} \frac{(100 - q_{\text{uc,cf}})}{\text{LHV}_{\text{cf}}}$$
 (3.6)

The combustion efficiency of the conical FBC (%LHV<sub>cf</sub>) was then quantified as:

$$\eta_{\rm cf} = 100 - (q_{\rm uc,cf} + q_{\rm ic,cf})$$
(3.7)

#### 3.6 Methods for optimization of operating variables

To determine the optimal operating variables (EF<sub>2</sub>, EA, and SA/TA), ensuring minimal "external" costs of the combustor for the selected co-firing options, a cost-based optimization method (Ninduangdee and Kuprianov, 2014) was applied in this work. An objective function for the optimization can be represented as:

$$J_{\rm ec} = Min(P_{\rm NOx}\dot{m}_{\rm NOx} + P_{\rm CO}\dot{m}_{\rm CO} + P_{\rm CxHy}\dot{m}_{\rm CxHy})$$
 (3.8)

In this study, the specific "external" costs of  $NO_x$  (as  $NO_2$ ) and  $C_xH_y$  (as  $CH_4$ ) were assumed to be  $P_{NOx} = 2400$  US\$/t and  $P_{CH4} = 330$  US\$/t, respectively, according to ESCAP-UN (1995). As reported in the related study (Salisdisouk, 1994; Wei, 2003), the ratio of  $P_{NOx}$  to  $P_{CO}$  generally ranges from 5 to 8. It was therefore decided to assume  $P_{CO} = 400$  US\$/t (for  $P_{NOx}/P_{CO} = 6$ ) in this optimization analysis.

For given operating conditions, the mass fluxes of  $NO_x$  (as  $NO_2$ ), CO, and  $C_xH_y$  (as  $CH_4$ ) emissions in Eq. (3.8) were predicted by taking into account the feed rate (kg/s) of the co-fired fuels, as well as the actual emission concentrations (ppm) measured at the cyclone exit, as:

$$\dot{m}_{NO_x} = 2.05 \times 10^{-6} (\dot{m}_{f1} + \dot{m}_{f2}) NO_x V_{dg,cf}$$
 (3.9)

$$\dot{m}_{\rm CO} = 1.25 \times 10^{-6} (\dot{m}_{\rm fl} + \dot{m}_{\rm f2}) \text{COV}_{\rm dg,cf}$$
 (3.10)

$$\dot{m}_{C_x H_y} = 0.71 \times 10^{-6} (\dot{m}_{f_1} + \dot{m}_{f_2}) C_x H_y V_{dg,cf}$$
 (3.11)

where  $V_{\rm dg,cf}$  is the volume of dry combustion products from the co-firing at actual excess air (Nm<sup>3</sup>/kg-fuel), determined according to Basu et al. (2000) by taking into account the mass fractions of the two fuels.

# 3.7 Study of time-related characteristics of the bed materials and PM during cofiring tests

To understand the interaction mechanism between the selected bed material and fuel ash during long term co-firing tests, a SEM-EDS: JEOL, JSM-6610LV scanning electron microscope (SEM), integrated with an energy dispersive X-ray spectrometer (EDS), was used to examine the physiochemical characteristics of individual grains sampled from the bed at the end of co-firing testing with different bed materials. The objectives of the SEM-EDS test were to investigate the distribution of coatings (or that of binding materials in agglomerates, if any) over the bed particle surface, and determine the elemental composition of the coating at some selected spots on a bed particle.

An X-ray fluorescence (XRF) system was employed to observe the time-related variation in the chemical composition of the used/reused bed materials (AS and AS/SS mixture), as well as that of PM.

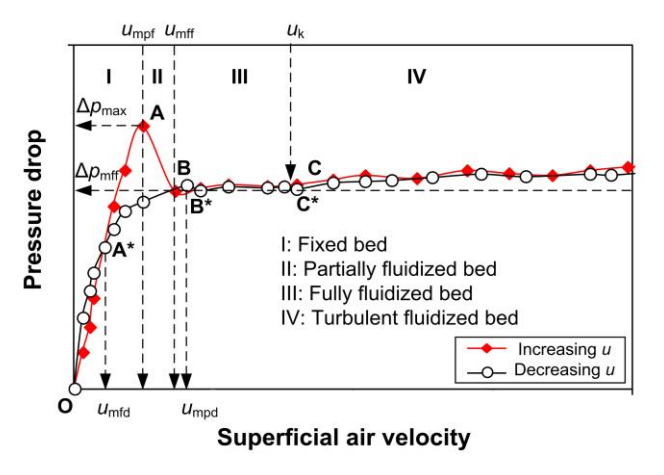
### Chapter 4

# Hydrodynamic Regimes and Characteristics of a Cone-Shaped Bed with a Sand-Biomass Binary Mixture

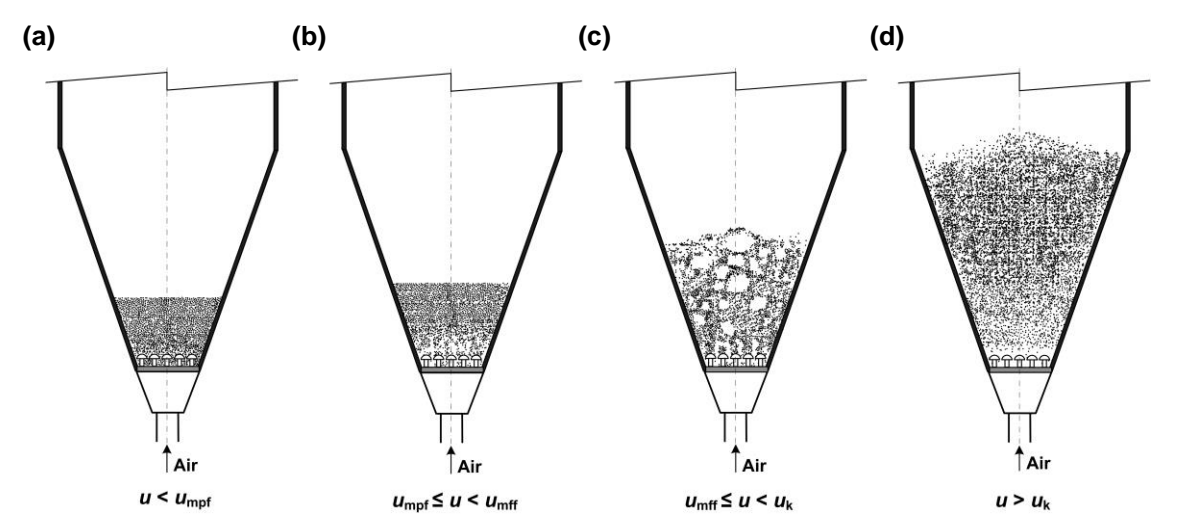
#### 4.1 Flow regimes of a cone-shaped bed

Fig. 4.1 shows a  $\Delta p$ -u diagram that was typical for the cold-state experiment on the cone-shaped bed using different bed materials; alumina sand, dolomite, and limestone (all of 0.3–0.5 mm particle sizes) for two experimental procedures: bed fluidization (solid symbols) and defluidization (open symbols). It can be seen in Fig. 4.1 that with increasing superficial air velocity (u), the pressure drop across the bed and the air distributor ( $\Delta p$ ) varied along the path O $\rightarrow$ A $\rightarrow$ B $\rightarrow$ C, showing the four sequent hydrodynamic regimes of the bed behavior: (I) fixed bed, (II) partially fluidized bed, (III) fully fluidized bed and (IV) turbulent fluidized bed, as indicated in Fig. 4.1. These hydrodynamic regimes have much in common with those found for the coneshaped/tapered beds using various bed materials and fluidizing fluids (Peng and Fan, 1997; Jing et al., 2000; Kaewklum and Kuprianov, 2008).

To facilitate understanding of the flow regimes and behaviors of the cone-shape fluidized beds, Fig. 4.2 illustrates the fluidizing behaviors of the gas-solid bed in this cone-shaped test rig, exhibiting different hydrodynamics regimes (corresponding to



**Fig. 4.1** A typical  $\Delta p$ -u diagram of a cone-shaped bed when using alumina/dolomite/limestone as bed material for fluidization/defluidization procedures.



**Fig. 4.2** Appearance of the cone-shaped bed in different hydrodynamic regimes: (a) fixed (stationary) bed, (b) partially fluidized bed, (c) fully fluidized bed, and (d) turbulent fluidized bed.

different regions in Fig. 4.2), depending on the superficial air velocity. Note that the bed behaviors and regimes, shown in Fig. 4.2, were based on visual observation during the cold-state hydrodynamic experiments for constructing the  $\Delta p$ -u diagram in Fig. 4.1.

The following is a summary of the flow regimes, occurring in the cone-shaped bed using alumina sand, dolomite, and limestone, all being fluidized by air:

I: Fixed-bed regime (O $\rightarrow$ A). Within the fixed-bed region, the  $\Delta p$ -u profile in Fig. 4.1 shows a quasi-linear relationship. With increasing u within this region,  $\Delta p$  linearly increased until it reached the maximum value ( $\Delta p_{\text{max}}$ ). Due to a relatively low rate of airflow in the fixed-bed regime, the bed particles did not move, and the bed was characterized by uniform voidage and fixed (static bed) height, as seen in Fig. 4.2a.

II: Partially fluidized-bed regime (A $\rightarrow$ B). This transition regime was, in effect, an apparent feature of cone-shaped and tapered beds (Peng and Fan, 1997; Jing et al., 2000). As seen in Fig. 4.1, when increasing u beyond critical point A,  $\Delta p$  abruptly reduced from  $\Delta p_{\text{max}}$  to  $\Delta p_{\text{mff}}$  (the pressure drop at the minimum velocity of full fluidization). At Point A, the lowest layer of the conical bed began to fluidize, resulting in a change in bed voidage and height, whereas the top layer of the bed was still static (as illustrated in Fig. 4.2b). The corresponding superficial air velocity, starting the partially fluidized bed

regime, is termed the minimum velocity of partial fluidization ( $u_{mpf}$ ) as proposed by Peng and Fan (1997).

III: Fully fluidized-bed regime (B $\rightarrow$ C). This regime began at Point B where the bed exhibited the full fluidization. At this point, the entire bed was involved in the fluidization, showing a random appearance of small-size bubbles at the top surface of the bed. The corresponding superficial air velocity, starting this regime, is termed the minimum velocity of full fluidization ( $u_{\rm mff}$ ), introduced by Peng and Fan (1997). With a further increase of u in this regime, but less than that of Point C, the frequency of appearance and size of the bubbles released from the fluidized bed increased, resulting in an expansion of the bed (i.e., increased bed height), as illustrated in Fig. 4.2c. However, as revealed by data in Fig. 4.1,  $\Delta p$  within this flow regime stayed nearly constant,  $\Delta p \approx \Delta p_{\rm mff}$ . This finding is similar to those found in experimental studies elsewhere (Peng and Fan, 1997; Jing et al., 2000; Kaewklum and Kuprianov, 2008).

IV: Turbulent fluidized-bed regime. With increasing superficial air velocity beyond Point C (see Fig. 4.1), the bed behavior has changed from the fully fluidized-bed regime (ended at Point C) to the turbulent fluidization regime. The corresponding superficial air velocity starting this regime is termed as the minimum velocity of turbulent fluidization ( $u_k$ ), as proposed by Peng and Fan (1997). During this regime, the movement of the bed particles became more violent and vigorous, and no bubbles were observed in the bed, as illustrated in Fig. 4.2d. Instead of the bubbles, one could see a turbulent motion of solid splashes and voids of gas of various sizes and shapes. Moreover, the turbulent fluidized bed exhibited a substantial expansion, occupying the (almost) entire volume of the cone-shaped section of the test rig. From the analysis of the  $\Delta p$ -u diagram in Fig. 4.1,  $\Delta p$  in this regime increased with higher u, which was mainly due to the effects of the pressure drop across the air distributor (to be discussed below).

On the contrary, during bed defluidization when superficial air velocity was reduced, causing a gradual change in the bed behavior from the turbulent fluidization regime (at Point C\*) to its entire defluidization at Point A\* (where the superficial air velocity was reduced to the value termed the maximum velocity of full defluidization,

 $u_{\rm mfd}$ ), the bed unavoidably passed Point B\* (where the upper layer of the bed was defluidized at the maximum velocity of partial defluidization,  $u_{\rm mpd}$ ), exhibiting the defluidization path C\* $\rightarrow$ B\* $\rightarrow$ A\* $\rightarrow$ O in Fig. 4.1. Thus, during the fluidization-defluidization procedures, the cone-shaped bed of the selected bed materials showed hysteresis in the  $\Delta p$ -u diagram.

However, the  $\Delta p$ -u diagram of the bed defluidization provided no useful information that could be used for optimal design and operation of the combustor, since at  $u_{\rm mfd} < u < u_{\rm mpd}$ , the upper region of the bed did not fluidize. For this reason and because of the segregation of sand and biomass particles during turbulent and bubbling fluidization regimes, it was decided to only use in this study the  $\Delta p$ -u diagrams (for variable bed properties and characteristics) obtained from the fluidization tests.

#### 4.2 Hydrodynamics of a cone-shaped bed using monodispersed particles

Fig. 4.3 shows  $\Delta p$ -u diagram of the cone-shaped bed using alumina sand, dolomite, and limestone (solid dots), and the contribution of the pressure drop across the air distributor (open dots) for variable u at distinct BHs. As seen in Fig. 4.3, the  $\Delta p$ -u diagrams of the cone-shaped beds with the selected bed materials exhibited similar trends, consequently, showing similar hydrodynamic regimes (indicated in Fig. 4.1), as described previously.

It can be seen in Fig. 4.3 that, with an increase of BH in the fixed-bed region, both the  $u_{\rm mpf}$  and the corresponding  $\Delta p_{\rm max}$  of all the beds showed a trend to increase, mainly due to the increase in the bed weight. This effect is typical for the conical gas-solid beds, as observed by Jing et al. (2000), Kaewklum et al. (2009), and Arromdee and Kuprianov (2012a). However, at given BH, these hydrodynamic characteristics of the bed using alumina sand were found to be somewhat greater than those of the other two beds. This fact can be attributed to the higher density of alumina sand, compared to those of dolomite and limestone.

With increasing u from  $u_{mpf}$  to  $u_{mff}$  during the partially fluidized-bed regime,  $\Delta p$  abruptly reduced by 20–30% (depending on the bed material and static bed height), which resulted in an appearance of a sharp peak on each  $\Delta p$ -u diagram in Fig. 4.3.

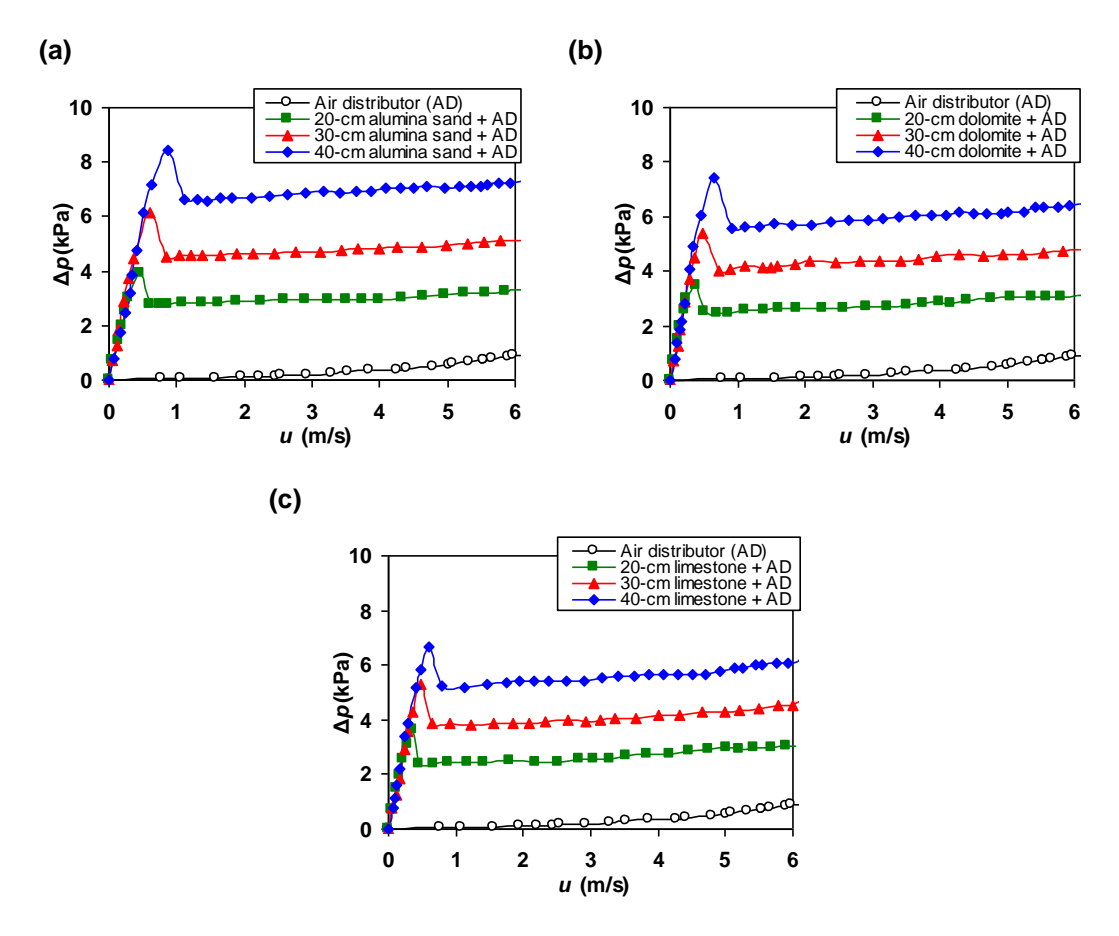


**Fig. 4.3** Pressure drop across the air distributor versus superficial velocity, and the  $\Delta p$ -u diagram of the bed (including effects of AD) using pure bed materials: (a) alumina sand, (b) dolomite, and (c) limestone for different static bed heights.

Similar findings were reported by Jing et al. (2000), Kaewklum et al. (2009), and Arromdee and Kuprianov (2012a). As revealed by the data in Fig. 4.3, when increasing BH during this regime, the  $u_{\rm mff}$  and corresponding  $\Delta p_{\rm mff}$  of all the beds increased, because of an increase in the total bed weight. In addition, the  $u_{\rm mff}$  and  $\Delta p_{\rm mff}$  of the bed using alumina sand were somewhat greater than those of the bed using dolomite and limestone, at identical BHs. For example, at BH = 30 cm,  $u_{\rm mff}$  for the alumina sand bed was 0.84 m/s ( $\Delta p_{\rm mff}$  = 4.5 kPa), whereas it was 0.72 m/s ( $\Delta p_{\rm mff}$  = 4.0 kPa) for the dolomite bed, and 0.65 m/s ( $\Delta p_{\rm mff}$  = 3.8 kPa) for the bed with limestone. This was mainly due to the above-mentioned difference in the density of the selected bed materials.

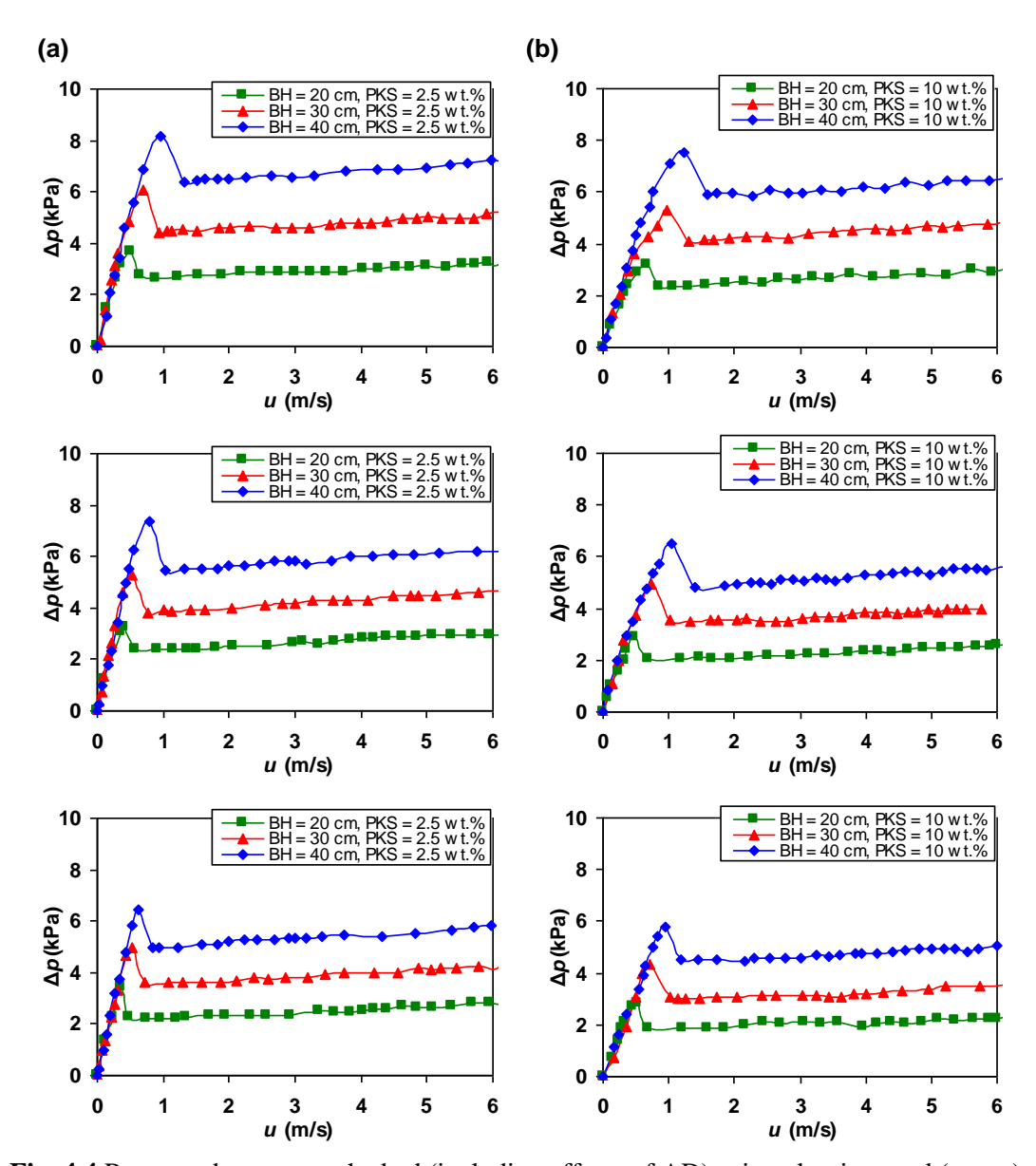


**Fig. 4.4** Pressure drop across the bed (including effects of AD) using alumina sand (upper), dolomite (middle), and limestone (lower) as the bed material mixed with PKS of 3–6 mm particle sizes in different proportions: (a) 2.5 wt.% and (b) 10 wt.%.

With increasing u in the fully fluidized bed and turbulent fluidized bed,  $\Delta p$  increased, at nearly the same rate for all the bed materials and selected BHs. This fact can be explained by the effects of the pressure drop across the air distributor. However, the contribution of the air distributor to the total  $\Delta p$  was relatively small about 1 kPa at u=6 m/s (see Fig. 4.3).

As found in the experimental tests, the fluidization regime of all the tested beds was switched from the fully fluidized-bed regime to the turbulent one at  $u_k$  1.5–3.0 m/s (depending on the bed material and bed height).

#### 4.3 Hydrodynamics of a cone-shaped bed with a sand-biomass binary mixture

#### 4.3.1 Behavior of a cone-shaped bed using a sand-PKS binary mixture

As an illustration, Fig. 4.4 depicts the  $\Delta p$ -u diagrams of the cone-shaped beds of alumina sand, dolomite, and limestone mixed with PKS of 3–6 mm particle sizes for the two PKS mass fractions in a binary mixture (MF = 2.5 wt.% and MF = 10 wt.%) at three static bed heights: BH = 20 cm, BH = 30 cm, and BH = 40 cm. It should be noted that the  $\Delta p$  in Fig. 4.4 included the combined effects of the pressure drop across the bed with the mixture and that across the air distributor (AD). As seen in Fig. 4.4, all the  $\Delta p$ -u diagrams of the bed with the binary mixtures exhibited similar hydrodynamic regimes and characteristics, as those for the monodispersed particle systems, however, with some effects from the biomass fraction on the binary mixture.

From the  $\Delta p$ -u diagrams in Fig. 4.4, with increasing proportion of PKS in the mixture (consequently, resulting in an increase of the biomass volume in the bed) at a fixed BH, both the  $u_{mpf}$  and the  $u_{mff}$  showed an increase. As the percentage of PKS in the mixture increased from 2.5 wt.% to 10 wt.% at BH = 30 cm, the  $u_{mff}$  of the alumina sand-PKS mixture increased from 0.9 m/s to 1.2 m/s, whereas that of the dolomite-PKS mixture increased from 0.8 m/s to 1.1 m/s, and from 0.6 m/s to 1.0 m/s for the limestone-PKS bed. This result can be explained by the presence of biomass particles in the bed, which led to a noticeable increase in the bed voidage. On the contrary, the  $\Delta p_{max}$  and the  $\Delta p_{mff}$  showed a slight reduction with an increase in the percentage of PKS in the binary mixture, which can be explained by the decreased total weight of the bed. These results were in agreement with those found in the cylindrical/rectangular-shaped beds (Rao and Bheemarasetti, 2001; Sun et al., 2008a; Zhang et al., 2009).

In addition, with higher percentage of biomass in the mixture, the difference between the  $u_{mff}$  and the  $u_{mpf}$  in all the tests was somewhat greater. Nevertheless, like in the trials with the monodispersed particle systems, the transition of the bed behavior from

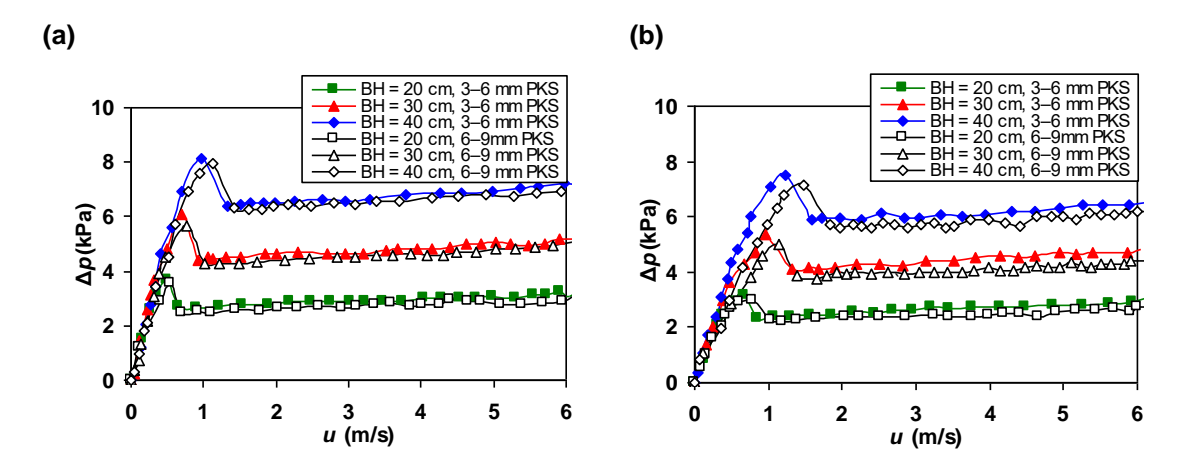


Fig. 4.5 Effects of the static bed height and biomass particle size on the  $\Delta p$ -u diagram of alumina sand mixed with PKS (including effects of AD) in different proportions: (a) 2.5 wt.% and (b) 10 wt.%.

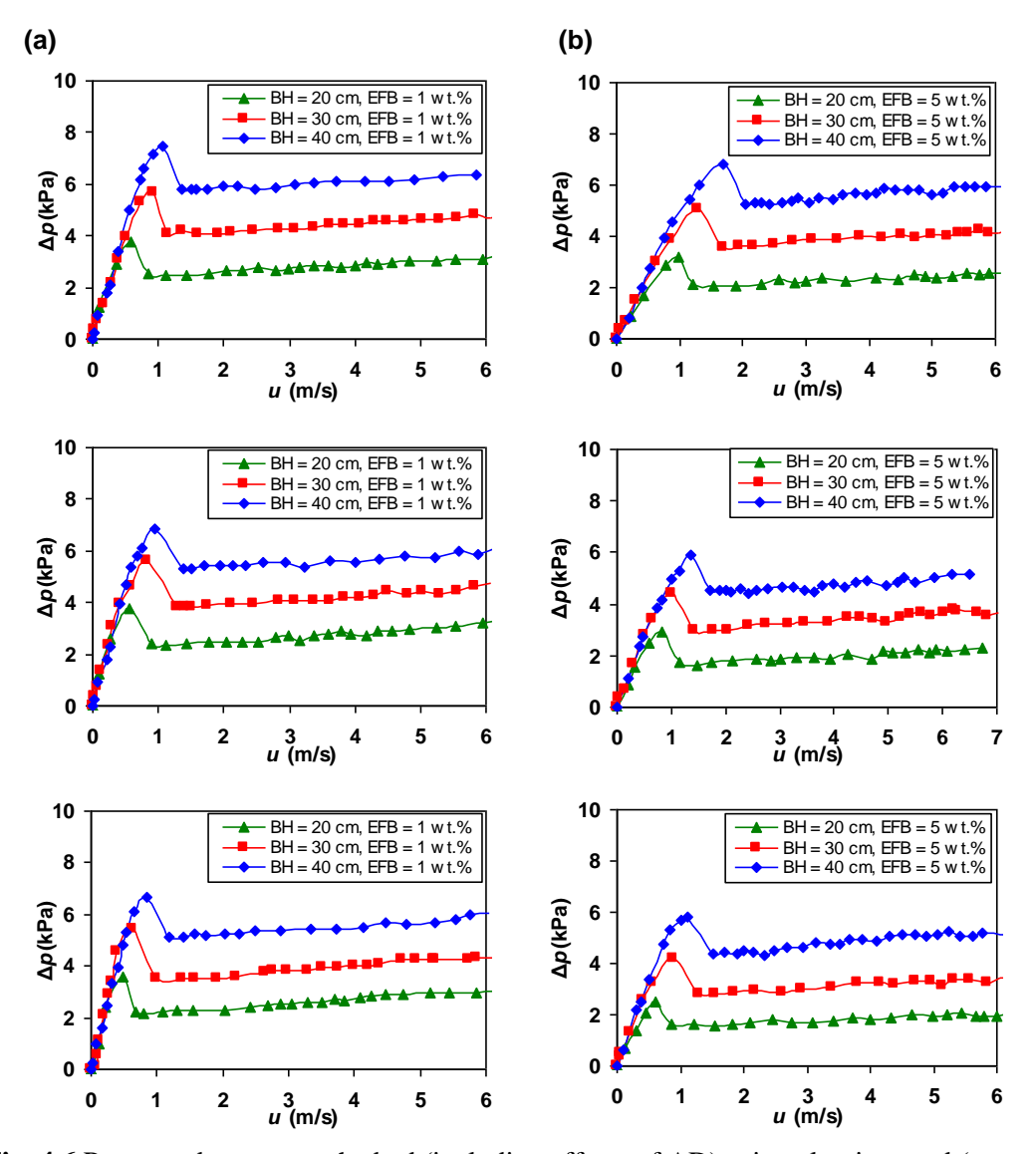
the stationary mode to the fully fluidized-bed regime was accompanied by stepwise changes in the superficial air velocity (u) as well as in the total pressure drop  $(\Delta p)$ , and this result was strengthened by the effects from the static bed height.

Fig. 4.5 shows the  $\Delta p$ -u diagrams of the bed of alumina sand mixed with PKS of two size groups: 3–6 mm and 6–9 mm, for the same ranges of BH and MF in the binary mixture, as in Fig. 4.4. When compared between the trials for MF = 2.5 wt.% (Fig. 4.5a), the  $\Delta p$ -u diagrams of the binary mixture for the two particle size groups were quite similar, indicating the minor effects from the biomass particle size on the major hydrodynamic characteristics of the bed. However, the particle size of PKS had more noticeable effects on the hydrodynamic characteristics of the bed at the increased MF (10 wt.%), as seen in Fig. 4.5b. With coarser biomass particles, the  $u_{\rm mpf}$  and the  $u_{\rm mff}$  exhibited an increase at fixed BH, likely in response to an increase in the "effective" density and diameter of solid particles, as follows from the analysis using Eqs. (3.1) and (3.2). At fixed BH, the corresponding pressure drops ( $\Delta p_{\rm max}$  and  $\Delta p_{\rm mff}$ ) for the beds with the coarser particles were somewhat lower than those of the smaller ones because of the reduced bed weight.

#### 4.3.2 Behavior of a cone-shaped bed with a sand-EFB binary mixture

Fig. 4.6 shows the  $\Delta p$ -u diagrams of the cone-shaped beds of alumina sand/dolomite/limestone mixed with EFB at MF = 1 wt.% and MF = 5 wt.% at three

static bed heights. As seen, the  $\Delta p$ -u diagrams in Fig. 4.6 exhibited similar hydrodynamic regimes and characteristics as those determined for the pure bed materials and the sand-PKS mixture. However, the profiles in Fig. 4.6 were not as smooth as those depicted in Fig.s 4.3 and 4.4. This result was likely due to fibrous structure of EFB (previously-addressed in Chapter 4), which could lead to higher frictional forces between the bed grains and the EFB fibers and, accordingly, a greater momentum of airflow required to overcome this, compared to the monodispersed particles, and sand-PKS binary mixtures.



**Fig. 4.6** Pressure drop across the bed (including effects of AD) using alumina sand (upper), dolomite (middle), and limestone (lower) as the bed material mixed with EFB in different proportions: (a) 1 wt.% and (b) 5 wt.%.

In addition, the  $u_{\rm mpf}$  and the  $u_{\rm mff}$  of the binary mixtures of sand-EFB were significantly greater than that of sand-PKS beds when compared at similar static bed height (even at the lower biomass percentage in the mixture). This fact can be attributed to the substantially lower solid densities of EFB particles, leading to greater voidage of

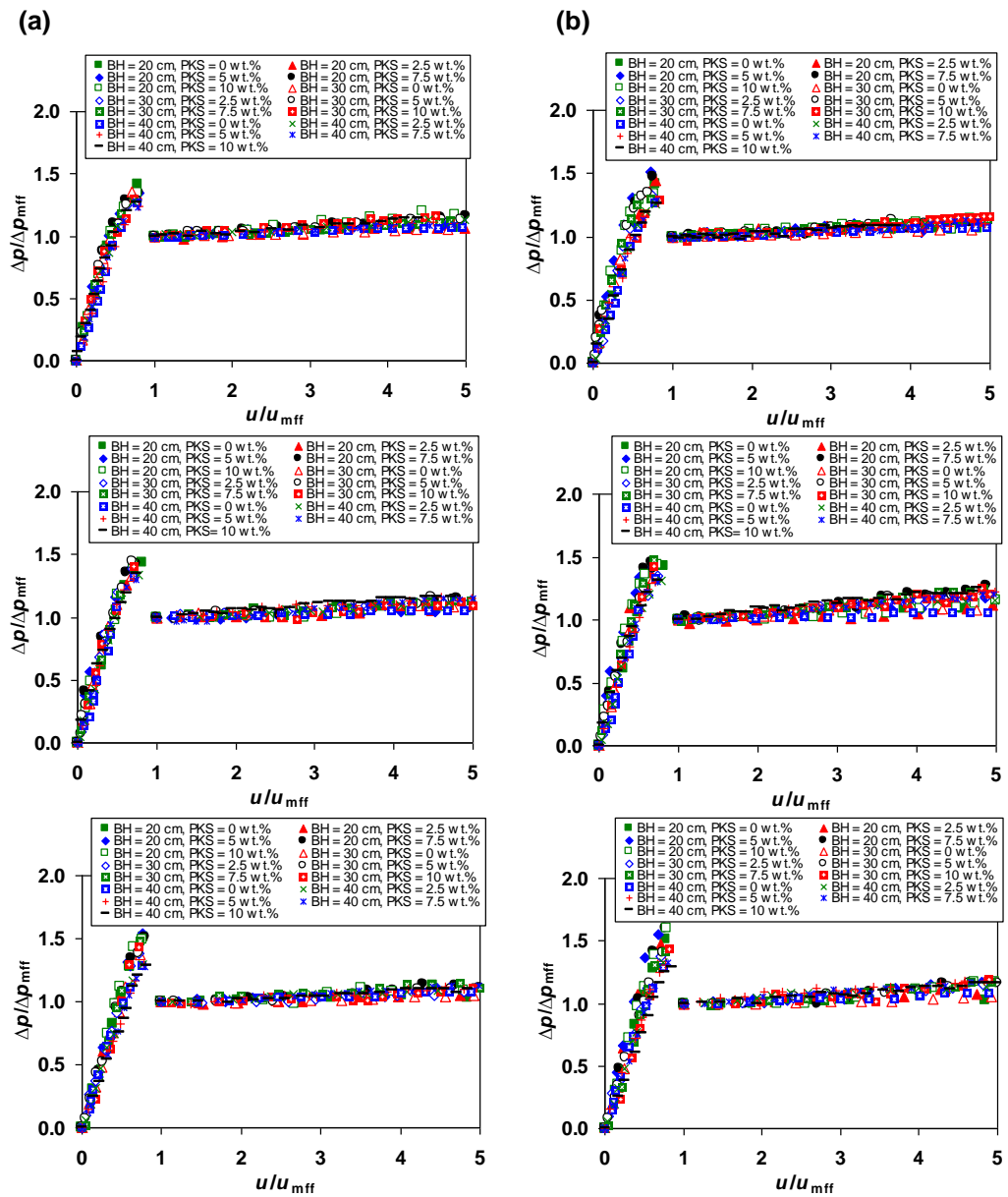


**Fig. 4.7** Relative pressure drop (including effects of AD) versus the relative superficial air velocity of the cone-shaped bed using alumina sand (upper graphs), dolomite (middle graphs), and limestone (lower graphs) mixed with (a) 3–6 mm PKS particles size and (b) 6–9 mm PKS particles in various proportions at different static bed heights.

the sand-EFB mixture. Differences between  $u_{\rm mpf}$  and  $u_{\rm mff}$  became more substantial as the proportion of EFB in the mixture increased, and this effect was strengthened at higher BH. Nevertheless, at a fixed static bed height, the corresponding pressure drops ( $\Delta p_{\rm max}$  and  $\Delta p_{\rm mff}$ ) for the sand-EFB mixture were lower than those of the sand-PKS mixture, mainly due to the decreased bed weight.

## 4.4 Relative hydrodynamic characteristics of a cone-shaped bed with sand-biomass binary mixtures

Fig. 4.7 depicts the dependencies of the relative pressure drop across the air distributor and sand-biomass bed  $(\Delta p/\Delta p_{\rm mff})$  on relative superficial air velocity  $(u/u_{\rm mff})$ 

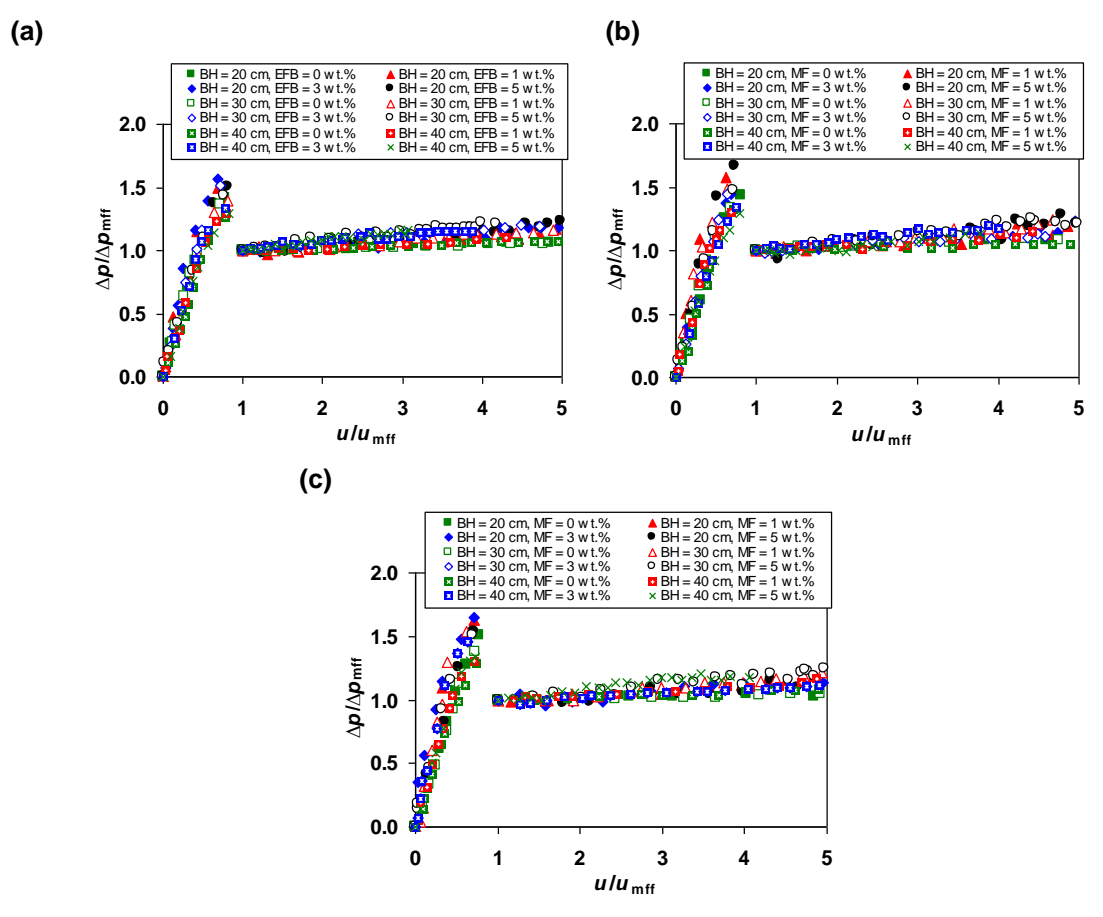


**Fig. 4.8** Relative pressure drop (including effects of AD) versus the relative superficial air velocity of the cone-shaped bed using (a) alumina sand, (b) dolomite, and (c) limestone mixed with EFB in various proportions at different static bed heights.

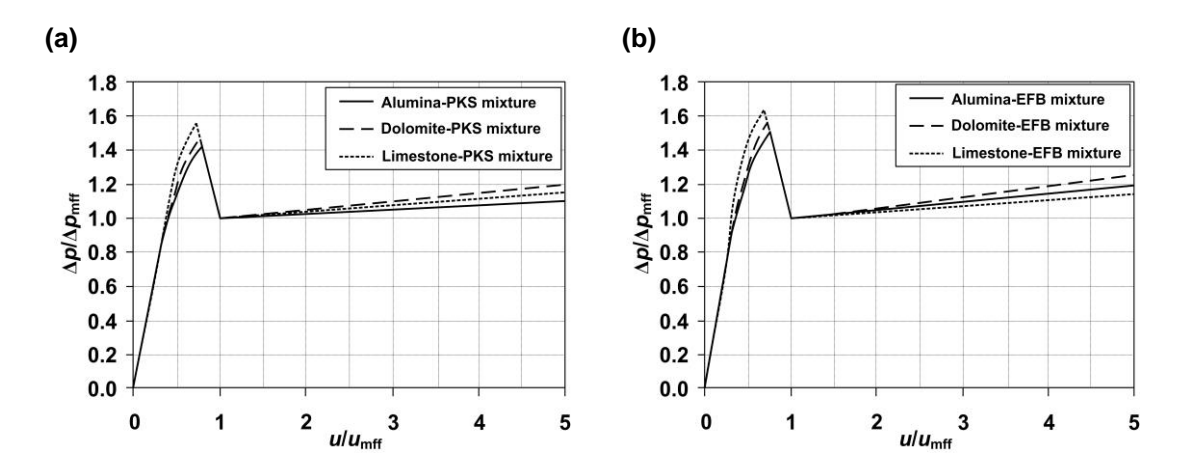


**Fig. 4.9** Nomograph for determining the pressure drop across the cone-shaped bed and AD when using of (a) sand-PKS and (b) sand-EFB binary mixtures.

for the tests with the selected bed materials mixed with PKS in different proportions for the two size groups at different static bed height. The findings in Fig. 4.7 revealed that  $(\Delta p/\Delta p_{\rm mff}) = f(u/u_{\rm mff})$ , obtained via treatment of the experimental data from different test runs, were almost independent of operating conditions, exhibiting an apparent similarity of the dimensionless characteristics, and therefore the feasibility of fitting by a single line with sufficient accuracy.

The dependencies of the relative total pressure drop  $(\Delta p/\Delta p_{\rm mff})$  on the relative superficial air velocity  $(u/u_{\rm mff})$  of the cone-shaped bed for the selected bed material mixed with EFB in different proportions at different BHs are shown in Fig. 4.8. Like with PKS, the dimensionless curves in Fig. 4.8 for the tests with EFB showed such similarity between the bed materials.

Within the fixed-bed region characterized by a significant increase in the pressure drop, the  $\Delta p/\Delta p_{\rm mff}$  for all the tests with two biomasses exhibited a quasi-linear dependence of  $\Delta p/\Delta p_{\rm mff}$  on  $u/u_{\rm mff}$ . For the fully and turbulent fluidized-bed regimes, the  $\Delta p/\Delta p_{\rm mff}$  of the binary mixtures exhibited slight positive gradients,  $d(\Delta p/\Delta p_{\rm mff})/d(u/u_{\rm mff})$ , however, to a different extent. These gradients were mainly due to the above-mentioned contribution of the air distributor to the total pressure drop across the bed–distributor system.

Based on these relative hydrodynamic characteristics, a Nomograph representing the dependences of  $\Delta p/\Delta p_{\rm mff}$  on  $u/u_{\rm mff}$  for different bed regimes was developed and proposed for practical use to predict the  $\Delta p$  for any fixed u.

Fig. 4.9 depicts the Nomograph for predicting the total pressure drop across the cone-shaped bed, using the selected bed materials mixed with PKS/EFB, whose validity is limited by the range of operating variables used in this study (bed material type and properties, static bed height, mass fraction of biomass, biomass particle size, and cone angle), plotted based on the fitting curves previously derived for different regimes of the selected binary mixtures.

Knowing the numerical values of  $u_{\rm mff}$  and  $\Delta p_{\rm mff}$  for the particular operating variables (the biomass percentage in a binary mixture, biomass particle size, and static bed height) one can predict the total pressure drop,  $\Delta p$ , for any arbitrary superficial air velocity within the specified ranges of the operating variables (fuel feed rate and excess air specified for the combustion tests).

### 4.5 Empirical models for predicting major hydrodynamic characteristics of a coneshaped bed with a binary mixture of the bed material mixed with palm kernel shell

By using the  $u_{\rm mff}$  obtained from the trials with selected bed materials under various operating conditions (static bed height, biomass fraction in a binary mixture, and "effective" particle size of the bed), empirical equations for estimating  $u_{\rm mff}$  of a coneshaped bed (of the 40° cone angle) with different sand-PKS mixtures were derived as:

• for a binary mixture of alumina sand and PKS (at  $R^2 = 0.96$ ):

$$u_{\rm mff} = \frac{1.06 \times 10^{-3} \,\mu}{\rho_{\rm g} d_{\rm p,eff}} \,\text{Ar}^{1.11} \left(\frac{h}{D_{\rm o}}\right)^{0.85} \tag{4.1}$$

• for a binary mixture of dolomite and PKS (at  $R^2 = 0.96$ ):

$$u_{\text{mff}} = \frac{2.58 \times 10^{-5} \,\mu}{\rho_{\circ} d_{\text{neff}}} \text{Ar}^{1.55} \left(\frac{h}{D_{\text{o}}}\right)^{0.69} \tag{4.2}$$

• for a binary mixture of limestone and PKS (at  $R^2 = 0.97$ ):

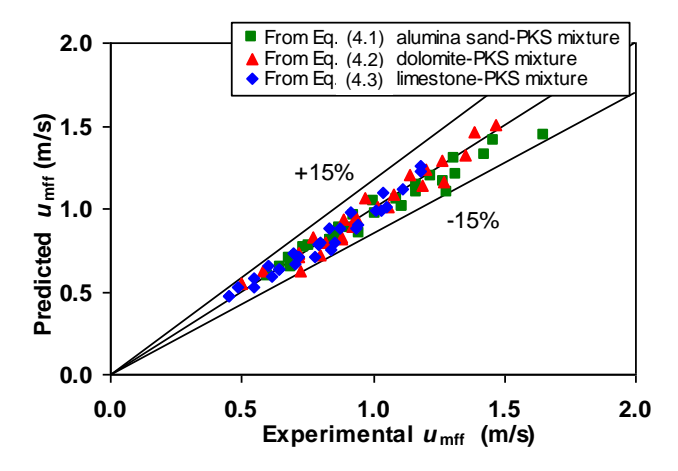


**Fig. 4.10** Comparison between the predicted and experimental  $u_{mff}$  for the cone-shaped beds using alumina sand, dolomite, and limestone mixed with PKS.

$$u_{\text{mff}} = \frac{3.69 \times 10^{-5} \,\mu}{\rho_{\text{g}} d_{\text{p,eff}}} \,\text{Ar}^{1.52} \left(\frac{h}{D_{\text{o}}}\right)^{0.75}$$
(4.3)

The derived correlations in Eqs. (4.1)–(4.3) provide an accurate fitting, at high value of  $R^2$ , for all the trials. To validate the developed models, the predicted (by Eqs. (4.1)–(4.3)) and experimental  $u_{\rm mff}$  values were compared, as presented in Fig. 4.10. It can be seen in Fig. 4.10 that the values of  $u_{\rm mff}$  predicted by the models were in a good agreement with the experimental ones, which stayed within a  $\pm 15\%$  error band with respect to the corresponding average of  $u_{\rm mff}$ .

The relationships for determining  $\Delta p_{\rm mff}$  were derived for the case studies as:

• for a binary mixture of alumina sand and PKS (at  $R^2 = 0.98$ ):

$$\Delta p_{\rm mff} = 3.17 u_{\rm mff}^{-0.39} \left(\frac{h}{D_{\rm o}}\right)^{1.64}$$
 (4.4)

• for a binary mixture of dolomite and PKS (at  $R^2 = 0.98$ ):

$$\Delta p_{\rm mff} = 2.77 u_{\rm mff}^{-0.33} \left(\frac{h}{D_{\rm o}}\right)^{1.45}$$
 (4.5)

• for a binary mixture of limestone and PKS (at  $R^2 = 0.99$ ):

$$\Delta p_{\rm mff} = 2.28 u_{\rm mff}^{-0.51} \left(\frac{h}{D_o}\right)^{1.54}$$
 (4.6)

Fig. 4.11 depicts the  $\Delta p_{\rm mff}$  determined by Eqs. (4.4)–(4.6) and that obtained from the corresponding experiments. As seen from the data in Fig. 4.11, most of the predicted  $\Delta p_{\rm mff}$  were close to the experimental values, with the deviation being within  $\pm 10\%$  for all the experiments.

Based on the Nomograph in Fig. 4.9a, the pressure drop across the cone-shaped bed of a sand-PKS mixture can be estimated for any arbitrary u using the values of  $u_{\rm mff}$  and  $\Delta p_{\rm mff}$ , predicted by Eqs. (4.1)–(4.6).

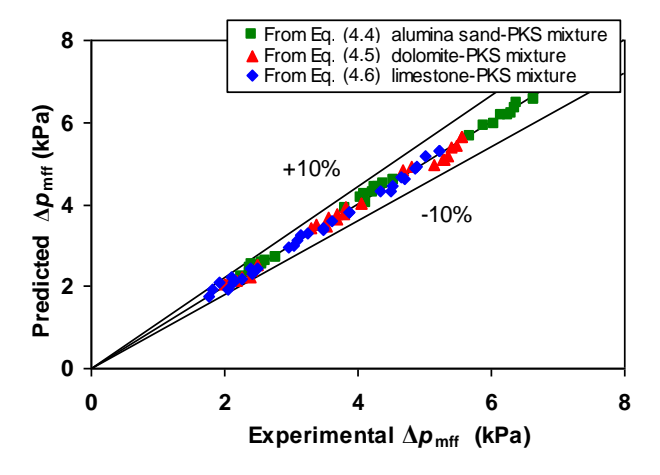


Fig. 4.11 Comparison of between the predicted and experimental  $\Delta p_{\rm mff}$  for the cone-shaped beds using alumina sand, dolomite, and limestone mixed with PKS.

#### Chapter 5

# Co-firing of Oil Palm Residues in a Fuel Staged Fluidized-bed Combustor using Mixtures of Alumina and Silica Sand as the Bed Material

## 5.1 Optimizing operating parameters for co-firing PKS and EFB using pure alumina sand as the bed material

To optimize the energy fraction of EFB (EF<sub>2</sub>) and excess air (EA) according to the cost-based optimization method presented in Section 3.6, the major gaseous emissions (CO,  $C_xH_y$ , and NO) were measured for the ranges of EF<sub>2</sub> (from 0 to 0.25) and EA (from some 20% to about 80%) when (co-)firing PKS and EFB in the conical FBC using alumina sand as bed material (for preventing bed agglomeration).

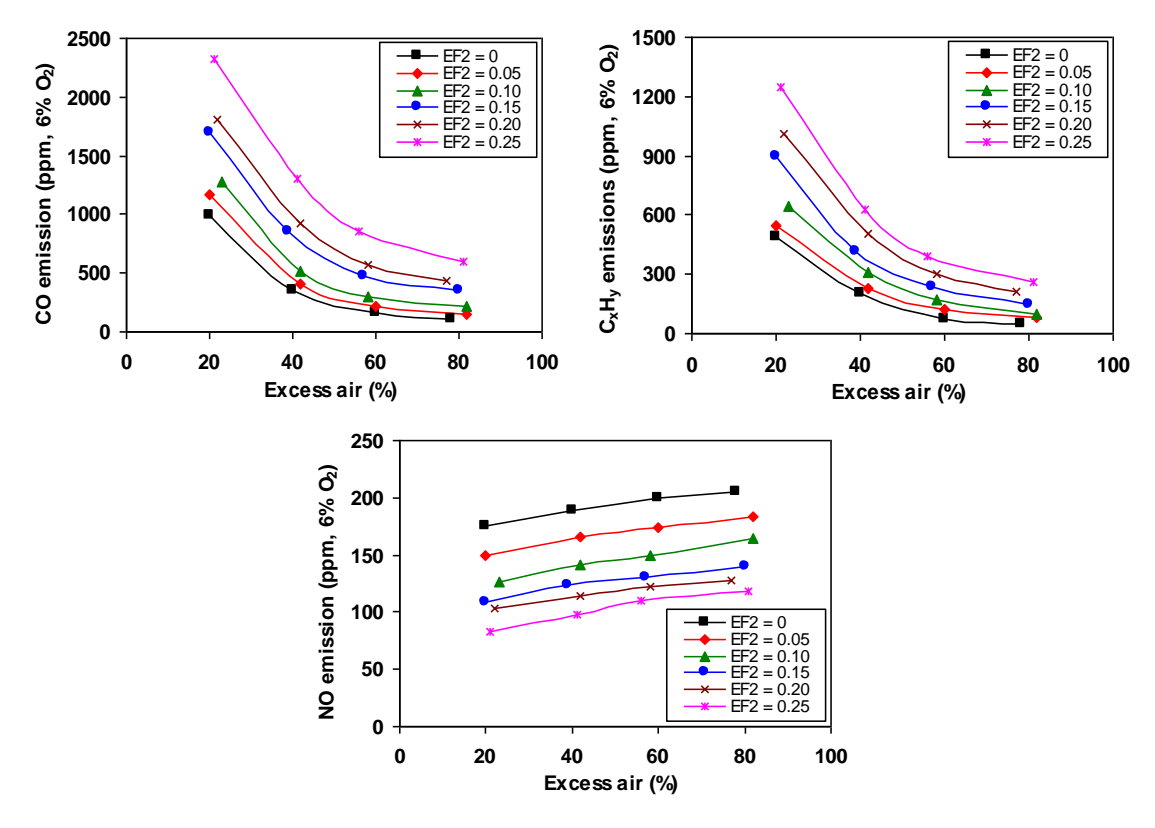


**Fig. 5.1.** Effects of the energy fraction of EFB in the total fuel supply (EF<sub>2</sub>) and excess air on the CO, C<sub>x</sub>H<sub>y</sub> (as CH<sub>4</sub>), and NO emissions when co-firing PKS and EFB in the conical FBC using alumina sand as the bed material.

Fig. 5.1 depicts the CO,  $C_xH_y$ , and NO emissions (all at 6%  $O_2$  and on a dry gas basis) from the preliminary tests on this fuel staged combustor, using alumina sand as the bed material, when co-firing PKS and EFB at the specified ranges of EF<sub>2</sub> and EA, as compared to those for firing PKS alone (EF<sub>2</sub> = 0). It can be seen in Fig. 5.1 that all the emissions had noticeable effects from the two operating parameters. However, the opposite trends were observed from EF<sub>2</sub> and EA, the most significant at 20–40% EA.

With increasing EF2 (at similar EA), both CO and CxHy emissions were higher, mainly due to the strengthening effects from injection of EFB into the secondary combustion zone, whereas with a greater amount of EA (at fixed EF2), these two emissions decreased at a variable rate. On the contrary, an increase in EF2 (at constant EA) caused a noticeable reduction in the NO emission, mainly due to the increased concentrations of CO and CxHy in the secondary combustion zone (to be discussed below), both enhancing the rate of NO reduction reactions in this region (Baukal, 2001; Nussbaumer, 2003; Werther et al., 2000). However, higher EA (at fixed EF2) led to a greater emission of NO, which can be generally attributed to the fuel-NO formation mechanism (Werther et al., 2000).

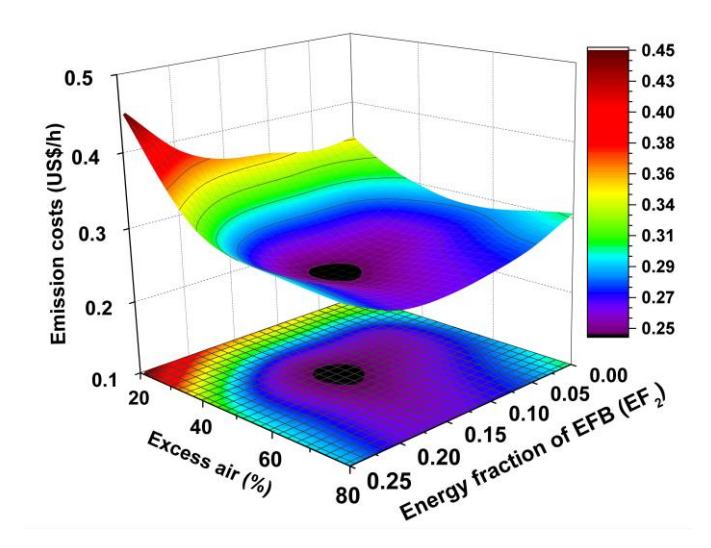


**Fig. 5.2.** Effects of the energy fraction of EFB (EF<sub>2</sub>) and excess air on the "external" costs of co-firing PKS and EFB in the conical FBC using alumina sand as the bed material.

Fig. 5.2 shows the "external" (emission) costs of the co-combustion of PKS and EFB in the conical FBC predicted from Eqs. (3.8)–(3.11) by using the measured CO,  $C_xH_y$ , and NO emissions, as well as other relevant parameters, all quantified for the ranges of EF<sub>2</sub> and EA. From Fig. 5.2, the effects of EF<sub>2</sub> and EA on the "external" costs were substantial. With increasing EF<sub>2</sub> at relatively low amounts of EA, the total emission costs increased to a significant level, mainly due to the enhanced impacts of the CO and  $C_xH_y$  emissions. On the contrary, the effects of NO on the costs were more significant with diminishing EF<sub>2</sub> and/or higher EA.

As follows from the optimization, the minimal "external" costs were found at  $EF_2 \approx 0.15$  and  $EA \approx 55\%$  (see Fig. 5.2). Under these conditions, the major emissions can be controlled at acceptable levels, i.e., below the national emission limits for biomass-fueled industrial applications: 740 ppm for CO and 205 ppm for NO (on a dry gas basis, as corrected to 6% O2 in the flue gas) (PCD, 2018). Furthermore, the fuel-staged co-combustion of PKS and EFB at the optimal  $EF_2$  and EA led to a noticeable NO emission reduction, by about 35%, compared to firing pure PKS.

### 5.2 Effects of operating variables on the heat losses and combustion efficiency of the combustor (co-)fired with PKS and EFB

Table 5.1 shows the combustion-related heat losses and the combustion efficiency of the conical FBC (quantified by using the method provided in Subsection 3.4.5), together with the relevant parameters required for their prediction. For each (co-)combustion fuel option, both heat losses showed a reduction as EA was increased at fixed  $EF_2$ , following the behavior of unburned carbon content in the fly ash (see Appendix F), as well as CO and  $C_xH_y$  at stack.

As seen in Table 5.1, the combustion efficiency was characterized by its maximum at EA = 60-80%, which, however, exhibited a small reduction with increasing EF<sub>2</sub>: from 99.6–99.7% (for firing pure PKS) to 98.6–98.5% (at EF<sub>2</sub> = 0.25). Thus, the fuel staging had basically a minor impact on the combustion efficiency of this conical FBC compared to that of EA.

**Table 5.1** Emissions and the combustion efficiency of the conical FBC using alumina sand as bed material when co-firing PKS and EFB at different operating conditions.

Excess air	O <sub>2</sub> <sup>a</sup>	Carbon	COa	C <sub>x</sub> H <sub>v</sub> <sup>a</sup>	Heat loss (	%) due to:	Combustion	
(vol.%)	(vol.%)	in PM (wt.%)	(ppm)	(ppm)	unburned carbon	incomplete combustion	efficiency (%)	
			Firing 44	.2 kg/h PKS	$E(EF_2=0)$			
20	3.6	3.74	990	487	0.19	0.99	98.8	
40	6.1	2.28	360	200	0.11	0.45	99.4	
60	7.9	2.14	160	74	0.11	0.21	99.6	
78	9.2	1.87	110	49	0.09	0.15	99.7	
		Co-firing 41	.9 kg/h P	KS and 4.2	kg/h EFB (EF <sub>2</sub> =	0.05)		
20	3.6	5.32	1170	548	0.29	1.16	98.5	
42	6.3	4.92	410	230	0.27	0.54	99.2	
60	7.9	4.89	220	120	0.26	0.32	99.4	
82	9.5	4.33	150	78	0.23	0.24	99.5	
	•	Co-firing 39	0.7 kg/h P	KS and 8.4	kg/h EFB (EF <sub>2</sub> =	0.10)		
23	4.1	5.47	1278	640	0.33	1.39	98.3	
42	6.3	5.4	520	311	0.32	0.73	99.0	
58	7.8	5.03	300	169	0.30	0.45	99.2	
82	9.5	4.83	220	101	0.29	0.34	99.4	
	(	Co-firing 37.	5 kg/h PK	KS and 12.7	kg/h EFB (EF <sub>2</sub>	= 0.15)		
20	3.8	4.79	1700	893	0.30	1.91	97.8	
39	6.0	4.17	860	418	0.26	1.07	98.7	
57	7.7	4.15	470	240	0.26	0.68	99.6	
80	9.4	3.76	360	150	0.23	0.54	99.7	
	(	Co-firing 35.	.3 kg/h PK	KS and 16.9	kg/h EFB (EF <sub>2</sub>	= 0.20)		
22	4.1	8.04	1810	1008	0.58	2.19	97.2	
42	6.4	4.56	930	502	0.32	1.29	98.4	
58	7.8	4.02	570	303	0.28	0.87	98.8	
77	9.2	4.00	440	211	0.28	0.71	99.1	
	(	Co-firing 33.	1 kg/h Pk	KS and 21.1	kg/h EFB (EF <sub>2</sub>	= 0.25)		
21	4.0	3.31	2330	1244	0.24	2.79	97.0	
41	6.3	2.47	1300	629	0.18	1.72	98.1	
56	7.7	2.23	860	392	0.16	1.23	98.6	
81	9.5	2.06	600	259	0.15	0.97	98.8	
Measured at s	tack		-					

<sup>&</sup>lt;sup>a</sup> Measured at stack.

The optimal energy fraction of EFB in the total fuel supply (EF $_2 \approx 0.15$ ) seems to be a reasonable parameter, which was used at further stages of this thesis work (in case studies with the AS/SS bed mixtures). Indeed, lowering of EF $_2$  would lead to a lesser NO

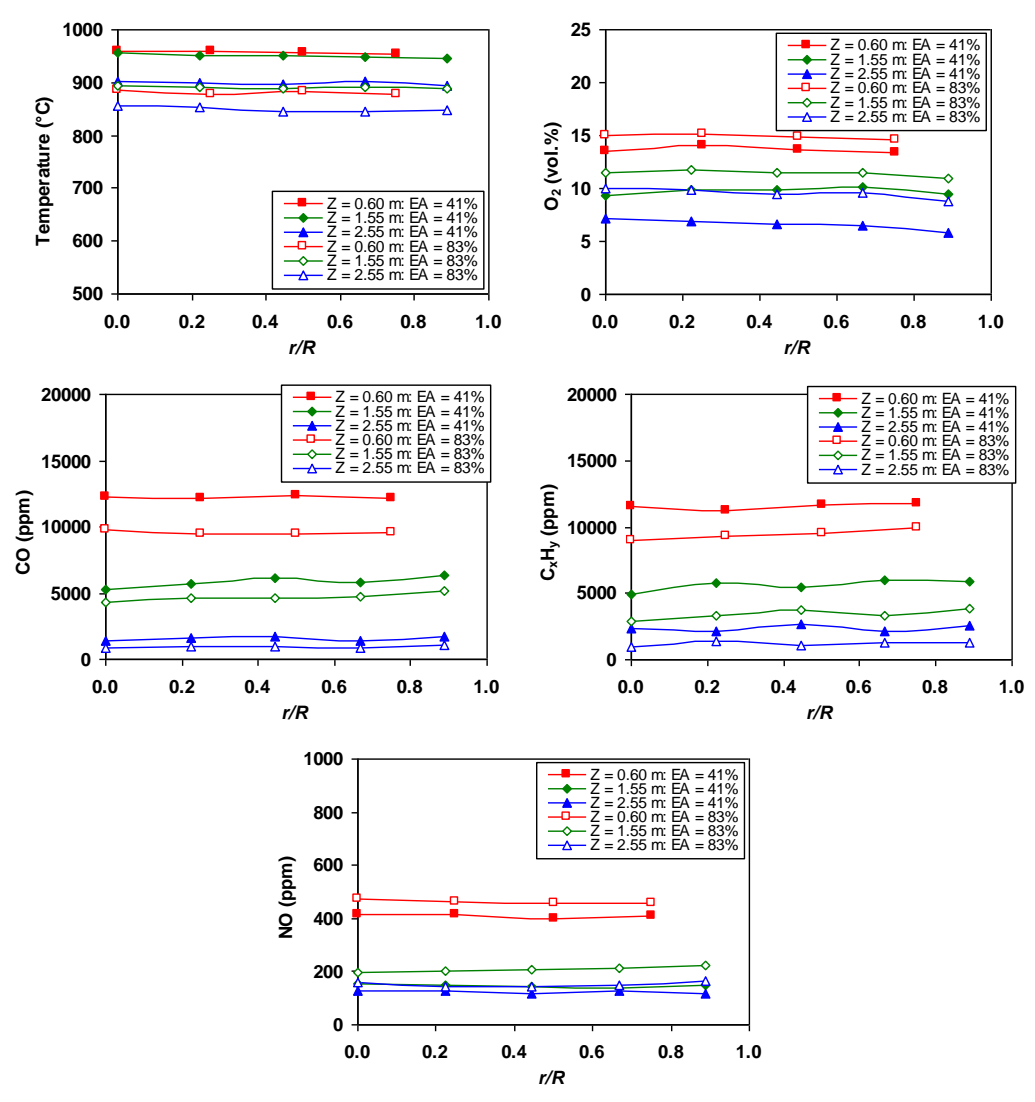


Fig. 5.3. Radial profiles of temperature,  $O_2$ , CO,  $C_xH_y$  (as  $CH_4$ ), and NO in the conical FBC using alumina sand as the bed material when co-firing PKS and EFB at  $EF_2 = 0.15$  for two excess air values:  $EA \approx 40\%$  and  $EA \approx 80\%$ .

emission reduction, whereas higher values of  $EF_2$  would result in the increased CO and  $C_xH_y$  emissions, as well as higher risk of bed agglomeration.

## 5.3 Radial profiles temperature and gas concentrations inside the conical FBC combustor co-fired with PKS and EFB at the optimal energy fraction of EFB

Fig. 5.3 presents the distribution of temperature and gas concentrations ( $O_2$ , CO,  $C_xH_y$  as  $CH_4$ , and NO) in the radial direction inside this combustor with the alumina sand bed, at three selected levels (Z) above the air distributor, when co-firing PKS and EFB at

the optimal energy fraction of EFB, EF<sub>2</sub> = 0.15 (as determined from the above optimization procedure), for the two excess air values ( $\sim$ 40% and  $\sim$ 80%). It can be seen in Fig. 5.3 that the radial temperature and gas concentration profiles were fairly uniform at all three levels above the air distributor despite that the secondary fuel (EFB) was injected over the fluidized bed. This result can be attributed to the highly intensive gas—solid and gas—gas mixing across the reactor in various regions inside this fuel staged combustor operated at substantially different amounts of excess air. Based on this, it was decided to use axial profiles of the temperature and gas concentrations in further analysis of the combustion and emission performance of the conical FBC when using different bed materials.

From the visual observation of the bed material (alumina sand), no features of bed agglomeration were found after finishing these preliminary tests, which lasted for ~20 h in total.

### 5.4 Effects of excess air on combustion characteristics and pollutant behaviors inside the reactor using a mixture of alumina and silica sand as the bed material

Fig. 5.4 depicts the distribution of combustion characteristics (temperature and  $O_2$ ) and that of CO,  $C_xH_y$  (as  $CH_4$ ), and NO along the reactor centerline for the cocombustion tests at  $EF_2 = 0.15$  and variable excess air, when using a (50% AS + 50% SS) mixture as the bed material to reduce the bed material cost. As seen in Fig. 5.4, the axial temperature profiles were fairly uniform, similar to case studies of individual burning of PKS and EFB in this conical FBC (Ninduangdee and Kuprianov, 2013; Ninduangdee and Kuprianov, 2016). There were some effects of EA on the bed temperature, as well as on the maximum temperature, the latter was observed in the vicinity of the secondary fuel injection. Thus, with increasing EA within the range, the maximum temperature dropped noticeably, from 940 °C to 840 °C, basically caused by air dilution effects. However, the behavior of axial  $O_2$  profiles pointed at the substantial consumption of  $O_2$  (or high rate of PKS burnout) within the conical section, and a low rate of fuel oxidation in the upper regions of the reactor. With higher EA,  $O_2$  increased at all points along the reactor height, mainly because of the increased airflow rate.

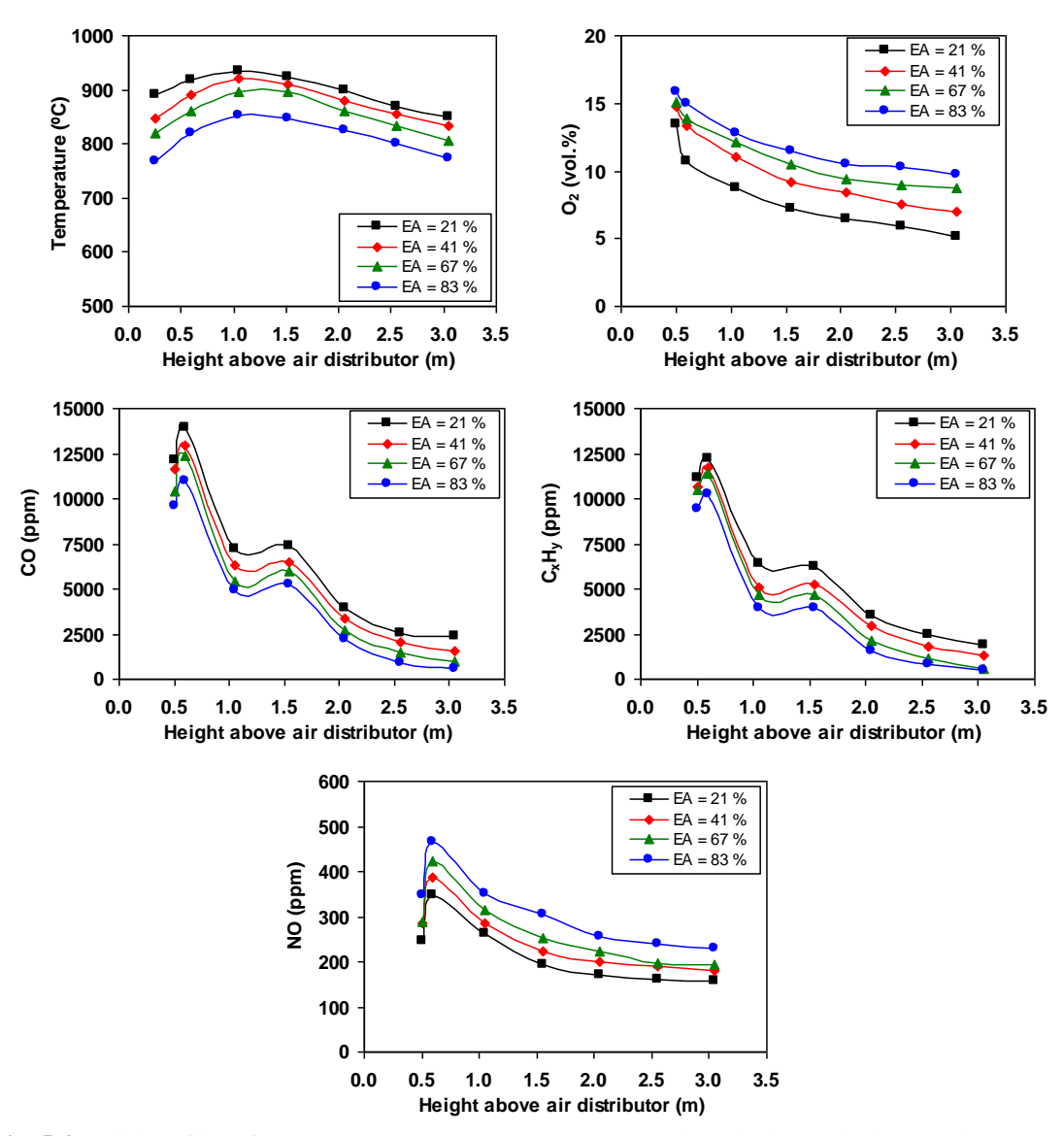


**Fig. 5.4.** Axial profiles of temperature,  $O_2$ , CO,  $C_xH_y$  (as  $CH_4$ ), and NO in the conical FBC using a (50% AS + 50% SS) mixture as the bed material when co-firing PKS and EFB at a constant energy fraction of EFB (EF<sub>2</sub> = 0.15) for variable excess air.

Unlike with the temperature and  $O_2$ , the CO and  $C_xH_y$  axial profiles showed the apparent effects from fuel staging, namely, the formation of two peaks at Z=0.6 m (in the vicinity of PKS injection) and Z=1.5 m (caused by EFB injection). It should be noted that the second (upper) peaks of CO and  $C_xH_y$  played an important role in NO reduction in the secondary combustion zone, leading eventually to the reduced NO emission from this fuel staged reactor, as compared to burning pure PKS at similar EA

(as shown in the preliminary tests with alumina sand). With lowering EA (at fixed  $EF_2$ ), the second peaks of CO and  $C_xH_y$  were higher, indicating a greater potential for NO emission reduction via fuel staging.

In the meantime, as seen in Fig. 5.4, all axial profiles of NO had only one peak, observed in the vicinity of PKS injection (i.e., at  $Z \approx 0.6$  m), which was proportionally correlated with EA (according to the fuel-NO formation mechanism (Werther et al., 2000). The "cut off" of a second NO peak can be attributed to the generation of elevated CO and light hydrocarbon radicals in the secondary combustion zone. The NO–CO and NO–CH<sub>i</sub> reactions were generally responsible for the effective NO reduction in this zone with lowered O<sub>2</sub> (Nussbaumer, 2003; Sirisomboon and Kuprianov, 2017; Suheri and Kuprianov, 2015; Werther et al., 2000), preventing the formation of the second NO peak in the vicinity of EFB injection, and thus, ensuring a smooth decrease of NO in the reactor region at Z > 0.6 m, at nearly the same rate for all EA values.

### 5.5 Effects of excess air and bed material type on the emissions and combustion efficiency

Table 5.2 shows the CO,  $C_xH_y$  (as  $CH_4$ ), and NO emissions (all at 6%  $O_2$  and on a dry gas basis), the predicted heat losses (due to unburned carbon and incomplete combustion), and the combustion efficiency of the conical FBC co-fired with PKS and EFB at  $EF_2 = 0.15$ , for the actual amount of EA (or  $O_2$  at stack) in test runs with the selected bed materials (AS/SS mixtures). The contents of unburned carbon in PM (required for quantifying the associated heat loss) for all the test runs are included in Table 5.2 as well.

It appears that all presented characteristics were substantially affected by EA. With increasing EA within the range, the unburned carbon content in PM and the emission concentrations of CO and  $C_xH_y$  decreased for the three AS/SS bed mixtures, leading to a noticeable reduction in the combustion-related heat losses, and consequently, improvement in the combustion efficiency of the conical FBC. However, for each bed material, the NO emission increased as EA was higher, complying with the fuel-NO

**Table 5.2** Emissions, heat losses, and combustion efficiency of the conical FBC, co-fired with PKS and EFB at a constant energy fraction of EFB ( $EF_2 = 0.15$ ) and variable excess air when using selected AS/SS mixtures as bed material.

Excess air	-	Carbon in PM	Emissions <sup>a</sup> (ppm):			Heat loss	Combustion				
(vol.%)	(vol.%)	(wt.%)	CO	$C_xH_y$	NO	unburned carbon	incomplete combustion	efficiency (%)			
		Testing w	ith the (7	'5% AS -	- 25% S	S) bed mixtu					
24	4.4	2.48	1542	1070	123	0.15	2.13	97.7			
42	6.6	1.90	701	425	126	0.12	1.04	98.8			
53	7.4	1.27	436	364	142	0.08	0.85	99.1			
82	9.5	1.16	310	121	152	0.07	0.45	99.5			
		Testing w	ith the (5	50% AS -	+ 50% S.	S) bed mixtu	re				
21	4.4	9.33	2225	1860	152	0.62	3.44	95.9			
41	6.5	5.72	1230	1100	173	0.36	2.32	97.3			
59	8.0	2.11	580	450	187	0.13	1.18	98.7			
83	9.7	1.66	445	362	200	0.1	1.03	98.9			
	Testing with the (25% AS + 75% SS) bed mixture										
22	4.2	9.72	1895	1725	146	0.65	3.08	96.3			
40	6.3	9.66	1060	960	172	0.64	2.19	97.2			
57	7.8	1.82	560	420	189	0.11	1.04	98.9			
82	9.4	1.79	325	271	198	0.11	0.75	99.1			

<sup>&</sup>lt;sup>a</sup> At 6% O<sub>2</sub> (on a dry gas basis)

formation mechanism, and because of the weakening effects from the NO reduction reactions.

Data in Table 5.2 shows that a bed mixture with a higher proportion of AS resulted in a lower NO emission from this combustor at similar EA. Furthermore, during co-firing of PKS and EFB at EF<sub>2</sub>  $\approx 0.15$  and EA  $\approx 55\%$  with pure alumina sand (100% AS), the NO emission was as low as 125 ppm (see Fig. 2). From the data in Table 5 under similar operating conditions, this emission was lower than that in the tests with the AS/SS bed mixtures: about 145 ppm, 185 ppm, and 190 ppm when using the bed materials with 75%, 50%, and 25% of AS, respectively. These results can be generally attributed to the higher catalytic reactivity of AS, as compared with SS, for the (reduction) reaction of NO with CO (Li et al., 2014; Wang et al., 2012). From Table 5.2, high (up to 99.5%) combustion efficiency and acceptable CO and NO emissions (below the national emission limits (PCD, 2018) can be achieved through the co-firing of PKS and EFB at

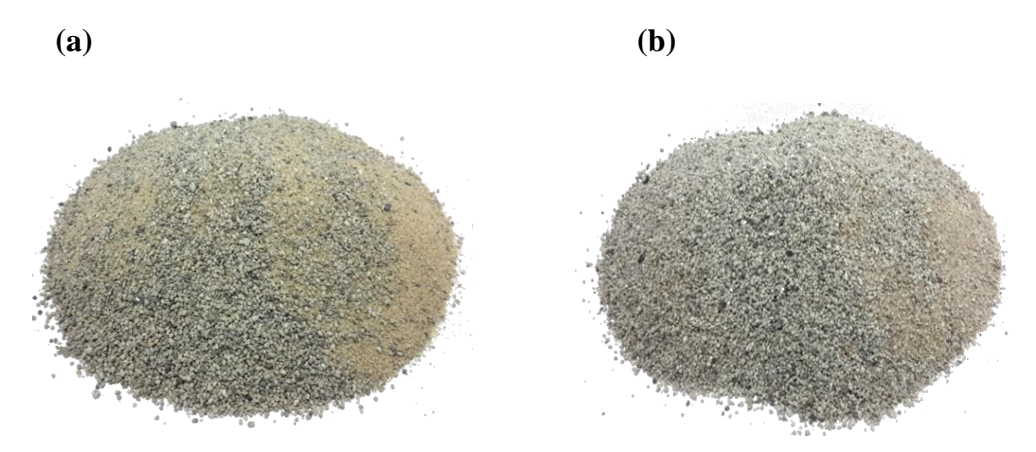


**Fig. 5.5.** Appearance of the bed materials: (a) a (75% AS + 25% SS) mixture after the 22-h co-combustion tests, and (b) a (50% AS + 50% SS) mixture after 26-h testing.

50-80% excess air in the proposed fuel staged conical FBC with the selected AS/SS bed mixtures.

A test for burning the base fuel (pure PKS) at EA  $\approx$  55% using a (50% AS + 50% SS) mixture as the bed material yielded an NO emission of about 250 ppm (at 6% O<sub>2</sub> and on a dry gas basis) that was higher than the national emission limit for this pollutant. Thus, co-firing of PKS and EFB under optimal operating conditions (EF<sub>2</sub>  $\approx$  0.15 and EA  $\approx$  55%) with this bed mixture resulted in the reduction of the NO emission by about 25% (as compared to burning the base fuel) and ensured that the CO and NO emission concentrations were within the above-mentioned national emission limits.

### 5.6 Physical condition and particle size distribution of the bed material at different operating times

To investigate the time-related behavior of the bed material, "long-term" experiments for co-firing of PKS and EFB at the optimal operating conditions (EF $_2$  = 0.15 and EA 50%) were performed on the conical FBC using three bed mixtures with different AS/SS ratios. Visual observations of the selected bed mixtures showed apparent changes in a physical appearance of the bed materials with time.

As revealed by visual inspections at different time instants, no bed agglomeration occurred in the conical FBC co-fired with PKS and EFB for the entire experimental time period when using (75% AS + 25% SS) and (50% AS + 50% SS) bed mixtures. Fig. 5.5

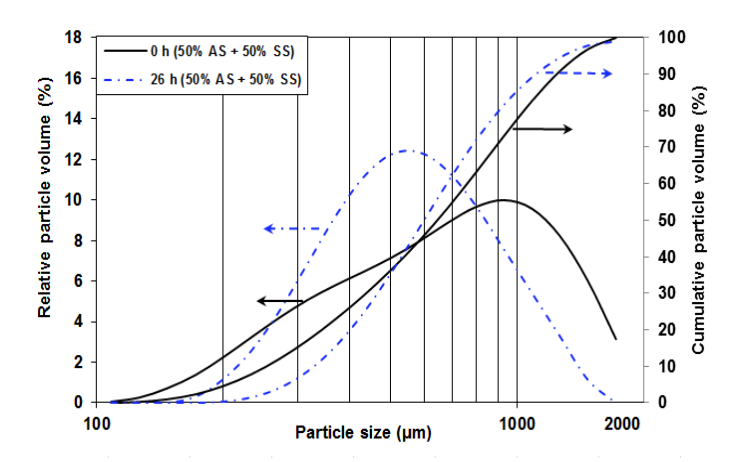


Fig. 5.6. Comparison of the particle size distribution between the original and reused bed materials when using the (50% AS + 50% SS) bed mixture.

depicts the physical apperance of these bed materials after finishing the tests for 22 h and 26 h, respetively. This apperance seems to be normal, as the two materials consisted of AS and SS grains capable to fluidize and be used in further reactor operation.

Fig. 5.6 depicts the particle size distribution of original and reused bed materials for the (50% AS + 50% SS) bed mixtures, i.e., for the co-combustion tests when bed agglomeration was not observed despite a relatively high proportion of SS in the bed material. The analysis of the particle size distribution showed a apparent/substantial reduction in the mean bed particle size within the entire experimental time period: from about 950  $\mu$ m to 558  $\mu$ m. This fact can be solely explained by breakage and attrition of SS grains fluidized in the bed, despite the fact that the AS grains basically increase their mean particle size during the fluidized-bed combustion of high-alkali biomass with pure AS as bed material (Ninduangdee and Kuprianov, 2015).

#### 5.7 SEM-EDS analysis of the used/reused bed materials

As revealed by visual inspections of the bed material for the entire experimental time, no bed agglomeration occurred in the conical FBC during co-combustion of PKS and EFB at the optimal EF<sub>2</sub> and EA, when the AS/SS bed mixtures contained 50% of AS or higher. Fig. 5.7 shows the SEM images and respective EDS compositions at different

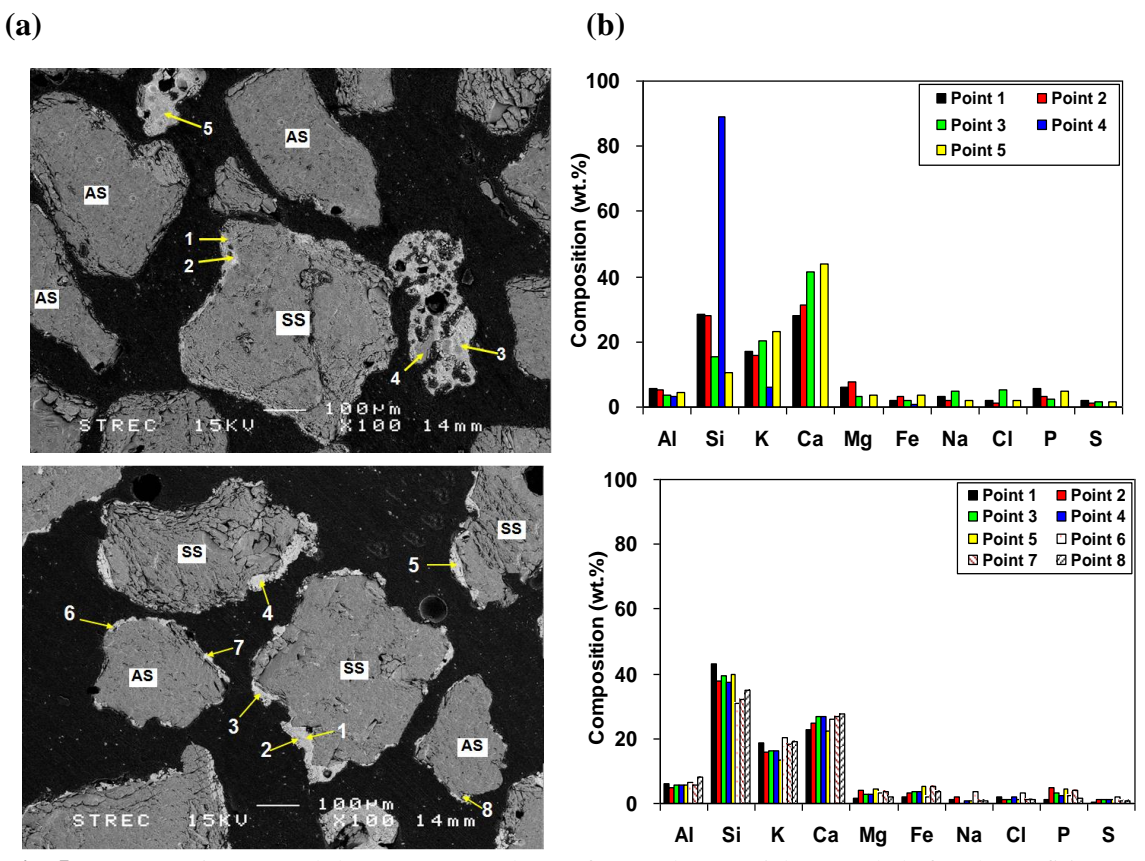


**Fig. 5.7.** (a) SEM images and (b) EDS spot analyses of AS and SS particles sampled after the co-firing tests on the conical FBC using a (75% AS + 25% SS) mixture (upper micrograph) and a (50% AS + 50% SS) mixture (lower micrograph) as the bed material under optimal operating conditions.

spots on some SS and AS particles, sampled after the co-firing test series with the (75% AS + 25% SS) and (50% AS + 50% SS) mixtures, lasting 24 h and 26 h, respectively.

From the SEM image of the bed particles collected after the tests with the (75% AS + 25% SS) bed mixture (Fig. 5.7a, upper micrograph), the bed grains of both AS and SS exhibited a normal appearance. As seen in Fig. 5.7a (Points 1 and 2), SS particles were coated by a thin layer with brighter areas, mainly rich in Ca, Si, and K but also containing minor proportions of Al, Mg, Fe, and P, whereas no coating layers on the AS particles were detected. The bed material included a small proportion of the ash-derived melts (e.g., at Point 3), generally rich in Ca, K, and Si, the major constituents of low-melting (adhesive) K<sub>2</sub>O–CaO–SiO<sub>2</sub> eutectics originating from the PKS and EFB ashes (Lin et al., 2003; Ninduangdee and Kuprianov, 2015). It was also found that some small

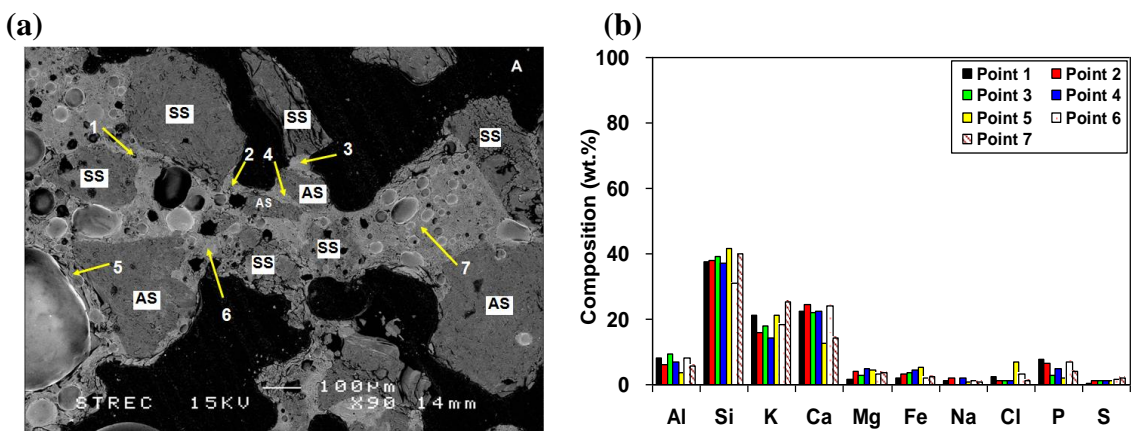


**Fig. 5.8.** (a) SEM image and (b) EDS spot analysis of agglomerates, sampled after 17-h co-firing tests on the conical FBC using a (25% AS + 75% SS) mixture as the bed material under optimal operating conditions.

particles of SS with high content of Si (e.g., indicated as Point 4) were adhered by the ash melts at Point 3. However, fine alumina particles, generated due to collisions and attrition of bed grains in this turbulent fluidized bed with predominant content of AS, were adhered by the partly molten chars/ashes and adsorbed by the bed grain coatings (when formed), decreasing adhesiveness of the melts and bed grains, and thus, preventing bed agglomeration (Ninduangdee and Kuprianov, 2016).

The SEM image of the bed particles sampled after the tests with the (50% AS + 50% SS) bed mixture (see Fig. 5.7a, lower micrograph) revealed that both AS and SS grains were covered with the coatings, of up to 40 µm in thickness, generally observed on the SS bed particles. From the EDS analysis, the elemental composition at some selected spots on the coatings of both AS and SS particles were quite similar, basically dominated by Si, Ca, and K, and included minor proportions of Al, Mg, Fe, and P. However, compared to the previous case, a greater proportion of SS in the bed material, and consequently, a higher proportion of fine SS particles in the fluidized bed (generated from the grains attrition) shifted the content of Si in all EDS spot analyses to a higher level. This indicates the increased adhesiveness of both ash melts and grain coatings, resulting in more intensive coating of the bed particles.

As reported in a number of studies on the fluidized-bed combustion of biomass in systems using quartz/silica sand as the bed material, the coating of an individual bed

particle may consist of several superimposed layers with different compositions, depending on the analysis of biomass ash and that of the bed material (Brus et al., 2005; Chaivatamaset and Tia, 2015; Öhman et al., 2000). However, as seen in the SEM micrographs in Fig. 6a, the coatings of both SS and AS grains were (almost) consistent in chemical composition.

Summarizing the results presented in Fig. 5.7, the coatings on the AS and SS particles were likely formed due to: (i) interaction of bed grains with partly molten fuel-char and ash particles, (ii) migration of the ash melts, generally consisting of low-melting K and K–Ca silicates, onto the surface of AS and SS particles, causing a grain coating in some surface areas, and (iii) adsorption of fine solid particles (generated in attrition of bed grains and fuel ash in a fluidized bed) onto the coated grain surface, thus affecting the coating adhesiveness (Brus et al., 2005).

In the experiments with the (25% AS + 75% SS) mixture, bed defluidization was observed in the conical FBC after 17 h of combustor running. Some agglomerates were sampled and then analyzed for their physical and chemical properties. Fig. 5.8 shows the SEM–EDS analysis of agglomerates collected from this bed material after an emergent shutdown of the combustor. The SEM image in Fig. 5.8a revealed that the agglomerates were formed by binding the bed particles of different chemical compositions and sizes. The binding material that bonded the particles was rich in Si, K, and Ca with minor contents of Al, Mg, P, and Fe. The quantity and quality (i.e., chemical composition) of the binding materials at different spots in Fig. 5.8a indicated: (1) the formation of low-melting  $K_2O$ – $SiO_2$  and  $K_2O$ –CaO– $SiO_2$  eutectics (generally formed on the surface of SS particles as a result of reaction of K-rich vapor species from biomass ash with  $SiO_2$  in SS grains) and (ii) the small contribution of the ash melts to bed agglomeration.

It can be concluded that with a greater proportion of SS in a AS/SS mixture, the risk of (or tendency for) bed agglomeration increased significantly, mainly due to an increase in the SS surface area, on which the ash-derived K-rich vapor compounds reacted with SiO<sub>2</sub> in SS, enhancing the bed agglomeration tendency.

**Table 5.3**Composition of the bed materials used/reused in the conical FBC during co-firing of PKS and EFB under optimal operating conditions at different time instants of combustor operation.

Operating time (h)		Composition (as oxides, wt.%):								
	$Al_2O_3$	SiO <sub>2</sub>	CaO	MgO	Na <sub>2</sub> O	K <sub>2</sub> O	Fe <sub>2</sub> O <sub>3</sub>	$P_2O_5$		
Testing with the (75% AS + 25% SS) bed mixture										
6 (used bed material)	30.50	56.50	3.27	0.73	0.38	6.52	1.02	0.70		
14 (reused bed material)	19.40	64.20	4.58	0.94	0.38	7.77	1.17	0.85		
24 (reused bed material)	18.00	65.90	5.18	0.93	0.28	6.92	1.51	0.84		
	Testing	with the (.	50% AS +	50% SS) i	bed mixtur	·e	l			
8 (used bed material)	18.50	72.20	1.36	0.22	0.29	5.07	0.77	0.20		
13 (reused bed material)	15.90	72.50	2.81	0.39	0.27	6.28	1.12	0.33		
21 (reused bed material)	13.00	74.10	3.33	0.54	0.22	6.83	1.05	0.52		
26 (reused bed material)	10.80	74.80	3.66	0.63	0.21	7.95	1.10	0.55		
Testing with the (25% AS + 75% SS) bed mixture										
8 (used bed material)	10.70	81.00	1.07	0.20	0.29	5.69	0.74	0.15		

### 5.8 Time-related changes in compositions of the bed materials and particulate matter

Table 5.3 shows the composition of the bed mixtures, used/reused in the conical FBC during the co-firing tests for different operating time instants. Because of early bed agglomeration, the composition of the bed material, originally represented by the (25% AS + 75% SS) mixture, is presented in Table 5.3 only for the 8-h operating period. Due to the coating of AS and SS grains and because of presence of some PM retained in the bed, the ash-forming elements, particularly K, Ca, Mg, and Fe, showed an increase in their contents in all the bed mixtures with operating time. However, Al (that is responsible for mitigating bed agglomeration) showed a gradual time-domain decrease in the selected bed mixtures, which pointed at the diminishing capability of each bed material to withstand bed agglomeration. Note that the content of all constituents in a bed were noticeably affected by the bed AS/SS ratio.

Table 5.4 presents the composition of PM originating from the co-combustion of PKS and EFB for the same bed materials and operating times, as in Table 5.3. The results in Tables 5.3 and 5.4 indicate the significant mutual impact of the bed mixture and fuel ash during co-combustion of PKS and EFB. However, as seen in Table 5.4, in the test series with different AS/SS bed mixtures, the contents of Al and Si in PM were greater at all time instants, compared to those in the fuel ashes of the selected PKS/EFB mixture. This fact was likely due to carryover of fine particles rich with Al and Si (generated during the attrition of AS/SS grains in the fluidized bed), which joined the PM. Carryover of Al-rich particles from the fluidized bed contributed to a time-related decrease of Al<sub>2</sub>O<sub>3</sub> in the bed material during the co-combustion tests (see Table 5.3).

**Table 5.4**Composition of particulate matter originating from the co-firing of PKS and EFB in the conical FBC under optimal operating conditions when using selected AS/SS mixtures as the bed material for different operating times.

Operating time (h)	Composition (as oxides, wt.%):									
	$Al_2O_3$	SiO <sub>2</sub>	CaO	MgO	Na <sub>2</sub> O	K <sub>2</sub> O	Fe <sub>2</sub> O <sub>3</sub>	$P_2O_5$	Cl	
	Testing with the (75% AS + 25% SS) bed mixture									
6 (used bed material)	9.13	34.40	34.40	3.64	1.20	7.50	2.36	3.47	1.47	
14 (reused bed material)	4.03	43.40	33.10	2.91	0.58	6.99	2.10	3.49	0.91	
24 (reused bed material)	3.99	45.40	33.80	2.47	0.44	6.20	1.87	2.90	0.75	
	Testing	g with the	e (50% A.	S + 50%	SS) bed n	nixture				
8 (used bed material)	8.82	41.80	37.00	1.51	0.76	3.85	1.93	1.80	0.57	
13 (reused bed material)	6.75	43.00	35.70	1.92	0.75	4.51	2.25	2.29	0.64	
21 (reused bed material)	4.85	41.40	31.40	4.10	0.53	7.77	2.23	3.94	1.31	
26 (reused bed material)	3.88	43.10	29.60	3.32	0.44	9.56	2.44	3.71	1.55	
	Testing with the (25% AS + 75% SS) bed mixture									
8 (used bed material)	5.54	55.10	25.90	1.92	0.40	5.06	1.97	2.32	0.29	

#### Chapter 6

### Fluidized Bed Co-combustion of Rice Husk Pellets and Moisturized Rice Husk: The Effects of Co-combustion Methods on Gaseous Emissions

#### 6.1. Distribution of temperature and $O_2$ in the conical FBC

Fig. 6.1 shows the axial temperature and  $O_2$  profiles in the combustor for the selected co-combustion techniques, co-fired with PRH and MRH at  $EF_2 = 0.15$  (Fig. 6.1a) and  $EF_2 = 0.25$  (Fig. 6.1b), and  $EA \approx 40\%$  with different SA/TA (applied in the reburning tests), as compared with the conventional combustion of the base fuel (PRH) at the specified EA.

In all trials, the axial temperature profiles were rather uniform, particularly in the fluidized bed region (i.e., within the conical section of the combustor). There were some effects of  $EF_2$  and SA/TA on the bed temperature, including its maximum. When burning the base fuel on its own, a maximum bed temperature of about 920 °C was observed in the vicinity of PRH injection (at Z=0.6 m). However, during co-combustion of premixed PRH and MRH, the bed temperature was lower than that for firing pure PRH: by 10 °C at  $EF_2=0.15$  and by 35 °C at  $EF_2=0.25$ , likely due to the increased moisture content in the fuel blend.

In the tests for fuel staging with bottom air injection, the temperature at all points in the bottom region was lower, compared to the other co-firing options. This was mainly due to the reduced feeding of PRH that resulted in an increased (local) excess air ratio at the primary combustion zone (i.e., in the fluidized bed). Because of the effects from secondary fuel injection, the maximum temperature for  $EF_2 = 0.15$ , 910 °C, was observed at a higher level, Z = 1.15 m (i.e., beyond the conical section), compared to burning pure PRH. However, during fuel-staged co-combustion at  $EF_2 = 0.25$  (i.e., at a higher feed rate of MRH), the maximum temperature, 890 °C, was shifted to Z = 1.6 m due to the strengthened effects from the secondary fuel.

It can be seen in Fig. 6.1 that during the reburning tests at SA/TA = 0.2 and SA/TA = 0.4, the temperatures inside the reactor were basically higher, as compared to

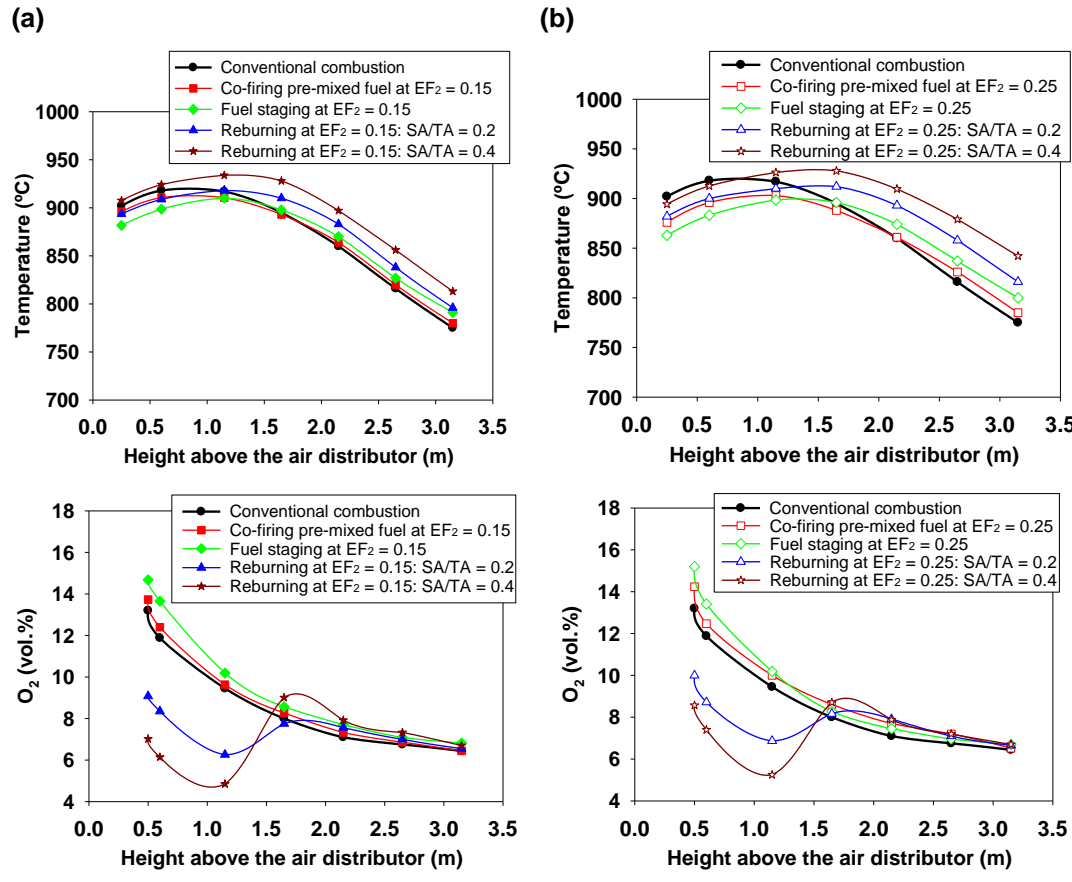


Fig. 6.1. Axial profiles of temperature and  $O_2$  in the conical FBC co-fired with PRH and MRH at EA  $\approx$  40%, using different co-firing options for (a)  $EF_2 = 0.15$  and (b)  $EF_2 = 0.25$ , in comparison with the conventional combustion of PRH.

the other two co-firing options for similar  $EF_2$ . This is mainly due to the lowered (local) excess air ratio in the primary combustion zone. Injection of secondary air at Z=1.65 m resulted in the higher maximum temperature in the reburning tests, because of delayed oxidation of combustibles formed in the reburn zone and, therefore, shifting this temperature to a higher level (Z). Note that the maximum temperature in the reburning tests was almost independent of  $EF_2$ . However, it was noticeably affected by SA/TA: 915 °C for SA/TA = 0.2 and 930 °C for SA/TA = 0.4, observed at Z=1.15 m for  $EF_2=0.15$  and at Z=1.6 m for  $EF_2=0.25$ .

In all the test runs, the temperature showed a gradual decrease in the upper part of the combustor, mainly because of the heat loss across the reactor walls, at nearly the same rate. Therefore, the difference between the axial temperature profiles for the selected (co-)combustion methods was primarily affected by the magnitude and location of the maximum temperature in each test run. As a result, in the reburning tests at  $EF_2 = 0.25$  and SA/TA = 0.4, the temperatures at similar points in the reactor top were higher, as compared to other test series.

From Fig. 6.1, the axial profiles of  $O_2$  in the tests for burning pure PRH, co-firing of premixed PRH and MRH, and fuel-staged co-combustion of the two fuels showed similar trends, with weak effects from EF<sub>2</sub>. In these three test series, a substantial axial gradient of  $O_2$  was observed in the lower part of the reactor (Z < 1.6 m), comprising primary and secondary combustion zones, whereas in the upper region of the reactor,  $O_2$  consumption and, respectively, fuel oxidation occurred along the combustor height with an insignificant rate.

However, in the reburning tests (when air staging was used along with fuel staging), the  $O_2$  behavior was substantially different. In the primary and reburn zones,  $O_2$  was noticeably lower, compared to the other three test series, which likely caused the above-mentioned delay in oxidation of the secondary fuel. It should be noted that by  $Z \approx 1.7$  m,  $O_2$  regained to a level comparable with the other test series. At the reactor top (Z = 3.2 m),  $O_2$  showed the concentration values that were similar to those for the other (co-)combustion techniques, which were correlated with the selected amount of EA (40%).

#### 6.2. Formation and oxidation of CO and C<sub>x</sub>H<sub>y</sub> inside the conical FBC

Fig. 6.2 shows the axial profiles of CO and  $C_xH_y$  (as  $CH_4$ ) in the conical FBC for the same (co-)firing techniques and operating parameters, as in Fig. 6.1. In all the test runs, these profiles showed two specific regions: (i) rapid generation of CO and  $C_xH_y$  in the bottom region of the combustor and (ii) gradual oxidation of these pollutants in the upper region of the reactor.

The axial CO and  $C_xH_y$  profiles for burning pure PRH, as well as for the co-firing of pre-mixed PRH and MRH, showed similar shapes, with a concentration peak at  $Z \approx 0.6$  m, i.e., at the level of PRH (or PRH/MRH mixture) injection.

In the bottom region, CO and C<sub>x</sub>H<sub>y</sub> increased drastically along the combustor height in all test series, primarily due to rapid devolatilization of PRH and fuel-char

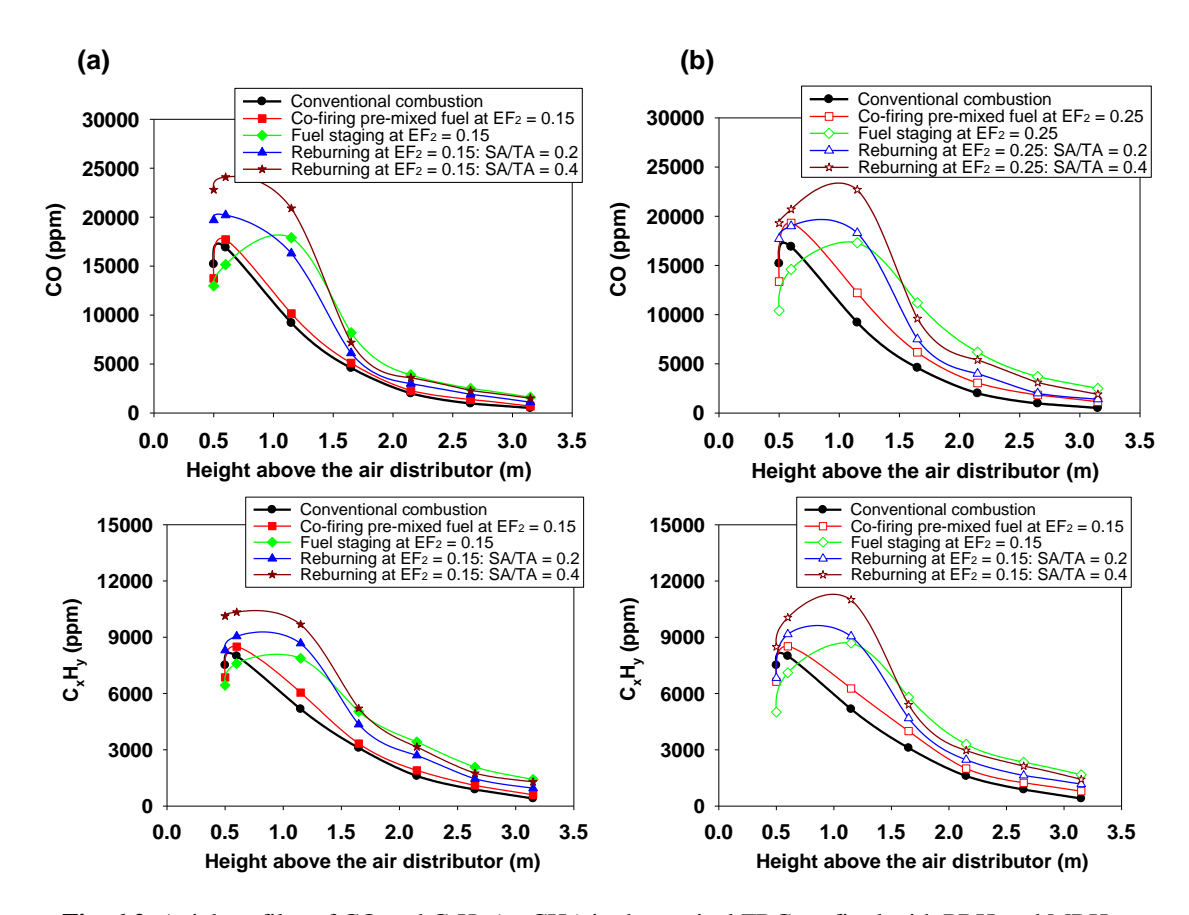


Fig. 6.2. Axial profiles of CO and  $C_xH_y$  (as  $CH_4$ ) in the conical FBC co-fired with PRH and MRH at  $EA \approx 40\%$ , using different co-firing options for (a)  $EF_2 = 0.15$  and (b)  $EF_2 = 0.25$ , in comparison with the conventional combustion of PRH.

oxidation (at a lesser extent), both contributing to CO formation. The two pollutants were oxidized in this region at low rates, compared to their formation rates. According to (Turns, 2006), CO was generally oxidized to  $CO_2$  by O and OH radicals, whereas the  $C_xH_y$  oxidation involved two stages: (i) breakdown of  $C_xH_y$  to CO and (ii) further oxidation of CO to  $CO_2$ .

It can be seen in 6.2 that when co-firing premixed PRH and MRH, CO and  $C_xH_y$  at all points along the combustor height were somewhat higher, compared to burning pure PRH. This is mainly due to the reduced bed temperature (see Fig. 6.1), which led to the lower rates of CO and  $C_xH_y$  oxidation in the primary combustion zone.

From Fig. 6.2, the use of fuel staging with bottom air injection led to the lowest level of both CO and  $C_xH_v$  in the primary combustion zone (i.e., in the fluidized bed).

This fact can be attributed to the reduced feed rate of the primary fuel (PRH) that resulted in the increased (local) excess air ratio at the reactor bottom. Both these factors enhanced the CO and  $C_xH_y$  oxidation rate in the primary combustion zone despite the reduced bed temperatures (as seen in Fig. 6.1). However, when using reburning, CO and  $C_xH_y$  in the primary combustion zone were highest, as compared to other test series. This is mainly due to the substantially decreased  $O_2$  at Z < 1. 5 m, which resulted in a lowered rate of CO and  $C_xH_y$  oxidation at the combustor bottom.

Note that, in the trials for fuel staging and reburning, CO and  $C_xH_y$  in the secondary/reburn zone were substantially higher than those for the two other test series: for individual burning of PRH and co-firing of pre-mixed PRH and MRH. This result can be explained by the rapid devolatilization of the secondary fuel injected into the reactor at Z = 1.15 m. Furthermore, when using reburning, the reduced  $O_2$  concentrations resulted in a lower rate of CO and  $C_xH_y$  oxidation in both the primary and reburn zones. The highest peaks of CO and  $C_xH_y$  were therefore observed in the reburning tests at SA/TA = 0.4 with weak effects from EF<sub>2</sub>. However, an increase of EF<sub>2</sub> from 0.15 to 0.25 shifted the peaks of CO and  $C_xH_y$  from the primary combustion zone to a level close to MRH injection in the reburn zone, as can be seen in Fig. 6.2.

In the region above the secondary fuel injection, where oxidation reactions prevailed, both CO and  $C_xH_y$  decreased gradually along the reactor height to their minimum values at the reactor top. In the reburning tests, CO and  $C_xH_y$  rapidly decreased downstream from the point of injection of secondary air (particularly at SA/TA = 0.4), which enhanced their oxidation rates in the middle region of the reactor. As a result, a substantial amount of heat was released in the vicinity of secondary air injection, which resulted in the increased temperatures in the cylindrical section of the reactor during reburning tests, especially at highest EF<sub>2</sub> and SA/TA (see Fig. 6.1).

#### 6.3. Formation and reduction of NO inside the reactor

During biomass combustion, NO is mainly formed from volatile matter in a fuel, via oxidation of volatile NH<sub>3</sub> and HCN in multiple routes of the fuel-NO formation mechanism (with proportional effects of fuel-N, excess air, and temperature), whereas the

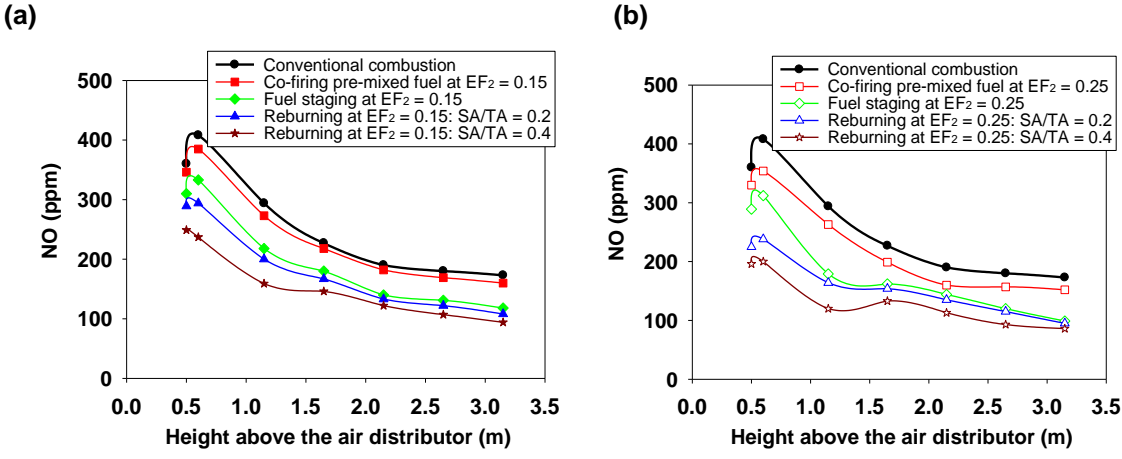


**Fig. 6.3.** Axial profiles NO in the conical FBC co-fired with PRH and MRH at EA  $\approx$  40%, using different co-firing options for (a) EF<sub>2</sub> = 0.15 and (b) EF<sub>2</sub> = 0.25, in comparison with the conventional combustion of PRH.

contributions of thermal-NO and prompt-NO are reported to be minor (Werther et al., 2000; Winter et al., 1999). However, due to secondary reactions, such as the catalytic reduction of NO by CO on the char/ash surfaces (Karlström et al., 2017; Lu et al., 2009; Zhong et al., 2002) and homogeneous reactions of NO with some radicals (such as CH<sub>i</sub>, NH<sub>2</sub>/NH, and HCCO) in a flame (Ballester et al., 2008; Casaca and Costa, 2009; Smoot et al., 1998; Winter et al., 1999), NO formed in the primary reactions is reduced to a substantial extent.

Fig. 6.3 depicts the axial profiles of NO in the conical FBC for the same (co-)firing techniques and operating parameters, as in Figs. 2 and 3. Note that in all the trials, the contribution of  $NO_2$  to  $NO_x$  was negligible. In the analysis below,  $NO_x$  is therefore represented only by NO.

It can be seen in Fig. 6.3 that at Z < 0.6 m, NO was rapidly formed from volatile nitrogenous species in PRH (or PRH/MRH mixture), according to the above-mentioned fuel-NO formation mechanism, attaining a peak in the vicinity of fuel injection in all the test runs.

During co-firing of the pre-mixed fuels at any selected EF<sub>2</sub>, NO at all points inside the combustor was lower, compared to burning PRH alone. An increase in EF<sub>2</sub> from 0.15 to 0.25 led to an insignificant reduction of NO at each point, generally because of the higher

CO and  $C_xH_y$ , both being a source of  $CH_i$  and HCCO radicals, enhancing the NO reduction reactions (Ballester et al., 2008; Casaca and Costa, 2009).

From Fig. 6.3, during experiments for fuel staging at  $EF_2 = 0.15$  and  $EF_2 = 0.25$ , NO (including the peak values) was noticeable lower than in the test series for burning pure PRH and co-firing premixed PRH and MRH at similar EA. The reduced NO peaks can be explained by the lowered bed temperatures for both  $EF_2$  (see Fig. 6.1), despite that the local excess air ratio in the primary combustion zone increased because of the reduced feeding of PRH. When  $EF_2$  increased from 0.15 to 0.25, a significant reduction of NO was observed at 0.6 m < Z < 1.15 m. This fact can be attributed to the higher concentrations of CO and  $C_xH_y$  in the vicinity of secondary fuel injection, which enhanced the catalytic reduction and homogeneous reactions of NO in the secondary combustion zone with higher feeding of the MRH. Apart from this, at greater  $EF_2$ , the concentration of fuel chars in the secondary combustion zone was higher, which facilitated the catalytic reduction of NO in this zone.

In the reburning tests, the NO concentrations in the reactor bottom (at Z < 0.6 m), and consequently, the NO peak were substantially lower than those in the other test series, mainly due to the higher concentration of reducing species, such as CO and  $C_xH_y$ , in this region. It should be noted that the axial NO profiles in the reburning tests exhibited the significant impacts of the secondary air. With increasing SA/TA at fixed EA and EF<sub>2</sub> (i.e., with decreasing the air-to-fuel ratio in both the primary and reburn zones), NO in the primary combustion zone showed a noticeable decrease, mainly due to the lowered  $O_2$  (see Fig. 6.1). However, there was a substantial increase of both CO and  $C_xH_y$  in the two zones, which enhanced the rate of the secondary (reduction) reactions in the lower part of the combustor (Shu et al., 2015).

In the upper regions of the combustor, NO showed a gradual decrease along the combustor height in all test series. The rate of NO reduction at each point was dependent on the NO formation/reduction history (in the primary combustion zone), as well as on the levels of CO and  $C_xH_y$  in the secondary/reburn zone. Note that, at  $EF_2=0.25$ , a low secondary peak of NO can be observed in Fig. 6.3b in the vicinity of the secondary air

injection (at  $Z \approx 1.65$  m), which was likely caused by the NO formed from oxidation of nitrogeneous volatile species, released from MRH.

At a lowered level of  $O_2$ , the role of  $NH_2/NH$  (generated from volatile nitrogenous species in rice husk) for NO reduction in the two combustion zones was important in the reburning tests (Casaca and Costa, 2009; Salzmann and Nussbaumer, 2001). Taking into account the reduced formation of NO in the primary combustion zone and highest levels of CO and  $C_xH_y$  in the reburn zone, the reburning method showed the highest potential for the NO reduction among the co-firing techniques studied in this work.

Due to generation of substantial concentrations of CO and  $C_xH_y$  in the secondary combustion zone, the fuel-staged co-firing of PRH and MRH with bottom air injection also showed its effectiveness in terms of NO reduction, however, at a lesser extent compared to reburning.

#### 6.4. Effects of the co-firing options on gaseous emissions

Fig. 6.4 depicts the CO,  $C_xH_y$  (as  $CH_4$ ), and NO emissions (all represented on a dry gas basis and at 6%  $O_2$ ) from the conical FBC (co-)fired with PRH and MRH under variable operating parameters using the proposed co-firing methods. For comparison, the national emission limits of CO (740 ppm) and NO (205 ppm), both represented on a dry gas basis and at 6%  $O_2$ , are shown in Fig. 6.4.

It can be seen in Fig. 5 that, in all the co-firing tests, the CO and  $C_xH_y$  emissions from the combustor were higher than in the tests for burning PRH alone, following the formation and oxidation of these pollutants in different regions inside the reactor. However, an increase in the CO and  $C_xH_y$  emissions during the co-firing of pre-mixed PRH and MRH (see Fig. 6.4a) was less important, compared to the fuel-staged and reburning tests.

With increasing EA within the range (at fixed EF<sub>2</sub> and SA/TA), both CO and  $C_xH_y$  emissions decreased in all the test runs, mainly due to the enhanced oxidation reactions in all regions inside the reactor. At higher values (60–80%), EA showed its weak influence on these emissions. However, an increase of the two emissions was observed with higher EF<sub>2</sub> and SA/TA (at fixed EA), mainly due to strengthening effects

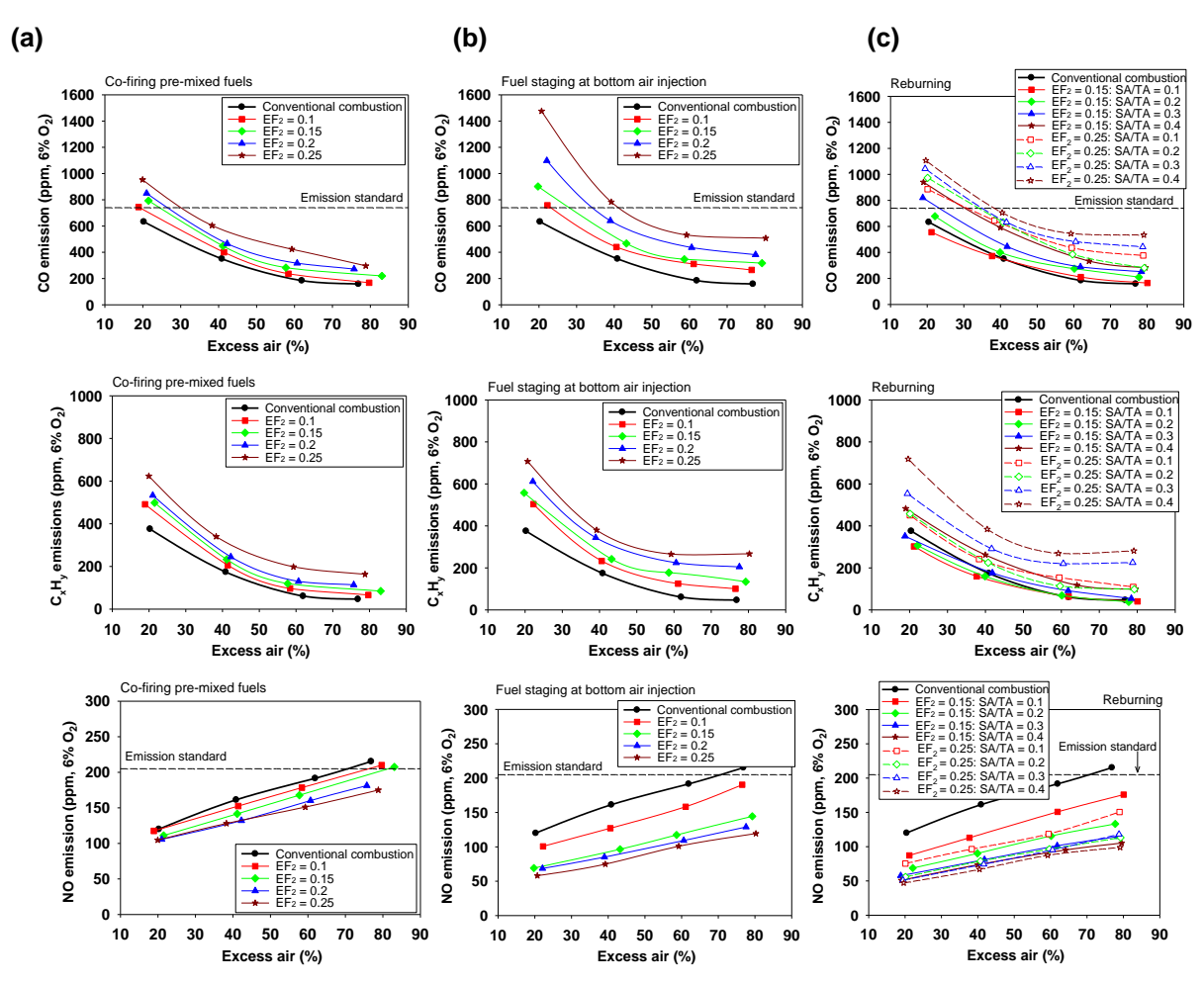


**Fig. 6.4.** Emissions of CO (upper),  $C_xH_y$  as  $CH_4$  (middle), and NO (lower) from the conical FBC when co-firing PRH/MRH under variable operating conditions using: (a) pre-mixed fuels, (b) fuel staging with bottom air injection, and (c) reburning.

to minimize the environmental impacts by the combustor (as discussed below).

#### 6.5. Combustion efficiency

Table 6.1 shows the predicted combustion-related heat losses (due to unburned carbon and incomplete combustion) and the combustion efficiency of the conical FBC, co-fired with PRH and MRH using the proposed co-combustion methods, along with the results for burning pure PRH. Data required for determining the actual amount of excess air and the heat losses, such as unburned carbon content in the PM and actual  $O_2$ , CO, and  $C_xH_y$  (as  $CH_4$ ) at stack, are also included in Table 6.1 for all the test series and runs.

**Table 6.1**Combustion heat losses and efficiency of the conical FBC (co-)fired with PRH and MRH using selected (co-)firing techniques at variable operating parameters.

(co-)firing				ating pa	rameters.					
	Secondar			CO	$C_xH_y$	Unburned	Heat loss (%) due to:		Combustion	
fraction of		air (%)	stack	(ppm)	(ppm)	carbon in	Unburned	Incomplete	efficiency	
secondary	air ratio		(vol.%)			PM (wt.%)	carbon	combustion	(%)	
fuel (EF <sub>2</sub> )	(SA/TA)						carbon	combustion		
Convention	ial combu.	stion of	PRH							
0	0	21	3.7	742	440	3.63	0.81	0.82	98.4	
		41	6.2	350	174	3.15	0.70	0.41	98.9	
		62	8.1	160	53	2.09	0.46	0.17	99.4	
		77	9.1	126	37	1.98	0.44	0.14	99.4	
Co-firing o	f premixed			1	1		1			
0.15	0	22	3.9	923	580	1.62	0.41	1.06	98.5	
0.13	U	41	6.2	448	233	1.59	0.40	0.53	99.1	
		58	7.7	253	107	1.77	0.45	0.30	99.3	
		83	9.6	169	65	1.52	0.43	0.30	99.4	
0.25	0	20	3.7	1100	720	1.32	0.35	1.27	98.4	
0.23	U	38	5.9					_	98.4	
		59		604	340 172	1.55	0.43	0.73	98.8	
		79	7.9 9.3	367 229		1.09	0.30	0.46	_	
Co finino I	DII and A				126	1.07	0.29	0.35	99.4	
Co-firing F							_		_	
0.15	0	20	3.7	1080	668	2.12	0.54	1.45	98.0	
		43	6.4	467	242	2.49	0.64	0.56	98.8	
		59	7.8	313	160	2.51	0.64	0.37	99.0	
		79	9.3	253	107	2.30	0.59	0.27	99.1	
0.25	0	20	3.7	1704	817	2.09	0.78	1.51	97.7	
		39	6.0	783	380	1.96	0.63	0.76	98.6	
		59	7.9	464	232	2.13	0.65	0.44	98.9	
		80	9.4	391	206	2.33	0.61	0.35	99.0	
Co-firing F	PRH and M	IRH usi	ng a rebu	rning te	chnique					
0.15	0.2	22	3.9	778	352	1.94	0.49	0.74	98.8	
		40	6.0	400	160	2.17	0.55	0.41	99.0	
İ		60	7.9	240	60	2.05	0.52	0.22	99.3	
İ		78	9.2	165	30	2.44	0.62	0.15	99.2	
İ	0.4	19	3.5	1108	569	2.27	0.58	1.05	98.4	
İ		40	6.1	591	262	2.50	0.64	0.60	98.8	
		64	8.2	284	100	2.68	0.69	0.30	99.0	
		80	9.3	220	77	1.81	0.46	0.26	99.3	
0.25	0.2	20	3.7	1142	537	2.57	0.72	1.13	98.2	
0.23	0.2	41	6.2	632	225	2.35	0.65	0.63	98.7	
		60	7.9	339	100	3.33	0.94	0.35	98.7	
		79	9.3	220	82	2.89	0.81	0.28	98.9	
	0.4	20	3.7	1300	844	2.47	0.69	1.48	97.8	
	0.7	40	6.2	705	384	2.74	0.09	0.85	98.4	
		59	7.9	480	237	3.26	0.77	0.62	98.5	
		79	9.3	+			0.60	_	98.8	
	L	17	7.3	418	220	2.15	0.00	0.63	70.0	

An analysis of the heat losses and combustion efficiency of the conical FBC

showed the weak influence of the co-firing methods, but important effects of operating conditions on these characteristics. When burning PRH alone (i.e., at  $EF_2 = 0$ ), the heat loss due to unburned carbon decreased from 0.81% to 0.44%, whereas the heat loss due to incomplete combustion diminished from 0.82% to 0.14%, as EA ranged from about 20% to 80%. As a result, with increasing EA within the range, the combustion efficiency of the reactor fired with pure PRH showed some improvement, from 98.4% to 99.4%.

Note that, in the tests for co-firing premixed PRH and MRH in different proportions ( $EF_2 = 0.15$  and  $EF_2 = 0.25$ ), the combustion efficiencies were close to those for firing pure PRH at similar amounts of EA. However, when using fuel staging with bottom air injection, the combustion efficiency of the conical FBC was lower (by 0.3-0.5%), compared to co-firing premixed PRH and MRH at similar operating conditions ( $EF_2$  and EA). This result was mainly due to an insignificant increase of the two heat losses (both were slightly higher at greater  $EF_2$ ) caused by the secondary fuel injection. In the reburning tests, the combustion efficiency was affected by the three operating parameters ( $EF_2$ , EA, and SA/TA). Because of the effects from both fuel and air staging, the minimal combustion efficiencies, 97.8–98.8%, were observed at highest  $EF_2$  and SA/TA for EA from 20–80%.

#### 6.6. Optimal operating conditions

Fig. 6.5 depicts the 3-D surfaces representing the emission costs of the co-firing of PRH and MRH with the selected co-combustion methods, which were obtained using Eqs. (3.8)–(3.11) and the above-reported CO,  $C_xH_y$ , and NO emissions, as well as other relevant parameters, all quantified for the ranges of EF<sub>2</sub>, EA, and SA/TA. From Fig. 6.5, the operating conditions showed the substantial effects on the emission costs. At relatively low EA, but elevated EF<sub>2</sub> and/or SA/TA, the emission costs for all the co-firing methods were generally high, mainly due to contributions of the CO and  $C_xH_y$  emissions. The effects of the NO emissions on the "external" costs were significant when co-firing PRH/MRH with high EA at relatively low EF<sub>2</sub> and/or SA/TA.

As seen in Figs. 6.5a and b,  $EF_2 = 0.15$  and EA = 45% were optimal for the cocombustion of pre-mixed PRH and MRH, as well as for their co-firing using fuel staging

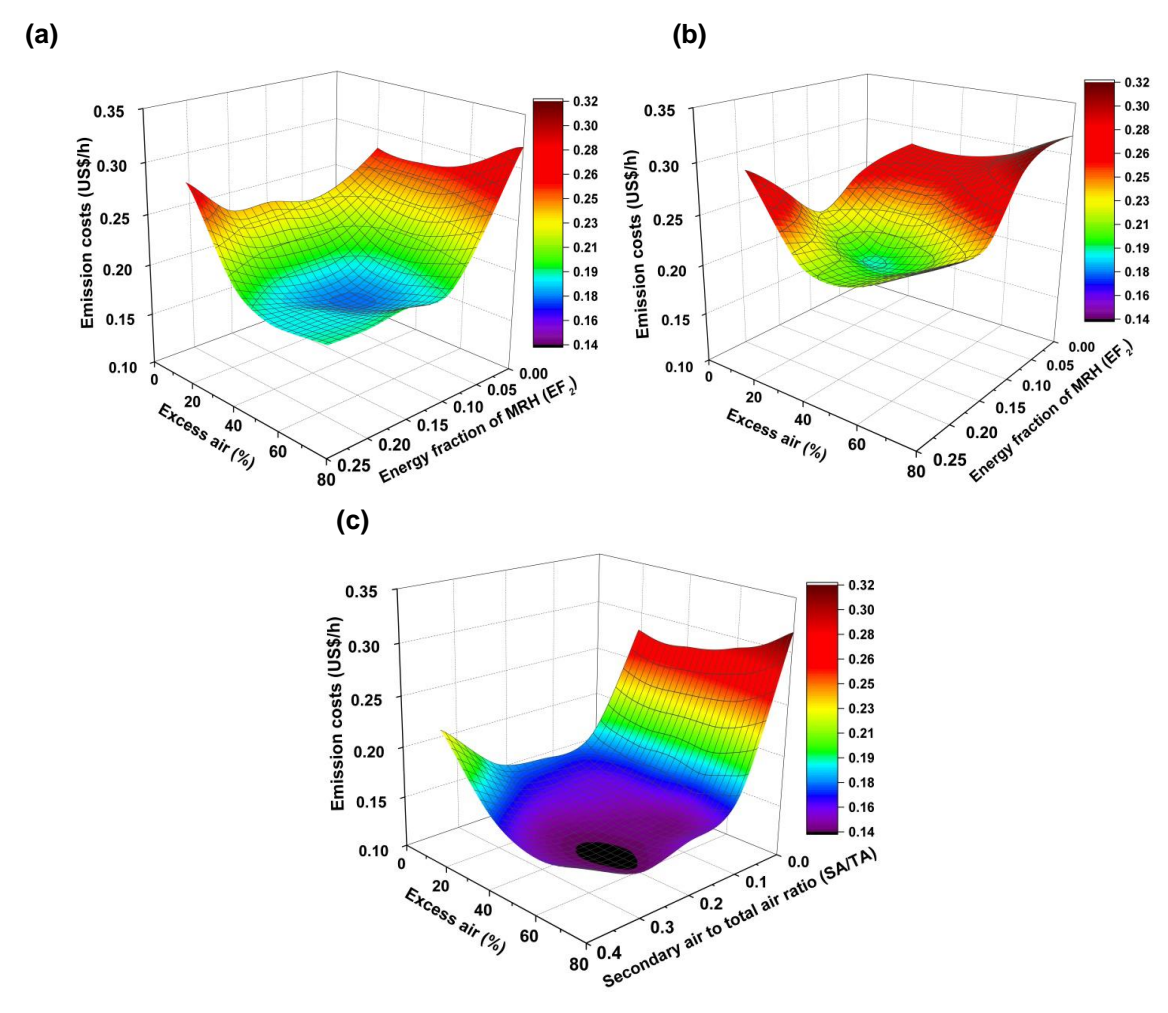


Fig. 6.5. Emission ("external") costs of the conical FBC co-fired with PRH and MRH under variable operating conditions using: (a) a feedstock of the pre-mixed fuels, (b) fuel staging at bottom air injection, and (c) reburning at  $EF_2 = 0.15$ .

with bottom air injection. Under these operating conditions, the "external" costs of the conical FBC were minimal for both co-combustion methods. For the reburning technique, EA and SA/TA were optimized for  $EF_2 = 0.15$  that (as mentioned above) was optimal for the first and second co-firing techniques. From Fig. 6c, EA = 50% and SA/TA = 0.25 were optimal for the co-firing using reburning at  $EF_2 = 0.15$ .

It can be seen in Table 3 that under optimal operating parameters, the combustor ensured high (about 99%) combustion efficiency, which was close for the selected cofiring methods.

Table 6.2 compares the CO, C<sub>x</sub>H<sub>y</sub>, and NO emissions (all on a dry gas basis and at 6% O<sub>2</sub>), as well as the NO emission reduction, for the co-combustion techniques at the optimal operating parameters. For comparability, Table 6.2 presents the corresponding emission values for burning pure PRH at excess air of 45% and 50%. Through the co-firing of PRH and MRH under optimal operating conditions, a noticeable/substantial reduction of the NO emission from the combustor can be achieved, as compared to burning PRH alone: by 13% (145 ppm against 167 ppm) when co-firing the pre-mixed fuels, by 37% (106 ppm against 167 ppm) for fuel-staged co-combustion of PRH and MRH at bottom air injection, and by 53% (82 ppm against 176 ppm) when using the reburning technique.

However, under these operating conditions, the CO emission may increase by 90–130 ppm, as compared with burning pure PRH, to a level of 380–450 ppm (depending on the co-combustion method), which is substantially lower than the national emission limit for CO (740 ppm). From Table 6.2, during co-combustion of PRH and MRH, the  $C_xH_y$  emissions may increase by 50–85 ppm, as compared to firing PRH on its own, to 170–235 ppm in different co-firing techniques.

**Table 6.2**Major gaseous emissions from the conical FBC co-fired with PRH and MRH at optimal operating parameters when using the selected co-combustion methods, as compared with burning pure PRH at similar excess air.

(Co-)combustion method	Operating parameters	Emission	NO		
(Co )combustion method	Operating parameters	СО	$C_xH_y$	NO	emission reduction
Conventional combustion of	EA = 45%	320	150	167	
a base fuel (PRH)	EA = 50%	270	120	176	
Co-firing premixed fuels	$EF_2 = 0.15, EA = 45\%$	410	220	145	13%
Co-firing using fuel staging	$EF_2 = 0.15\%$ , $EA = 45\%$	450	235	106	37%
Co-firing using reburning	EF <sub>2</sub> = 0.15%, EA = 50%, SA/TA = 0.25	380	170	82	53%

<sup>&</sup>lt;sup>a</sup> At 6% O<sub>2</sub> on a dry gas basis

# Chapter 7

Co-firing of Pelletized Cassava Rhizome and Eucalyptus Bark in a Fluidized Bed: Studies on the Effects of Co-firing Methods and Bed Material Type on the Combustor Performance and Time-Related Bed Behavior

# 7.1 Combustion and emission characteristics inside the conical FBC using silica sand as the bed material

Fig. 7.1 shows the axial profiles of temperature and  $O_2$  in the conical FBC (with silica sand as the bed material), co-firing PCR and EB at different energy fractions,  $EF_2 = 0.15$  (Fig. 7.1a) and  $EF_2 = 0.25$  (Fig. 7.1b), at excess air of about 40%. In this figure, the axial temperature and  $O_2$  profiles from the tests for fuel staging and reburning (at SA/TA = 0.2 and SA/TA = 0.4) are compared to those for the conventional combustion of PCR ( $EF_2 = 0$ ).

In all test runs, the axial temperature profiles were fairly uniform, exhibiting the effects of EF<sub>2</sub> and SA/TA (the latter using reburning). It can be seen in Fig. 7.1 that the temperatures at all points in the bottom region (including the peak temperature) during fuel-staged co-combustion of PCR and EB were lower, as compared to firing pure PCR and co-firing using reburning. This was mainly due to the reduced feed rate of the primary fuel (at fixed airflow through the air distributor), resulting in an increased excess air ratio in this region. With increasing EF<sub>2</sub> from 0.15 to 0.25 in the fuel-staged co-combustion tests, the bed temperature showed a decrease, whereas the temperature at the reactor top was apparently higher than that in the test for burning pure PCR, mainly due to a greater amount of heat released in the secondary combustion zone.

However, the bed temperature in the reburning tests was higher, as compared to co-firing PCR and EB with fuel staging at similar EF<sub>2</sub>, mainly due to the reduced excess air ratio in the primary zone (caused by the air staging). This effect was more significant with greater SA/TA. An increase in EF<sub>2</sub> from 0.15 to 0.25 shifted the peak temperature from Z = 1.1 m to Z = 1.3 m, likely due to the delayed oxidation of combustibles in the primary combustion zone. At the reactor top, the temperature at the greatest EF<sub>2</sub> and

SA/TA was higher, as compared to other tests, because of a greater heat release downstream of the reburn zone.

From Fig. 7.1, the axial  $O_2$  profiles for the conventional burning of the base fuel and fuel-staged co-combustion tests were similar, showing a gradual decrease along the reactor height, with almost no effects from  $EF_2$ .

However, in the tests for reburning, the  $O_2$  profiles exhibited a different behavior, compared to the other two options, showing substantially lower  $O_2$  at the reactor bottom, herefore, a higher potential of  $NO_x$  reduction in both the primary and reburn zones (Werther et al., 2000). The profiles exhibited a noticeable influence of SA/TA and insignificant effects from EF<sub>2</sub>. Due to the secondary air injection,  $O_2$  in the tests for reburning increased at the upper part of the reactor to a level similar to that in the other options.

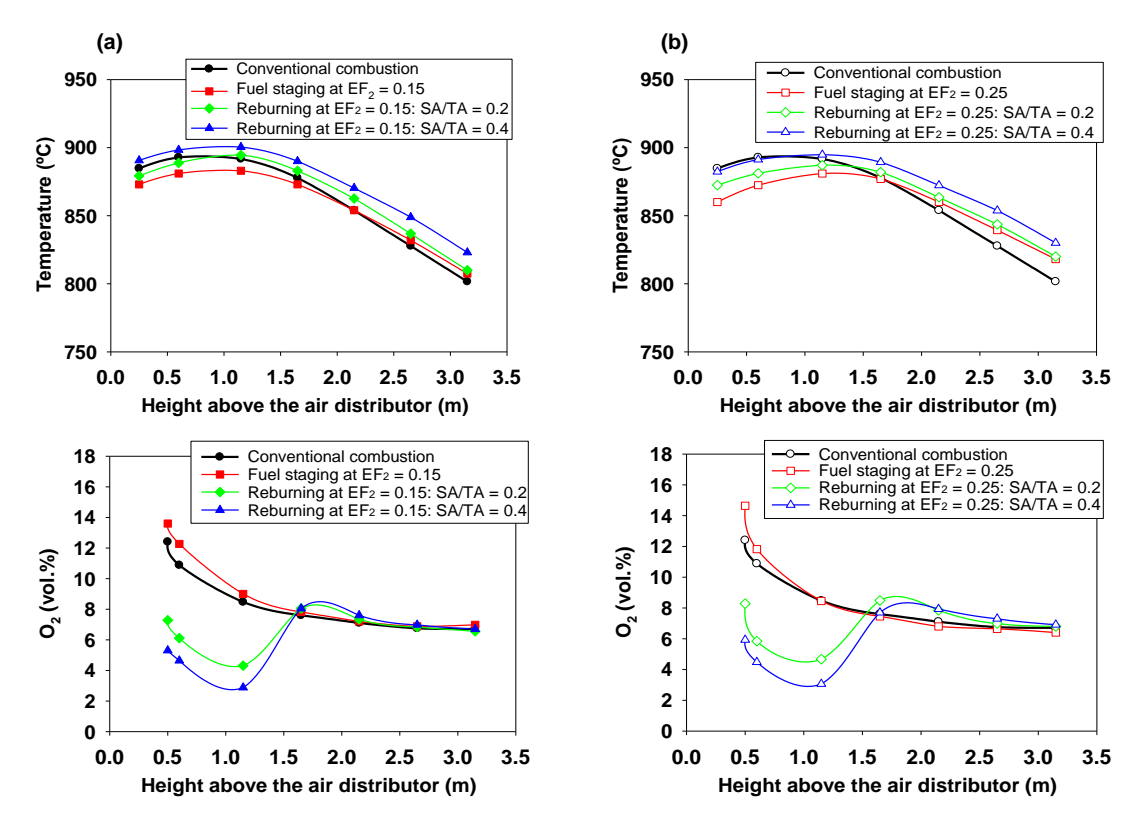


**Fig. 7.1.** Axial profiles of temperature and  $O_2$  in the conical FBC co-fired with PCR and EB at (a)  $EF_2 = 0.15$  and (b)  $EF_2 = 0.25$ , using fuel staging and reburning at excess air of about 40%, compared to conventional combustion of PCR.

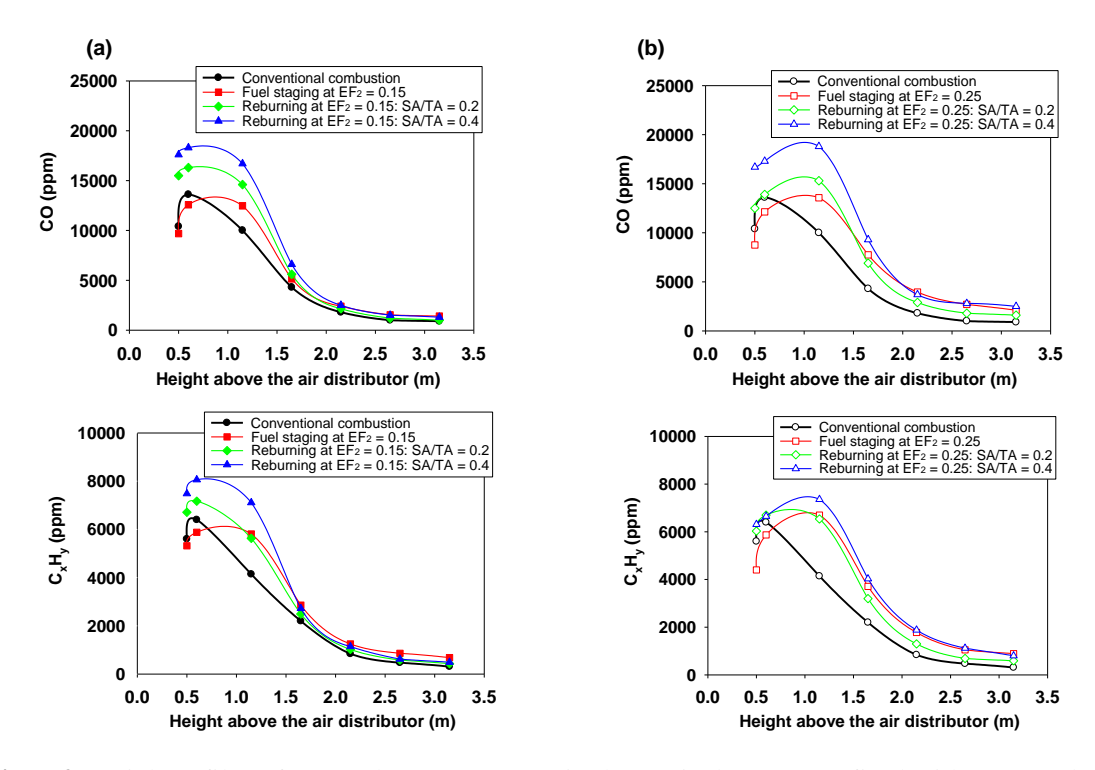


**Fig. 7.2.** Axial profiles of CO and  $C_xH_y$  (as  $CH_4$ ) in the conical FBC (co-)fired with PCR and EB at (a)  $EF_2 = 0.15$  and (b)  $EF_2 = 0.25$ , using fuel staging and reburning at excess air of about 40%, compared to conventional combustion of PCR.

Fig. 7.2 shows the axial profiles of CO and  $C_xH_y$  (as  $CH_4$ ) in the conical FBC for the same (co-)combustion options and operating parameters, as in Fig. 7.1. In all the tests, these profiles showed two specific regions, pointing at rapid (net) formation of both pollutants in the bottom region of the conical FBC, as well as at high rates of CO and  $C_xH_y$  oxidation in the upper region (in effect, in the cylindrical section) of the reactor.

In the bottom region of the reactor, CO and  $C_xH_y$  increased to their maximum values (peaks), mainly due to rapid devolatilization of the base (primary) fuel and fuel-char oxidation (at a lesser extent), both contributing to the CO formation (Werther et al., 2000). In the meantime, the two pollutants were oxidized in the reactor bottom at rates significantly lower than the corresponding formation rates. According to Turns (2006), CO is generally oxidized  $_2$  by O and OH radicals, whereas the  $C_xH_y$  oxidation involves two major routes: (i) breakdown of  $C_xH_y$  to CO and (ii) further oxidation of CO to CO<sub>2</sub>.

In the vicinity of secondary/reburn fuel injection (i.e., at Z = 1.15 m), CO and  $C_xH_y$  in the tests with fuel staging and reburning techniques were noticeably higher than those for burning the base fuel alone, showing their peaks at  $EF_2 = 0.25$ . In the reactor regions downstream from the CO and  $C_xH_y$  peaks, that were dependent on the co-firing method and  $EF_2$  value, the oxidation rates of both pollutants were greater than their formation rates, which resulted in a decrease of CO and  $C_xH_y$  along the combustor height to the minimal values at the combustor top.

In Fig. 7.2, CO and  $C_xH_y$  in the primary combustion zone in the tests for fuel staging were close to those for the conventional combustion of PCR. However, the greatest difference between CO ( $C_xH_y$ ) from the co-firing tests for fuel staging and CO ( $C_xH_y$ ) from burning pure PCR was found to occur at Z=1.15 m, and this difference increased with greater EF<sub>2</sub> in the experiments for fuel staging.

A similar trend was observed when comparing CO ( $C_xH_y$ ) of the co-firing tests using reburning with the test for conventional combustion of the base fuel. However, when co-firing PCR and EB using reburning, the CO and  $C_xH_y$  in both the primary and reburn zones were substantially higher, as compared to other options, mainly due to the decreased  $O_2$ , leading to the lower rates of CO and  $C_xH_y$  oxidation in the two zones. The highest CO and  $C_xH_y$  were observed at all points along the combustor height in the co-firing test using reburning at  $EF_2 = 0.25$  and SA/TA = 0.4, thus providing a greater NO emission reduction in this conical FBC, compared to the fuel staging technique (to be discussed below).

Fig. 7.3 depicts the axial profiles of NO in the conical FBC for the same (co)combustion options and operating conditions, as in Figs. 7.1 and 7.2. In all the test runs, the concentration of  $NO_2$  in  $NO_x$  was negligible. In the below analysis,  $NO_x$  is therefore represented only by NO.

Similar to CO and  $C_xH_y$ , the axial NO profiles showed two specific regions in the combustor in all the test runs. In the bottom reactor region (at Z < 0.6 m), NO formed from volatile nitrogenous species in the primary fuel, mainly via oxidation of volatile NH<sub>3</sub> and HCN in multiple routes of the fuel-NO formation mechanism (including the

proportional effects of fuel-N, excess air, and temperature) (Werther et al., 2000; Winter et al., 1999). Due to secondary reactions, such as the catalytic reduction of NO by CO (on the surface of the fuel char/ash particles) and homogeneous reactions of NO with radicals, such as CH<sub>i</sub>, NH<sub>2</sub>/NH, and HCCO, some part of NO formed in the primary reactions was decomposed in this region (Karlström et al., 2017; Nussbaumer, 2003; Zhong et al., 2002). However, the rate of NO formation reactions in this region was significantly higher than those of the secondary reactions, which resulted in a rapid increase of NO to its peak at the point of base/primary fuel injection.

From Fig. 7.3, the NO peak in the tests for reburning was significantly lower, compared to the other two options, mainly due to the decreased  $O_2$  (diminishing NO formation rate) and significant concentrations of CO and  $C_xH_y$  (enhancing NO reduction reactions) in the bottom region of the conical FBC (see Figs. 7.1 and 7.2). With increasing SA/TA (leading to lower  $O_2$ ) and/or decreasing EF<sub>2</sub> (resulting in higher CO and  $C_xH_y$ ), the (net) rate of NO formation in the bottom region of the combustor (and accordingly, the NO peak) in the reburning test was lower. In the upper region of the combustor (at Z > 0.6 m), NO exhibited a decrease along the combustor height (at a variable rate) in all the test runs, as the rate of NO reduction in this part of the reactor prevailed over NO formation, despite the use of secondary/reburn fuel in the co-firing tests.

It can be seen in Fig. 7.3 that during the tests for fuel staging, the rate of NO

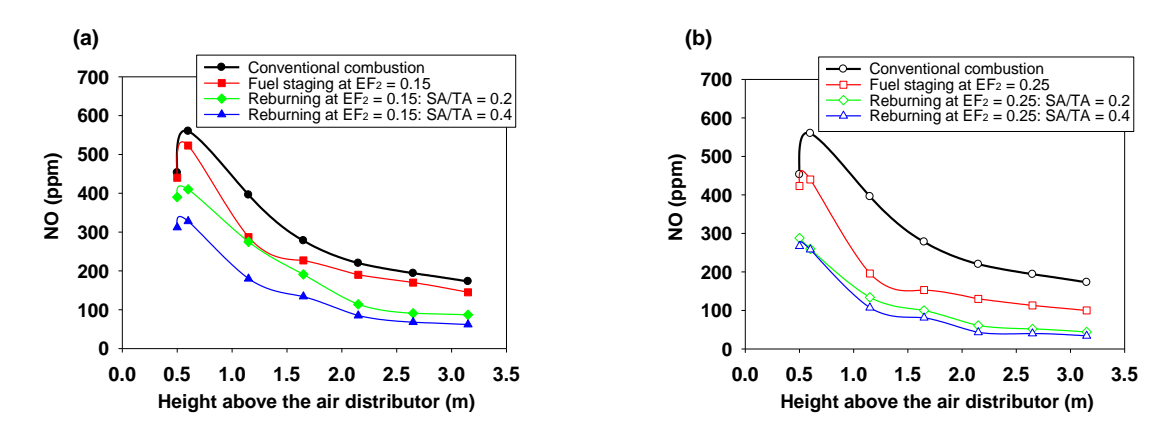


Fig. 7.3. Axial profiles NO in the conical FBC (co-)fired with PCR and EB at (a)  $EF_2 = 0.15$  and (b)  $EF_2 = 0.25$ , using fuel staging and reburning at excess air of about 40%, compared to conventional combustion of PCR

reduction at 0.6 m < Z < 1.5 m was noticeably higher than that for the conventional burning of PCR, particularly at a higher feeding rate of EB (i.e., at EF<sub>2</sub> = 0.25), which led to the lowered NO at the reactor top. This result was primarily achieved due to elevated CO and  $C_xH_y$  in the vicinity of secondary fuel (EB) injection, which enhanced the NO reduction reactions in the secondary combustion zone.

However, during the co-firing with reburning, the NO reduction at 0.6 m < Z < 1.5 m was helped by the lowered  $O_2$  (see Fig. 7.1) and high levels of CO and  $C_xH_y$  (see Fig. 7.2) in the reburn zone (Shu et al., 2015). Some influence of SA/TA was observed (at insignificant effects of EF<sub>2</sub>) on the NO reduction rate in this region.

As seen in Fig. 7.3, the NO peak correlated with NO at the reactor top in all (co-)firing tests. Therefore, it is suggested that during the co-firing of PCR and EB using reburning, the local NO reduction in the primary combustion zone (due to very low  $O_2$  and high CO and  $C_xH_y$ ) played an important role in the overall reduction of NO emission from the conical FBC. This indicates the great potential of the reburning method in NO emission reduction, as compared to the fuel-staged co-combustion.

# 7.2 Effects of (co-)combustion techniques on the emissions and combustion efficiency

Fig. 7.4 depicts the CO, C<sub>x</sub>H<sub>y</sub> (as CH<sub>4</sub>), and NO emissions (all on a dry gas basis and at 6% O<sub>2</sub>) from the conical FBC with the silica sand bed, (co-)fired with PCR and EB using fuel staging and reburning, under variable operating conditions. For comparison, this figure shows similar characteristics for burning the base fuel alone.

It can be seen in Fig. 7.4 that in the co-firing tests with fuel staging/reburning, the CO and  $C_xH_y$  emissions from the combustor were higher (at any fixed EA), as compared to burning PCR alone, showing an increase with higher EF<sub>2</sub> (at fixed SA/TA in reburning tests), i.e., with a greater proportion of the secondary fuel injected into the reactor at a higher level (Z = 1.15 m). However, with increasing EA from ~20% to ~40% at given EF<sub>2</sub> (and fixed SA/TA in reburning tests), both emissions decreased along the reactor height at variable rates.

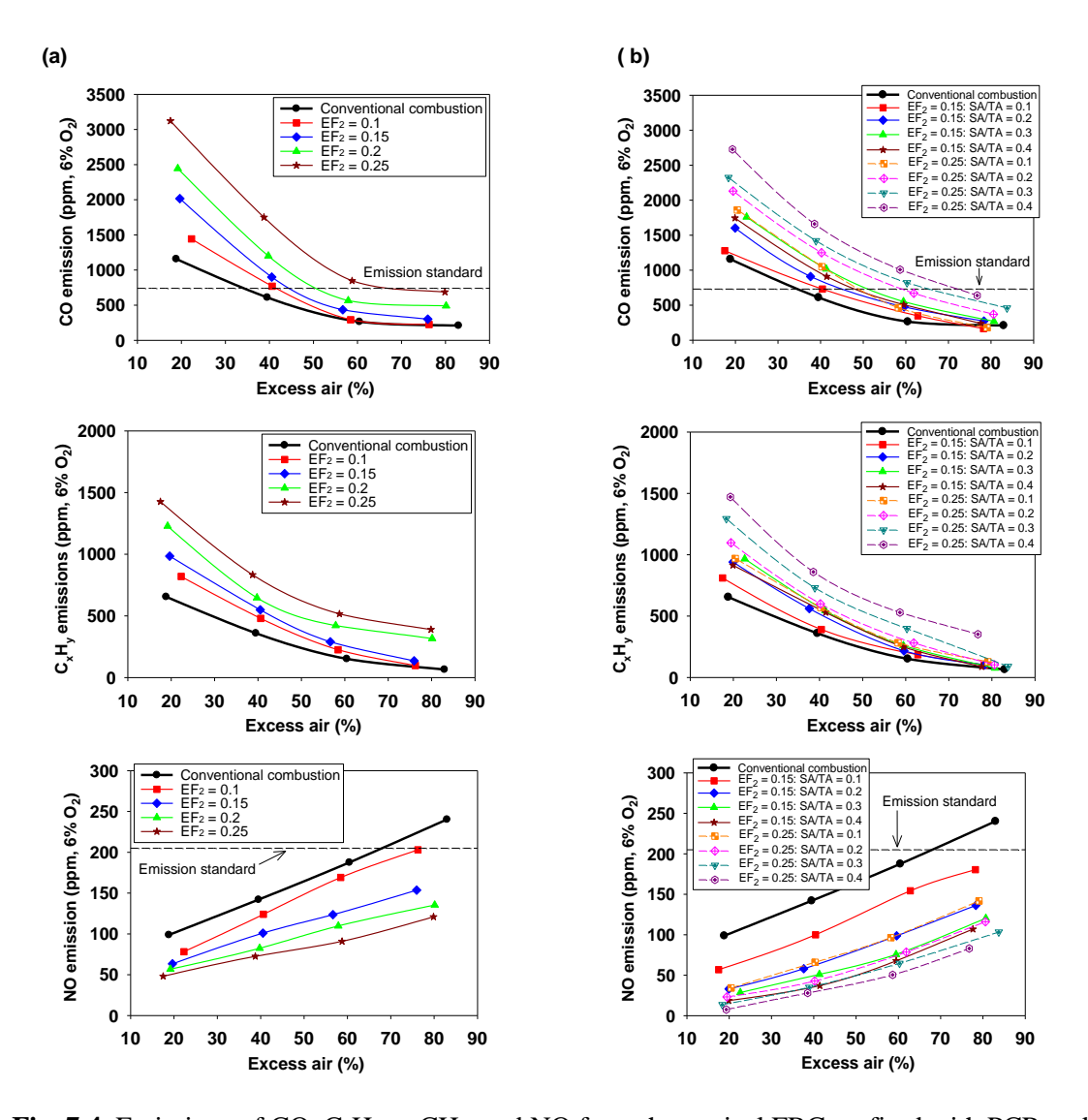


**Fig. 7.4.** Emissions of CO, C<sub>x</sub>H<sub>y</sub> as CH<sub>4</sub>, and NO from the conical FBC co-fired with PCR and EB under variable operating conditions, using (a) fuel staging and (b) reburning, compared to conventional combustion of PCR.

Compared to the conventional combustion of PCR at fixed EA, the selected cofiring techniques resulted in a lower NO emission from the combustor, mainly due to: (1) elevated CO and  $C_xH_y$  in the secondary combustion zone (when using fuel staging at bottom air injection), and (2) substantially lowered  $O_2$  and increased CO and  $C_xH_y$  in the primary and reburn zone when using the reburning technique, as discussed previously. In the meantime, with increasing EA (when other operating parameters were fixed), the NO emission from the combustor increased, following the fuel-NO formation mechanism (Werther et al., 2000; Winter et al., 1999).

As revealed by the results in Fig. 7.4, a significant NO reduction that can be achieved at lower EA but greater  $EF_2$  and/or SA/TA, i.e., when the CO and  $C_xH_y$ 

**Table 7.1**Heat losses and combustion efficiency of the conical FBC co-fired with PCR and EB, using fuel staging and reburning techniques at variable operating parameters, compared to burning pure PCR (bed material: silica sand).

Energy	nergy Secondary Excess		O <sub>2</sub> at Unburned		CO	$C_xH_y$	Heat loss (%) due to :		Combustion
	of to total a	iir air (%)	stack	carbon in	(ppm)	(ppm)	unburned	incomplete	efficiency
secondary fue	elratio		(vol.%)	PM (wt.%)			carbon	combustion	(%)
EF <sub>2</sub> )	(SA/TA)						Carbon	comoustion	
Conventiona	l combustion	of PCR							
0	0	19	3.6	12.3	1360	770	1.49	1.18	97.3
		40	6.1	1.96	610	360	0.21	0.65	99.1
		60	8.0	2.30	230	132	0.25	0.28	99.5
		83	9.5	3.25	160	50	0.36	0.16	99.5
Co-combusti	on of PCR ar	ıd EB usi	ng fuel sta	aging	•	•	•	1	•
$EF_2 = 0.15$	0	20	3.8	1.72	2370	1157	0.33	1.82	97.8
		41	6.2	1.14	900	549	0.23	0.93	98.8
		57	7.7	0.92	390	260	0.18	0.48	99.3
		76	9.1	0.78	240	108	0.15	0.26	99.6
$EF_2 = 0.25$	0	18	3.7	2.14	3690	1686	0.56	2.58	96.9
		39	6.1	1.57	1750	833	0.41	1.48	98.1
		59	7.9	1.17	740	451	0.31	0.83	98.9
		80	9.4	1.42	530	300	0.37	0.65	99.0
Co-combusti	on of PCR ar	ıd EB usi	ng reburn	ing			•	II.	
$EF_2 = 0.15$	0.2	20	3.8	7.42	1602	940	1.57	1.56	96.9
		38	5.9	2.79	910	561	0.56	0.93	98.5
		60	7.9	2.88	476	217	0.58	0.40	99.0
		78	9.3	2.07	272	104	0.41	0.21	99.4
	0.4	20	3.8	3.33	1745	915	0.67	1.65	97.7
		41	6.3	3.19	910	530	0.65	0.92	98.4
		59	7.9	2.73	508	248	0.55	0.46	99.0
		78	9.2	3.04	239	88	0.61	0.19	99.2
$EF_2 = 0.25$	0.2	19	3.8	3.64	2130	1097	0.95	1.90	97.1
		40	6.2	2.82	1250	600	0.74	1.07	98.2
		62	8.1	2.79	670	281	0.73	0.53	98.7
		81	9.4	2.90	370	103	0.76	0.24	99.0
	0.4	19	3.9	3.76	2727	1471	0.99	2.48	96.5
		39	6.1	3.45	1660	860	0.91	1.47	97.6
		59	7.9	3.39	1008	529	0.90	0.90	98.2
		77	9.2	2.57	639	353	0.67	0.59	98.7

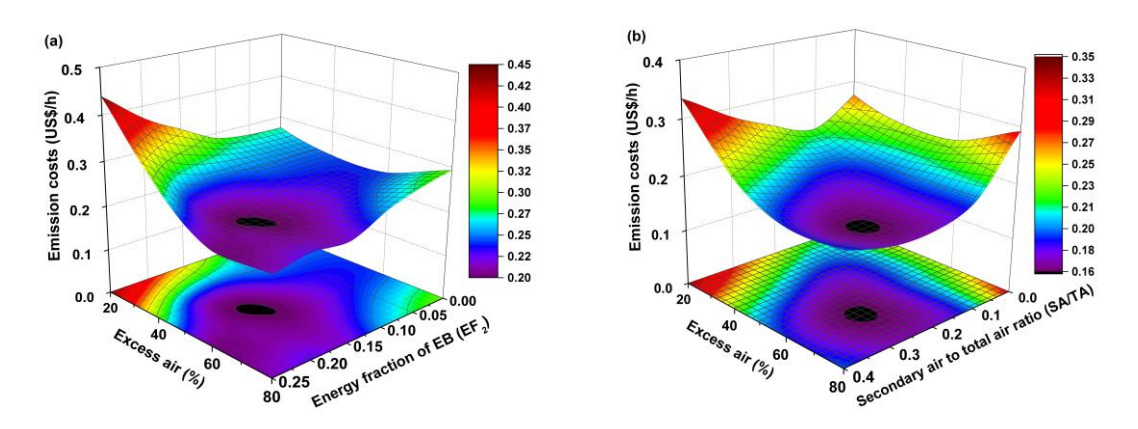
emissions were substantially high. It is also noted that the key operating parameters (EA on one hand versus EF<sub>2</sub> and SA/TA on the other hand) have opposite impacts on the NO and CO/C<sub>x</sub>H<sub>y</sub> emissions characteristics. It caused a necessity to perform an optimization analysis of the operating parameters (as discussed below) to ensure acceptable values of the major gaseous emissions for minimal environmental impacts from the co-firing.

Table 7.1 shows the predicted combustion-related heat losses and combustion efficiency of the conical FBC with the silica sand bed, for the three tests series at variable operating parameters. Experimental data required for determining an (actual) amount of excess air and combustion-related heat losses, such as unburned carbon content in the PM and actual  $O_2$ , CO, and  $C_xH_y$  (as  $CH_4$ ) at stack, are also included in Table 4 for individual runs.

From Table 7.1, in all test series, the heat loss due to unburned carbon decreased with increasing EA (at fixed EF<sub>2</sub> and SA/TA), pointing at a higher rate of fuel-char oxidation. At the lowest EA ( $\sim$ 20%), the heat loss was highest in all test series, showing however rather close values at EA = 40–80%. However, in the co-firing of PCR and EB using fuel staging and reburning at fixed EA, this heat loss somewhat increased with higher EF<sub>2</sub> and/or SA/TA, mainly due to the fuel/air staging effects.

It can be seen in Table 7.1 that  $EF_2$ , SA/TA, and EA have strong effects on the CO and  $C_xH_y$  emissions, and consequently, the heat loss due to incomplete combustion, which exhibited regular trends in response to the variation in the operating parameters. Thus, an increase in EA (at fixed  $EF_2$  and EA) led to a significant decrease of this heat loss, mainly due to the enhanced rates of CO oxidation and EA0 decomposition. In contrast, with increasing  $EF_2$  and/or EA1 (at fixed EA2), the heat loss due to incomplete combustion increased, to a different extent.

Taking into account the combined effects of the two heat losses, the combustion efficiency of the conical FBC can be improved by increasing EA (at fixed EF<sub>2</sub> and SA/TA). However, the two co-firing techniques lead to a deterioration of the combustion efficiency, as compared to firing pure PCR, particularly at higher EF<sub>2</sub> and SA/TA.



**Fig. 7.5** Emission costs of the conical FBC co-fired with PCR and EB under variable operating conditions using: (a) fuel staging with bottom air injection and (b) reburning at  $EF_2 = 0.15$  (bed material: silica sand).

# 7.3 Optimal operating parameters for the co-combustion techniques with fuel staging and reburning

Fig. 7.5 shows the "external" costs of the co-firing PCR and EB in the conical FBC with silica sand bed, predicted using the measured CO,  $C_xH_y$ , and NO emissions (see Fig. 7.4), as well as other relevant parameters, all quantified for the ranges of EF<sub>2</sub> and EA. It can be seen in Fig. 7.5 that the effects of EF<sub>2</sub>, EA, and SA/TA on the "external" costs were substantial. At relatively low EA, but elevated EF<sub>2</sub> and/or SA/TA, the emission costs for the two co-firing techniques were high, mainly due to the noticeable CO and  $C_xH_y$  emissions. The impact of the NO emission on the "external" costs was significant, particularly when using high EA and maintaining EF<sub>2</sub> and/or SA/TA at low levels. From Fig. 7.5, EF<sub>2</sub> = 0.15 and EA  $\approx 50\%$  were optimal for co-firing of PCR and EB in this combustor using fuel staging with bottom air injection, whereas EA  $\approx 60\%$  and SA/TA  $\approx 0.25$  were the most appropriate for co-firing with the reburning technique at similar EF<sub>2</sub>. As compared to burning PCR (a base fuel) at similar EA, fuel staging and reburning techniques operated under optimal conditions can reduce the NO emission from the reactor by  $\sim 30\%$  and  $\sim 60\%$ , respectively (see Fig. 7.4).

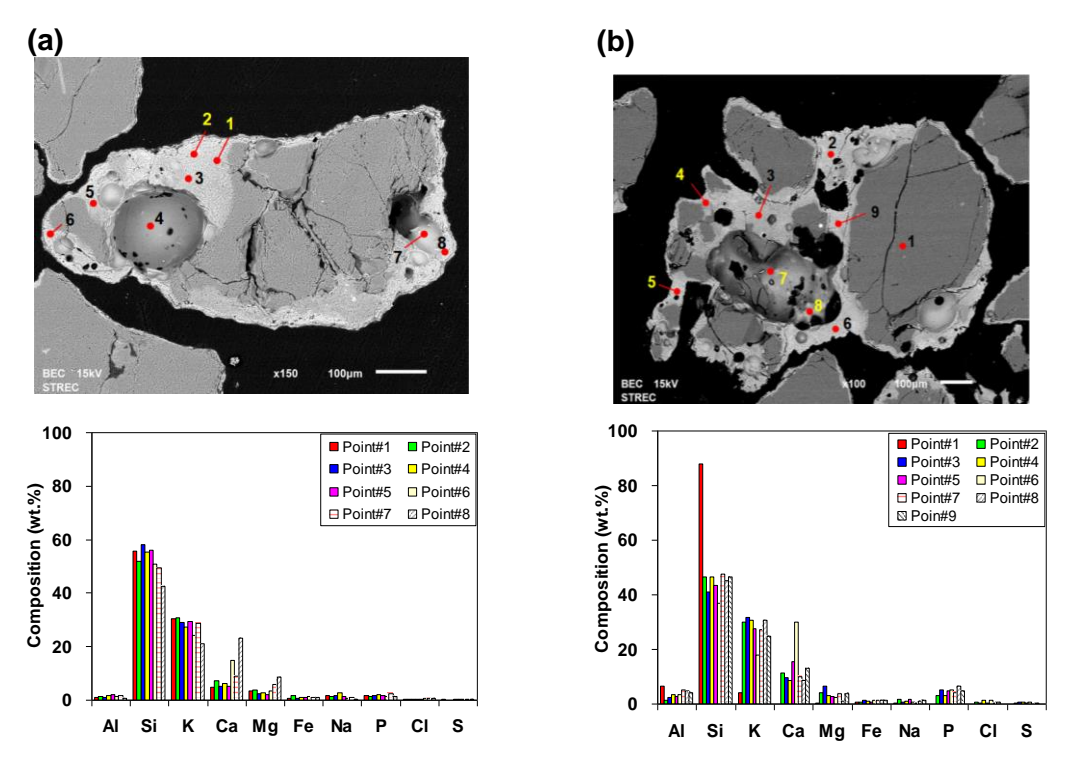


**Fig. 7.6.** SEM-EDS spot analyses of the bed agglomerates sampled after 8-h co-firing tests on the conical using (a) fuel staging and (b) reburning (bed material: silica sand).

## 7.4 SEM-EDS analysis of the bed materials

From the co-firing tests with SS as the bed material, a small proportion of the sand (~5 wt.% when using fuel staging and ~10% in reburning tests) was subjected to agglomeration within a short operating time (~8 h). Fig. 7.6 shows the SEM–EDS spot analysis of agglomerates collected after the tests for fuel staging and reburning. The micrographs in Fig. 7.6 reveal that the agglomerates were formed via binding of bed particles with different shapes and sizes. The binding material that bonded the SS particles was rich in Si, K, and Ca, the components of K<sub>2</sub>O–CaO–SiO<sub>2</sub> and K<sub>2</sub>O–SiO<sub>2</sub> eutectics with low melting points (Nuutinen et al., 2004; Öhman et al., 2000; Scala and Chirone, 2008), whereas the contents of Al, Mg, and Fe (basically increasing the melting point of the binding material) were negligible. The adhesive eutectics were generated on the surfaces of SS grains as a particle coating, which likely formed due to two mechanisms: (1) reaction of SiO<sub>2</sub> in the sand with K-rich compounds vaporized from fuel

ash, and (2) migration of ash-derived melts, released from the partly-melted fuel chars/ashes, onto the SS grain surfaces. As seen in Fig. 7.6 and found in visual bed observations, the agglomeration occurred in the reburning tests was more intensive, compared to the tests for fuel staging, mainly because of the higher bed temperatures (see Fig. 7.1). To avoid bed agglomeration for a relatively long time, it was therefore decided to perform long-term co-firing tests with alternative bed materials using a reburning technique in this conical FBC.

As revealed by visual inspections of the bed materials at different operating times, no bed agglomeration occurred in the conical FBC during the reburning tests with pure AS and the AS/SS mixture. During the experiments with distinct bed materials, the operating parameters were maintained at  $EF_2 = 0.15$ , EA = 50%, and SA/TA = 0.2 (i.e., close to optimal ones, as quantified in the preceded section). As an example, Fig. 7.7 presents the SEM micrographs and EDS spot analyses of AS and AS/SS particles sampled from PM after finishing the 30-h experiments with the selected bed materials. From Fig. 7.7, the AS grains had a partly coated surface, and the bed particle coatings on

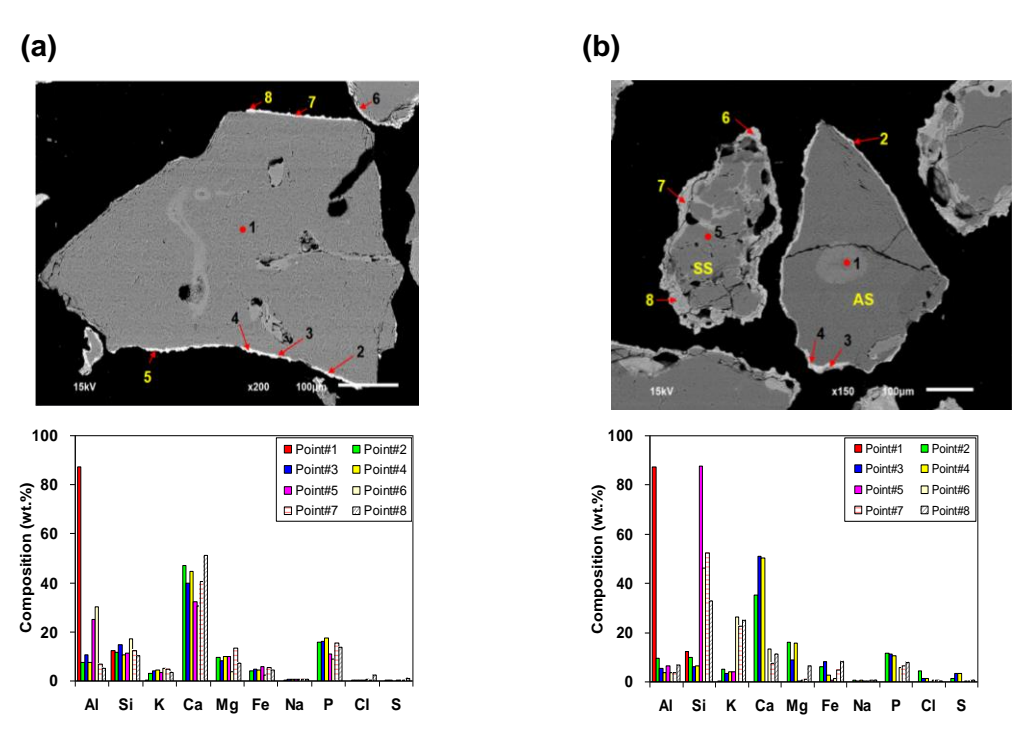


**Fig. 7.7.** SEM-EDS spot analyses of the bed particles sampled after 30-h reburning tests on the conical FBC using (a) alumina sand and (b) AS/SS mixture as the bed material.

both micrographs (see Figs. 7.7a and 7.7b) were thin and similar in thickness. Since Al<sub>2</sub>O<sub>3</sub> in the bed material did not react with K-rich compounds vaporized from the fuel ash, the coating layer on the AS grains likely formed due to: (1) collisions of AS grains with the partly molten char/ash particles in the fluidized bed, (2) migration of ash melts onto the grain surfaces, forming the ash-melt coatings (Visser, 2004). Due to insignificant K and substantial/noticeable contents of Ca, Mg, Al, Fe, and P in the AS coatings, the adhesiveness of the coating layers (at the actual bed temperatures) was low (Visser, 2004; Nuutinen et al., 2004), thus resisting bed agglomeration.

In the AS/SS bed sampled after the tests, SS grains had a greater (up to 40  $\mu$ m thick) coating layer compared to that of AS grains (up to 15  $\mu$ m thick), as seen in Fig. 7.7. This can be attributed to the "coating-induced" mechanism for formation of a coating layer, mainly as a result of interactions of SiO<sub>2</sub> in the SS grains with K-rich species vaporized from the fuel ash (Visser, 2004).

When using AS and AS/SS beds, fine alumina-rich particles (generated in the turbulent fluidized bed due to collisions and attrition of AS grains), were adhered to by the partly molten chars and ashes, decreasing the adhesiveness of the melts transferred onto the surface of bed grains. Apart from this, fine alumina-rich particles can be absorbed by the grain coatings (when formed), resulting in the higher melting point of eutectics/melts in the coatings. These factors increase the resistance of the bed grains to bed agglomeration when burning high-alkali PCR and EB in this conical FBC when using pure AS and the AS/SS mixture as the bed material.

# 7.5 Time-related changes in compositions of the bed materials and particulate matter

Table 7.2 presents the composition of the bed materials used/reused in the conical FBC and that of PM generated during co-combustion of PCR and EB using reburning at  $EF_2 = 0.15$ , EA = 50%, and SA/TA = 0.2, for selected operating times. It can be seen that the compositions of the bed materials were subjected to time-domain changes. Due to the coating of AS and SS grains and because of the presence of some PM retained in the bed (in spite of 1.5-h blowing after the reactor shut down), ash-forming

compounds, such as SiO<sub>2</sub>, CaO, K<sub>2</sub>O, MgO, Fe<sub>2</sub>O<sub>3</sub>, and P<sub>2</sub>O<sub>5</sub>, showed a time-domain increase of their fractions in both bed materials, i.e., accumulation of the ash-derived compounds in the bed. In the meantime, Al<sub>2</sub>O<sub>3</sub> responsible for preventing bed agglomeration showed a gradual decrease with operating time, mainly due to (i) "dilution" of Al<sub>2</sub>O<sub>3</sub> by the above-mentioned ash-related species and (ii) carryover of some alumina fine particles (generated in the fluidized bed in collisions and attrition of AS grains) from the reactor. This fact indicated a gradual time-domain decrease of the bed capability to withstand bed agglomeration.

Data in Table 7.2 reveal that in the two test series, the content of  $Al_2O_3$  in PM was greater than that in the ash of the "equivalent" fuel at all time instants. This directly pointed at the occurrence of carryover of fine alumina-rich particles, which joined PM. A time-domain decrease of  $Al_2O_3$  in PM was likely due to a similar trend exhibited by  $Al_2O_3$  in the two bed materials.

**Table 7.2**Composition of the bed materials used/reused in the conical FBC and that of PM generated during co-combustion of PCR and EB using a reburning technique, for different time instants of combustor operation

Operating time (h)	Composition (wt.%)										
	$Al_2O_3$	$SiO_2$	CaO	$K_2O$	Na <sub>2</sub> O	MgO	$Fe_2O_3$	$P_2O_5$	Cl	$SO_3$	
Bed samples from ti	he tests w	ith alumir	ia sand								
8	58.71	34.43	2.46	1.73	0.32	0.49	0.54	0.89	0.04	0.09	
16	46.56	44.38	3.41	2.31	0.3	0.66	0.72	1.27	0.04	0.1	
23	42.94	46.91	4.01	2.49	0.28	0.81	0.88	1.53	0.04	0.11	
30	39.71	49.12	4.22	2.59	0.23	0.84	0.96	1.54	0.05	0.13	
Bed samples from ti	he tests w	ith alumir	a and sili	ca sand r	nixted in e	qual propo	ortions				
8	19.86	66.74	5.16	4.02	0.12	1.08	0.99	1.62	0.03	0.07	
16	17.45	69.23	4.95	4.12	0.13	1.03	1.1	1.55	0.03	0.06	
23	12.14	65.82	11.42	4.18	0.1	1.42	1.36	2.05	0.07	0.27	
30	10.89	67.4	11.54	4.14	0.13	1.46	1.59	2.03	0.06	0.23	
Particulate matter f	from the t	ests with a	alumina se	and	· · · · · · · · · · · · · · · · · · ·						
8	9.02	63.27	10.77	6.38	0.33	2.13	2.67	3.5	0.44	0.79	
16	5.52	57.17	15.53	7.32	0.27	2.87	2.99	4.81	0.6	2.06	
23	6.13	60.03	13.95	6.78	0.24	2.58	3.12	4.19	0.53	1.62	
30	5.06	63.78	12.55	6.78	0.19	2.37	2.71	3.95	0.42	1.28	
Particulate matter f	from the t	ests with a	alumina a	nd silica	sand mixte	ed in equal	proportion	ns			
8	5.44	48.81	21.88	7.59	0.45	3.2	3.44	4.42	1.01	2.58	
16	5.03	60.67	14.01	7.02	0.26	2.87	2.8	4.37	0.55	1.46	
23	4.39	40.66	31.02	8.32	0.27	3.19	3.57	3.95	1.15	1.93	
30	4.77	42.75	28.12	8.34	0.28	3.05	3.68	4.23	1.16	2.26	

## **Chapter 8**

## **Conclusions and Recommendations**

### 8.1 Conclusions

The potential of potential of three co-firing methods: (i) burning pre-mixed fuels, (ii) using fuel staging with bottom air injection, and (iii) using reburning for reducing NO<sub>x</sub> emissions during biomass-biomass co-combustion in a fluidized-bed combustor has been investigated. Effects of the proposed co-combustion techniques, operating conditions, bed material type on the behavior of major pollutants (CO, C<sub>x</sub>H<sub>y</sub>, and NO) in different reactor regions, as well as on the emissions and combustion efficiency of the combustor, are studied in detail and compared for the proposed co-combustion methods. For safe co-firing of the selected biomasses, alumina sand (AS), mixed with silica sand (SS) in different proportions, is used as the bed material to inhibit bed agglomeration.

Prior to the (co-)combustion tests, a cold-state hydrodynamic study has been performed in a cone-shaped fluidized bed using the alternative (sand-like) bed materials, with the main goal to investigate the major hydrodynamic characteristics and regimes of the bed with a sand-biomass binary mixture for variable superficial velocity of air (u) fluidizing the bed. The  $\Delta p$ -u diagrams of the cone-shaped bed have been obtained for a range of operating variables, and then used for determining the hydrodynamic regimes and characteristics of the bed. The following conclusions have been derived from the results obtained in this study:

- four sequent hydrodynamic regimes (fixed-bed, partially fluidized-bed, fully fluidized-bed, and turbulent fluidized-bed regimes) are observed in the cone-shaped fluidized bed when varying the air superficial velocity from 0 to 6 m/s;
- a static bed height of 30 cm seems to be appropriate (irrespective of the bed material) for (co-)firing of the selected biomasses as ensuring (i) stable fluidization of the bed (at reasonable  $u_{\rm mff}$ ), and (ii) sustained ignition and combustion of biomass in a coneshaped fluidized bed;

- empirical models for predicting  $u_{\rm mff}$  and  $\Delta p_{\rm mff}$  of cone-shaped fluidized beds with binary mixtures (or pure bed materials) have been developed in this work. The  $u_{\rm mff}$  and  $\Delta p_{\rm mff}$  predicted by the proposed models show good agreement with those obtained experimentally, thus, indicating the validity of the models;
- a Nomograph has been proposed for practical use to assess the total pressure drop across a cone-shaped bed (with a binary mixture) and air distributor for any required superficial air velocity, for a range of operating variables.

The findings of the co-combustion studies reveal that the proposed co-firing methods exhibit a great potential for NOx emission reduction, however, with different extents. Based on the findings, the following conclusions have been derived:

- the effects of operating parameters, such as the energy fraction of secondary/reburn fuel in the total fuel supply (EF<sub>2</sub>), excess air (EA), and the secondary-to-total air ratio (SA/TA) in the reburning tests, on the combustion and emission characteristics of the combustor are noticeable;
- the selected co-firing techniques create reducing conditions for NO (due to substantial CO and  $C_xH_v$ ) in the primary and secondary/reburn zones;
- by using the proposed co-combustion techniques, the combustor ensures high (~99%) combustion efficiency and reduced NO emission: by about 15% when co-firing pre-mixed fuels, by 40% for the fuel-staged co-combustion, and by 55% when using reburning, as compared to burning the base fuel alone;
- some increase in the CO and  $C_xH_y$  emissions, consequently leading to a lower combustion efficiency, is observed when using the proposed co-firing techniques;
- when using silica sand (conventional bed material) in the co-firing of PCR and EB combustor, a small proportion of agglomerates can be formed in the fluidized bed within a quite short time ( $\sim$ 8 h) of combustor operation with both co-firing techniques. The agglomerates are formed in a silica sand bed by binding materials, such as low-melting-point  $K_2O$ –CaO– $SiO_2$  and  $K_2O$ – $SiO_2$  eutectics, formed on the surface of silica sand grains;

- with a proportion of alumina sand in the bed mixture of greater than 50% (by wt.), bed agglomeration can be prevented in the combustor for a relatively long operational time;
- however, both alternative bed materials show time-domain changes in their
  physiochemical characteristics, pointing at a gradual decrease of the bed capability to
  withstand agglomeration, mainly due to continuous carryover of fine alumina-rich
  particles (generated in the fluidized bed in collisions and attrition of the AS grains) from
  the combustor.

### 8.2 Recommendations for the future work

Given below are some recommendations for future research studies:

- other biomasses/wastes with elevated/high content of nitrogen should be studied;
- other alternative bed materials (with low cost) decreasing the bed agglomeration can be considered for the biomass-biomass co-combustion in a fluidized-bed combustor;
  - effects of reburning on fluidization quality of the bed should be investigated;
- to assess a capability of the selected bed materials for a practical use, the tests should be performed for longer time;
- the knowledge obtained from this research project should employed in practice.

## References

- Adams, B.R., Harding, N.S. 1998. Reburning using biomass for NOx control. *Fuel Processing Technology*, 54(1), 249-263.
- Akpulat O, Varol M, Atimtay AT. Effect of freeboard extension on co-combustion of coal and olive cake in a fluidized bed combustor. *Bioresource Technology*. 2010;101:6177–6184.
- Arromdee, P., Kuprianov, V.I. 2012. Combustion of peanut shells in a cone-shaped bubbling fluidized-bed combustor using alumina as the bed material. *Applied Energy*, 97, 470-482.
- Ballester, J., Ichaso, R., Pina, A., González, M.A., Jiménez, S. 2008. Experimental evaluation and detailed characterisation of biomass reburning. *Biomass and Bioenergy*, 32(10), 959-970.
- Baukal, C.E. Jr. 2001. The John Zink Combustion Handbook. CRC Press, New York.
- Brus, E., Öhman, M., Nordin, A. 2005. Mechanisms of Bed Agglomeration during Fluidized-Bed Combustion of Biomass Fuels. *Energy & Fuels*, 19(3), 825-832.
- Casaca, C., Costa, M. 2009. NOx control through reburning using biomass in a laboratory furnace: Effect of particle size. *Proceedings of the Combustion Institute*, 32(2), 2641-2648.
- Chaivatamaset, P., Sricharoon, P., Tia, S. 2011. Bed agglomeration characteristics of palm shell and corncob combustion in fluidized bed. *Applied Thermal Engineering*, 31(14–15), 2916–2927.
- Chaivatamaset, P., Tia, S. 2015. The characteristics of bed agglomeration during fluidized bed combustion of eucalyptus bark. *Applied Thermal Engineering*, 75, 1134-1146.
- Chakritthakul, S., Kuprianov, V.I. 2011. Co-firing of eucalyptus bark and rubberwood sawdust in a swirling fluidized-bed combustor using an axial flow swirler. *Bioresource Technology*, 102(17), 8268-8278.

- Chyang, C.-S., Qian, F.-P., Lin, Y.-C., Yang, S.-H. 2008. NO and N2O Emission Characteristics from a Pilot Scale Vortexing Fluidized Bed Combustor Firing Different Fuels. *Energy & Fuels*, 22(2), 1004-1011.
- Department of Alternative Energy Development and Efficiency. The Renewable and Alternative Energy Development Plan for 25 Percent in 10 Years (AEDP 2012-2021). Available from: http://www4.dede.go.th/dede/images/stories/pdf/dede\_aedp\_2012\_21.pdf (accessed on June 8, 2018).
- Department of Alternative Energy Development and Efficiency (DEDE), Ministry of Energy, Thailand. Thailand alternative energy situation 2016 (accessed September 5, 2018). Available from:

  http://www.dede.go.th/ download/state 59/thailand%20alternative2016.pdf.
- Fernández Llorente, M.J., Escalada Cuadrado, R., Murillo Laplaza, J.M., Carrasco García, J.E. (2006). Combustion in bubbling fluidised bed with bed material of limestone to reduce the biomass ash agglomeration and sintering. *Fuel*, 85(14–15), 2081–2092.
- Geldart, D. (1973). Types of gas fluidization. *Powder Technology*, 7(5), 285–292.
- Harding, N.S., Adams, B.R. 2000. Biomass as a reburning fuel: a specialized cofiring application. Biomass and Bioenergy, 19(6), 429-445.
- Jing, S., Hu, Q., Wang, J., Jin, Y. (2000). Fluidization of coarse particles in gas-solid conical beds. Chemical Engineering and Processing: Process Intensification, 39(4), 379–387.
- Kaewklum, R., Kuprianov, V.I. (2008). Theoretical and experimental study on hydrodynamic characteristics of fluidization in air-sand conical beds. *Chemical Engineering Science*, 63(6), 1471–1479.
- Karlström, O., Perander, M., DeMartini, N., Brink, A., Hupa, M. 2017. Role of ash on the NO formation during char oxidation of biomass. *Fuel*, 190, 274-280.
- Kaynak B, Topal H, Atimtay AT. Peach and apricot stone combustion in a bubbling fluidized bed. *Fuel Processing Technology*. 2005;86:1175–1193.

- Khan, A.A., de Jong, W., Jansens, P.J., Spliethoff, H. 2009. Biomass combustion in fluidized bed boilers: Potential problems and remedies. *Fuel Processing Technology*, 90(1), 21-50.
- Kicherer, A., Spliethoff, H., Maier, H., Hein, K.R.G. 1994. The effect of different reburning fuels on NOx-reduction. *Fuel*, 73(9), 1443-1446.
- Kouprianov, V.I., Permchart, W. 2003. Emissions from a conical FBC fired with a biomass fuel. *Applied Energy*, 74(3), 383-392.
- Kunii, D., Levenspiel, O. 1991. Fluidization engineering. 2nd ed. Wiley, Massachusetts.
- Kuprianov, V.I., Arromdee, P. 2013. Combustion of peanut and tamarind shells in a conical fluidized-bed combustor: A comparative study. *Bioresource Technology*, 140, 199-210.
- Kuprianov, V.I., Janvijitsakul, K., Permchart, W. 2006. Co-firing of sugar cane bagasse with rice husk in a conical fluidized-bed combustor. *Fuel*, 85(4), 434-442.
- Kuprianov, V.I., Permchart, W., Janvijitsakul, K. 2005. Fluidized bed combustion of predried Thai bagasse. *Fuel Processing Technology*, 86(8), 849-860.
- Leckner, B., Åmand, L.E., Lücke, K., Werther, J. 2004. Gaseous emissions from cocombustion of sewage sludge and coal/wood in a fluidized bed. *Fuel*, 83(4), 477-486.
- Li, J., Yang, B., Cheng, G. 2003. Affinity adsorption and hydrodynamic behavior in a tapered-bed of upward flow. *Biochemical Engineering Journal*, 15(3), 185–192.
- Li, S., Yu, J., Wei, X., Guo, X., Chen, Y. 2014. Catalytic reduction of nitric oxide by carbon monoxide over coal gangue hollow ball. *Fuel Processing Technology*, 125, 163-169.
- Lin, W., Dam-Johansen, K., Frandsen, F. 2003. Agglomeration in bio-fuel fired fluidized bed combustors. *Chemical Engineering Journal*, 96(1), 171-185.
- Lu, P., Xu, S.-R., Zhu, X.-M. 2009. Study on NO heterogeneous reduction with coal in an entrained flow reactor. *Fuel*, 88(1), 110-115.

- Madhiyanon T., Sathitruangsak P., Soponronnarit S., 2010. Combustion characteristics of rice-husk in a short-combustion -chamber fluidized-bed combustor (SFBC). *Applied Thermal Engineering*, 30,347–353.
- Madhiyanon, T., Lapirattanakun, A., Sathitruangsak, P., Soponronnarit, S. 2006. A novel cyclonic fluidized-bed combustor (ψ-FBC): Combustion and thermal efficiency, temperature distributions, combustion intensity, and emission of pollutants. *Combustion and Flame*, 146(1), 232-245.
- Madhiyanon, T., Sathitruangsak, P., Soponronnarit, S. 2009. Co-combustion of rice husk with coal in a cyclonic fluidized-bed combustor (ψ-FBC). *Fuel*, 88(1), 132-138.
- Ninduangdee, P., Kuprianov, V.I. 2013. Study on burning oil palm kernel shell in a conical fluidized-bed combustor using alumina as the bed material. *Journal of the Taiwan Institute of Chemical Engineers*, 44(6), 1045-1053.
- Ninduangdee, P., Kuprianov, V.I. 2014. Combustion of palm kernel shell in a fluidized bed: Optimization of biomass particle size and operating conditions. *Energy Conversion and Management*, 85, 800-808.
- Ninduangdee, P., Kuprianov, V.I. 2015. Combustion of an oil palm residue with elevated potassium content in a fluidized-bed combustor using alternative bed materials for preventing bed agglomeration. *Bioresource Technology*, 182, 272-281.
- Ninduangdee, P., Kuprianov, V.I. 2016. A study on combustion of oil palm empty fruit bunch in a fluidized bed using alternative bed materials: Performance, emissions, and time-domain changes in the bed condition. *Applied Energy*, 176, 34-48.
- Nussbaumer, T. 2003. Combustion and Co-combustion of Biomass: Fundamentals, Technologies, and Primary Measures for Emission Reduction. *Energy & Fuels*, 17(6), 1510-1521.
- Nuutinen, L.H., Tiainen, M.S., Virtanen, M.E., Enestam, S.H., Laitinen, R.S. 2004. Coating Layers on Bed Particles during Biomass Fuel Combustion in Fluidized-Bed Boilers. *Energy & Fuels*, 18(1), 127-139.
- Öhman, M., Nordin, A., Skrifvars, B.-J., Backman, R., Hupa, M. 2000. Bed Agglomeration Characteristics during Fluidized Bed Combustion of Biomass

- Fuels. Energy & Fuels, 14(1), 169-178.
- Okasha, F. 2007. Staged combustion of rice straw in a fluidized bed. Experimental Thermal and Fluid Science, 32(1), 52-59.
- Olazar, M., San Jose, M.J., Aguayo, A.T., Arandes, J.M., Bilbao, J. 1992. Stable operation conditions for gas-solid contact regimes in conical spouted beds. Industrial & Engineering Chemistry Research, 31(7), 1784–1792.
- Olofsson, G., Ye, Z., Bjerle, I., Andersson, A. 2002. Bed agglomeration problems in fluidized-bed biomass combustion. *Industrial & Engineering Chemistry Research*, 41(12), 2888–2894.
- Pollution Control Department, Ministry of Natural Resources and Environment, Thailand. Air Pollution Standards for Industrial Sources (accessed December 22, 2018). Available from: http://www.pcd.go.th/info\_serv/reg\_std\_airsnd03.html.
- Peng, Y., Fan, L.T. 1997. Hydrodynamic characteristics of fluidization in liquid-solid tapered beds. *Chemical Engineering Science*, 52(14), 2277–2290.
- Permchart, W., Kouprianov, V.I. 2004. Emission performance and combustion efficiency of a conical fluidized-bed combustor firing various biomass fuels. *Bioresource Technology*, 92(1), 83-91.
- Qian, F.P., Chyang, C.S., Huang, K.S., Tso, J. 2011. Combustion and NO emission of high nitrogen content biomass in a pilot-scale vortexing fluidized bed combustor. *Bioresource Technology*, 102(2), 1892-1898.
- Sahu, S.G., Chakraborty, N., Sarkar, P. 2014. Coal–biomass co-combustion: An overview. *Renewable and Sustainable Energy Reviews*, 39, 575-586.
- Salzmann, R., Nussbaumer, T. 2001. Fuel Staging for NOx Reduction in Biomass Combustion: Experiments and Modeling. Energy & Fuels, 15(3), 575-582.
- Sami, M., Annamalai, K., Wooldridge, M. 2001. Co-firing of coal and biomass fuel blends. *Progress in Energy and Combustion Science*, 27(2), 171-214.
- Scala, F., Chirone, R. 2008. An SEM/EDX study of bed agglomerates formed during fluidized bed combustion of three biomass fuels. *Biomass and Bioenergy*, 32(3), 252-266.

- Shi, Y.F., Yu, Y.S., Fan, L.T. (1984). Incipient fluidization condition for a tapered fluidized bed. *Industrial & Engineering Chemistry Fundamentals*, 23(4), 484–489.
- Shu, Y., Zhang, F., Wang, H., Zhu, J., Tian, G., Zhang, C., Cui, Y., Huang, J. 2015. An experimental study of NO reduction by biomass reburning and the characterization of its pyrolysis gases. *Fuel*, 139, 321-327.
- Sirisomboon, K., Kuprianov, V.I. 2017. Effects of Fuel Staging on the NO Emission Reduction during Biomass–Biomass Co-combustion in a Fluidized-Bed Combustor. *Energy & Fuels*, 31(1), 659-671.
- Smoot, L.D., Hill, S.C., Xu, H. 1998. NOx control through reburning. *Progress in Energy and Combustion Science*, 24(5), 385-408.
- Suheri, P., Kuprianov, V.I. 2015. Co-Firing of Oil Palm Empty Fruit Bunch and Kernel Shell in a Fluidized-Bed Combustor: Optimization of Operating Variables. *Energy Procedia*, 79, 956-962.
- Sun, Z., Jin, B., Zhang, M., Liu, R., Zhang, Y. 2008. Experimental studies on cotton stalk combustion in a fluidized bed. *Energy*, 33(8), 1224-1232.
- Sun, Z., Shen, J., Jin, B., Wei, L. 2010. Combustion characteristics of cotton stalk in FBC. *Biomass and Bioenergy*, 34(5), 761-770.
- Turn, S.Q., Jenkins, B.M., Jakeway, L.A., Blevins, L.G., Williams, R.B., Rubenstein, G., Kinoshita, C.M. 2006. Test results from sugar cane bagasse and high fiber cane co-fired with fossil fuels. *Biomass and Bioenergy*, 30(6), 565-574.
- Turns, S.R. 2006. An Introduction to Combustion: Concepts and Applications. international ed. McGraw-Hill, Singapore.
- US DOE, The U.S. Department of Energy and the Babcock & Wilcox Company Energy and Environmental Research Corporation New York State Electric & Gas Corporation. Clean Coal Technology, Reburning Technologies for the Control of Nitrogen Oxides Emissions from Coal-Fired Boilers, Topical Report Number 14, May 1999. Available from: http://www.netl.doe.gov/File%20Library/Research/Coal/major%20demonstrations/cctdp/Round3/topical14.pdf, (accessed on January 8, 2015).

- Vamvuka D, Sfakiotakis S, Kotronakis M. Fluidized bed combustion of residues from oranges' plantations and processing. *Renewable Energy*. 2012;44:231–237.
- Vamvuka, D., Sfakiotakis, S., Kotronakis, M. 2012. Fluidized bed combustion of residues from oranges' plantations and processing. *Renewable Energy*, 44, 231-237.
- Visser, H.J.M., Van Lith, S.C., Kiel, J.H.A. 2008. Biomass ash-bed material interactions leading to agglomeration in FBC. *Journal of Energy Resources Technology*, 130(1), pp. 0118011–0118015.
- Vuthaluru, H.B., Zhang, D.-k. (2001a). Effect of Ca- and Mg-bearing minerals on particle agglomeration defluidisation during fluidised-bed combustion of a South Australian lignite. *Fuel Processing Technology*, 69(1), 13–27.
- Vuthaluru, H.B., Zhang, D.K. (2001b). Remediation of ash problems in fluidised-bed combustors. *Fuel*, 80(4), 583–598.
- Wang, C.a., Du, Y., Che, D. 2012. Investigation on the NO Reduction with Coal Char and High Concentration CO during Oxy-fuel Combustion. *Energy & Fuels*, 26(12), 7367-7377.
- Werther, J., Saenger, M., Hartge, E.U., Ogada, T., Siagi, Z. 2000. Combustion of agricultural residues. *Progress in Energy and Combustion Science*, 26(1), 1-27.
- Winter, F., Wartha, C., Hofbauer, H. 1999. NO and N<sub>2</sub>O formation during the combustion of wood, straw, malt waste and peat. *Bioresource Technology*, 70(1), 39-49.
- Youssef, M.A., Wahid, S.S., Mohamed, M.A., Askalany, A.A. 2009. Experimental study on Egyptian biomass combustion in circulating fluidized bed. *Applied Energy*, 86(12), 2644–2650.
- Zevenhoven-Onderwater, M., Öhman, M., Skrifvars, B.-J., Backman, R., Nordin, A., Hupa, M. 2006. Bed agglomeration characteristics of wood-derived fuels in FBC. *Energy & Fuels*, 20(2), 818–824.
- Zhong, B.J., Shi, W.W., Fu, W.B. 2002. Effects of fuel characteristics on the NO reduction during the reburning with coals. *Fuel Processing Technology*, 79(2), 93-106.

# **Project Outputs**

### International Journals

- 1. Kuprianov, V.I., Ninduangdee, P., and Suheri, P. (2018). Co-firing of oil palm residues in a fuel staged fluidized-bed combustor using mixtures of alumina and silica sand as the bed material, *Applied Thermal Engineering*, Vol. 144, 5 November 2018, pp. 371-382. ISI Q1, Impact factor = 3.771
- Ninduangdee, P. and Kuprianov, V.I. (2018). Experimental investigation and empirical modeling of flow regimes and hydrodynamic characteristics of a cone-shaped bed using sand-biomass binary mixtures, *Chemical Engineering* and *Processing - Process Intensification*, Vol. 131, September 2018, pp. 1-11.
   ISI Q1, Impact factor = 2.826
- Ninduangdee, P. and Kuprianov, V.I. (2018). Fluidized bed co-combustion of rice husk pellets and moisturized rice husk: The effects of co-combustion methods on gaseous emissions, *Biomass and Bioenergy*, Vol. 112, May 2018, pp. 73-84.
   ISI Q1, Impact factor = 3.358
- Ninduangdee, P. and Kuprianov, V.I. (2018). Co-combustion of rice husk pellets and moisturized rice husk in a fluidized-bed combustor using fuel staging at a conventional air supply, *Songklanakarin Journal of Science and Technology*, Vol. 40, No. 5, September-October 2018, pp. 1081-1089. ISI Q2

## International conferences

- 1. Se, C., Kuprianov, V.I., Ninduangdee, P. (2018). Co-firing cassava rhizome and eucalyptus bark in a fluidized-bed combustor using reburning: combustor performance and time-related bed behavior, *Proceedings of the International Conferene on Green Energy for Sustainable Development*, 24-26 October 2018, Phuket, Thailand, 8 p.
- 2. Ninduangdee, P., Se, C., Kuprianov, V.I. (2018). Time-related bed behavior in a fluidized-bed combustor co-firing pelletized cassava rhizome and eucalyptus bark: a comparative study between conventional and alternative bed materials, *Proceedings of the 6th Asian Conference on Innovative Energy and*

- Environmental Chemical Engineering, 4-7 November 2018, Sun Moon Lake, Taiwan, pp. 277-282.
- 3. Se, C., Kuprianov, V.I., Ninduangdee, P. (2018). Co-combustion of pelletized cassava rhizome and eucalyptus bark for reducing NOx in a fluidized-bed combustor, *Proceedings of the 6th Asian Conference on Innovative Energy and Environmental Chemical Engineering*, 4-7 November 2018, Sun Moon Lake, Taiwan, pp. 271-276.
- 4. Siricharuanun, T., Rerkpisut, N., Boonsai, P., Ninduangdee, P., and Kuprianov, V.I. (2018). Co-combustion characteristics of pelletized cassava rhizome and eucalyptus bark: thermogravimetric analysis and kinetic modeling, *Proceedings of the 6th Asian Conference on Innovative Energy and Environmental Chemical Engineering*, 4-7 November 2018, Sun Moon Lake, Taiwan, pp. 425-430.
- 5. Se, C., Ninduangdee, P., and Kuprianov, V.I. (2018). Co-firing of pelletized cassava rhizome and eucalyptus bark in a fluidized bed: studies on the effects of co-firing methods and bed material type on the combustor performance and time-related bed behavior, *Proceedings of the 26th European Biomass Conference and Exhibition*, 14-17 May 2018, Copenhagen, Denmark, pp. 378-389.
- 6. Kuprianov, V. I. and Ninduangdee, P. (2017). Experimental study on the biomass–biomass co-combustion for reducing NOx in a fluidized-bed combustor: a comparison between the co-firing techniques, *Proceedings of the 25th European Biomass Conference and Exhibition*, 12-15 June 2017, Stockholm, Sweden, p. 384-392.
- 7. Ninduangdee, P. and Kuprianov, V.I. (2016). Study on co-combustion of pelletized and moisturized rice husks in a cone-shaped fluidized-bed combuster using fuel staging for reducing NOx emissions: optimization of operating variables, *Proceedings of the 7th TSME International Conference on Mechanical Engineering (TSME-ICoME 2016)*, 13-16 December 2016, Chiang Mai, Thailand, 8 p.

- 8. Kuprianov, V. I. and Ninduangdee, P. (2016). Interaction between biomass ash and bed material during combustion of oil palm residues in a fluidized bed of alumina sand, *Proceedings of the 5th Asian Conference on Innovative Energy and Environmental Chemical Engineering (ASCON-IEEChE 2016)*, 13-16 November 2016, Yokohama, Japan, pp. 126-131.
- 9. Ninduangdee, P. and Kuprianov, V.I. (2016). Co-combustion of pelletized and moisturized rice husks in a fluidized-bed combustor using fuel staging and reburning for reducing NOx emissions, *Proceedings of the 5th Asian Conference on Innovative Energy and Environmental Chemical Engineering* (ASCON-IEEChE 2016), 13-16 November 2016, Yokohama, Japan, pp. 615-620.
- 10. Kuprianov, V. I., Ninduangdee, P., and Suheri, P. (2016). Fuel-staged cocombustion of high-alkali oil palm residues in a fluidized-bed combustor using mixtures of alumina and silica sand to prevent bed agglomeration, *The 24th European Biomass Conference and Exhibition (EUBCE 2016)*, 6-9 June 2016, Amsterdam, The Netherlands, pp. 420-428.

**Appendices: Paper Reprints** 



Contents lists available at ScienceDirect

# Chemical Engineering & Processing: Process Intensification

journal homepage: www.elsevier.com/locate/cep



# Experimental investigation and empirical modeling of flow regimes and hydrodynamic characteristics of a cone-shaped bed using sand-biomass binary mixtures



Pichet Ninduangdee<sup>a</sup>, Vladimir I. Kuprianov<sup>b,\*</sup>

a Department of Mechanical Engineering, Faculty of Engineering and Industrial Technology, Phetchaburi Rajabhat University, Phetchaburi 76000, Thailand
 b School of Manufacturing Systems and Mechanical Engineering, Sirindhorn International Institute of Technology, Thammasat University, P.O. Box 22, Thammasat Rangsit Post Office, Pathum Thani, 12121, Thailand

### ARTICLE INFO

Keywords:
Cone-shaped fluidized bed
Binary mixture
Flow regime
Hydrodynamic characteristics
Empirical model

#### ABSTRACT

Flow regimes and hydrodynamic characteristics of a cone-shaped bed, the key element of a fluidized-bed combustor, were studied in this work. Prior to the cold-state experiments, the bed material (alumina sand/dolomite/limestone) was premixed with palm kernel shell in different proportions of the biomass in a binary mixture: 0, 2.5, 7.5, and 10 wt.%. In a test series with the selected bed material, the pressure drop across the bed and air distributor ( $\Delta p$ ) was measured versus superficial air velocity at the air distributor exit (u), for three static bed heights (20, 30, and 40 cm). Four sequent flow regimes were found in the sand-biomass bed with for the selected range of u. The findings revealed the effects of operating variables on the major hydrodynamic characteristics: minimum velocity of partial fluidization ( $u_{mpf}$ ), minimum velocity of full fluidization ( $u_{mff}$ ) and corresponding pressure drops ( $\Delta p_{max}$  and  $\Delta p_{mff}$ ), and entire  $\Delta p - u$  diagram of the bed. The mathematical models for predicting  $u_{mff}$  and  $\Delta p_{mff}$ , were empirically developed, both exhibiting good agreement with experimental data. A nomograph for the assessment of the pressure drop across the conical bed with the binary mixture at any arbitrary superficial air velocity has been proposed in this work.

### 1. Introduction

Fluidized-bed systems are widely used in various industrial applications, mainly related to chemical and energy conversion processes [1–4]. Due to excellent gas–solid mixing in a bed, fluidized-bed systems have become important competitors in combustion applications. Compared to other combustion techniques (e.g., stoker-fired and pulverized fuel firing systems), fluidized-bed boilers and combustors offer a number of important advantages, such as wide fuel flexibility, better heat transfer characteristics, thermal homogeneity, and relatively low temperatures inside a system, resulting in lower  $NO_x$  emissions from a boiler/combustor [5–7]. With the use of co-firing of fuels with dedicated combustion properties, the  $NO_x$  emissions can be substantially reduced via fuel staging and reburning, as compared to burning a base fuel in a conventional fluidized-bed system [8].

To provide an optimal design of a fluidized-bed combustion system, a knowledge of the hydrodynamic characteristics of a gas-solid fluidized bed is required. For constructing a new system, these characteristics are important to: (i) obtain the best/optimal reactor design, (ii)

select proper auxiliary equipment for a combustion system, and (iii) quantify a possible range of combustion operating conditions [9]. In addition, the hydrodynamics has been reported to play a vital role in the combustion and heat transfer characteristics of a fluidized-bed reactor [10,11].

A number of research studies have investigated flow regimes and hydrodynamic characteristics of columnar (cylindrical/prismatic) fluidized gas—solid beds, widely used in fluidized-bed combustion systems, and reported that the minimum fluidization velocity,  $u_{\rm mf}$ , and the corresponding pressure drop across the bed,  $\Delta p_{\rm mf}$ , are important hydrodynamic characteristics of these conventional fluidized-bed systems [12,13].

During the last few decades, fluidized-bed combustion has been increasingly employed in the combustion of various biomass fuels, with the aim to decrease the emissions and, thus, minimize the environmental impact of the energy production. In a biomass fluidized-bed combustion system, quartz/silica sand is normally employed as the bed material, to facilitate effective mixing between solids and gases (combustion products), and thus, ensure stable ignition and combustion of

E-mail address: ivlaanov@siit.tu.ac.th (V.I. Kuprianov).

<sup>\*</sup> Corresponding author.

Nomenclature			Superficial air velocity at the air distributor exit (m/s) Minimum velocity of turbulent bed fluidization (m/s)				
$A_{\rm a}$	Net cross-sectional area of airflow at the air distributor exit (m <sup>2</sup> )	$u_{ m k}$ $u_{ m mf}$	Minimum fluidization velocity (used for columnar beds) (m/s)				
Ar	Archimedes number (–)	$u_{ m mfd}$	Maximum velocity of full defluidization of the bed (m/s)				
BH	Static bed height (experimental parameter) (cm)	$u_{ m mff}$	Minimum velocity of full fluidization (of entire bed ma-				
$D_{ m o}$	Diameter at the conical bed lower section (at the air dis-		terial) (m/s)				
	tributor exit) (m)	$u_{\mathrm{mpd}}$	Maximum velocity of partial bed defluidization (m/s)				
$d_{ m BM}$	Mean diameter of bed material particles (m)	$u_{ m mpf}$	Minimum velocity of partial bed fluidization (m/s)				
$d_{ m PKS}$	Mean diameter of palm kernel shell particles (m)	$w_{ m BM}$	Weight (mass) fraction of a bed material (wt.%)				
$d_{ m p,eff}$	Effective diameter of solid particles in a binary mixture (m)	$w_{ m PKS}$	weight (mass) fraction of a biomass (palm kernel shell) (wt.%)				
g	Gravitational acceleration (m/s <sup>2</sup> )						
h			Greek symbols				
MF	Biomass fraction in a binary mixture (wt.%)						
$\Delta p$	Total pressure drop (across the bed and air distributor)	α	Cone angle of a conical bed (º)				
	(kPa)	μ	Dynamic viscosity of a fluidizing gas (air) (N s/m <sup>2</sup> )				
$\Delta p_{ m max}$	Total pressure drop at the minimum velocity of partial	$\rho_{BM}$	Solid density of a bed material (kg/m³)				
	fluidization (kPa)	$\rho_{\text{g}}$	Density of a fluidizing gas (kg/m³)				
$\Delta p_{ m mf}$	Pressure drop across the bed at the minimum fluidization	$\rho_{PKS}$	Solid density of palm kernel shell (kg/m³)				
	velocity (used for columnar beds) (kPa)	$\rho_p$ or $\rho_s$	Solid density of bed material particles (kg/m³)				
$\Delta p_{ m mff}$	Total pressure drop at the minimum velocity of full flui- dization (kPa)	$\rho_{p,eff}$	Effective density of a binary mixture (kg/m <sup>3</sup> )				
$Q_a$	$Q_a$ Rate of airflow through the bed (binary mixture) (m <sup>3</sup> /s)		Abbreviations				
Re	Reynolds number (–)						
Re <sub>mff</sub>	Reynolds number at the minimum velocity of full fluidi-	AD	Air distributor				
*****	zation (–)	PK	Palm kernel shell				

fuel particles in the fluidized bed. However, when firing biomasses with high/elevated alkali-metal contents using the conventional bed material, the fluidized-bed combustion systems encounter bed agglomeration [14–16]. To inhibit this problem, the use of alternative bed materials, such as alumina sand, dolomite, and limestone, have been proposed [17,18]. Commonly, these bed materials are rather expensive, compared to silica sand. Due to some advantages, such as a lesser amount and/or cost of the bed material and a lower pressure drop across the fluidized bed [9,19], fluidized-bed combustion systems with a conical/tapered bed are treated to be promising techniques, compared to those using cylindrical and prismatic beds (with similar bed heights), particularly when using costly bed materials [17–19].

The hydrodynamic behavior and characteristics of conical/tapered fluidized beds are reported to be quite different, as compared to cylindrical and prismatic fluidized beds. In a conical/tapered fluidized bed, the cross-sectional area of the bed increases along the bed height. This geometrical feature results in a reduction of the fluidizing gas velocity along the axial distance in the bed, leading to an insignificant pressure gradient along the bed height and, consequently, to a steady operation of the conical/tapered fluidized beds [20-23]. However, compared to the systems using a wedge-shaped bed (also termed a tapered bed), fluidized-bed combustors with a cone-shaped bed are typically operated in a turbulent fluidization regime (mainly due to the relatively small airflow area at the air distributor exit), even at reduced combustor loads and/or lowered excess air [17,18]. This regime ensures highly intensive mixing processes in the reactor bottom and results in a substantial expansion of the conical fluidized bed [23], which is favorable for mitigating "melt-inducted" bed agglomeration in a combustion system [17].

Because of the gas velocity axial gradient, the bed material may exhibit different flow regimes in different layers of the conical/tapered bed at relatively low gas flow rates [20,23]. As reported in a number of research papers, the minimum velocity of full fluidization ( $u_{\rm mff}$ ) and corresponding pressure drop across the bed ( $\Delta p_{\rm mff}$ ) are crucial characteristics of conical and tapered fluidized beds [9,24–26], and are used for quantifying the possible range of superficial air velocity, ensuring a

desirable fluidization mode for stable burning of biomass in the fluidized bed at the specified load [24]. Unlike  $u_{\rm mf}$  (basically applicable for columnar beds), depending on physical properties of a bed material (solid density, bed particle size, sphericity, and voidage) [12,13],  $u_{\rm mff}$  of a conical/tapered bed takes into account the combined effects from the bed physical properties and geometry (the latter is characterized by static bed height, cone angle, and diameter at the lower base), as well as from the air injection/distribution technique [9,26,31].

Only limited studies have reported empirical models for predicting  $u_{\rm mff}$  and  $\Delta p_{\rm mff}$  of a reactor with the cone-shaped/tapered bed, using a single bed material fluidized by air [25,26]. The models include the above-mentioned physical properties and geometrical characteristics of the bed, as well as the properties of the fluidizing agent (density and viscosity). Besides, the model in Ref [26]. takes into account the effects of bed voidage and particle sphericity. However, the proposed models have been developed for either large taper angles [25] or small cone angles [26], which are substantially different from that (of about 40°) ensuring bubbling fluidization regime [31], favorable for fluidized-bed combustion systems.

Note that in a fluidized-bed combustion system fired with biomass, solid particles in the entire bed are not the only bed material particles but also fuel char/ash particles (up to 5 wt.%) [27]. Thus, an understanding of hydrodynamic behavior and characteristics of a fluidized bed, containing both sand and biomass particles (binary mixture), is important for the optimal design and operation of biomass-fueled fluidized-bed combustion systems using cone-shaped beds. However, no reliable models for predicting  $u_{\rm mff}$  and  $\Delta p_{\rm mff}$  of a conical bed with a binary (sand–biomass) mixture, which can be operated in a bubbling/turbulent fluidization regime, has been reported in the literature.

The main objective of this work was to examine the flow regimes and hydrodynamic characteristics of a cone-shaped fluidized bed, using three bed materials (alumina sand, dolomite, and limestone), as well as those of a binary mixture in different proportions of the bed material and biomass. At the first stage of this work, the effects of static bed height, biomass weight fraction in the binary mixture, and biomass particle size on the flow regimes and hydrodynamic characteristics of

the bed fluidized by airflow were experimentally investigated. Afterwards, empirical models for predicting major hydrodynamic characteristics (such as minimum velocity of full fluidization,  $u_{\rm mff}$ , and corresponding total pressure drop across the bed and air distributor,  $\Delta p_{\rm mff}$ ) of the cone-shaped bed with a specified binary mixture (i.e., for the ranges of weight fraction of the bed material and biomass) were developed.

### 2. Methods

### 2.1. Experimental setup

Fig. 1 depicts the test rig, which was constructed to reproduce the configuration of a conical fluidized-bed combustor, used in a number of previous experimental works on individual firing and co-firing of various biomass fuels [17–19]. The experimental rig was made of 1-mm thick galvanized steel and consisted of two sections: (1) a cone-shaped section with a 40° cone angle and 250 mm inner diameter at the bottom base, and (2) a cylindrical section of 2000 mm height and 1000 mm inner diameter. A transparent plexiglass window, installed on the conical wall of the apparatus, was used to monitor the bed behavior during the tests. Two digital cameras (Fujifilm FinePix HS20 EXR) were used to record the particles movement in different bed fluidization regimes. The experimental rig was also equipped with measuring devices and instruments (see Fig. 1). A 25-hp air blower was used to supply fluidizing air to the test rig through an air pipe of 100 mm inner diameter.

Air was injected into the bed through an air distributor, as shown in Fig. 2. The air distributor consisted of nineteen bubble-cap stand pipes arranged in staggered order on the steel plate of the 250-mm diameter distributor plate, as depicted in Fig. 2a. An individual stand pipe had sixty four holes, each of 2 mm in diameter, distributed evenly over the pipe surface, and also six rectangular slots of 3 mm width and 15 mm height, located under a cap of 47 mm diameter. Airflow from each individual stand pipe penetrated into the space between the pipes

through the hole and slots in a radial direction (as represented in Fig. 2b), ensuring a quasi-uniform distribution of the airflow over the air distributor plate, and thus, preventing a spouting fluidization regime of the gas–solid bed. The net cross-sectional area of airflow at the distributor exit (calculated as the difference between area of the 250-mm-diameter plate and total area occupied by the caps) was  $A_{\rm air}=0.016\,{\rm m}^2.$ 

The airflow rate  $(Q_{\rm air})$  was adjusted by a globe valve arranged downstream from the blower, and this operating variable was controlled by using an orifice-type flowmeter equipped with a U-tube manometer (see Fig. 1). A multifunction flowmeter "Testo-512" with an L-type Pitot tube was used to measure air velocity across the air pipe in the calibration tests. The relationship between  $Q_{\rm air}$  (quantified in these set-up tests by integrating the velocity profile across the air pipe) and the valve opening was determined prior to the experimental study. The measurement accuracy of air velocity was within  $\pm$  0.03 m/s for the range of airflow rates. However, due to some errors in physical measurements of the pipe inner diameter (  $\pm$  1%) and axial air velocity (  $\pm$  2%), the measurement uncertainty in airflow rate was  $\pm$  3%. For selected operating conditions (i.e., for the particular test run), the superficial air velocity at the distributor exit was quantified as  $u=Q_{\rm air}/A_{\rm air}$ .

The total pressure drop across the distributor–bed system ( $\Delta p$ ), comprising the air–solid bed and the air distributor (AD), was measured for variable superficial air velocity at the air distributor exit (u) by using another U-tube manometer with two static pressure probes. One probe was arranged in the air duct below the air distributor, while the other one was fixed at a level 0.7 m above the air distributor plate, as shown in Fig. 1.

### 2.2. Bed materials and biomass used for preparing binary mixtures

Three bed materials (alternative to silica sand conventionally used in biomass-fueled fluidized-bed combustion systems): alumina sand, dolomite, and limestone with similar sieved particle sizes of

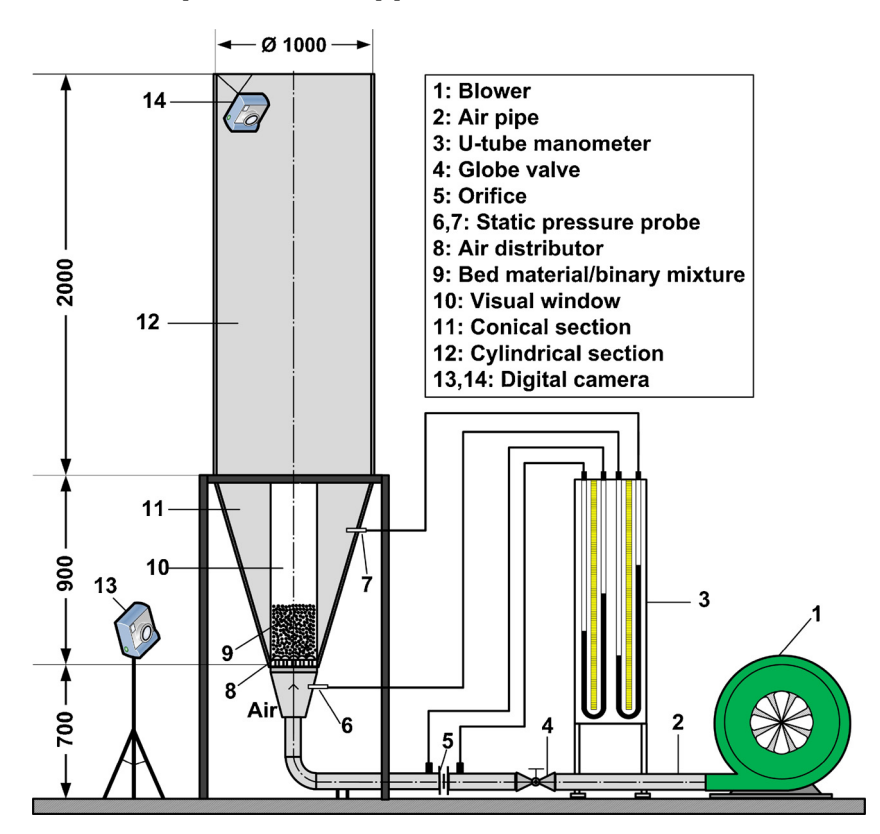


Fig. 1. Schematic diagram of the experimental setup for this cold-state hydrodynamic study (unit: mm).

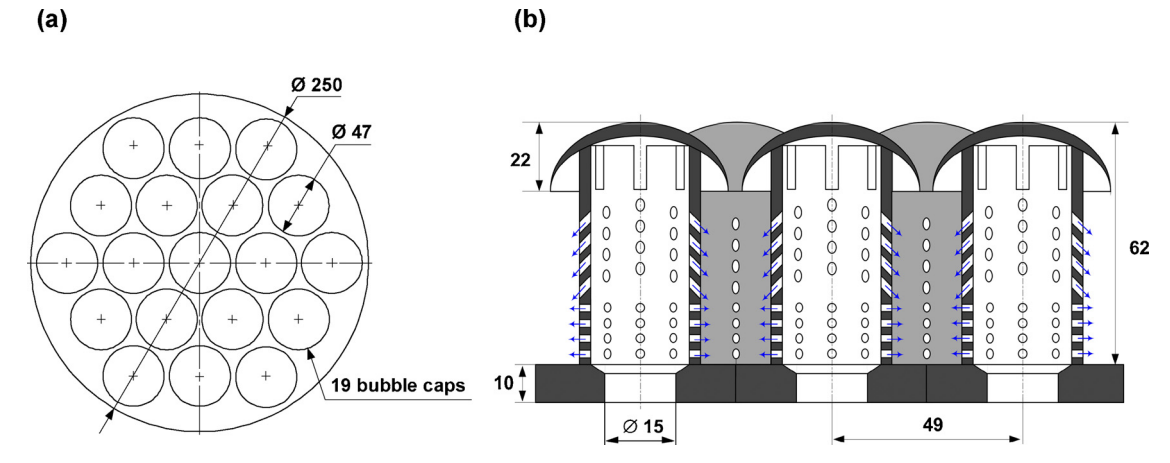


Fig. 2. Bubble-cap air distributor of an experimental rig: (a) arrangement of bubble caps on the air distributor plate, and (b) longitudinal view of stand pipes (unit: mm).

 $0.3\text{--}0.5\,\text{mm}$ , were used in this work. The mean particle size of the selected bed materials was determined with a "Mastersizer 2000" particle size analyzer to be:  $480\,\mu\text{m}$  for alumina sand,  $415\,\mu\text{m}$  for dolomite, and  $450\,\mu\text{m}$  for limestone. The solid density of these bed materials was quite different:  $3500\,\text{kg/m}^3$  for alumina,  $2900\,\text{kg/m}^3$  for dolomite, and  $2600\,\text{kg/m}^3$  for limestone. According to the particle size and density, these bed materials were categorized as Geldart-B particles [28], which are generally used for ensuring sustainable fluidization, and correspondingly, excellent mixing between gas and solids in fluidized-bed combustion systems.

Palm kernel shell (PKS) with a solid density of  $1500\,\mathrm{kg/m^3}$  was used as the tested biomass in this experimental work. Due to the irregular shape and large particle size of "as-received" PKS, the biomass was shredded and categorized into two size groups of particles: 3–6 mm and 6–9 mm by sieving. The mean particle size of a particular size group was obtained according to Refs. [12,29] to be: 4.7 mm for the 3–6 mm size group, and 7.9 mm for the 6–9 mm size group.

### 2.3. Experimental procedures

The bed material (alumina sand/dolomite/limestone) was premixed with PKS of each size group in different mass fractions (MF) of biomass in the binary mixture: 0 wt.% (when using only bed material), 2.5 wt.%, 5 wt.%, 7.5 wt.%, and 10 wt.%. Prior to the tests, the bed material (binary mixture) was placed in the conical module of the rig forming a loosely packed bed. For each MF, the tests were performed for three selected static bed heights (BHs): 20, 30, and 40 cm.

For fixed BH and MF, the pressure drop across the bed ( $\Delta p$ ) was measured versus superficial air velocity (u), to provide data for plotting the  $\Delta p-u$  diagram of the conical bed. Afterwards, the  $\Delta p-u$  diagram was used for determining major flow regimes and hydrodynamic characteristics of the bed. For fixed BH and MF, the superficial air velocity ranged from 0 m/s to up to 6 m/s, to observe different flow regimes of the bed. Note that the tests with pure bed materials were performed for both fluidization (via increasing u) and defluidization (via decreasing u) of the bed, whereas experiments with the selected binary mixtures were performed only for bed fluidization. All the tests were performed at the ambient temperature (30  $\pm$  2 °C) and pressure at the air blower inlet. The relevant properties of air used in this study were therefore assumed for a mean temperature of 30 °C: dynamic viscosity  $\mu = 1.86 \times 10^{-5}$  N·s/ m² and density  $\rho_g = 1.165$  kg/m³ [30].

### 2.4. Methods for empirical modeling $u_{mff}$ and $\Delta p_{mff}$ of a binary mixture

In this work, the model for predicting the minimum velocity of full fluidization ( $u_{\rm mff}$ ) for a cone-shaped bed with a binary mixture was

developed using statistical analysis of experimental data, as shown in some previous relevant studies [31–33].

To determine  $u_{\rm mff}$  based on analytical approach, the relationship between the Reynolds number corresponding to the minimum velocity of full fluidization (Re<sub>mff</sub>) and the Archimedes number (Ar) is required. To obtain this relationship (that can be simplified with some assumptions before its practical use), a dimensional analysis of the model, describing the behavior of umff for variable physical properties (including bed voidage and particle sphericity) and geometrical characteristics of a conical/tapered bed [23,31] should be performed. However, this approach is not feasible in the current studies dealing with binary bed mixtures of an inert bed material and biomass. Compared to this analytical approach, the statistical analysis applied in this work is based on limited input data: the density and viscosity of the fluidizing agent (air) and the density of the bed material, as well as geometrical characteristics of the cone-shaped bed, such as the cone angle  $(\alpha)$ , bed height (h), and bed diameter at the lower section  $(D_0)$ . With these variables, the relationship  $Re_{mff} = f(Ar,h,D_0,\alpha)$  can be empirically developed for the range of operating conditions, assuming  $h \approx$ BH and  $\alpha = 40^{\circ}$ , and thus, avoiding the use of the bed voidage and particle sphericity in this analysis.

Due to a significant difference in the density and particle size of the bed material and biomass (the components of a binary mixture), the effective density ( $\rho_{p,eff}$ ) and effective diameter ( $d_{p,eff}$ ) of the solid bed mixture (consisting of the inert bed material and PKS) [34,35] were used, which are determined from:

$$\frac{1}{\rho_{\text{p,eff}}} = \frac{w_{\text{BM}}}{\rho_{\text{BM}}} + \frac{w_{\text{PKS}}}{\rho_{\text{PKS}}} \tag{1}$$

$$\frac{1}{d_{\text{p,eff}}\rho_{\text{p,eff}}} = \frac{w_{\text{BM}}}{d_{\text{BM}}\rho_{\text{BM}}} + \frac{w_{\text{PKS}}}{d_{\text{PKS}}\rho_{\text{PKS}}}$$
(2)

where  $w_{\rm BM}$  and  $w_{\rm PKS}$  are the weight (mass) fractions of the bed material and PKS,  $\rho_{\rm BM}$  and  $\rho_{\rm PKS}$  are the densities of the bed material and PKS, and  $d_{\rm BM}$  and  $d_{\rm PKS}$  are the mean diameters of the bed material and PKS particles, respectively.

Taking into account the effects of  $\rho_{p,eff}$  and  $d_{p,eff}$  determined from Eqs. (1) and (2), the Reynolds number for the state of full fluidization of the bed ( $u=u_{mff}$ ), and the Archimedes number, both applicable for a conical/tapered fluidized bed, can be represented as:

$$Re_{mff} = \frac{\rho_{g} u_{mff} d_{p,eff}}{\mu}$$
(3)

$$Ar = \frac{\rho_{\rm g} d_{\rm p,eff}^3(\rho_{\rm p,eff} - \rho_{\rm g})g}{\mu^2}$$
 (4)

Using Eqs. (3) and (4), a formula for quantifying  $u_{\rm mff}$  of the bed is expressed as:

$$u_{\rm mff} = a_1 \left(\frac{\mu}{\rho_{\rm g} d_{\rm p,eff}}\right) A r^{b_1} \left(\frac{h}{D_{\rm o}}\right)^{c_1}$$
(5)

In this work, a relationship for predicting  $\Delta p_{\rm mff}$  was developed based on the dimensional analysis of Ergun's equation, modified for conical/tapered beds [31,32], by taking into account the apparent effects of  $u_{\rm mff}$  and the bed geometry. In a general form, this relationship is:

$$\Delta p_{\rm mff} = a_2 (u_{\rm mff})^{b_2} \left(\frac{h}{D_0}\right)^{c_2}$$
 (6)

In Eqs. (5) and (6), the coefficients and exponents  $(a_1, b_1, c_1, a_2, b_2,$  and  $c_2)$  were determined by using a multiple linear regression analysis of experimental data.

### 3. Results and discussion

#### 3.1. Flow regimes of a cone-shaped fluidized bed

Fig. 3 shows a typical  $\Delta p$ –u diagram of a cone-shaped bed using a pure bed material (alumina sand, dolomite, and limestone) with a single range, 0.3–0.5 mm, of particle sizes for two experimental procedures: fluidization (solid symbols) and defluidization (open symbols), with ambient air being the fluidizing agent. As seen in Fig. 3, with increasing superficial air velocity (u) within the selected range, the (total) pressure drop across the bed and air distributor ( $\Delta p$ ) varies following the path  $O \rightarrow A \rightarrow B \rightarrow C$  and further. Four sequent flow regimes of the bed were observed during the test run for bed fluidization: (I) fixed bed, (II) partially fluidized bed, (III) fully fluidized bed, and (IV) turbulent fluidized bed, as indicated in Fig. 3. These flow regimes have much in common with those found for cone-shaped and tapered beds using various bed materials and fluidizing agents [23,24,32].

To facilitate an understanding of the flow regimes and behaviors of the cone-shape fluidized beds, Fig. 4 illustrates the gas–solid bed (observed in this cone-shaped test rig at different levels of u), exhibiting four hydrodynamics regimes corresponding to the regimes (regions) in Fig. 3

The following is a summary of the flow regimes, occurring in this cone-shaped bed using the selected bed materials fluidized by air:

I: Fixed-bed regime (O  $\rightarrow$  A). Within the fixed-bed region, the  $\Delta p$ -u profile in Fig. 3 shows a quasi-linear relationship. With increasing u within this region,  $\Delta p$  linearly increases until it reached the maximum value ( $\Delta p_{\rm max}$ ). Due to a relatively low rate of airflow in the fixed-bed regime, the bed particles do not move, and the gas–solid bed is characterized by fixed (static) bed height and uniform bed voidage (see Fig. 4a).

II: Partially fluidized-bed regime (A  $\rightarrow$  B). This transition regime is, in effect, an apparent feature of cone-shaped and tapered beds [23,31]. From Fig. 3, when increasing u beyond critical point A,  $\Delta p$  abruptly decreases from  $\Delta p_{\rm max}$  to the pressure drop at the minimum velocity of full fluidization ( $\Delta p_{\rm mff}$ ). At Point A, the lowest layer of the conical bed begins to fluidize, resulting in an axial change in bed voidage, whereas the top layer of the bed is still static (see Fig. 4b). The corresponding superficial air velocity, starting the partially fluidized-bed regime, is termed the minimum velocity of partial fluidization ( $u_{\rm mpf}$ ) [23].

III: Fully fluidized-bed regime (B  $\rightarrow$  C). This regime begins at Point B where the bed exhibits the full fluidization. At this point, the entire bed is involved in the fluidization, showing a random appearance of small-size bubbles at the top surface of the bed. The corresponding superficial air velocity, starting this regime, is termed the minimum velocity of full fluidization ( $u_{\rm mff}$ ) [23]. With a further increase of u in this regime, but less than that of Point C, the frequency of appearance and size of the bubbles released from the fluidized bed increases, resulting in an expansion of the bed (i.e., increased bed height), as illustrated in Fig. 4c.

However, as revealed by data in Fig. 3,  $\Delta p$  within this flow regime stays nearly constant,  $\Delta p \approx \Delta p_{\rm mff}$ , similar to those reported elsewhere [26,31,32].

IV: Turbulent fluidized-bed regime. With increasing superficial air velocity beyond Point C (see Fig. 3), the bed behavior changes from the fully fluidized-bed regime (ending at Point C) to the turbulent fluidization regime. The corresponding superficial air velocity starting this regime is termed the minimum velocity of turbulent fluidization  $(u_k)$ , as proposed in Ref. [23]. During this regime, the movement of the bed particles became more violent and vigorous, and no bubbles are observed in the bed (see Fig. 4d). Instead of bubbles, one can see a turbulent motion of solid splashes and voids of gas of various sizes and shapes. Moreover, the turbulent fluidized bed exhibits a substantial expansion, occupying the (almost) entire volume of the cone-shaped section of the test rig. From the analysis of the  $\Delta p$ -u diagram in Fig. 3,  $\Delta p$  in this regime increases with higher u, which is mainly due to the effects of the pressure drop across the air distributor (as discussed below).

Note that the bed defluidization (via decreasing u) causes a gradual change in the bed behavior, from the turbulent fluidization regime (at Point C\*) to its entire defluidization at Point A\*, where the superficial air velocity decreases to the maximum velocity of full defluidization ( $u_{\rm mfd}$ ). During this process, the bed unavoidably passes Point B\* (where the upper layer of the bed is defluidized at the maximum velocity of partial defluidization,  $u_{\rm mpd}$ ), exhibiting the path  $C^* \to B^* \to A^* \to O$ . Thus, during the fluidization-defluidization procedures, the coneshaped bed of the selected bed materials shows a hysteresis in the  $\Delta p$ -u diagram.

However, the  $\Delta p-u$  diagram of the bed defluidization provides no useful information that can be used for optimal design and operation of the combustor, since at  $u_{\rm mfd} < u < u_{\rm mpd}$ , the upper region of the bed is not fluidized. For this reason, it was decided to study and analyze the  $\Delta p-u$  diagrams only from the fluidization tests.

# 3.2. Hydrodynamic characteristics of a cone-shaped bed using pure bed materials

Fig. 5 shows the  $\Delta p-u$  diagrams of the cone-shaped bed using alumina sand, dolomite, and limestone (solid dots) as the bed material with the selected particle sizes, as well as the contribution of the pressure drop across the air distributor (open dots) to  $\Delta p$ , for variable u at different static bed heights (BHs). As seen in Fig. 5, at a given bed material and BH, the conical bed exhibits similar trends in the behavior of  $\Delta p$  and similar flow regimes (indicated in Fig. 3), as described previously.

The  $\Delta p$ -u diagrams reveal that an increase of BH results in higher

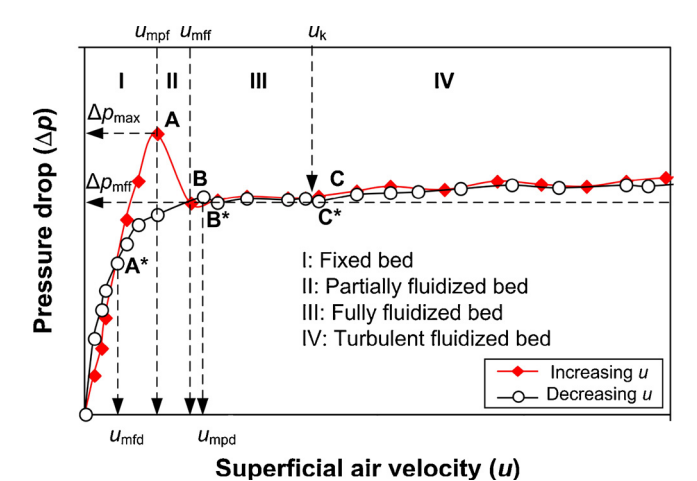


Fig. 3. Typical  $\Delta p$ —u diagram of a cone-shaped bed, using alumina sand/dolomite/limestone as the bed material for fluidization/defluidization procedures.

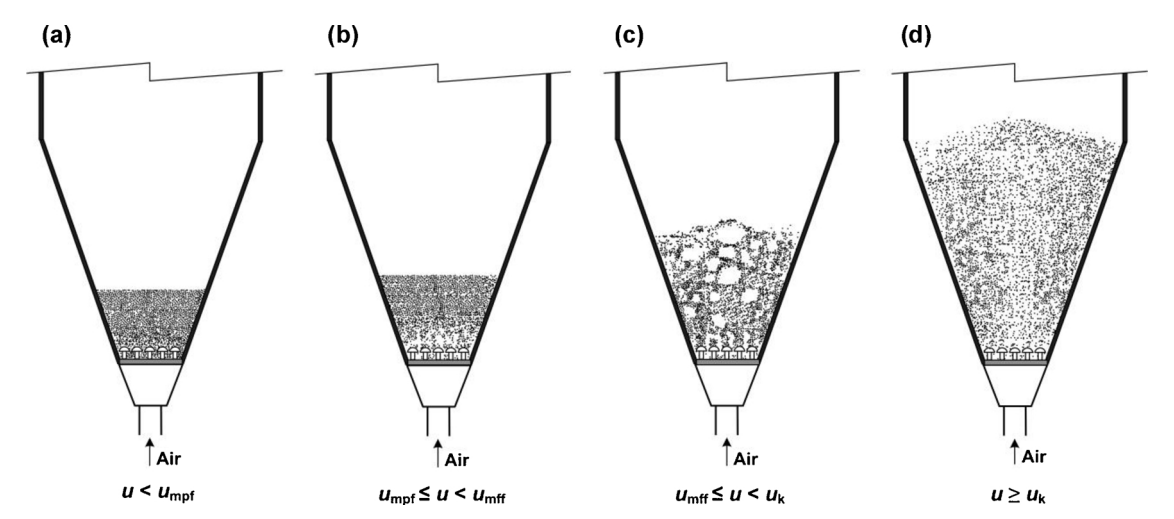


Fig. 4. Appearance of the cone-shaped bed in different flow regimes: (a) fixed (stationary) bed, (b) partially fluidized bed, (c) fully fluidized bed, and (d) turbulent fluidized bed.

 $u_{\rm mpf}$  and  $\Delta p_{\rm max}$  (at the end of the fixed-bed region) of all the beds, mainly due to the increase in the bed weight. This effect is quite typical for conical gas–solid beds [24,31,32]. However, at a given BH,  $u_{\rm mpf}$  and  $\Delta p_{\rm max}$  of the alumina sand bed are somewhat greater than those of the other two bed materials. This fact can be attributed to the higher density of alumina sand, compared to those of dolomite and limestone.

With increasing u from  $u_{\rm mpf}$  to  $u_{\rm mff}$  during the partially fluidized-bed regime,  $\Delta p$  abruptly decreases by 20–30% (depending on the bed material and static bed height), which results in the appearance of a sharp peak at  $u=u_{\rm mpf}$  on each  $\Delta p$ –u diagram in Fig. 5. Similar findings have been reported elsewhere [26,32]. Like with  $u_{\rm mpf}$  and  $\Delta p_{\rm max}$ , an increase

of BH leads to higher  $u_{\rm mff}$  and  $\Delta p_{\rm mff}$  (at the end of the partially fluidized-bed regime) of all the tested beds, mainly because of the greater bed weight. Moreover, the  $u_{\rm mff}$  and  $\Delta p_{\rm mff}$  of a bed with alumina sand are somewhat greater than those of a bed using dolomite and limestone as the bed material, at identical BHs. It can be seen in Fig. 5 that at the identical BH = 30 cm,  $u_{\rm mff}$  for the alumina sand bed is 0.84 m/s (at  $\Delta p_{\rm mff} = 4.5$  kPa), whereas it is 0.72 m/s (at  $\Delta p_{\rm mff} = 4.0$  kPa) for the dolomite bed, and 0.65 m/s (at  $\Delta p_{\rm mff} = 3.8$  kPa) for the bed with limestone. This is mainly attributed to the above-mentioned difference in the density of the selected bed materials.

With increasing u within the fully fluidized-bed and turbulent

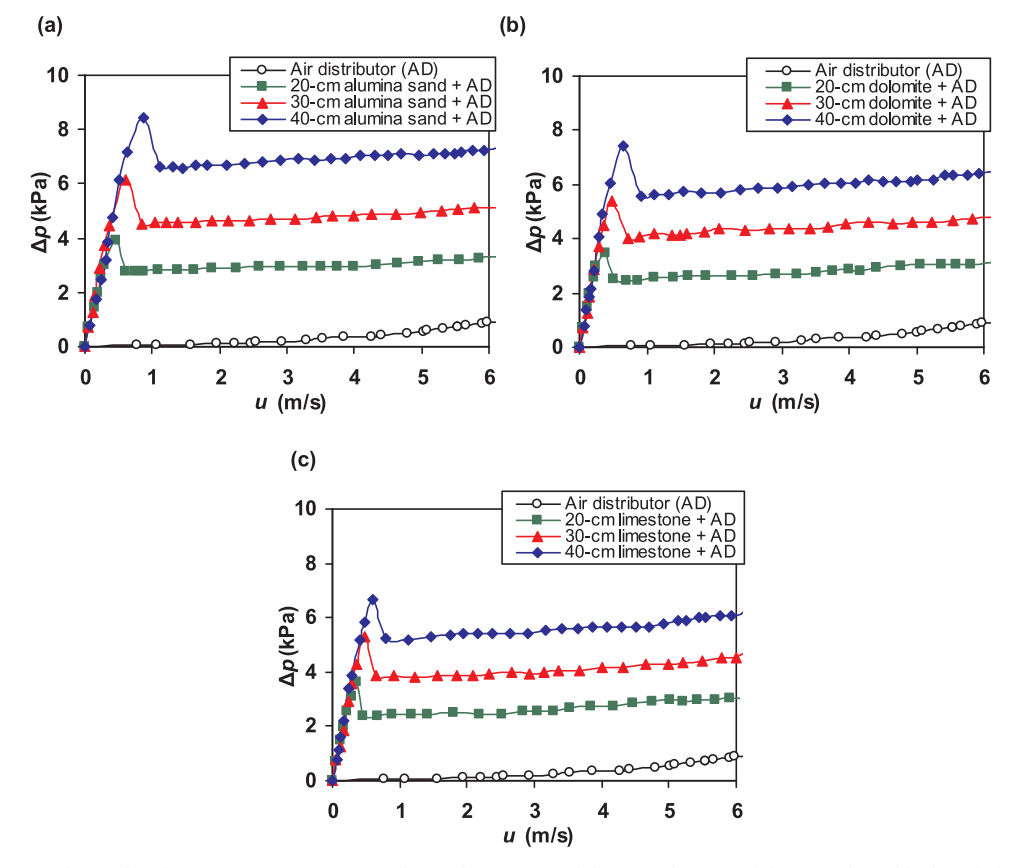


Fig. 5. Pressure drop across the air distributor (AD) versus superficial air velocity (u), and the  $\Delta p$ –u diagram of the cone-shaped bed (including effects of AD), using pure bed materials: (a) alumina sand, (b) dolomite, and (c) limestone, for different static bed heights (20 cm, 30 cm, and 40 cm).

fluidized-bed regimes,  $\Delta p$  increases at nearly the same rate for all the bed materials and BHs. This can be explained by the effects of the pressure drop across the air distributor. However, the contribution of the pressure drop across the air distributor to the total  $\Delta p$  is small, about 1 kPa at u=6 m/s (see Fig. 5).

As found in this work, the bed flow regime shifts from the fully fluidized-bed regime to the turbulent one at the  $u_{\rm k}$  values of 1.5–3.0 m/s (depending on the bed material and BH).

# 3.3. Hydrodynamic characteristics of a cone-shaped bed using a sand-biomass binary mixture

### 3.3.1. Effects of biomass proportion in a binary mixture

As an illustration, Fig. 6 compares the  $\Delta p$ –u diagrams of the coneshaped bed of alumina sand, dolomite, and limestone mixed with the PKS of 3–6 mm particle sizes, between the minimum (2.5 wt.%) and maximum (10 wt.%) mass fractions of biomass in the binary mixture, for the three specified BHs (20 cm, 30 cm, and 40 cm). Like in Fig. 5,  $\Delta p$  in Fig. 6 includes the combined effects of the pressure drop across the fixed/fluidized bed and that across the air distributor (AD), leading to a

slight increase of  $\Delta p$  at  $u>u_{\rm mff}$ . As seen in Fig. 6, all the  $\Delta p$ –u diagrams of the bed with the binary mixtures show similar hydrodynamic regimes and characteristics, as those exhibited by the pure bed materials at specified BHs, however, with minor effects from the PKS mass fraction in the binary mixture.

From the  $\Delta p$ -u diagrams in Fig. 6, with an increasing proportion of PKS in the mixture (i.e., with a greater content of biomass in the binary mixture), both the  $u_{\rm mpf}$  and the  $u_{\rm mff}$  show an increase at a fixed BH. For instance, as the percentage of PKS in the mixture increases from 2.5 wt. % to 10 wt.% at BH = 30 cm, the  $u_{\rm mff}$  of the alumina sand–PKS mixture increases from 0.9 m/s to 1.2 m/s, whereas that of the dolomite–PKS mixture increases from 0.8 m/s to 1.1 m/s, and from 0.6 m/s to 1.0 m/s for the limestone–PKS bed. This result can be explained by the presence of biomass particles in the bed, which leads to a noticeable increase in the bed voidage. On the contrary, the  $\Delta p_{\rm max}$  and the  $\Delta p_{\rm mff}$  show a slight decrease with an increase in the percentage of PKS in the binary mixture, which can be explained by the decreased total weight of the bed. All these experimental results were in agreement with those found in columnar (cylindrical and prismatic) beds [36,37].

In addition, with a higher percentage of biomass in the mixture, the

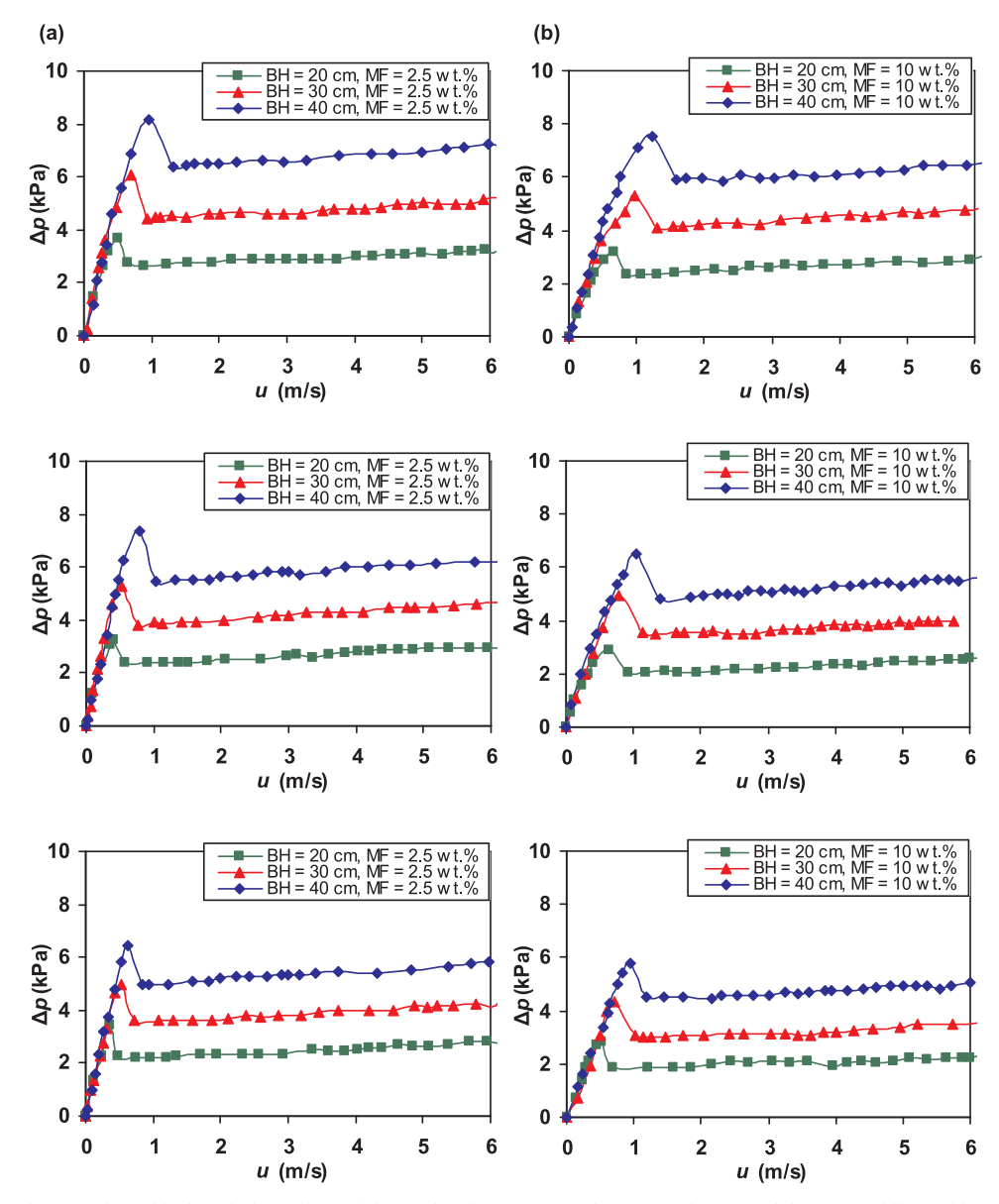


**Fig. 6.** Δ*p*–*u* diagram of the cone-shaped bed (including effects of the air distributor), using alumina sand (*upper*), dolomite (*middle*), and limestone (*lower*) as the bed material, mixed with palm kernel shell of 3–6 mm particle sizes and mass fraction (MF) of (a) 2.5 wt.% and (b) 10 wt.%, for different static bed heights (BHs).

difference between the  $u_{\rm mff}$  and the  $u_{\rm mpf}$  becomes greater at any fixed BH, as seen in Fig. 6. Nevertheless, like in the tests with the pure bed materials, the transition of the bed behavior from the stationary mode to the fully fluidized-bed regime exhibits itself by stepwise (rapid) changes in both superficial air velocity (from  $u_{\rm mpf}$  to  $u_{\rm mff}$ ) and total pressure drop (from  $\Delta p_{\rm max}$  to  $\Delta p_{\rm mff}$ ).

#### 3.3.2. Effects of biomass particle size

Fig. 7 shows the  $\Delta p-u$  diagrams of the bed of alumina sand mixed with PKS of two size groups: 3–6 mm and 6–9 mm, for the same ranges of BH and MF of the biomass in a binary mixture, as in Fig. 6. Compared with tests for MF = 2.5 wt.% (see Fig. 7a), the  $\Delta p-u$  diagrams of the binary mixture for the two particle size groups are quite similar, indicating the minor effects from the biomass particle size on the major hydrodynamic characteristics of the bed. However, the particle size of PKS has more noticeable effects on the hydrodynamic characteristics of the bed at the increased MF (10 wt.%), as seen in Fig. 7b. With coarser biomass particles, the  $u_{\rm mpf}$  and the  $u_{\rm mff}$  exhibit an insignificant increase (at a fixed BH), likely in response to an increase in the "effective" density and diameter of solid particles in the binary mixture, as follows from the analysis using Eqs. (1) and (2).

As can be compared between Fig. 7a and b, the pressure drops  $\Delta p_{\rm max}$  and  $\Delta p_{\rm mff}$  for the beds with a greater proportion of PKS in the binary mixture are somewhat lower than those with the lowest biomass content in the mixture at identical BHs, because of the reduced bed weight.

#### 3.4. Empirical models for predicting $u_{mff}$ and $\Delta p_{mff}$

Through the statistical data analysis (see Section 2.4), the empirical constants/exponents  $a_1$ ,  $b_1$ , and  $c_1$  from Eq. (5) were quantified for the cone-shaped bed (of the  $40^\circ$  cone angle) using a binary mixture of alumina sand/dolomite/limestone and biomass for the ranges of operating conditions (static bed height, biomass fraction in the binary mixture, and the "effective" solid particle size of the bed). By taking into account the numerical values of  $a_1$ ,  $b_1$ , and  $c_1$ , the  $u_{\rm mff}$  can be predicted for the selected options of the bed material as:

• for a binary mixture of alumina sand and biomass ( $R^2 = 0.96$ )

$$u_{\rm mff} = \frac{1.06 \times 10^{-3} \mu}{\rho_{\rm g} d_{\rm p,eff}} A r^{1.11} \left(\frac{h}{D_{\rm o}}\right)^{0.85}$$
 (7)

• for a binary mixture of dolomite and biomass ( $R^2 = 0.96$ )

$$u_{\rm mff} = \frac{2.58 \times 10^{-5} \mu}{\rho_{\rm g} d_{\rm p,eff}} \text{Ar}^{1.55} \left(\frac{h}{D_{\rm o}}\right)^{0.69}$$
(8)

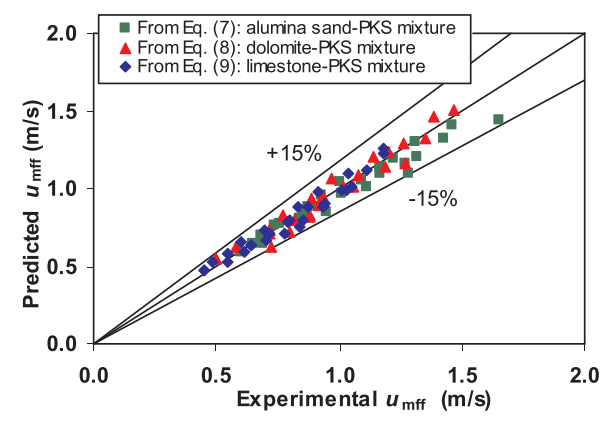


Fig. 8. Comparison between the predicted and experimental values of  $u_{\rm mff}$  for cone-shaped beds using alumina sand, dolomite, and limestone, mixed with palm kernel shell (PKS).

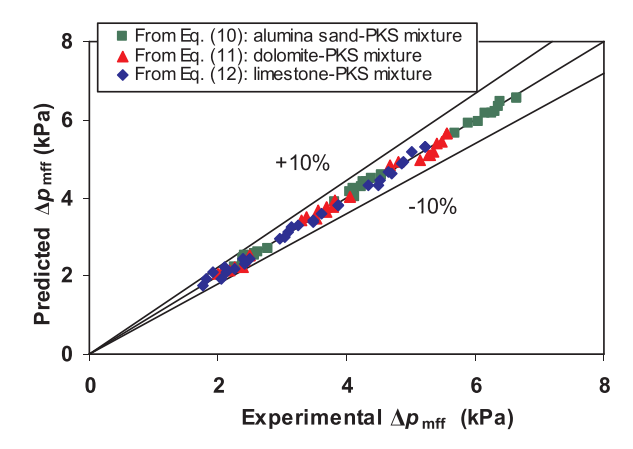
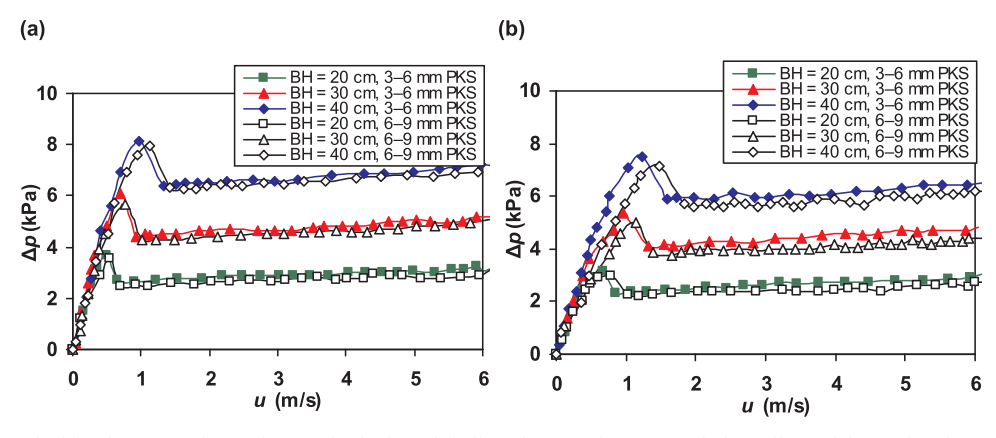


Fig. 9. Comparison between the predicted and experimental values of  $\Delta p_{\rm mff}$  (including effects of the air distributor) for cone-shaped beds using alumina sand, dolomite, and limestone, mixed with palm kernel shell (PKS).

• for a binary mixture of limestone and biomass ( $R^2 = 0.97$ )

$$u_{\text{mff}} = \frac{3.69 \times 10^{-5} \mu}{\rho_{\text{g}} d_{\text{p,eff}}} \text{Ar}^{1.52} \left(\frac{h}{D_{\text{o}}}\right)^{0.75}$$
(9)

The developed empirical models represented by Eqs. (7)–(9) provide an accurate fit, at a high value of  $\mathbb{R}^2$ , for all tests. To validate the models, the predicted and experimental values of  $u_{\rm mff}$  were compared,



**Fig. 7.** Effects of the static bed height (BH) and particle size of palm kernel shell on the  $\Delta p$ –u diagram (including effects of the air distributor) of alumina sand mixed with the biomass of different proportions: (a) 2.5 wt.% and (b) 10 wt.%.

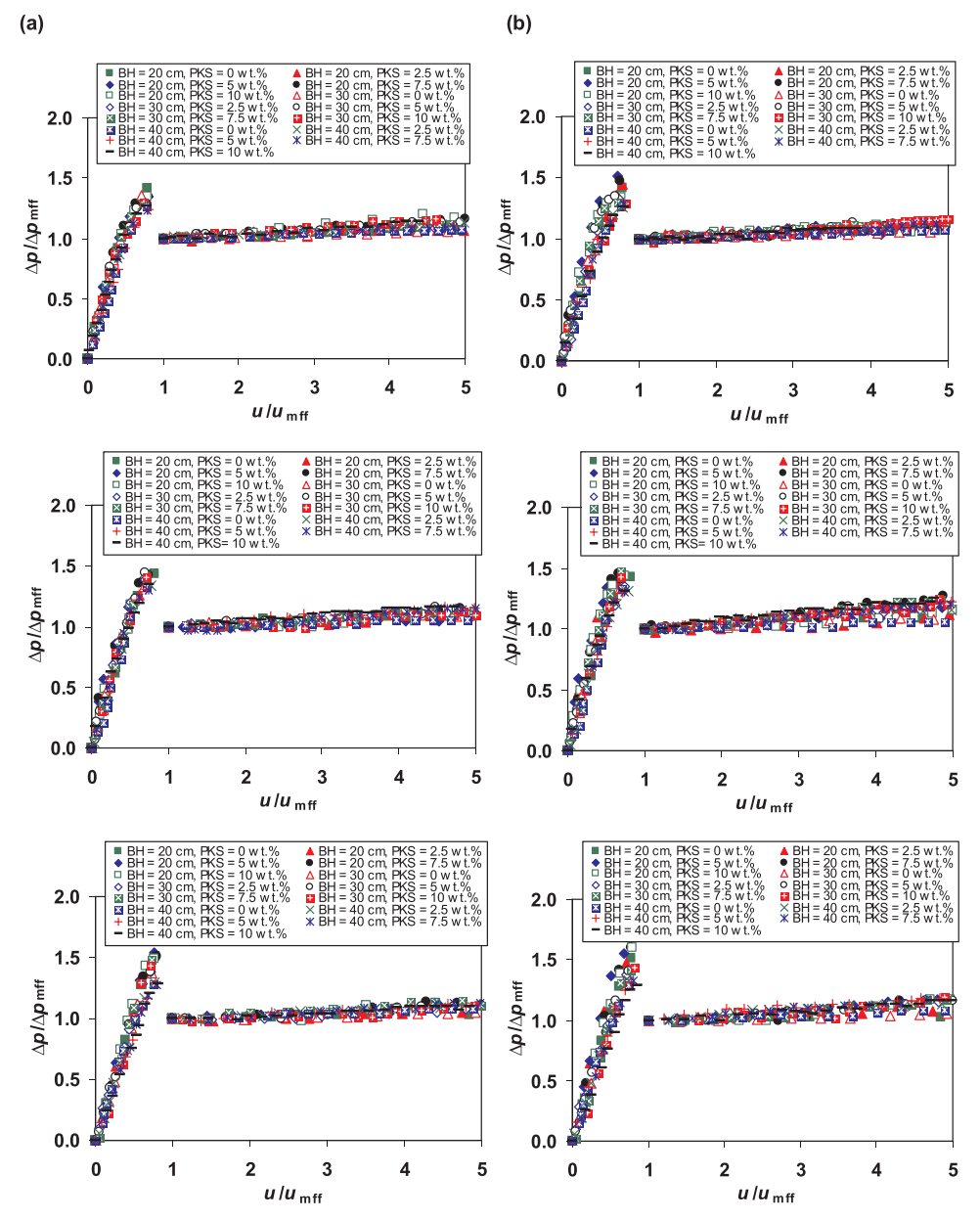


Fig. 10. Relative pressure drop (including effects of AD) versus relative superficial air velocity of the cone-shaped bed, using alumina sand (*upper*), dolomite (*middle*), and limestone (*lower*) mixed with palm kernel shell (PKS) of (a) 3–6 mm and (b) 6–9 mm particle sizes, in various proportions at different static bed heights (BHs).

as presented in Fig. 8. It can be seen in Fig. 8 that the values of  $u_{\rm mff}$  predicted by the models are in a good agreement with the experimental ones, which stay within a  $\pm$  15% error band with respect to the corresponding average of  $u_{\rm mff}$ .

With empirical constants/exponents  $a_2$ ,  $b_2$ , and  $c_2$  from Eq. (6) determined via experimental data treatment, the  $\Delta p_{\rm mff}$  can be predicted for the selected options of the bed material as:

• for a binary mixture of alumina sand and biomass ( $R^2 = 0.98$ )

$$\Delta p_{\rm mff} = 3.17 u_{\rm mff}^{-0.39} \left(\frac{h}{D_0}\right)^{1.64} \tag{10}$$

• for a binary mixture of dolomite and biomass ( $R^2 = 0.98$ )

$$\Delta p_{\rm mff} = 2.77 u_{\rm mff}^{-0.33} \left(\frac{h}{D_{\rm o}}\right)^{1.45} \tag{11}$$

• for a binary mixture of limestone and biomass ( $R^2 = 0.99$ )

$$\Delta p_{\rm mff} = 2.28 u_{\rm mff}^{-0.51} \left(\frac{h}{D_0}\right)^{1.54}$$
 (12)

Fig. 9 depicts the  $\Delta p_{\rm mff}$  predicted by the models and that from the tests with the selected bed materials and operating conditions. As revealed by the data in Fig. 9, most of the predicted  $\Delta p_{\rm mff}$  are close to the experimental values, with the deviation within  $\pm$  10% for all the tests.

#### 3.5. Modeling relative hydrodynamic characteristics

Fig. 10 depicts the dependencies of the relative pressure drop across the sand-biomass bed and air distributor ( $\Delta p/\Delta p_{\rm mff}$ ) on the relative superficial air velocity ( $u/u_{\rm mff}$ ) for the experimental tests with the selected bed materials, mixed with biomass in different proportions, for the two size groups and different BHs. As seen in Fig. 10, the

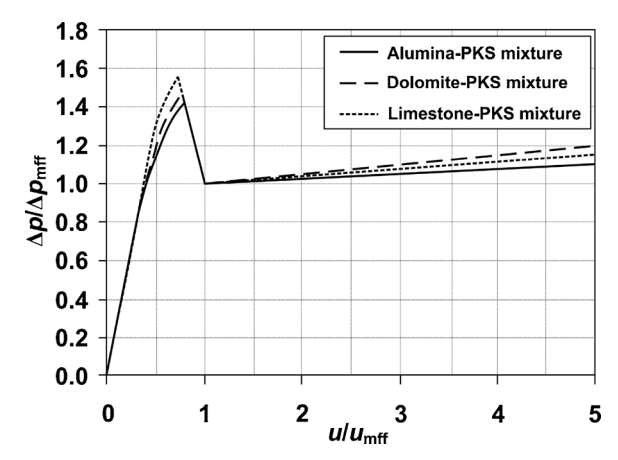


**Fig. 11.** Nomograph for determining the pressure drop across the cone-shaped bed (including effects of the air distributor), using various mixtures of alumina sand/dolomite/limestone with biomass (PKS).

relationships  $\Delta p/\Delta p_{\rm mff} = f(u/u_{\rm mff})$  are almost independent of the operating conditions, showing, however, a weak effect from the bed material and similarity (in shape) between the test runs.

In all the tests, within the fixed-bed region characterized by a significant increase in the pressure drop,  $\Delta p/\Delta p_{\rm mff}$  of the binary mixtures exhibit a quasi-linear dependence on  $u/u_{\rm mff}$  for the two groups of biomass particle sizes, as can be compared between Fig. 10a and b. Note that a peak of  $\Delta p/\Delta p_{\rm mff}$  (occurring at  $u=u_{\rm mpf}$ ) is slightly affected by the bed material type, showing, however, its independence of the operating parameters. Within the fully and turbulent fluidized-bed regimes,  $\Delta p/\Delta p_{\rm mff}$  of the binary mixtures shows an insignificant (positive) gradient,  $d(\Delta p/\Delta p_{\rm mff})/d(u/u_{\rm mff})$ , which is slightly dependent on the bed material type. This gradient is mainly due to the above-mentioned contribution of the air distributor to the total pressure drop across the bed—distributor system ( $\Delta p$ ).

Based on the relative hydrodynamic characteristics, a nomograph showing the dependence of  $\Delta p/\Delta p_{\rm mff}$  on  $u/u_{\rm mff}$  for different flow regimes was developed, as depicted in Fig. 11, for its practical use. Based on the nomograph, one can predict the pressure drop across the bed and air distributor ( $\Delta p$ ) for any arbitrary superficial air velocity (u), using the  $u_{\rm mff}$  and  $\Delta p_{\rm mff}$  estimated from Eqs. (7)–(12) (depending on the bed material type).

From Fig. 11, the contribution of the air distributor to the total pressure drop ( $\Delta p$ ) increased with higher relative superficial velocity, however to different extent for the selected bed materials. For instance, at  $u/u_{\rm mff}=5$ , the relative pressure drop across the air distributor is about 10% when using alumina sand as the bed material, but near 20% with dolomite.

#### 4. Conclusions

Flow regimes and hydrodynamic characteristics of a cone-shaped fluidized bed with a binary mixture, containing an inert bed material (alumina sand/dolomite/limestone) mixed with biomass (palm kernel shell), have been experimentally studied for variable operating parameters (static bed height, proportion of biomass in the binary mixture, and biomass particle size). With the selected cone angle of the bed (40°) and particle sizes of the bed material, the spouting bed regime can be avoided for the ranges of operating parameters. When varying the superficial air velocity (u) from 0 to 6 m/s at the specified operating conditions, four sequent flow regimes: (1) fixed bed, (2) partially fluidized bed, (3) fully fluidized bed, and (4) turbulent fluidized bed, are observed in the conical bed. Static bed height and proportion of biomass in the binary mixture have important effects on the major hydrodynamic characteristics of the bed with a binary mixture: minimum velocity of partial fluidization ( $u_{\rm mpf}$ ), minimum velocity of full

fluidization  $(u_{\rm mff})$  and corresponding pressure drops across the bed and air distributor  $(\Delta p_{\rm max}$  and  $\Delta p_{\rm mff})$ , and entire  $\Delta p_{-}u$  diagram of the bed. The biomass particle size has weak effects on the major hydrodynamic characteristics.

Empirical models for determining  $u_{\rm mff}$  and  $\Delta p_{\rm mff}$  of a cone-shaped fluidized bed with the selected bed materials mixed with biomass have been developed in this work. The  $u_{\rm mff}$  and  $\Delta p_{\rm mff}$  predicted by the proposed models show good agreement with those obtained experimentally for similar operating parameters. A nomograph representing the dependence  $\Delta p/\Delta p_{\rm mff} = f(u/u_{\rm mff})$  has been developed and proposed for the practical use to assess the total pressure drop across the bed of 40° cone angle (with a binary mixture) and air distributor ( $\Delta p$ ) for any arbitrary superficial air velocity (u) at the desired (specified) operating parameters of a fluidized-bed combustor.

#### Acknowledgment

The authors wish to acknowledge the financial support from the Thailand Research Fund and Thammasat University (Contract No. BRG 5980005).

#### References

- M.E.E. Abashar, Dimethyl ether synthesis in a multi-stage fluidized bed reactor, Chem. Eng. Process. 122 (2017) 172–180.
- [2] I. Petersen, J. Werther, Experimental investigation and modeling of gasification of sewage sludge in the circulating fluidized bed, Chem. Eng. Process. 44 (2005) 717–736.
- [3] J. De Wilde, Gas-solid fluidized beds in vortex chambers, Chem. Eng. Process. 85 (2014) 256–290.
- [4] F.J. dos Santos, L. Goldstein, Experimental aspects of biomass fuels in a bubbling fluidized bed combustor, Chem. Eng. Process. 47 (2008) 1541–1549.
- [5] J. Werther, M. Saenger, E.-U. Hartge, T. Ogada, Z. Siagi, Combustion of agricultural residues, Prog. Energy Combust. 26 (2000) 1–27.
- [6] C.-S. Chyang, F.-P. Qian, Y.-C. Lin, S.-H. Yang, NO and N<sub>2</sub>O Emission characteristics from a pilot scale vortexing fluidized bed combustor firing different fuels, Energy Fuels 22 (2008) 1004–1011.
- [7] C.-S. Chyang, F. Duan, S.-M. Lin, J. Tso, A study on fluidized bed combustion characteristics of corncob in three different combustion modes, Bioresour. Technol. 116 (2012) 184–189.
- [8] P. Ninduangdee, V.I. Kuprianov, Fluidized bed co-combustion of rice husk pellets and moisturized rice husk: the effects of co-combustion methods on gaseous emissions, Biomass Bioenergy 112 (2018) 73–84.
- [9] R. Kaewklum, V.I. Kuprianov, Theoretical and experimental study on hydrodynamic characteristics of fluidization in air–sand conical beds, Chem. Eng. Sci. 63 (2008) 1471–1479.
- [10] K. Shahzad, M. Saleem, M. Kazmi, Z. Ali, S. Hussain, N.A. Akhtar, Effect of hydrodynamic conditions on emissions of NO<sub>8</sub>, SO<sub>2</sub>, and CO from co-combustion of wheat straw and coal under fast fluidized bed condition, Combust. Sci. and Technol. 188 (2016) 1303–1318.
- [11] H.M. Abdelmotalib, M.A. Youssef, A.A. Hassan, S.B. Youn, I.-T. Im, Numerical study on the wall to bed heat transfer in a conical fluidized bed combustor, Int. J. Precis. Eng. Manuf. 16 (2015) 1551–1559.
- [12] D. Kunii, O. Levenspiel, Fluidization Engineering, 2nd ed., Wiley, Massachusetts, 1991.
- [13] J.R. Grace, Contacting modes and behaviour classification of gas-solid and other two-phase suspensions, Can. J. Chem. Eng. 64 (1986) 353–363.
- [14] P. Chaivatamaset, P. Sricharoon, S. Tia, B. Bilitewski, The characteristics of bed agglomeration/defluidization in fluidized bed firing palm fruit bunch and rice straw, Appl. Therm. Eng. 70 (2014) 737–747.
- [15] E. Brus, M. Öhman, A. Nordin, Mechanisms of bed agglomeration during fluidized-bed combustion of biomass fuels, Energy Fuels 19 (2005) 825–832.
- [16] M. Bartels, W. Lin, J. Nijenhuis, F. Kapteijn, J.R. van Ommen, Agglomeration in fluidized beds at high temperatures: mechanisms, detection and prevention, Prog. Energy Combust. 34 (2008) 633–666.
- [17] P. Ninduangdee, V.I. Kuprianov, A study on combustion of oil palm empty fruit bunch in a fluidized bed using alternative bed materials: performance, emissions, and time-domain changes in the bed condition, Appl. Energy 176 (2016) 34–48.
- [18] P. Ninduangdee, V.I. Kuprianov, Combustion of an oil palm residue with elevated potassium content in a fluidized-bed combustor using alternative bed materials for preventing bed agglomeration, Bioresour. Technol. 182 (2015) 272–281.
- [19] P. Ninduangdee, V.I. Kuprianov, Study on burning oil palm kernel shell in a conical fluidized-bed combustor using alumina as the bed material, J. Taiwan Inst. Chem. Eng. 44 (2013) 1045–1053.
- [20] M. Kwauk, Fluidization: Idealized and Bubbleless, with Applications, Science and Press, New York, 1992.
- [21] J. Li, B. Yang, G. Cheng, Affinity adsorption and hydrodynamic behavior in a tapered-bed of upward flow, Biochem. Eng J. 15 (2003) 185–192.
- [22] Y.F. Shi, Y.S. Yu, L.T. Fan, Incipient fluidization condition for a tapered fluidized

- bed, Ind. Eng. Chem. Fundam. 23 (1984) 484-489.
- [23] Y. Peng, L.T. Fan, Hydrodynamic characteristics of fluidization in liquid-solid tapered beds, Chem. Eng. Sci. 52 (1997) 2277–2290.
- [24] P. Arromdee, V.I. Kuprianov, Combustion of peanut shells in a cone-shaped bubbling fluidized-bed combustor using alumina as the bed material, Appl. Energy 97 (2012) 470–482.
- [25] L. Gan, X. Lu, Q. Wang, Experimental and theoretical study on hydrodynamic characteristics of tapered fluidized beds, Adv. Powder Technol. 25 (2014) 824–831.
- [26] M. Rasteh, F. Farhadi, A. Bahramian, Hydrodynamic characteristics of gas-solid tapered fluidized beds: experimental studies and empirical models, Powder Technol. 283 (2015) 355–367.
- [27] P. Basu, Combustion and Gasification in Fluidized Beds, CRC Press, Taylor and Francis Group, London, 2006.
- [28] D. Geldart, Types of gas fluidization, Powder Technol. 7 (1973) 285-292.
- [29] M.Z. Abdullah, Z. Husain, S.L. Yin Pong, Analysis of cold flow fluidization test results for various biomass fuels, Biomass Bioenergy 24 (2003) 487–494.
- [30] B.R. Munson, T.H. Okiishi, W.W. Huebsch, A.P. Rothmayer, Fundamentals of Fluid Mechanics, 7th ed., John Wiley & Sons, Inc., New Jersey, 2013.
- [31] S. Jing, Q. Hu, J. Wang, Y. Jin, Fluidization of coarse particles in gas-solid conical

- beds, Chem. Eng. Process. 39 (2000) 379-387.
- [32] R. Kaewklum, V.I. Kuprianov, P.L. Douglas, Hydrodynamics of air–sand flow in a conical swirling fluidized bed: a comparative study between tangential and axial air entries, Energy Convers. Manage. 50 (2009) 2999–3006.
- [33] M. Olazar, M.J. San Jose, A.T. Aguayo, J.M. Arandes, J. Bilbao, Stable operation conditions for gas-solid contact regimes in conical spouted beds, Ind. Eng. Chem. Res. 31 (1992) 1784–1792.
- [34] D.C. Sau, S. Mohanty, K.C. Biswal, Prediction of critical fluidization velocity and maximum bed pressure drop for binary mixture of regular particles in gas-solid tapered fluidized beds, Chem. Eng. Process. 47 (2008) 2114–2120.
- [35] W. Du, L. Zhang, B. Zhang, S. Bao, J. Xu, W. Wei, X. Bao, Flow regime transition and hydrodynamics of spouted beds with binary mixtures, Powder Technol. 281 (2015) 138–150.
- [36] T.R. Rao, J.V. Ram Bheemarasetti, Minimum fluidization velocities of mixtures of biomass and sands, Energy 26 (2001) 633–644.
- [37] Y. Zhang, B. Jin, W. Zhong, Experimental investigation on mixing and segregation behavior of biomass particle in fluidized bed, Chem. Eng. Process. 48 (2009) 745–754

FISEVIER

Contents lists available at ScienceDirect

### **Applied Thermal Engineering**

journal homepage: www.elsevier.com/locate/apthermeng



#### Research Paper

# Co-firing of oil palm residues in a fuel staged fluidized-bed combustor using mixtures of alumina and silica sand as the bed material



Vladimir I. Kuprianov<sup>a,\*</sup>, Pichet Ninduangdee<sup>b</sup>, Priatna Suheri<sup>a</sup>

- <sup>a</sup> School of Manufacturing Systems and Mechanical Engineering, Sirindhorn International Institute of Technology, Thammasat University, P.O. Box 22, Thammasat Rangsit Post Office, Pathum Thani 12121, Thailand
- b Division of Mechanical Engineering, Faculty of Engineering and Industrial Technology, Phetchaburi Rajabhat University, Phetchaburi 76000, Thailand

#### HIGHLIGHTS

- Two oil palm residues are co-fired in a fluidized-bed combustor using fuel staging.
- Mixture of alumina and silica sand is used as the bed material to inhibit bed agglomeration.
- Proportion of secondary fuel affects combustion and emission performance of the combustor.
- The proposed combustion method can reduce 25-35% of NO emission.
- Higher proportion of silica sand in the bed increases the bed agglomeration tendency.

#### ARTICLE INFO

# Keywords: Oil palm residues Co-firing Fluidized bed NO emission reduction Bed agglomeration prevention

#### ABSTRACT

Oil palm kernel shell (base fuel) and empty fruit bunch (secondary fuel) with elevated/high potassium contents were co-fired in a conical fluidized-bed combustor with bottom air injection using fuel staging to reduce NO emission. During the co-firing tests at a fixed heat input into the combustor and variable excess air, alumina sand (AS), mixed with silica sand (SS) in different proportions, was used as the bed material to inhibit bed agglomeration. The study revealed that the effects of energy fraction of the secondary fuel in the total heat input (EF $_2$ ) and excess air (EA) on the major gaseous emissions and combustion efficiency of the conical FBC were substantial. Under optimal operating conditions (EF $_2 \approx 0.15$  and EA  $\approx 55\%$ ), the combustor with the selected bed material can be co-fired at minimal "external" costs and reduced NO emission, as compared to burning the base fuel alone. By using AS/SS bed mixtures with a prevailing proportion of rather expensive AS, bed agglomeration can be prevented for a relatively long operating time. However, the AS/SS beds exhibited time-related alterations in physiochemical characteristics. With a higher SS content in the AS/SS mixture, the NO emission somewhat increased, mainly because of the lowered catalytic activity of the bed for the NO–CO reaction, whereas the bed material showed a diminished capability to withstand bed agglomeration.

#### 1. Introduction

In Thailand, palm kernel shell (PKS) and empty fruit bunch (EFB), residues from the Thai palm oil industry, are important bioenergy resources showing a great potential as a fuel in direct combustion applications. In 2016, due to substantial availability of PKS and EFB, the domestic energy potential of these two oil palm residues accounted for about 80 PJ [1].

Fluidized-bed combustion systems (boiler furnaces and combustors) are recognized as most appropriate techniques for effective conversion of biomass into energy. These systems have a number of important

advantages over grate-firing and pulverized fuel-firing systems, such as excellent gas-solid and gas-gas mixing, intensive heat transfer, thermal homogeneity, low emissions, and high combustion efficiency [2–4]. However, individual burning of "as-received" PKS and EFB with fluidized-bed combustion techniques may cause some operational problems from fuel properties. Previous studies revealed that firing of PKS with elevated fuel-N is generally accompanied by substantial NO emission [5,6], whereas fluidized-bed combustion of "as-received" (high-moisture) EFB in a fluidized bed is expected to be unstable (or even not feasible) because of the lowered bed temperatures [7,8].

Co-firing (or co-combustion) is an effective tool to remedy both

E-mail address: ivlaanov@siit.tu.ac.th (V.I. Kuprianov).

<sup>\*</sup> Corresponding author.

environmental and operational problems, commonly occurring in systems burning a single problematic fuel (such as a fuel with low calorific value, elevated fuel-N and fuel-S, and/or containing low-melting ash). Co-firing is reported to be flexible for fuel type (fossil and biomass fuels, combustible wastes, and refuse-derived fuels), and has shown its effectiveness in stoker-fired, pulverized fuel-fired, and fluidized-bed combustion systems [8-12]. A large number of research papers have addressed the co-combustion of coal pre-mixed with biomass in pulverized coal-fired boilers. These research studies have revealed that cocombustion results in a significant reduction of CO<sub>2</sub>, NO<sub>x</sub>, and SO<sub>2</sub> emissions and provides some other benefits, such as higher combustion stability and lower costs of heat and power production, compared to firing coal alone [12-15]. However, not much information has been reported on the co-firing of two or more biomasses in a single combustion technique. Some pioneering studies on biomass-biomass cocombustion in grate-fired and fluidized-bed combustion systems have shown that through co-firing of a problematic fuel with one of better quality (or with dedicated fuel properties), the combustion and emission performance, and the operational safety of a combustion system can be substantially improved [8,9,16].

Staged combustion methods/techniques (such as air staging, fuel staging, and reburning) have been proposed to control/mitigate  $NO_x$ emissions in various combustion systems (co-)fired with a fossil fuel and biomass, particularly in coal-fired power plants [17]. Some pilot studies on the combustion of various types of biomass in grate-fired and fluidized-bed combustion systems have shown a substantial NO<sub>x</sub> reduction (~70%) via the use of air staging [18-20]. Furthermore, with a reburning method (that combines air staging and fuel staging), higher (up to 80%)  $NO_x$  reduction can be achieved, as demonstrated in some pilot studies on the co-firing of woody residues in a grate-fired system [9,18]. However, both air staging and reburning may cause negative impacts on the performance of a fluidized-bed combustion system, such as (i) deterioration of bed fluidization quality and (ii) elevated temperatures, either in a fluidized bed (in systems with air staging) or in a reburn zone (when using reburning) [18]. Therefore, the two methods can be generally recommended for co-firing biomass fuels with high melting-point ash. Apart from these drawbacks, air-staging and reburning techniques require a more complicated control of the fuel/air supply to a combustor/furnace, compared to conventional systems.

Unlike with the air-staging and reburning methods, the literature review has shown a lack of information on the application of fuel staging (e.g., via axial biasing) in biomass-fueled fluidized-bed combustion systems with bottom air injection [21], which is basically free of the above-mentioned drawbacks of air staging and reburning. In fuel staged co-firing of two fuels, a base (or primary) fuel is generally fed into the bottom region of a combustor/furnace, together with all combustion air, and therefore, burned in this region with excess air. In the meantime, a secondary fuel is injected into the combustor downstream from the primary combustion zone, to establish favorable conditions for NO reduction, mainly due to elevated CO and hydrocarbon radicals (such as  $CH_i$  and HCCO originated from  $C_xH_y$ ) participating in decomposition of NO in the secondary zone and leading, eventually, to a lower NO emission from the system [9,22,23].

Another operational problem of the fluidized-bed combustion of PKS and EFB is related to the ash composition of these two biomass fuels. With elevated/high contents of potassium in fuel ash, both oil palm residues have a strong propensity for bed agglomeration when burned in a fluidized bed of conventional material (quartz/silica sand). From pilot studies on burning PKS ( $K_2O = 5.6 \text{ wt.}\%$  in fuel ash) and EFB ( $K_2O = 21.4 \text{ wt.}\%$  in fuel ash) in a fluidized-bed combustor, the bed material (silica sand) is subject to severe bed agglomeration, which inevitably resulted in fast bed defluidization at typical bed temperatures [24–26]. Two groups of physiochemical mechanisms/processes, commonly termed "coating-induced" agglomeration and "melt-induced" agglomeration, are reported to be responsible for the formation of bed agglomerates when burning high-alkali biomass fuels in a

fluidized bed of silica/quartz sand [27]. While "coating-induced" agglomeration occurs due to sticky layers (coatings) formed on the bed grain surfaces (as a result of chemical reactions between the ash-derived K-rich species and SiO<sub>2</sub> in quartz/silica sand [28,29]), "melt-induced" agglomeration is generally caused by highly adhesive melts (released from partly molten chars/ashes), "serving" as a binding material in the formation of agglomerates [30].

Recent studies have proposed the use of alternative bed materials (i.e., containing no or a minor proportion of Si), such as alumina sand, limestone, and dolomite, to minimize (or prevent) bed agglomeration for a relatively long operating time during combustion of K-rich biomasses, including PKS and EFB [6.31.32]. It was also reported that during biomass combustion, the bed particles of limestone and dolomite were subject to intensive calcination, breakage, and attrition, leading to a substantial carryover of fine bed particles from the combustor, which required a recurrent substitution of the entrained bed material [6,31]. On the contrary, alumina sand is found to be relatively stable, both physically and chemically [31,32]. However, this bed material is rather expensive, as compared to silica/quartz sand, limestone, dolomite, and other types of minerals present in nature. Therefore, the use of mixed bed materials (alternative and conventional ones) seems to be an effective way to inhibit bed agglomeration at reduced bed material costs when burning K-rich biomass fuels in fluidized-bed systems.

This work aimed to study the combustion and emission performance of a fluidized-bed combustor with a cone-shaped bed (referred to as "conical FBC"), co-fired with PKS and EFB using fuel staging, to reduce NO emission from the combustor. To inhibit bed agglomeration at minimized bed material costs, alumina sand (AS), mixed with silica sand (SS) in different proportions, was used as the bed material in this conical FBC. The specific objectives of this work were: (1) to assess the optimal mass/energy fraction of the co-fired fuels in the total fuel supply and the optimal amount of excess air for the PKS/EFB co-firing, (2) to study the effects of fuel staging, excess air, and bed material type on the combustion and emission characteristics of the conical FBC, and (3) to investigate the influence of the AS/SS ratio on the physiochemical conditions of the selected bed mixtures at different operating times.

#### 2. Materials and methods

#### 2.1. Experimental facilities

Fig. 1 shows the experimental set up with the conical FBC and auxiliary equipment (Fig. 1a), as well as the design features and geometrical characteristics of the combustor (Fig. 1b). Besides the combustor, the experimental facilities included: (i) two screw-type fuel feeders delivering the co-fired fuels into the conical FBC at different levels, (ii) a 25-hp blower supplying combustion air, (iii) a cyclone collecting the particulate matter originated from the biomass (co-combustion, and (iv) a start-up diesel-fired burner.

The combustor consisted of a conical section of  $0.9\,\mathrm{m}$  height,  $40^\circ$  cone angle, and  $0.25\,\mathrm{m}$  inner diameter at the bottom plane, and a cylindrical section of  $2.5\,\mathrm{m}$  height and  $0.9\,\mathrm{m}$  inner diameter. As reported previously, the conical FBC has been used in a number of studies on individual burning of some problematic biomass fuels, including PKS and EFB [6,31,32]. However, compared to the previous studies, the combustor in the current work was equipped with an additional fuel feeder. During co-firing tests, a base (or primary) fuel and a secondary fuel were delivered into the conical FBC via separate routes. The primary fuel was injected into the conical section at  $Z=0.65\,\mathrm{m}$  above the air distributor, whereas the secondary fuel was introduced into the lower region of the cylindrical section at  $Z=1.15\,\mathrm{m}$  (as shown in Fig. 1b). This technique of fuel injection at different levels ensured fuel staging (or biasing) in the axial direction with a single air supply system.

Combustion air at the ambient temperature was supplied to the combustor by the above-mentioned blower, and then introduced into

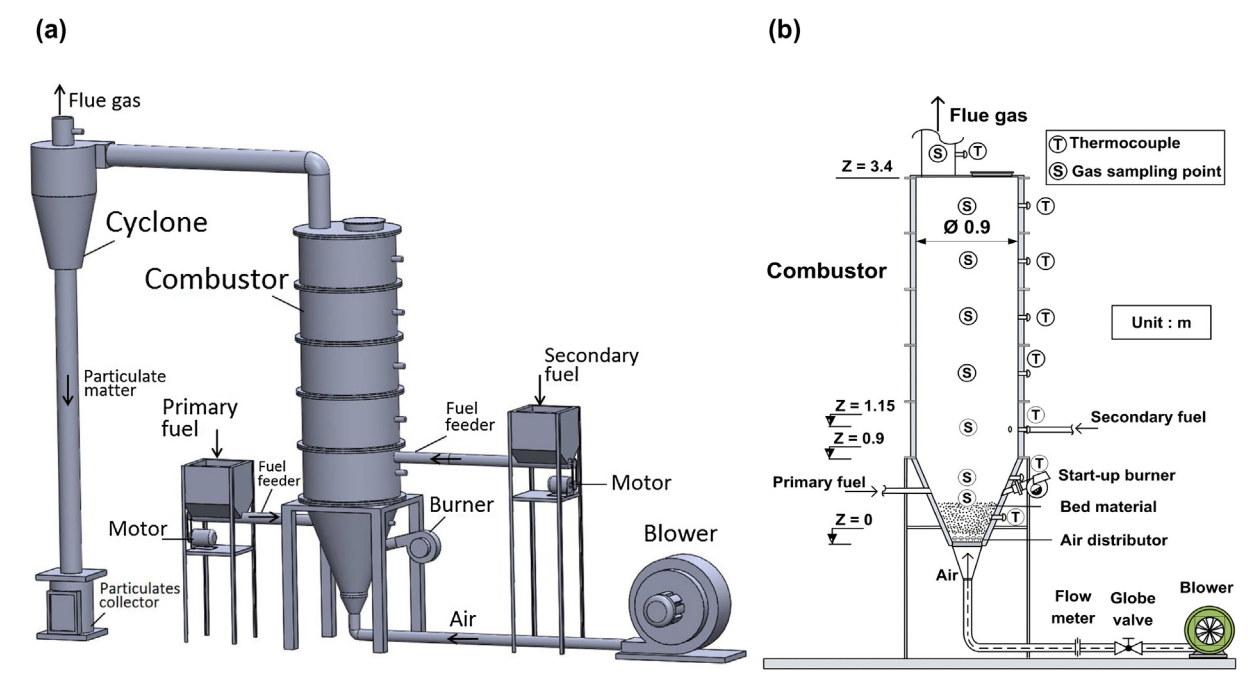


Fig. 1. (a) Experimental set up for fuel-staged co-firing tests and (b) design details of the conical FBC.

the bed material through the air distributor (as shown in Fig. 1b), which generated a fluidized gas–solid bed in the conical section. The air distributor was comprised of nineteen bubble-cap standpipes, closely arranged on the air distributor plate. Each standpipe had 64 holes of 2 mm in diameter, evenly distributed over the pipe outer surface, and six vertical slots ( $15 \, \text{mm} \times 3 \, \text{mm}$  in sizes) located right below a stand pipe cap of 47 mm in diameter. The proposed design of the air distributor ensured the uniform distribution of airflow over the bed, thus, avoiding bed spouting, at a small pressure drop across the device [6,33].

Eight stationary Chromel-Alumel thermocouples of type K were fixed at different levels inside the conical FBC, as well as at stack, to monitor the temperature along the combustor centerline during start up and transition modes of the combustor. In the start up mode, the bed material was preheated with a diesel-fired burner to a temperature of about 700 °C. Upon attaining this temperature, the start up burner was turned off, and the combustor was then operated using either the base fuel (when it was burned alone) or both primary and secondary fuels (in co-firing tests).

Combustion products were extracted through the gas sampling ports fixed on the combustor wall at different levels, as well as at the cyclone gas exit, as shown in Fig. 1. During experiments under specified operating conditions (parameters), the temperature and gas concentrations (O<sub>2</sub>, CO, C<sub>x</sub>H<sub>y</sub> as CH<sub>4</sub>, and NO<sub>x</sub> as NO) were measured in lateral and axial directions inside the conical FBC, as well as at stack, using a "Testo-350" gas analyzer. The measuring accuracies were:  $\pm$  5% of reading for the temperature up to 1200 °C,  $\pm$  0.2 vol.% for O<sub>2</sub>,  $\pm$  5% of reading for CO from 200 to 2000 ppm,  $\pm$  10% of reading for CO higher than 2000 ppm,  $\pm$  10% of reading for C<sub>x</sub>H<sub>y</sub> less than 40,000 ppm, and  $\pm$  5% of reading for NO less than 2000 ppm.

#### 2.2. The fuels

Pioneering studies on the biomass-biomass co-combustion using fuel staging with bottom air supply have revealed that a substantial reduction of NO emission can be achieved when primary and secondary biomass fuels comply with some requirements [22,23]. It is important that the lower heating value of the primary fuel be noticeably higher than that of the secondary fuel, which should contain a substantial amount of fuel moisture. This requirement ensures stable and high-efficiency combustion in the primary combustion zone, avoids a high temperature peak in the combustor, and results in the generation of elevated CO and CxHv (responsible for NO reduction) in the secondary combustion zone. It is desirable (but not compulsory) to use a secondary fuel with fuel-N lower than that of the primary fuel, to prevent an intensive formation of NO in the secondary combustion zone. Following these requirements, PKS was used in this work as the base (primary) fuel, while high-moisture, low-calorific EFB was selected to be the secondary fuel, when co-fired in the conical FBC.

The proximate and ultimate analyses, and the lower heating value of the two oil palm residues used in co-combustion tests are shown in Table 1. Based on the properties from Table 1, both PKS and EFB can be treated as low-ash, high-volatile biomass fuels. However, the lower heating value of PKS, LHV $_1=16.39\,\text{MJ/kg}$ , was substantially higher than that of EFB, LHV $_2=5.81\,\text{MJ/kg}$  (the latter was low because of the high fuel moisture content). Due to insignificant fuel-S in both oil palm residues ( $\sim\!0.1\,\text{wt.}\%$ ), the formation of SO $_2$  in the combustor and its impacts on the environment were neglected.

To assure a smooth fuel supply and stable operation of the conical FBC, PKS and EFB were shredded prior to co-firing tests. After shredding, the particle size of PKS ranged from 0.1 mm to 9 mm, whereas

**Table 1**Ultimate and proximate analyses and the lower heating value (LHV) of palm kernel shell (PKS) and empty fruit bunch (EFB).

Biomass fuel	Ultimate an	alysis (wt.%, o	n a dry and asl	n-free basis)		Proximate	Proximate analysis (wt.%, on an as-received basis)				
	C H N O S						VM				
PKS EFB	53.46 37.58	7.10 14.88	1.41 0.68	37.93 46.73	0.10 0.13	5.4 41.4	71.1 44.9	18.8 10.8	4.7 2.9	16.39 5.81	

**Table 2**Composition of fuel ash in PKS and EFB

Fuel ash	Comp	Composition (as oxides, wt.%)									
	$SiO_2$	$Al_2O_3$	$K_2O$	CaO	Na <sub>2</sub> O	MgO	$Fe_2O_3$	$P_2O_5$	$SO_3$	Cl	
Palm kernel shell	23.1	5.2	7.0	42.5	5.5	3.0	1.3	8.5	2.4	0.7	
Empty fruit bunch	15.1	2.8	42.2	19.5	-	4.2	3.4	5.3	2.5	3.7	

individual fibers of EFB were up to 10 mm in length.

The fuel ash analyses of PKS and EFB, both determined using a wavelength dispersive X-ray fluorescence spectrometer, are represented in Table 2. From this data, Ca, Si, K, and P were predominant in the PKS ash, whereas K, Ca, and Si were major elements in the ash of EFB. Elevated (in PKS) and significant (in EFB) K<sub>2</sub>O indicated a high propensity for bed agglomeration if these biomasses were burned in a fluidized bed of quartz/silica sand [28–30].

#### 2.3. The bed materials

To decrease the bed agglomeration tendency at a minimized bed cost, alumina sand (AS) mixed with silica sand (SS) in different proportions: (75% AS + 25% SS), (50% AS + 50% SS), and (25% AS + 75% SS), were used as the bed material in this conical FBC during co-firing experiments. Table 3 shows the composition of original AS and SS used for preparing the above-mentioned bed mixtures. Prior to mixing, both AS an SS were sieved to ensure that the particle size of the bed materials was within  $0.3-0.5\,\mathrm{mm}$ .

However, at the first stage of this work, mainly devoted to the optimization of the mass/energy fraction of the co-fired PKS and EFB, pure alumina sand was used as the bed material to entirely prevent bed agglomeration, as shown previously in studies of the individual burning of these oil palm residues in a conical FBC during long-running experiments [5,31].

Prior to co-combustion studies, "cold-state" experiments were performed on a test rig (with a configuration identical to the combustor conical section) using pure silica sand and pure alumina sand as the bed material. As found in these "cold-state" studies, when the superficial air velocity at the air distributor exit (u) was between the minimum velocity of full fluidization ( $u_{\rm mff}$ ) and the minimum velocity of turbulent fluidized-bed regime  $(u_k)$  [33], the cone-shaped bed fluidized and showed a bubbling fluidization regime for both bed materials. For PKS and EFB with the above-mentioned sand particle sizes and bed dimensions (cone angle, static bed height, and diameter of the lower base), the characteristic velocities were:  $u_{\rm mff} \approx 0.8\,{\rm m/s}$  and  $u_{\rm k} \approx 1.8\,{\rm m/s}$ s for AS, but somewhat lower,  $u_{\rm mff} \approx 0.7$  m/s and  $u_{\rm k} \approx 1.6$  m/s, for SS. For the selected AS/SS bed mixtures,  $u_{mff}$  and  $u_k$  were expected to be between those quantified for pure AS and SS. However, at  $u > u_k$ , the bed was operated in a turbulent fluidization regime, showing an expanded volume of the gas-solid mixture, compared to the bubbling fluidized-bed regime observed at  $u_{\text{mff}} \le u < u_{\text{k}}$  [33].

**Table 3**Composition of alumina sand (AS) and silica sand (SS) in the AS/SS bed mixtures, used as the bed material in the co-firing tests.

Bed material Composition (wt.%, as oxides)										
	$Al_2O_3$	$SiO_2$	CaO	MgO	K <sub>2</sub> O	Na <sub>2</sub> O	Fe <sub>2</sub> O <sub>3</sub>			
Alumina sand Silica sand	87.18 6.59	12.29 87.82	0.04 0.06	- 0.13	0.43 4.24	0.01 0.27	0.01 0.55			

**Table 4**Fuel feed rates of PKS and EFB in the co-firing tests at different mass/energy fractions of EFB in the total fuel supply.

Energy fraction of the secondary fuel (EFB)	Mass fraction of the secondary fuel (EFB)	Feed rate of PKS (kg/h)	Feed rate of EFB (kg/h)
0	0	43.9	0
0.05	0.09	41.7	6.2
0.10	0.17	39.5	12.4
0.15	0.25	37.3	18.6
0.20	0.32	35.1	24.8
0.25	0.39	32.9	31.0

#### 2.4. Experimental methods for co-combustion studies

For comparability between the co-firing options and operating conditions, the total heat input by both fuels into the conical FBC was constant (about  $200\,\mathrm{kW_{th}}$ ) throughout the work, whereas the energy fraction of the secondary fuel (EF<sub>2</sub>) and excess air (EA) were selected as independent operating parameters of the combustor in individual test runs. To assure this heat input, PKS and EFB were supplied into the conical FBC at respective mass flow rates ( $\dot{m}_1$  and  $\dot{m}_2$ ) for each specified value of EF<sub>2</sub>, defined as the ratio of energy contribution by EFB ( $\dot{m}_2$ LHV<sub>2</sub>) to the total heat input by the two fuels ( $\dot{m}_1$ LHV<sub>1</sub> +  $\dot{m}_2$ LHV<sub>2</sub>). For given EF<sub>2</sub>, the feed rates of PKS and EFB were determined using the above-mentioned heat input into the combustor and the lower heating value of the co-fired fuels. Table 4 presents the fuel feed rates of PKS and EFB, as well as the weight (mass) fraction of EFB (in the total fuel supply), for all the selected values of EF<sub>2</sub>.

Three groups (series) of co-firing tests, to determine the combustion and emission characteristics of the conical FBC at variable  $EF_2$  and EA, were performed with the selected bed materials. In different test series,  $EF_2$  was within the range from 0 (i.e., when firing pure PKS) to 0.25, whereas EA generally varied from 20% to 80% at fixed  $EF_2$ .

Taking into account: (i) feed rates of the co-fired fuels (see Table 4), (ii) amount of EA, (iii) stoichiometric amounts of air required for burning PKS (4.83 Nm<sup>3</sup>/kg) and EFB (3.19 Nm<sup>3</sup>/kg), both calculated according to Ref. [34]), and (iv) cross-sectional area of airflow (calculated as the difference between area of the 250-mm-diamter plate and total area occupied by the caps), the superficial air velocity at the air distributor exit (u) was assessed for the selected (co-)firing options. For instance, when burning pure PKS, the superficial air velocity varied from 4.9 to 7.3 m/s for 20-80% EA. However, during co-firing PKS and EFB at EF<sub>2</sub> = 0.25, the *u* showed the highest values (6.1-9.0 m/s) for a similar range of EA. It can therefore be concluded that, when using EF<sub>2</sub> and EA within the specified ranges, the combustor operated in the turbulent fluidized-bed regime in all test runs, as the values of *u* in these experiments were much higher than the above-reported  $u_k$  (1.6–1.8 m/ s) for pure alumina and silica sand. During this fluidization regime, the expanded bed occupied a predominant part of the conical section [33], thus ensuring "in-bed" injection of PKS, whereas EFB was introduced into the conical FBC at a level above the expanded bed (in the cylindrical section of the combustor).

## 2.4.1. Preliminary study on the conical FBC using pure alumina sand as the bed material

In the first (preliminary) stage of the present work, devoted to optimizing the operating parameters of the co-combustion, PKS and EFB were co-fired with 200 kW<sub>th</sub> heat input for five values of EF<sub>2</sub> (within the range of 0–0.25), whereas EA varied from 20% to 80% for each fuel option. In a trial at fixed EF<sub>2</sub> and EA, CO,  $C_xH_y$ , and NO emissions were measured at stack. The actual amount of EA for an individual test run was quantified according to Refs. [23,34], using experimental O<sub>2</sub>, CO, and  $C_xH_y$ . In this test series, alumina sand was used as the bed material to avoid bed agglomeration during the entire experimental period.

A cost-based optimization model [23,35] was used at this stage to

quantify the optimal values of  $EF_2$  and EA, leading to minimal "external" costs of the conical FBC. The "external" costs were mainly represented by emission costs, paying for the damage done by gaseous pollutants emitted from a combustion system to the environment and to humans [36]. Ignoring the effects of  $SO_2$  (as indicated above) and  $CO_2$  (due to its low specific "external" costs and weak effects of operating conditions on the  $CO_2$  emission rate), the objective function minimizes the "external" costs during co-firing PKS and EFB and takes the following form:

$$J_{\text{ec}} = \text{Min}(P_{\text{NOx}}\dot{m}_{\text{NOx}} + P_{\text{CO}}\dot{m}_{\text{CO}} + P_{\text{CxHy}}\dot{m}_{\text{CxHy}})$$
(1)

For fixed EF<sub>2</sub> and EA, the emission rates of  $NO_x$  (as  $NO_2$ ), CO, and  $C_xH_y$  (as  $CH_4$ ) in Eq. (1) were quantified using the feed rate (kg/s) of the co-fired fuels and corresponding (measured) emission concentration (ppm) of the pollutants as:

$$\dot{m}_{\text{NO}_{\text{x}}} = 2.05 \times 10^{-6} (\dot{m}_{\text{f1}} + \dot{m}_{\text{f2}}) \text{NO}_{\text{x}} V_{\text{dg,cf}}$$
 (2)

$$\dot{m}_{\rm CO} = 1.25 \times 10^{-6} (\dot{m}_{\rm f1} + \dot{m}_{\rm f2}) \text{COV}_{\rm dg,cf}$$
 (3)

$$\dot{m}_{C_x H_y} = 0.71 \times 10^{-6} (\dot{m}_{f1} + \dot{m}_{f2}) C_x H_y V_{dg,cf}$$
 (4)

where  $V_{\rm dg,cf}$  is the volume of dry flue gas (Nm<sup>3</sup>/kg-fuel) from co-firing of PKS and EFB (at actual EA), estimated according to Ref. [23] using the mass fractions of the co-combusted fuels.

However, the specific "external" costs of  $NO_x$  (as  $NO_2$ ) and  $C_xH_y$  (as  $CH_4$ ) were assumed to be  $P_{NOx}=2400$  US\$/t and  $P_{CxHy}=330$  US\$/t, respectively, as provided in Ref. [36]. As revealed in some relevant studies [37,38], the  $P_{NOx}/P_{CO}$  ratio typically varies from 5 to 8. It was therefore decided to assume  $P_{CO}=400$  US\$/t in this optimization analysis. At similar emission concentrations of the selected pollutants, the contribution of  $NO_x$  to the total "external" costs in Eq. (1) was predominant, about 10 times greater than for CO and 20 times greater than for  $C_xH_y$ . Thus, the reduction of  $NO_x$ , emitted from a combustion system, was a goal of paramount importance in this work.

At the final step of this preliminary stage, the temperature and gas concentrations were measured in the lateral direction inside the conical FBC co-fired at the optimal  $EF_2$ , for two values of excess air (EA = 40% and EA = 80%), at three levels (Z) to investigate the dependent variables for their uniformity across the combustor.

2.4.2. Study of combustion and emission characteristics inside the combustor using a mixture of alumina and silica sand as the bed material

To investigate the effects of EA on formation and oxidation/reduction of the major gaseous pollutants at different points in the conical FBC, a second series of co-combustion tests was performed with 200 kWth heat input using the optimal EF2, for four specified amounts of EA: 20%, 40%, 60%, and 80%. In this stage, a (50% AS + 50% SS) bed mixture was employed as the bed material. During a test run at given EA, the temperature, as well as  $O_2$ , CO,  $C_xH_y$ , and NO, were measured along the combustor centerline to obtain the axial profiles of the combustion and emission characteristics.

## 2.4.3. Study of effects of excess air and bed material on the major emissions and combustion efficiency of the conical FBC

In the third test series, the CO,  $C_xH_y$ , and NO emissions were measured in the flue gas for the range of EA, when using the above-mentioned three AS/SS bed mixtures, to access the impacts of EA and bed material type on the emission performance and combustion efficiency of the conical FBC. In this test series, PKS and EFB were co-fired at the optimal amount of EF<sub>2</sub>.

After each test run, particulate matter (PM), generally consisting of fly ash, was sampled and analyzed for unburned carbon. The heat loss due to unburned carbon and that due to incomplete combustion, both required for determining the combustion efficiency of the combustor, were predicted according to Ref. [23], using the concept of "equivalent fuel". Based on this concept, all relevant properties of the "equivalent

fuel" were quantified for a given  $EF_2$  as the weighted averages, by taking into account the corresponding properties of PKS and EFB and the mass fractions of the two co-fired fuels.

## 2.5. Characterization of the bed materials and particulate matter at different operating times

In order to study the behavior of the selected bed materials with time, a fourth series of co-firing tests was performed with the three selected AS/SS bed mixtures. For this purpose, the fuels were co-fired for a relatively long operating time at optimal (fixed)  $EF_2$  and EA, both quantified in the preceded studies.

To understand the interaction mechanism between the bed material and fuel ash during the fuel staged co-firing of PKS and EFB, a JEOL JSM-6400 scanning electron microscope (SEM), integrated with an energy dispersive X-ray spectrometer (EDS system), was used for examining the physiochemical characteristics of individual particles sampled from the bed mixtures after the co-firing tests. Prior to the SEM-EDS analysis, the specimens were prepared by mounting the sampled bed particles/agglomerates in an epoxy resin, cutting across them by a diamond saw, then polishing, and finally coating individual specimens with a thin layer of gold to make them electrically conductive. The objectives of the SEM-EDS test were to investigate the distribution of coatings over the bed particles (or that of binding materials in agglomerates), as well as to determine the elemental composition of coatings/materials at some selected spots on a specimen.

An X-ray fluorescence (XRF) system was employed to observe the time-related variation in the chemical composition of the selected AS/SS bed mixtures, as well as that of PM.

#### 3. Results and discussion

3.1. Optimizing operating parameters for co-firing PKS and EFB using pure alumina sand as the bed material

Fig. 2 depicts the CO,  $C_xH_y$ , and NO emissions (all at 6%  $O_2$  and on a dry gas basis) from the preliminary tests on this fuel staged combustor, using alumina sand as the bed material, when co-fired with PKS and EFB at the specified ranges of EF $_2$  and EA, as compared to those for firing PKS alone (EF $_2$  = 0). It can be seen in Fig. 2 that all the emissions had noticeable effects from the two operating parameters. However, the opposite trends were observed from EF $_2$  and EA, the most significant at 20–40% EA.

With increasing  $EF_2$  (at similar EA), both CO and  $C_xH_y$  emissions were higher, mainly due to the strengthening effects from injection of EFB into the secondary combustion zone, whereas with a greater amount of EA (at fixed  $EF_2$ ), these two emissions decreased at a variable rate. On the contrary, an increase in  $EF_2$  (at constant EA) caused a noticeable reduction in the NO emission, mainly due to the increased concentrations of CO and  $C_xH_y$  in the secondary combustion zone (to be discussed below), both enhancing the rate of NO reduction reactions in this region [2,9,22]. However, higher EA (at fixed  $EF_2$ ) led to a greater emission of NO, which can be generally attributed to the fuel-NO formation mechanism [2,39].

Fig. 3 shows the "external" (emission) costs of the co-combustion of PKS and EFB in the conical FBC predicted from Eqs. (1)–(4) by using the measured CO,  $C_xH_y$ , and NO emissions, as well as other relevant parameters, all quantified for the ranges of EF $_2$  and EA. From Fig. 3, the effects of EF $_2$  and EA on the "external" costs were substantial. With increasing EF $_2$  at relatively low amounts of EA, the total emission costs increased to a significant level, mainly due to the enhanced impacts of the CO and  $C_xH_y$  emissions. On the contrary, the effects of NO on the costs were more significant with diminishing EF $_2$  and/or higher EA.

As follows from the optimization, the minimal "external" costs were found at EF $_2 \approx 0.15$  and EA  $\approx 50\%$  (see Fig. 3). Under these conditions, the major emissions can be controlled at acceptable levels, i.e., below

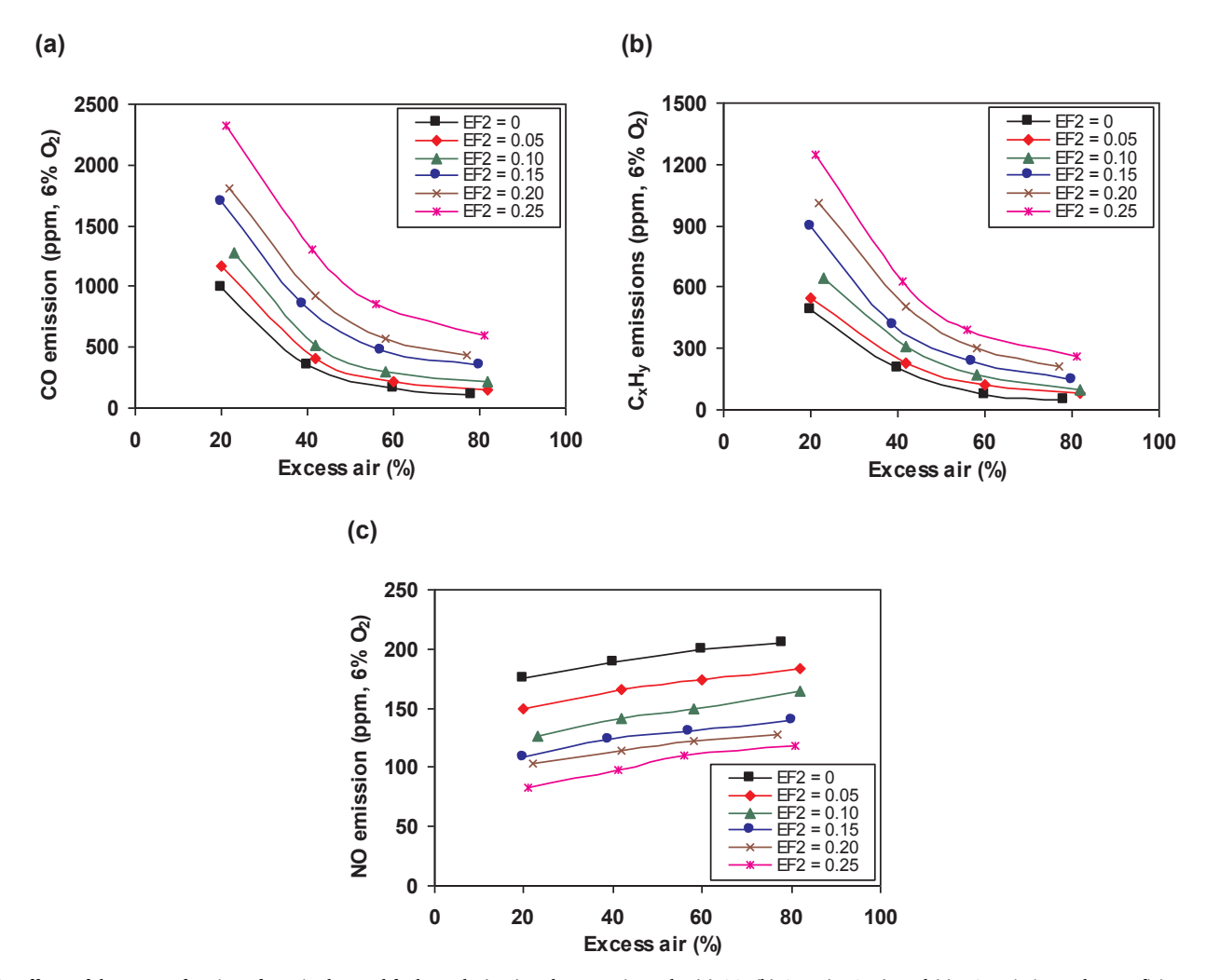


Fig. 2. Effects of the energy fraction of EFB in the total fuel supply (EF<sub>2</sub>) and excess air on the (a) CO, (b)  $C_xH_y$  (as  $CH_4$ ), and (c) NO emissions when co-firing PKS and EFB in the conical FBC using alumina sand as the bed material.

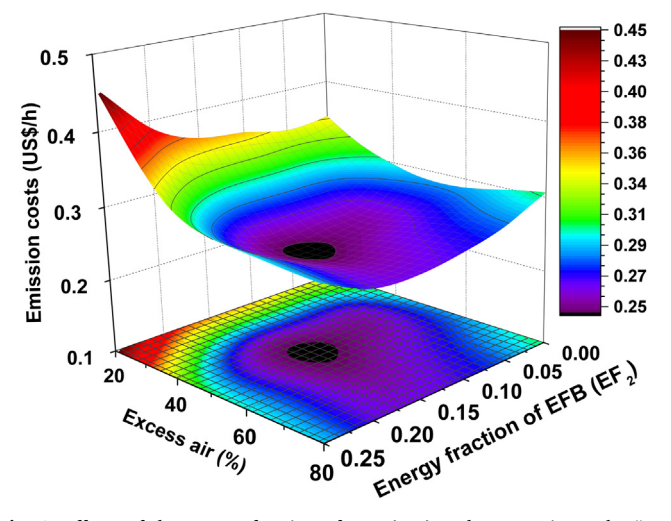


Fig. 3. Effects of the energy fraction of EFB  $(EF_2)$  and excess air on the "external" costs of co-firing PKS and EFB in the conical FBC using alumina sand as the bed material.

the national emission limits for biomass-fueled industrial applications: 740 ppm for CO and 214 ppm for NO (on a dry gas basis and at 6%  $O_2$  in the flue gas) [40]. Furthermore, the fuel-staged co-combustion of PKS and EFB at the optimal EF<sub>2</sub> and EA led to a noticeable NO emission

reduction, by about 35%, compared to firing pure PKS.

Fig. 4 presents the distribution of temperature and gas concentrations ( $O_2$ , CO,  $C_xH_y$  as  $CH_4$ , and NO) in the radial direction inside this combustor with the alumina sand bed, at three selected levels (Z) above the air distributor, when co-firing PKS and EFB at the optimal energy fraction of EFB,  $EF_2 = 0.15$  (as determined from the above optimization procedure), for the two excess air values ( $\sim$ 40% and  $\sim$ 80%). It can be seen in Fig. 4 that the radial temperature and gas concentration profiles were fairly uniform at all three levels above the air distributor despite that the secondary fuel (EFB) was injected over the fluidized bed. This result can be attributed to the highly intensive gas–solid and gas–gas mixing across the conical FBC in various regions inside this fuel staged combustor operated at substantially different amounts of EA. Based on this, it was decided to use axial profiles of the temperature and gas concentrations in further analysis of the combustion and emission performance of the conical FBC with different bed materials.

From the visual observation of the bed material (alumina sand), no features of bed agglomeration were found after finishing these preliminary tests, which lasted for  $\sim 20\,h$  in total.

3.2. Effects of excess air on combustion characteristics and pollutant behaviors inside the conical FBC using a mixture of alumina and silica sand as the bed material

Fig. 5 depicts the distribution of combustion characteristics (temperature and  $O_2$ ) and that of CO,  $C_xH_y$  (as  $CH_4$ ), and NO along the

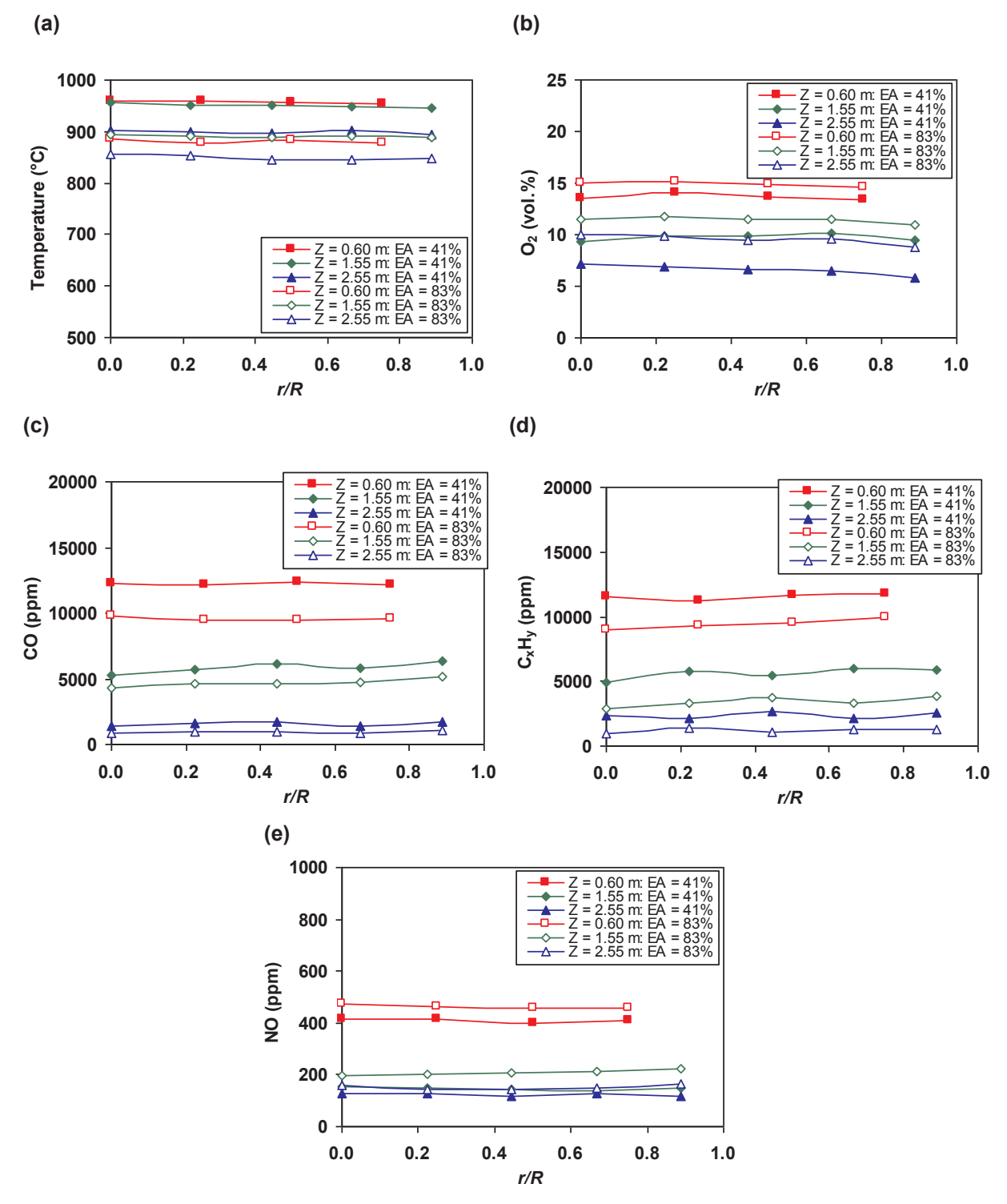


Fig. 4. Radial profiles of (a) temperature, (b)  $O_2$ , (c) CO, (d)  $C_xH_y$  (as  $CH_4$ ), and (e) NO in the conical FBC using alumina sand as the bed material when co-firing PKS and EFB at  $EF_2 = 0.15$  for two excess air values:  $EA \approx 40\%$  and  $EA \approx 80\%$ .

combustor centerline for the co-combustion tests at  $EF_2 = 0.15$  and variable excess air, when using a (50% AS + 50% SS) mixture as the bed material to reduce the bed material cost. As seen in Fig. 5a, the axial temperature profiles were fairly uniform, similar to case studies of individual burning of PKS and EFB in this conical FBC [5,31]. There were some effects of EA on the bed temperature, as well as on the maximum temperature, the latter was observed in the vicinity of the secondary fuel injection. Thus, with increasing EA within the range, the maximum temperature dropped noticeably, from 940 °C to 840 °C,

basically caused by air dilution effects. However, the behavior of axial  $\rm O_2$  profiles in Fig. 5b pointed at the substantial consumption of  $\rm O_2$  (or high rate of PKS burnout) within the conical section, and a low rate of fuel oxidation in the upper regions of the combustor. At higher EA,  $\rm O_2$  increased at all points along the combustor height because of the greater airflow rate.

Unlike with the temperature and  $O_2$ , the CO (Fig. 5c) and  $C_xH_y$  (Fig. 5d) axial profiles showed the apparent effects from fuel staging, namely, the formation of two peaks at  $Z=0.6\,\mathrm{m}$  (in the vicinity of PKS

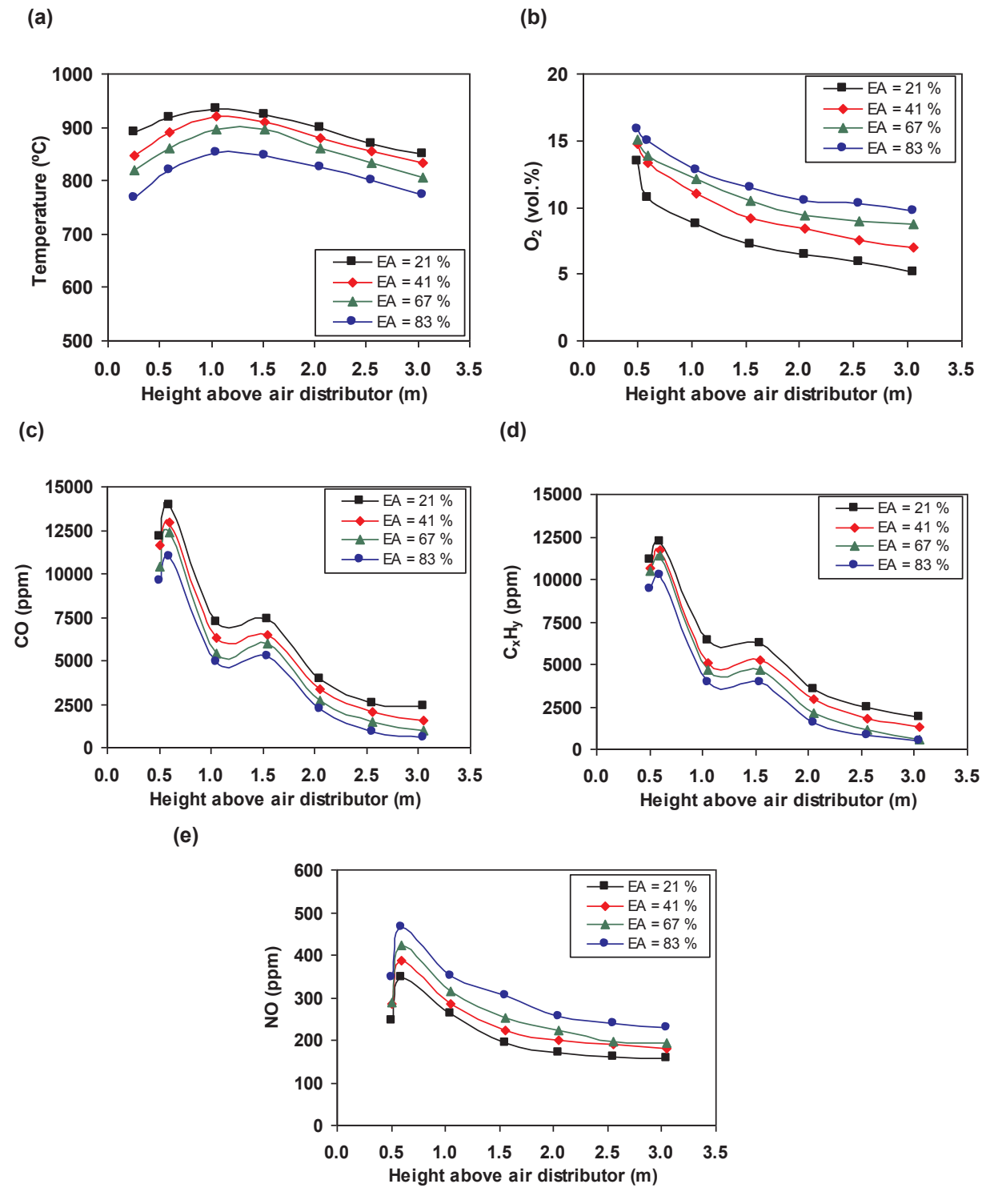


Fig. 5. Axial profiles of (a) temperature, (b)  $O_2$ , (c) CO, (d)  $C_xH_y$  (as  $CH_4$ ), and (e) NO in the conical FBC using a (50% AS + 50% SS) mixture as the bed material when co-firing PKS and EFB at a constant energy fraction of EFB (EF<sub>2</sub> = 0.15) for variable excess air.

injection) and  $Z=1.5\,\mathrm{m}$  (caused by EFB injection). It should be noted that the second (upper) peaks of CO and  $C_xH_y$  played an important role in NO reduction in the secondary combustion zone, leading eventually to the reduced NO emission from this fuel staged combustor, as compared to burning pure PKS at similar EA (as shown in the preliminary tests with alumina sand). With lowering EA (at fixed EF<sub>2</sub>), the second peaks of CO and  $C_xH_y$  were higher, indicating a greater potential for NO emission reduction via fuel staging.

In the meantime, as seen in Fig. 5e, all axial profiles of NO had only

one peak, observed in the vicinity of PKS injection (i.e., at  $Z \approx 0.6$  m), which was proportionally correlated with EA (according to the fuel-NO formation mechanism [2,39]). The "cut off" of a second NO peak can be attributed to the generation of elevated CO and light hydrocarbon radicals (CH<sub>i</sub>) in the secondary combustion zone. The NO–CO and NO–CH<sub>i</sub> reactions were generally responsible for the effective local NO reduction in this zone with lowered O<sub>2</sub> [2,9,22,23], preventing the formation of the second NO peak in the vicinity of EFB injection, and thus, ensuring a smooth decrease of NO in the combustor region at

Table 5 Emissions, heat losses, and combustion efficiency of the conical FBC, co-fired with PKS and EFB at a constant energy fraction of EFB ( $EF_2 = 0.15$ ) and variable excess air when using selected AS/SS mixtures as bed material.

Excess air (vol.%)	O <sub>2</sub> at stack (vol.%)	Carbon in PM (wt.%)	Emissio	n <sup>a</sup> (ppm)		Heat loss (%) due t	0	Combustion efficiency (%)	
			СО	$C_xH_y$	NO	Unburned carbon	Incomplete combustion		
Testing with the (75%	% AS + 25% SS) bed mi:	xture							
24	4.4	2.48	1542	1070	123	0.15	2.13	97.7	
42	6.6	1.90	701	425	126	0.12	1.04	98.8	
53	7.4	1.27	436	364	142	0.08	0.85	99.1	
82	9.5	1.16	310	121	152	0.07	0.45	99.5	
Testing with the (50%	% AS + 50% SS) bed mi:	xture							
21	4.4	9.33	2225	1860	152	0.62	3.44	95.9	
41	6.5	5.72	1230	1100	173	0.36	2.32	97.3	
59	8.0	2.11	580	450	187	0.13	1.18	98.7	
83	9.7	1.66	445	362	200	0.10	1.03	98.9	
Testing with the (259	% AS + 75% SS) bed mi:	xture							
22	4.2	9.72	1895	1725	146	0.65	3.08	96.3	
40	6.3	9.66	1060	960	172	0.64	2.19	97.2	
57	7.8	1.82	560	420	189	0.11	1.04	98.9	
82	9.4	1.79	325	271	198	0.11	0.75	99.1	

<sup>&</sup>lt;sup>a</sup> At 6% O<sub>2</sub> (on a dry gas basis).

#### $Z > 0.6 \,\mathrm{m}.$

## 3.3. Effects of excess air and bed material type on the emissions and combustion efficiency

Table 5 shows the CO,  $C_xH_y$  (as  $CH_4$ ), and NO emissions (all at 6%  $O_2$  and on a dry gas basis), the predicted heat losses (due to unburned carbon and incomplete combustion), and the combustion efficiency of the conical FBC co-fired with PKS and EFB at  $EF_2=0.15$ , for the actual amounts of EA (or  $O_2$  at stack) in test runs with the selected bed materials (AS/SS mixtures). The contents of unburned carbon in PM (required for quantifying the associated heat loss) for all the test runs are included in Table 5 as well.

It appears that all presented characteristics were substantially affected by EA. With increasing EA within the range, the unburned carbon content in PM and the emission concentrations of CO and  $C_x H_y$  decreased for the three AS/SS bed mixtures, leading to a noticeable reduction in the combustion-related heat losses, and consequently, improvement in the combustion efficiency of the conical FBC. However, for each bed material, the NO emission increased as EA was higher, complying with the fuel-NO formation mechanism, and because of the weakening effects from the NO reduction reactions.

Data in Table 5 shows that a bed mixture with a higher proportion of AS resulted in a lower NO emission from this combustor at similar EA. However, during co-firing of PKS and EFB at EF $_2\approx 0.15$  and EA  $\approx 55\%$  with pure alumina sand (100% AS), the NO emission was as low as 125 ppm (see Fig. 2). Under similar operating conditions, this emission was lower than that in the tests with the AS/SS bed mixtures: about 145 ppm, 185 ppm, and 190 ppm when using the bed materials with 75%, 50%, and 25% of AS, respectively, as can be seen in Table 5. These results can be generally attributed to the higher catalytic reactivity of AS, as compared with SS, for the (reduction) reaction of NO with CO [41,42]. From Table 5, high (up to 99.5%) combustion efficiency and acceptable CO and NO emissions (below the above-mentioned national emission limits [40]) can be achieved through the cofiring of PKS and EFB at 50–80% excess air in the proposed fuel staged conical FBC with the selected AS/SS bed mixtures.

A test for burning the base fuel (pure PKS) at EA  $\approx 55\%$  using a (50% AS + 50% SS) mixture as the bed material yielded an NO emission of about 250 ppm (at 6%  $O_2$  and on a dry gas basis) that was higher than the national emission limit for this pollutant. Thus, the co-firing of PKS and EFB under optimal operating conditions (EF $_2 \approx 0.15$  and EA  $\approx 55\%$ ) with this bed mixture resulted in the reduction of the NO

emission by about 25% (as compared to burning the base fuel alone) and ensured that the CO and NO emission concentrations were within the national emission limits.

#### 3.4. SEM-EDS analysis of the used/reused bed materials

As revealed by visual inspections of the bed material for the entire experimental time, no bed agglomeration occurred in the conical FBC during co-combustion of PKS and EFB at the optimal EF $_2$  and EA, when the AS/SS bed mixtures contained 50% of AS or higher. Fig. 6 shows the SEM images and respective EDS compositions at different spots on some SS and AS particles, sampled after the co-firing test series with the (75% AS + 25% SS) and (50% AS + 50% SS) mixtures, lasting 24 h and 26 h, respectively

From the SEM image of the bed particles collected after the tests with the (75% AS + 25% SS) bed mixture (Fig. 6a, upper micrograph), the bed grains of both AS and SS exhibited a normal appearance. As seen in Fig. 6a (Points 1 and 2), SS particles were coated by a thin layer (with brighter areas), mainly rich in Ca, Si, and K but also containing minor proportions of Al, Mg, Fe, and P, whereas no coating layers on the AS particles were detected. The bed material included a small proportion of the ash-derived melts (e.g., at Point 3), generally rich in Ca, K, and Si, the major constituents of low-melting (adhesive) K<sub>2</sub>O-CaO-SiO<sub>2</sub> eutectics originating from the PKS and EFB ashes [6,30]. It was also found that some small and fine particles of SS with high content of Si (e.g., indicated as Point 4) were adhered by the ash melts at Point 3. However, fine alumina particles, generated due to collisions and attrition of the bed grains in this turbulent fluidized bed with a predominant proportion of AS, were adhered by the partly molten chars/ashes and adsorbed by the bed grain coatings (when formed), decreasing adhesiveness of the melts and bed grains, and thus, preventing bed agglomeration [31].

The SEM images of the bed particles sampled after the tests with the (50% AS + 50% SS) bed mixture (see Fig. 6a, lower micrograph) revealed that both AS and SS grains were covered with the coatings, of up to 40  $\mu$ m in thickness, generally observed on the SS bed particles. From the EDS analysis, the elemental composition at some selected spots on the coatings of both AS and SS particles were quite similar, basically dominated by Si, Ca, and K, and also included minor proportions of Al, Mg, Fe, and P. However, compared to the previous case, a greater proportion of SS in the bed material, and consequently, a higher proportion of fine SS particles in the fluidized bed (generated from the grains attrition) shifted the content of Si in all EDS spot analyses to a

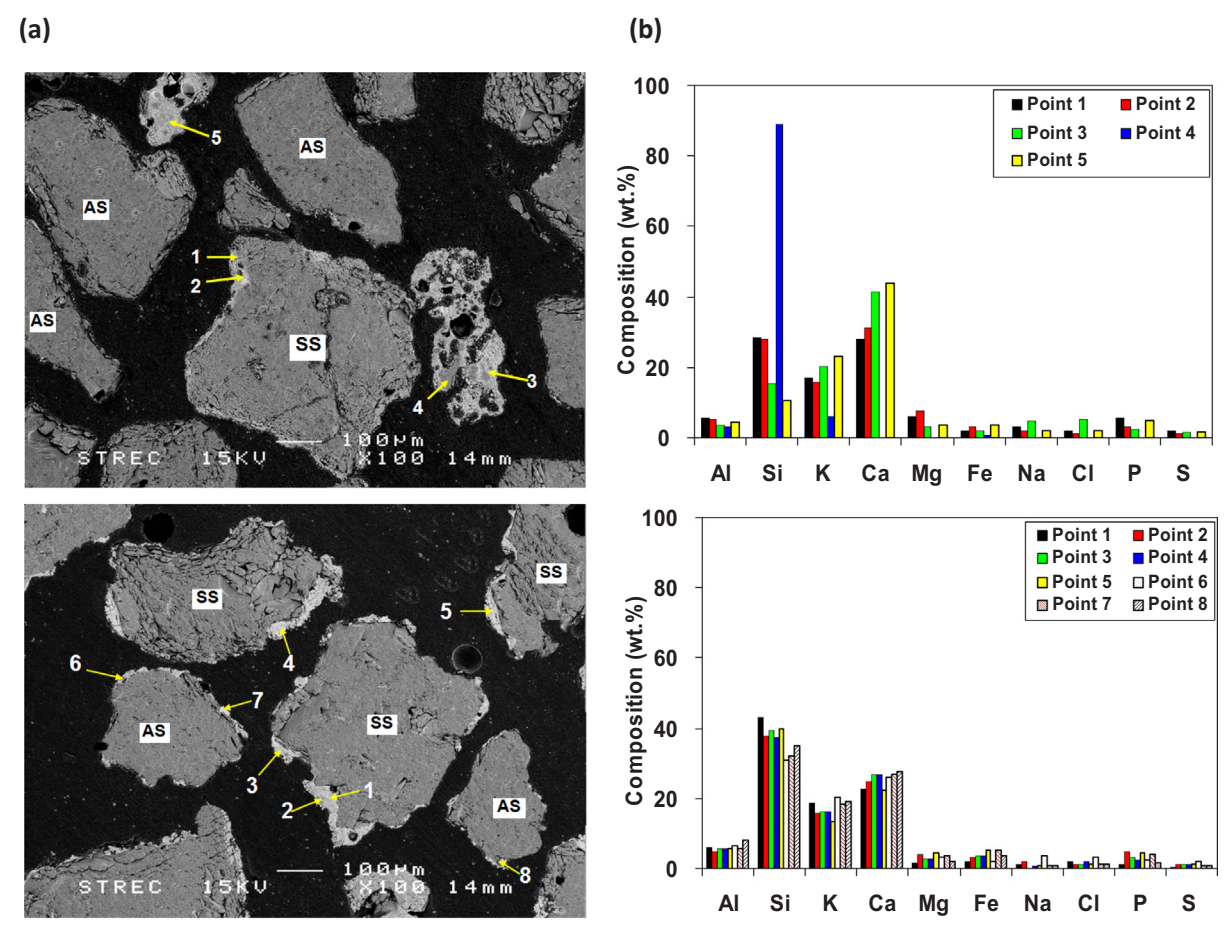


Fig. 6. (a) SEM images and (b) EDS spot analyses of AS and SS particles sampled after the co-firing tests on the conical FBC using a (75% AS + 25% SS) mixture (upper micrograph) and a (50% AS + 50% SS) mixture (lower micrograph) as the bed material under optimal operating conditions.

higher level. This indicates the increased adhesiveness of both the ash melts and grain coatings, resulting in more intensive coating of the bed particles.

As reported in a number of studies on the fluidized-bed combustion of biomass in systems using quartz/silica sand as the bed material, the coating of an individual bed particle may consist of several superimposed layers with different compositions, depending on the analysis of biomass ash and that of the bed material [28,29,43]. However, as seen in the SEM micrographs in Fig. 6a, the coatings of both SS and AS grains were (almost) consistent in chemical composition.

Summarizing the results presented in Fig. 6, the coatings on the AS and SS particles were likely formed due to: (i) interaction of bed grains with partly molten fuel-char and ash particles, (ii) migration of the ash melts, generally consisting of low-melting K and K–Ca silicates, onto the surface of AS and SS particles, causing a grain coating in some surface areas, and (iii) adsorption of fine solid particles (generated in attrition of bed grains and fuel ash in a fluidized bed) onto the coated grain surface, thus affecting the coating adhesiveness [29].

In the experiments with the (25% AS + 75% SS) mixture, bed defluidization was observed in the conical FBC after 17 h of combustor running. Some agglomerates were sampled and then analyzed for their physical and chemical properties. Fig. 7 shows the SEM–EDS analysis of agglomerates collected from this bed material after an emergent shutdown of the combustor. The SEM image in Fig. 7a revealed that the agglomerates were formed by binding the bed particles of different chemical compositions and sizes. The binding material that bonded the particles was rich in Si, K, and Ca with minor contents of Al, Mg, P, and Fe. The quantity and quality (i.e., chemical composition) of the binding materials at different spots in Fig. 7a indicated: (i) formation of low-

melting  $K_2O$ –SiO $_2$  and  $K_2O$ –CaO–SiO $_2$  eutectics (generally formed on the surface of SS particles as a result of reaction of K-rich vapor species from biomass ash with SiO $_2$  in SS grains) and (ii) small contribution of the ash melts to bed agglomeration.

It can be concluded that with a greater proportion of SS in a AS/SS mixture, the risk of (or tendency for) bed agglomeration increased significantly, mainly due to an increase in the SS surface area, on which the ash-derived K-rich vapor compounds reacted with  ${\rm SiO_2}$  in SS, forming low-melting-point eutectics, and thus enhancing the bed agglomeration tendency.

## 3.5. Time-related changes in compositions of the bed materials and particulate matter

Table 6 shows the composition of the bed mixtures, used/reused in the conical FBC during the co-firing tests for different operating time instants. Because of early bed agglomeration, the composition of the bed material, originally represented by the (25% AS + 75% SS) mixture, is presented in Table 6 only for the 8-h operating period. Due to the coating of AS and SS grains and because of presence of some PM retained in the bed, the ash-forming elements, particularly K, Ca, Mg, and Fe, showed an increase in their contents in all the bed mixtures with operating time. However, Al (responsible for mitigating bed agglomeration) showed a gradual time-domain decrease in the selected bed mixtures, which pointed at the diminishing capability of each bed material to withstand bed agglomeration. Note that the content of all constituents in a bed were noticeably affected by the bed AS/SS ratio.

Table 7 presents the composition of PM originating from the cocombustion of PKS and EFB for the same bed materials and operating

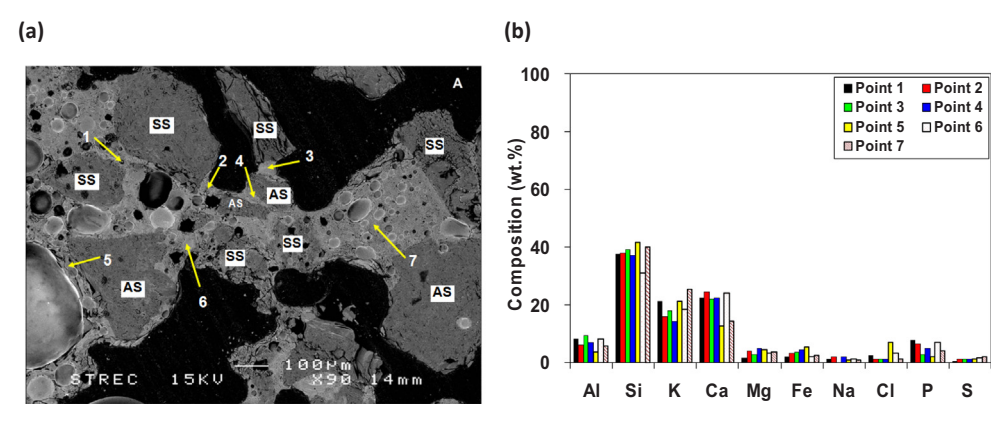


Fig. 7. (a) SEM image and (b) EDS spot analysis of agglomerates, sampled after 17-h co-firing tests on the conical FBC using a (25% AS + 75% SS) mixture as the bed material under optimal operating conditions.

Table 6
Composition of the bed materials used/reused in the conical FBC during cofiring of PKS and EFB under optimal operating conditions at different time instants of combustor operation.

Operating time (h)	Compo	sition (a	s oxide	s, wt.%	)			
	Al <sub>2</sub> O <sub>3</sub>	$SiO_2$	CaO	MgO	Na <sub>2</sub> O	K <sub>2</sub> O	Fe <sub>2</sub> O <sub>3</sub>	$P_2O_5$
Testing with the (75% A	S + 25%	SS) bed	mixtur	e				
6 (used bed material)	30.50	56.50	3.27	0.73	0.38	6.52	1.02	0.70
14 (reused bed material)	19.40	64.20	4.58	0.94	0.38	7.77	1.17	0.85
24 (reused bed material)	18.00	65.90	5.18	0.93	0.28	6.92	1.51	0.84
Testing with the (50% A	S + 50%	SS) bed	l mixtur	e				
8 (used bed material)	18.50	72.20	1.36	0.22	0.29	5.07	0.77	0.20
13 (reused bed material)	15.90	72.50	2.81	0.39	0.27	6.28	1.12	0.33
21 (reused bed material)	13.00	74.10	3.33	0.54	0.22	6.83	1.05	0.52
26 (reused bed material)	10.80	74.80	3.66	0.63	0.21	7.95	1.10	0.55
Testing with the (25% A	S + 75%	SS) bed	mixtur	e				
8 (used bed material)	10.70	81.00	1.07	0.20	0.29	5.69	0.74	0.15

times, as in Table 6. The results in Tables 6 and 7 indicate the significant mutual impact of the bed mixture and fuel ash during cocombustion of PKS and EFB. However, as seen in Table 7, in the test series with different AS/SS bed mixtures, the contents of Al and Si in PM were greater at all time instants, compared to those in the fuel ashes of the selected PKS/EFB mixture. This fact was likely due to carryover of fine particles rich with Al and Si (generated during the attrition of AS/SS grains in the fluidized bed), which joined the PM. Carryover of Al-rich particles from the fluidized bed contributed to a time-related decrease of  $Al_2O_3$  in the bed material during the co-combustion tests (as seen in Table 6).

#### 4. Conclusions

Oil palm kernel shell and empty fruit bunch with elevated/high potassium contents can be safely co-combusted in a fluidized-bed combustor with a cone-shaped bed using a mixture of alumina and silica sand as the bed material for decreasing the bed agglomeration tendency. Fuel staging, via injection of the biomass fuels into a combustor at different levels, leads to a substantial reduction in the NO emission from the combustor. The co-combustion of the selected oil palm residues at the optimal energy fraction of empty fruit bunch ( $\sim$ 0.15) and optimal excess air (50-55%) can ensure minimal "external" (emission) costs of the combustor at about 25–35% NO emission reduction (depending on the bed material type), compared to firing pure palm kernel shell. With a proportion of alumina sand in the bed mixture of greater than 50% (by wt.), bed agglomeration can be prevented in the combustor at reduced bed costs for a relatively long operational time. However, the bed material shows substantial time-domain changes in physical appearance and chemical composition, with a decrease in capability of the bed material to withstand bed agglomeration, especially when using mixtures with a relatively high proportion of silica sand in the bed mixture. When using a bed containing 75% silica sand mixed with 25% alumina sand, the bed material has a

Table 7
Composition of particulate matter originating from the co-firing of PKS and EFB in the conical FBC under optimal operating conditions when using selected AS/SS mixtures as the bed material for different operating times.

Operating time (h)	Composition (as oxides, wt.%)										
	$Al_2O_3$	$SiO_2$	CaO	MgO	Na <sub>2</sub> O	K <sub>2</sub> O	Fe <sub>2</sub> O <sub>3</sub>	$P_2O_5$	Cl		
Testing with the (75% AS + 25% a	SS) bed mixture										
6 (used bed material)	9.13	34.40	34.40	3.64	1.20	7.50	2.36	3.47	1.47		
14 (reused bed material)	4.03	43.40	33.10	2.91	0.58	6.99	2.10	3.49	0.91		
24 (reused bed material)	3.99	45.40	33.80	2.47	0.44	6.20	1.87	2.90	0.75		
Testing with the $(50\% AS + 50\%)$	SS) bed mixture										
8 (used bed material)	8.82	41.80	37.00	1.51	0.76	3.85	1.93	1.80	0.57		
13 (reused bed material)	6.75	43.00	35.70	1.92	0.75	4.51	2.25	2.29	0.64		
21 (reused bed material)	4.85	41.40	31.40	4.10	0.53	7.77	2.23	3.94	1.31		
26 (reused bed material)	3.88	43.10	29.60	3.32	0.44	9.56	2.44	3.71	1.55		
Testing with the $(25\% AS + 75\%)$	SS) bed mixture										
8 (used bed material)	5.54	55.10	25.90	1.92	0.40	5.06	1.97	2.32	0.29		

significant propensity for agglomeration, which may lead to fast bed defluidization in the combustor (within 17 h).

#### Acknowledgement

The authors wish to acknowledge the financial support from the Thailand Research Fund and Thammasat University (Contract No. BRG 5980005).

#### Appendix A. Supplementary material

Supplementary data associated with this article can be found, in the online version, at https://doi.org/10.1016/j.applthermaleng.2018.08.

#### References

- [1] Department of Alternative Energy Development and Efficiency, Ministry of Energy, Thailand. Thailand alternative energy situation, 2016. < http://www.dede.go.th/ download/state\_59/thailand%20alternative2016.pdf > (accessed 22.02.18).
- [2] J. Werther, M. Saenger, E.-U. Hartge, T. Ogada, Z. Siagi, Combustion of agricultural residues, Prog. Energy Combust. Sci. 26 (2000) 1–27.
- [3] W. Permchart, V.I. Kouprianov, Emission performance and combustion efficiency of a conical fluidized-bed combustor firing various biomass fuels, Bioresour. Technol. 92 (2004) 83–91.
- [4] T. Madhiyanon, P. Sathitruangsak, S. Soponronnarit, Combustion characteristics of rice-husk in a short-combustion-chamber fluidized-bed combustor (SFBC), Appl. Therm. Eng. 30 (2010) 347–353.
- [5] P. Ninduangdee, V.I. Kuprianov, Study on burning oil palm kernel shell in a conical fluidized-bed combustor using alumina as the bed material, J. Taiwan Inst. Chem. Eng. 44 (2013) 1045–1053.
- [6] P. Ninduangdee, V.I. Kuprianov, Combustion of an oil palm residue with elevated potassium content in a fluidized-bed combustor using alternative bed materials for preventing bed agglomeration, Bioresour. Technol. 182 (2015) 272–281.
- [7] V.I. Kouprianov, W. Permchart, Emissions from a conical FBC fired with a biomass fuel, Appl. Energy 74 (2003) 383–392.
- [8] S. Chakritthakul, V.I. Kuprianov, Co-firing of eucalyptus bark and rubberwood sawdust in a swirling fluidized-bed combustor using an axial flow swirler, Bioresour. Technol. 102 (2011) 8268–8278.
- [9] T. Nussbaumer, Combustion and co-combustion of biomass: fundamentals, technologies, and primary measures for emission reduction, Energy Fuels 17 (2003) 1510–1521.
- [10] K. Suksankraisorn, S. Patumsawad, B. Fungtammasan, Co-firing of Thai lignite and municipal solid waste (MSW) in a fluidised bed: Effect of MSW moisture content, Appl. Therm. Eng. 30 (2010) 2693–2697.
- [11] P. Sun, S. Hui, Z. Gao, Q. Zhou, H. Tan, Q. Zhao, T. Xu, Experimental investigation on the combustion and heat transfer characteristics of wide size biomass co-firing in 0.2 MW circulating fluidized bed, Appl. Therm. Eng. 52 (2013) 284–292.
- [12] M. Sami, K. Annamalai, M. Wooldridge, Co-firing of coal and biomass fuel blends, Prog. Energy Combust. Sci. 27 (2001) 171–214.
- [13] S.G. Sahu, N. Chakraborty, P. Sarkar, Coal-biomass co-combustion: an overview, Renew. Sustain. Energy Rev. 39 (2014) 575–586.
- [14] W.A.W.A.K. Ghani, A.B. Alias, R.M. Savory, K.R. Cliffe, Co-combustion of agricultural residues with coal in a fluidised bed combustor, Waste Manage. 29 (2009) 767–773.
- [15] L. Duan, Y. Duan, C. Zhao, E.J. Anthony, NO emission during co-firing coal and biomass in an oxy-fuel circulating fluidized bed combustor, Fuel 150 (2015) 8–13.
- [16] V.I. Kuprianov, K. Janvijitsakul, W. Permchart, Co-firing of sugar cane bagasse with rice husk in a conical fluidized-bed combustor, Fuel 85 (2006) 434–442.
- [17] IEA Clean Coal Center. Clean coal technologies. < http://www.iea-coal.org.uk/ site/2010/database-section/clean-coal-technologies > (accessed 22.02.18).
- [18] R. Salzmann, T. Nussbaumer, Fuel staging for NO<sub>x</sub> reduction in biomass

- combustion: experiments and modeling, Energy Fuels 15 (2001) 575-582.
- [19] C.-S. Chyang, F.-P. Qian, Y.-C. Lin, S.-H. Yang, NO and N<sub>2</sub>O emission characteristics from a pilot scale vortexing fluidized bed combustor firing different fuels, Energy Fuels 22 (2008) 1004–1011.
- [20] F. Duan, C.-S. Chyang, Y.-J. Wang, J. Tso, Effect of secondary gas injection on the peanut shell combustion and its pollutant emissions in a vortexing fluidized bed combustor, Bioresour. Technol. 154 (2014) 201–208.
- [21] C.E. Baukal Jr., The John Zink Combustion Handbook, CRC Press, New York, 2001.
- [22] P. Suheri, V.I. Kuprianov, Co-firing of oil palm empty fruit bunch and kernel shell in a fluidized-bed combustor: optimization of operating variables, Energy Proc. 79 (2015) 956–962.
- [23] K. Sirisomboon, V.I. Kuprianov, Effects of fuel staging on the NO emission reduction during biomass—biomass co-combustion in a fluidized-bed combustor, Energy Fuels 31 (2017) 659–671.
- [24] P. Chaivatamaset, P. Sricharoon, S. Tia, Bed agglomeration characteristics of palm shell and corncob combustion in fluidized bed, Appl. Therm. Eng. 31 (2011) 2916–2927.
- [25] P. Chaivatamaset, P. Sricharoon, S. Tia, B. Bilitewski, The characteristics of bed agglomeration/defluidization in fluidized bed firing palm fruit bunch and rice straw, Appl. Therm. Eng. 70 (2014) 737–747.
- [26] P. Chaivatamaset, P. Sricharoon, S. Tia, B. Bilitewski, A prediction of defluidization time in biomass fired fluidized bed combustion, Appl. Therm. Eng. 50 (2013) 722–731
- [27] H.J.M. Visser, The Influence of Fuel Composition on Agglomeration Behavior in Fluidized-Bed Combustion, Report No. ECN-C-04-54 Energy Research Center of Netherlands, 2004.
- [28] M. Öhman, A. Nordin, B.-J. Skrifvars, R. Backman, M. Hupa, Bed agglomeration characteristics during fluidized bed combustion of biomass fuels, Energy Fuels 14 (2000) 169–178.
- [29] E. Brus, M. Öhman, A. Nordin, Mechanisms of bed agglomeration during fluidized-bed combustion of biomass fuels, Energy Fuels 19 (2005) 825–832.
- [30] W. Lin, K. Dam-Johansen, F. Frandsen, Agglomeration in bio-fuel fired fluidized bed combustors, Chem. Eng. J. 96 (2003) 171–185.
- [31] P. Ninduangdee, V.I. Kuprianov, A study on combustion of oil palm empty fruit bunch in a fluidized bed using alternative bed materials: performance, emissions, and time-domain changes in the bed condition, Appl. Energy 176 (2016) 34–48.
- [32] V.I. Kuprianov, P. Arromdee, Combustion of peanut and tamarind shells in a conical fluidized-bed combustor: a comparative study, Bioresour. Technol. 140 (2013) 199–210.
- [33] P. Ninduangdee, V.I. Kuprianov, Experimental investigation and empirical modeling of flow regimes and hydrodynamic characteristics of a cone-shaped bed using sand-biomass binary mixtures, Chem. Eng. Process. 131 (2018) 1–11.
- [34] P. Basu, K. Cen, L. Jestin, Boilers and Burners, Springer, New York, 2000.
- [35] P. Ninduangdee, V.I. Kuprianov, Combustion of palm kernel shell in a fluidized bed: optimization of biomass particle size and operating conditions, Energy Convers. Manage. 85 (2014) 800–808.
- [36] ESCAP-UN, Energy Efficiency, New York, United Nations, 1995.
- [37] X. Wei, L. Zhang, H. Zhou, Evaluating the environmental value of pollutants in China power industry, Proceedings of the International Conference on Energy and the Environment, Shanghai, China, (2003).
- [38] L. Czarnowska, C.A. Frangopoulos, Dispersion of pollutants, environmental externalities due to a pulverized coal power plant and their effect on the cost of electricity, Energy 41 (2012) 212–219.
- [39] S.R. Turns, An Introduction to Combustion: Concepts and Applications, McGraw-Hill Series in Mechanical Engineering, Singapore, second ed., international ed., 2006
- [40] Pollution Control Department, Ministry of Natural Resources and Environment, Thailand, Air pollution standards for industrial sources. < http://www.pcd.go.th/ info\_serv/reg\_std\_airsnd03.html > (accessed 22.02.18).
- [41] S. Li, J.L. Yu, X.L. Wei, X.F. Guo, Y. Chen, Catalytic reduction of nitric oxide by carbon monoxide over coal gangue hollow ball, Fuel Process. Technol. 125 (2014) 163–169.
- [42] C. Wang, Y.B. Du, D.F. Che, Investigation on the NO reduction with coal char and high concentration CO during oxy-fuel combustion, Energy Fuels 26 (2012) 7367–7377.
- [43] P. Chaivatamaset, S. Tia, The characteristics of bed agglomeration during fluidized bed combustion of eucalyptus bark, Appl. Therm. Eng. 75 (2015) 1134–1146.

ELSEVIER

#### Contents lists available at ScienceDirect

### Biomass and Bioenergy

journal homepage: www.elsevier.com/locate/biombioe



#### Research paper

## Fluidized bed co-combustion of rice husk pellets and moisturized rice husk: The effects of co-combustion methods on gaseous emissions



Pichet Ninduangdee<sup>a</sup>, Vladimir I. Kuprianov<sup>b,\*</sup>

- Division of Mechanical Engineering, Faculty of Engineering and Industrial Technology, Phetchaburi Rajabhat University, Phetchaburi, 76000, Thailand
- b School of Manufacturing Systems and Mechanical Engineering, Sirindhorn International Institute of Technology, Thammasat University, P.O. Box 22, Thammasat Rangsit Post Office, Pathum Thani, 12121, Thailand

#### ARTICLE INFO

# Keywords: Rice husk Fluidized-bed combustor Co-firing techniques Co-firing optimization NO emission reduction

#### ABSTRACT

This work explores the potential of three co-combustion methods for reducing  $NO_x$  in a fluidized-bed combustor. Pelletized rice husk (base fuel) was co-fired with moisturized rice husk (secondary fuel) in this reactor using silica sand as the bed material. Four groups of experiments for (1) conventional combustion of rice husk pellets, (2) co-firing pre-mixed fuels, (3) co-firing using fuel staging with bottom air injection, and (4) co-firing using a reburning method combining fuel staging and air staging, were performed at a 200 kW heat input to the reactor. In the test series, the energy fraction of the secondary fuel in the total fuel supply (EF<sub>2</sub>) was within 0–0.25, with excess air (EA) varying from 20% to 80% at given EF<sub>2</sub>. During the reburning tests, the secondary-to-total air ratio (SA/TA) ranged from 0.1 to 0.4, at each EA. The findings revealed that the effects of EF<sub>2</sub>, EA, and SA/TA on the combustion and emission characteristics of the reactor were substantial. An optimization analysis was performed to determine the optimal EF<sub>2</sub>, EA, and SA/TA, leading to minimal emission costs of the applied co-firing techniques. Under optimal operating conditions, the combustor ensures high (~99%) combustion efficiency with minimum emission costs and reduced NO emission: by about 13% when co-firing pre-mixed fuels, by 37% for the fuel-staged co-combustion, and by 53% when using reburning, as compared to 167–176 cm<sup>3</sup> m<sup>-1</sup> from burning the base fuel alone. However, some increase in the CO and  $C_xH_y$  emissions was observed when using the proposed co-firing techniques.

#### 1. Introduction

In Thailand, rice husk is an important biomass energy resource, showing an energy potential of 93 PJ per year, mainly because of great availability and the relatively high calorific value of this agricultural residue [1]. Due to some advantages over grate firing and pulverized fuel firing techniques, bubbling, circulating, vortexing, and swirling fluidized-bed combustion systems (combustors/furnaces) are effective for converting rice husk into energy, mainly because of excellent solid-gas mixing, temperature homogeneity and effective emission control [2-6]. However, pioneering studies on these combustion systems have reported difficulties in achieving high combustion efficiency and controlling CO and NO<sub>x</sub> emissions, mainly because of elevated fuel-N and fuel-ash contents. In spite of moderate bed temperatures (typically, below 850 °C), the NO<sub>x</sub> emissions from the above-listed fluidizedbed combustors were elevated, up to about 200 cm<sup>3</sup> m<sup>-3</sup>, while the CO emission was within 800 cm<sup>3</sup> m<sup>-3</sup> (both at 6% O<sub>2</sub> on a dry gas basis). The combustion efficiency of properly designed and operated fluidizedbed combustion systems was 96-98%. Some studies on circulating,

vortexing, and swirling fluidized-bed combustors showed weak effects of air staging on  $NO_x$  and CO emissions when burning rice husk [4–6]. However, the use of flue gas recirculation in the vortexing fluidized-bed combustor resulted in relatively low  $NO_x$  emissions, 65–83 cm<sup>3</sup> m<sup>-3</sup> (at 11%  $O_2$  on a dry gas basis), mainly because of the lowered bed temperature (about 700 °C) and dilution effects from the recycled flue gas [7]

A cyclonic fluidized-bed combustor, ensuring biomass oxidation in a strongly swirled flow, has been developed for firing rice husk [8]. High, over 99%, combustion efficiency was achieved with this technique when burning rice husk under optimal operating conditions, mainly due to the reduced CO emission, below 400 cm $^3$ m $^{-3}$  (at 6%  $\rm O_2$  on a dry gas basis). However, the NO $_x$  emissions from the cyclonic fluidized-bed combustor were high, 350–425 cm $^3$ m $^{-3}$ , likely because of the high combustion intensity (or heat release rate per unit combustor volume) and elevated excess air, as compared to other fluidized-bed combustion systems.

Co-firing (or co-combustion) of two or more fuels with different properties is one of the most effective ways of improving the emission

E-mail address: ivlaanov@siit.tu.ac.th (V.I. Kuprianov).

<sup>\*</sup> Corresponding author.

P. Ninduangdee, V.I. Kuprianov

Biomass and Bioenergy 112 (2018) 73–84

performance of a combustion system, while maintaining its combustion efficiency at a relatively high level. Some related studies on grate-firing, pulverized fuel-firing, cyclone-firing, and fluidized-bed combustion systems revealed that the co-firing is flexible for fuel type (coal, biomass, RDF, combustible wastes, etc.) and combustion method [9–12]. However, the combustion and emission performance of a combustion system was affected by the method of fuel injection into the combustor/furnace.

A large number of studies on the co-firing of coal and biomass, commonly used as blended fuels in modified pulverized coal-fired boilers, have reported a reduced (net) production of  $CO_2$ , as well as a noticeable reduction in  $NO_x$  and  $SO_2$  emissions, compared to burning coal on its own [11–16]. Limited knowledge, regarding the co-firing of biomass with another biomass in a single fluidized-bed combustion system, is reported in the literature. However, some pilot studies revealed that biomass—biomass co-firing systems can effectively utilize problematic fuels (e.g., with unacceptable emission characteristics and/or very low calorific value) with lower emissions of  $NO_x$ , compared to burning the base fuel alone [17,18].

Fuel-staged combustion methods, such as fuel biasing and reburning, have been proposed to reduce  $NO_x$  in various combustion systems (co-)fired with coal/biomass. When using fuel biasing (a type of fuel staging), the base fuel is injected into the main (or primary) combustion zone together with combustion air, whereas the rest of the fuel or another fuel is added downstream of the primary zone with no air supply [19]. As a result, chemical reactions occurring in the secondary zone generate precursors (radicals) to participate in the reduction of  $NO_x$ , previously formed in the primary zone. A recent study on the co-firing of palm kernel shell (primary fuel) and high-moisture empty fruit bunch (secondary fuel) in a fluidized-bed combustor has revealed a 35% NO emission reduction that was achieved via the use of fuel-staged combustion with bottom air injection. However, the  $NO_x$  reduction level was found to depend on the mass/energy share of the secondary fuel and excess air used [20].

A reburning method has been suggested as one of the most effective solutions to reduce NO<sub>x</sub> emissions from different combustion systems. This method is, in fact, a combination of fuel staging and air staging [10]. The relevant processes occur within three sequent zones of the reactor: (i) primary zone where primary (main) fuel burns, (ii) reburn zone where the reburn (secondary) fuel is injected into the reactor to create fuel-rich conditions, resulting in a reduction of NOx formed in the preceding zone, and (iii) burnout zone, where the burnout (secondary) air is introduced for achieving complete combustion [21,22]. The reburning method has been extensively studied on large-scale pulverized coal-fired boilers and grate-fired biomass-fueled systems, with different types of reburn fuel. Some pioneering studies have reported that up to 70% NO<sub>x</sub> reduction can be achieved with this method, with no adverse effects on the operation of a combustion system [21-24]. However, very limited information on applications of both fuel staging and reburning in fluidized-bed systems co-firing different types of biomass has been reported in the literature.

The main purpose of this work was to explore the potential of three co-firing methods: (i) burning pre-mixed fuels, (ii) using fuel staging with bottom air injection, and (iii) using reburning, with the aim to reduce the  $\mathrm{NO}_x$  emissions of a fluidized-bed combustor co-fired with pelletized rice husk (PRH) and moisturized rice husk (MRH). Effects of operating conditions on the behavior of major pollutants (CO,  $C_x H_y$ , and NO) in different reactor regions, as well as on the emissions and combustion efficiency of the combustor, were compared for the proposed co-combustion methods. Special attention was given to the optimization of operating parameters, minimizing the emission costs of the co-firing techniques. The novelty of this work is knowledge on the influence of the selected co-combustion methods on the extent of NO emission reduction, as well as practical guidelines on optimal operating conditions, during biomass — biomass co-firing in fluidized-bed combustion systems.

#### 2. Materials and methods

#### 2.1. Experimental setup

A fluidized-bed combustor with a cone-shaped bed (referred to as a 'conical FBC') was used in this study. The experimental setup, including the conical FBC and auxiliary equipment (two air blowers, two screwtype fuel feeders, a cyclone for collecting particulate matter, and a diesel-fired start up burner), is shown in Fig. 1. The combustor consisted of two steel sections assembled coaxially: (1) a conical section of 0.9 m height with 40° cone angle and 0.25 m inner diameter at the bottom plane, and (2) a cylindrical section of 2.5 m height and 0.9 m inner diameter. A more detailed description of the combustor's configuration has been provided in previous studies on individual firing of biomass with this combustion technique [25,26].

In the current work, during the test runs for individual firing PRH and co-firing pre-mixed PRH and MRH, the base fuel and the biomass mixtures were supplied into the reactor by using a single fuel feeder located at level  $Z=0.6\,\mathrm{m}$  above the air distributor, whereas the combustion air was injected into the bottom (conical) section of the conical FBC by an  $18.7\,\mathrm{kW}$  air blower through the air distributor at the reactor bottom. The air distributor, comprising nineteen bubble-cap standpipes (closely arranged on the distributor plate), induced fluidization of the bed material in the conical section. Each stand pipe had 64 holes of  $2\,\mathrm{mm}$  in diameter, evenly arranged over the pipe outer surface, and six vertical slots ( $15\,\mathrm{mm} \times 3\,\mathrm{mm}$  in sizes) at the top of the pipe. The proposed design of the air distributor ensured quite uniform distribution of airflow over the bed (i.e., avoiding bed spouting) with an insignificant pressure drop across the device [26].

To perform co-firing tests for fuel staging and reburning methods, the combustor was additionally equipped with a secondary fuel feeder and a secondary air system (the latter was used in reburning tests). During the tests of these two groups, primary and secondary fuels were delivered separately into the reactor by the two screw-type fuel feeders, as shown in Fig. 1. The primary fuel was injected into the fluidized bed at  $Z=0.6\,\mathrm{m}$  above the air distributor, whereas the secondary fuel was introduced into the cylindrical section of the combustor, at  $Z=1.15\,\mathrm{m}$ , by a secondary fuel feeder. Primary (or fluidizing) air was injected into the bed by the above-mentioned 18.7 kW air blower through the air distributor, whereas in reburning tests, the secondary air (SA) was tangentially introduced into the reactor at  $Z=1.65\,\mathrm{m}$  by a secondary 3.7 kW blower.

#### 2.2. Fuels and bed material

As shown in previous studies on fuel-staged biomass co-combustion with bottom air supply, a substantial reduction of the  $NO_x$  emissions can be achieved when primary and secondary biomass fuels comply with two major requirements [20,27]. Firstly, the calorific value of a primary fuel should be noticeably higher than that of the secondary fuel, mainly due to substantial moisture content in the secondary fuel. This requirement ensures stable and high-efficiency combustion in the primary combustion zone, avoiding a high temperature peak inside the reactor. Secondly, it is desirable (but not compulsory) to use a secondary fuel with the fuel-N content lower than that in the primary fuel, to prevent intensive NO formation in the secondary combustion zone. With the use of reburning, the  $NO_x$  reduction is expected to be more significant, as compared with the fuel-staged co-combustion, mainly due to the more active mitigation of NO formation reactions and strengthening of secondary (NO reduction) reactions in the primary and reburn zones.

In this work, pelletized rice husk (PRH) was used as the base (primary) fuel, while low-calorific moisturized rice husk (MRH) was selected to be the secondary fuel. PRH was supplied by a local company manufacturing pelletized biomass fuels. Prior to the pelleting process that used a flat-die fuel pellet machine, "as-received" rice husk was

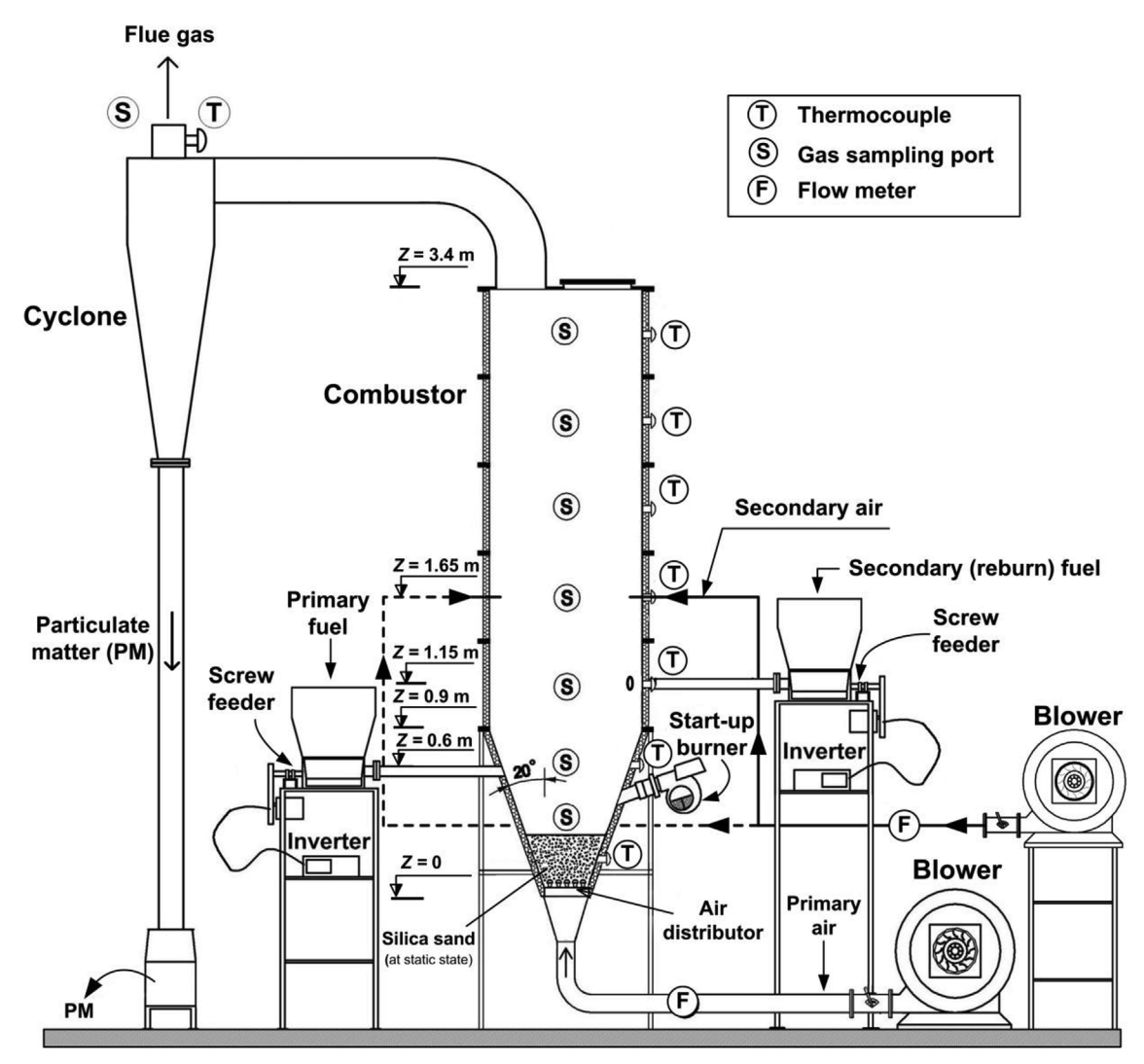


Fig. 1. Schematic diagram of the experimental setup for co-combustion experiments.

conveyed to a sieving system (to remove solid impurities) and then ground by a grinding mill to the specified particle size. At a next step, ground rice husk was fed, together with a specified amount of water, into a 75 kW pelletizer, which pressed the ground biomass into cylindrical pellets of 6 mm in diameter and about 15 mm in length. At the final stage, the pellets were spread onto a wire screen for cooling and drying, and afterwards, were packed in fabric sacks to keep stable fuel quality for a relatively long time. Prior to testing, MRH was prepared by adding a specified amount of water to "as-received" rice husk, supplied from a local rice mill. The MRH particles were (on average) about 2 mm in width, 0.5 mm thick, and 10 mm in length.

The proximate and ultimate analyses, as well as the lower heating values of PRH and MRH, are represented in Table 1. The analyses

showed a significant difference in properties of the two fuels. Due to substantially higher fuel-moisture content in MRH, the lower heating value of this secondary fuel,  $LHV_{\rm f2}=10.6~MJ/kg$ , was noticeably lower than that of the primary fuel,  $LHV_{\rm f1}=15.1~MJ/kg$ . Because of insignificant fuel-S in both fuels, this work disregarded all issues related to the formation and emission of  $SO_2$  during (co-)firing PRH and MRH.

The fuel ash of both fuels included 85-95% SiO<sub>2</sub> and 1.5-2.5% K<sub>2</sub>O with negligible amounts of other ash-related elements, and therefore, was not reactive to all types of bed material, indicating a low propensity of rice husk for bed agglomeration [28]. Therefore, a conventional bed material, silica sand with  $2500 \, \text{kg m}^{-3}$  solid density,  $0.3-0.5 \, \text{mm}$  particle sizes, containing 88% SiO<sub>2</sub> (by weight), was used in this combustor. In all experiments, the bed height was maintained at  $30 \, \text{cm}$ 

Table 1
Properties of pelletized rice husk (PRH) and moisturized rice husk (MRH), used in co-combustion experiments.

Biomass	Proximate a	analysis, mass fra	ection (%) <sup>a</sup>		Ultimate a	Ultimate analysis, mass fraction (%) <sup>b</sup>					
	w	VM	FC	A	С	Н					
PRH	9.81	64.9	15.39	9.90	53.89	6.28	38.83	0.98	0.02	15.1	
MRH	29.56	41.9	14.33	14.21	53.25	5.35	40.70	0.68	0.02	10.6	

<sup>&</sup>lt;sup>a</sup> On "as-fired" basis, after pre-treatment of "as-received" rice husk,

<sup>&</sup>lt;sup>b</sup> On dry and ash-free basis.

P. Ninduangdee, V.I. Kuprianov

Biomass and Bioenergy 112 (2018) 73-84

(under static conditions).

As observed in "cold-state" experiments on a test rig with the configuration identical to the combustor conical section, when the superficial air velocity at the air distributor exit (u) was between the minimum velocity of full fluidization ( $u_{\rm mff}$ ) and the minimum velocity of turbulent fluidized-bed regime ( $u_{\rm k}$ ), the cone-shaped bed of silica sand fluidized by airflow showed a bubbling fluidization regime. From the "cold-state" experiments, for the conical bed of silica sand with the specified sand particle sizes and bed dimensions (cone angle, static bed height, and diameter of the lower base), the characteristic velocities were:  $u_{\rm mff} \approx 0.7~{\rm m\,s}^{-1}$  and  $u_{\rm k} \approx 1.6~{\rm m\,s}^{-1}$ . At  $u > u_{\rm k}$ , the fluidized bed turned into a turbulent fluidization regime, exhibiting an expanded volume of the bed gas – solid mixture, compared to the bubbling fluidized bed. Similar behavior of the conical bed (however, at different  $u_{\rm mff}$  and  $u_{\rm k}$ ) has been reported for some alternative bed materials, such as alumina sand, dolomite, and limestone [26].

#### 2.3. Experimental methods for the co-combustion tests

At the preliminary stage of this work, a test series for burning pure PRH, using bottom air injection into the reactor, was performed to obtain combustion and emission characteristics of the base fuel. During the tests, PRH was fed into the reactor by the lower fuel feeder. In the main study, three series of co-firing tests, aimed at reducing  $NO_x$  emissions from the combustor, were conducted: (i) co-firing of premixed PRH and MRH, (ii) co-firing of the selected fuels using fuel staging with bottom air injection, and (iii) co-firing of the two types of rice husk using a reburning technique (combining fuel and air staging). For comparability, all test series were performed at a constant (200 kW) heat input to the conical FBC. This allowed using the energy fraction of the secondary fuel (EF2) as an independent operating parameter in the co-combustion tests.

To ensure the specified heat input, PRH and MRH were delivered into the combustor with respective mass flow rates ( $\dot{m}_{\rm fl}$  and  $\dot{m}_{\rm f2}$ ) at any given EF<sub>2</sub>, defined as the energy share of MRH ( $\dot{m}_{\rm f2}$ LHV<sub>f2</sub>) in the total heat input to the reactor ( $\dot{m}_{\rm fl}$ LHV<sub>f1</sub> +  $\dot{m}_{\rm f2}$ LHV<sub>f2</sub>). In this work, the trials (except for reburning) were performed for five values of EF<sub>2</sub>: 0 (i.e., for firing pure PRH), 0.1, 0.15, 0.2, and 0.25. Table 2 shows the feed rates of the primary and secondary fuels, as well as the mass fraction of MRH in the total fuel supply, for each selected EF<sub>2</sub>.

In all four test series, the experiments were performed at four specified amounts of excess air (EA) at stack: 20%, 40%, 60%, and 80%. For each test run, an actual value of EA was determined according to Ref. [29], by using relationships provided in Appendix A and taking into account actual  $O_2$ , CO, and  $C_xH_y$  (as  $CH_4$ ), all measured at stack with a "Testo-350" gas analyzer. The measuring accuracies of the gas concentrations were:  $\pm~0.2\%$  for  $O_2$  (as a volume fraction),  $\pm~5\%$  of reading for CO from 200 to  $2000~cm^3~m^{-3}$ ,  $\pm~10\%$  of reading for CO higher than  $2000~cm^3~m^{-3}$ ,  $\pm~10\%$  of reading for  $C_xH_y$  (as  $CH_4$ ), and  $\pm~5\%$  of reading for NO not over  $2000~cm^3~m^{-3}$ .

To save experimental time and fuels, the reburning tests were conducted at two (close to typical) values of the secondary fuel energy fraction [20,27]:  $EF_2 = 0.15$  and  $EF_2 = 0.25$  for the above-mentioned

Table 2
Feed rate of pelletized rice husk (PRH) and moisturized rice husk (MRH) in the cocombustion tests at different energy/mass fractions of the secondary fuel (MRH) in total
fuel supply.

Energy fraction of MRH (EF <sub>2</sub> )	MRH feed rate (kg $h^{-1}$ )	PRH feed rate (kg h <sup>-1</sup> )	Mass fraction of MRH (MF <sub>2</sub> )
0	0	47.7	0
0.10	6.8	42.9	0.14
0.15	10.2	40.5	0.20
0.20	13.6	38.1	0.26
0.25	17.0	35.8	0.32

range of EA. However, at each (fixed) EA, the reburning tests were performed for four secondary-to-total air (SA/TA) ratios: 0.1, 0.2, 0.3, and 0.4.

To investigate the effects of the applied co-firing methods and operating variables (EF<sub>2</sub>, EA, and SA/TA) on the co-combustion characteristics, as well as on the formation and oxidation/reduction of the gaseous pollutants inside the conical FBC, temperature,  $O_2$ , CO,  $C_xH_y$  (as  $CH_4$ ), and NO were measured along the reactor centerline, using the "Testo-350" gas analyzer, for some selected operating conditions.

To study the influence of the operating variables on the gaseous emissions and combustion efficiency of the conical FBC, the CO, CxHv (as CH<sub>4</sub>), and NO<sub>y</sub> (as NO) emission concentrations were measured at stack, along with O<sub>2</sub>, for the specified EF<sub>2</sub>, EA, and SA/TA. In all test runs, fly ash was sampled and analyzed for unburned carbon. Afterwards, the combustion efficiency of the conical FBC was determined for each run using the heat-loss method, according to Ref. [29]. However, in the current work, the heat loss due to unburned carbon and that due to incomplete combustion, were predicted based on a concept of "equivalent fuel", as proposed in Ref. [27] and presented in Appendix B. The relevant properties of "equivalent fuel", such as the lower heating value (LHV<sub>cf</sub>, in units of kJ kg<sup>-1</sup>), the ash content (Acf, as a mass fraction in units of %), and the volume of dry flue gas  $(V_{\rm dg,cf}, \text{ in units of m}^3 \text{ kg}^{-1} \text{ under standard conditions}), \text{ were quantified}$ by taking into account the corresponding properties and mass fractions (the latter as weighting factors) of the co-fired PRH and MRH [27].

By taking into account: (i) the stoichiometric amount of air required for burning 1 kg "equivalent fuel" (V<sup>0</sup>, in units of m<sup>3</sup> kg<sup>-1</sup> under standard conditions, calculated according to Refs. [27,29]), (ii) the feed rate of the co-fired PRH and MRH, (iii) the amount of excess air, and (iv) the cross-sectional area of airflow, the superficial air velocity at the air distributor exit (u) was assessed for the selected (co-)combustion options. For instance, when burning pure PRH with  $V^0 = 4.15 \,\mathrm{m}^3\,\mathrm{kg}^{-1}$ the superficial velocity varied within 4.1-6.2 m s<sup>-1</sup> for 20-80% EA. However, during co-firing PRH and MRH using reburning at  $EF_2 = 0.25$ and SA/TA = 0.4 (when  $V^0$  counted for  $3.68 \,\mathrm{m}^3 \,\mathrm{kg}^{-1}$  at a reduced flowrate of the primary air), the values of u were lowest (1.7–2.5 m s<sup>-1</sup>) for the same range of EA, as compared to the other three test series. Thus, when using the selected operating parameters (EF2, EA and SA/ TA), the combustor was operated in the turbulent fluidized-bed regime, as u was greater than the above-reported  $u_k$  for the silica sand bed of the selected configuration. During this fluidization regime, the expanded bed occupied a predominant part of the conical section, ensuring "inbed" injection of PRH, whereas MRH was injected into the reactor above the expanded bed.

#### 2.4. Optimization method for operating variables

To determine the optimal operating variables (EF $_2$ , EA, and SA/TA), ensuring minimal "external" costs of the combustor for the selected cocombustion options, a cost-based optimization method [27,30] was applied in this work. The "external" costs were mainly represented by emission costs, paying for the damage done by gaseous pollutants emitted from a combustion system to the environment and humans [31], thus disregarding damage costs associated with long-term climate change. Ignoring the effects of SO $_2$  (because of its negligible emission) and CO $_2$  (due to the low specific "external" costs of CO $_2$  and weak effects of operating conditions on the CO $_2$  emission rate), the objective function to minimize the "external" costs of co-combustion of PRH and MRH can be represented as:

$$J_{\text{ec}} = \text{Min}(P_{\text{NOx}}\dot{m}_{\text{NOx}} + P_{\text{CO}}\dot{m}_{\text{CO}} + P_{\text{CxHy}}\dot{m}_{\text{CxHy}})$$
(1)

In this study, the specific "external" costs of NO<sub>x</sub> (as NO<sub>2</sub>) and C<sub>x</sub>H<sub>y</sub> (as CH<sub>4</sub>) were assumed to be  $P_{\rm NOx} = 2400~\rm s~t^{-1}$  and  $P_{\rm CH4} = 330~\rm s~t^{-1}$ , respectively, according to Ref. [31]. As reported in some related study [6,32,33], the ratio of  $P_{\rm NOx}$  to  $P_{\rm CO}$  generally ranges from 5 to 8. It was therefore decided to assume  $P_{\rm CO} = 400~\rm s~t^{-1}$  (for  $P_{\rm NOx}/P_{\rm CO} = 6$ ) in this

P. Ninduangdee, V.I. Kuprianov

Biomass and Bioenergy 112 (2018) 73-84

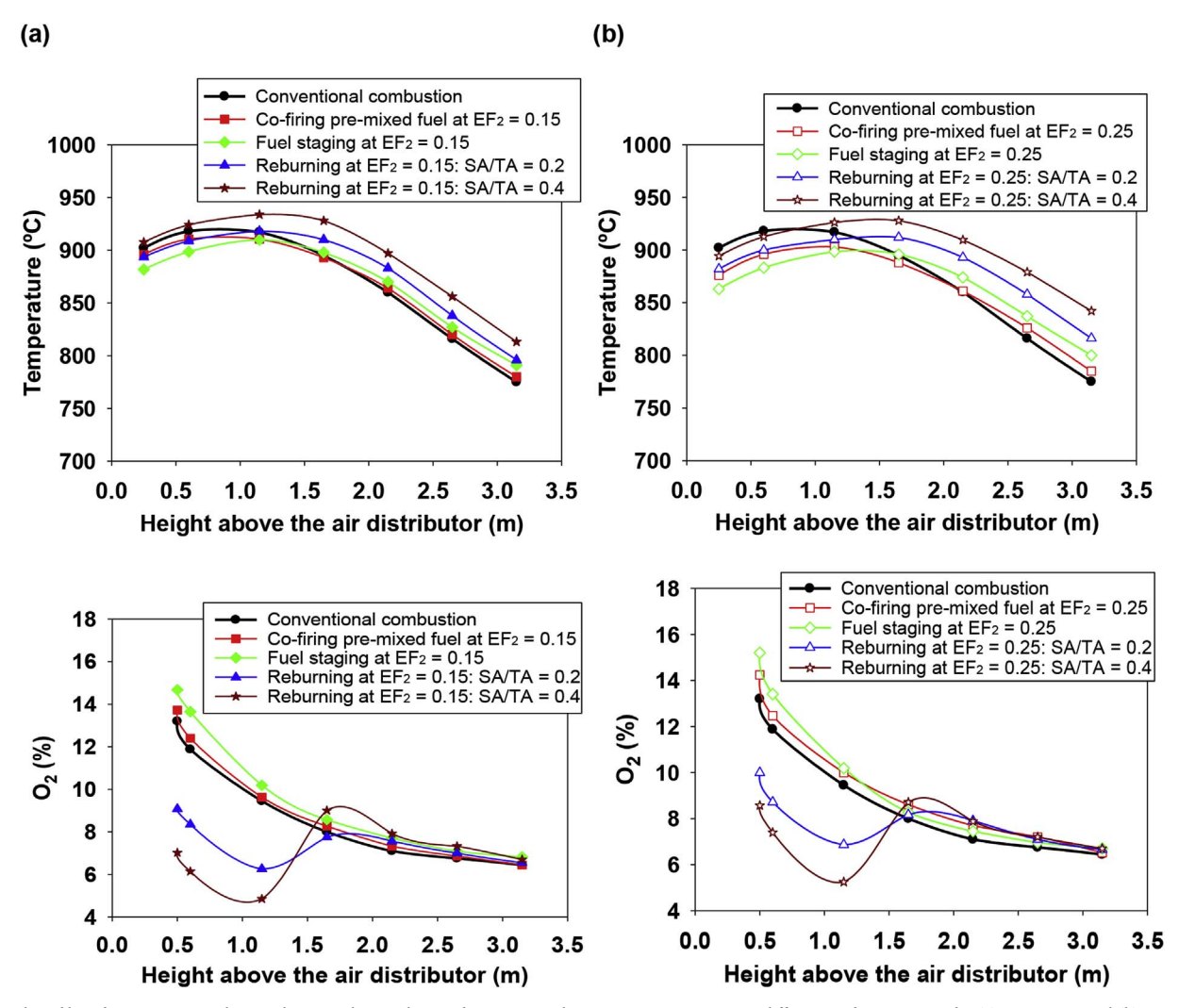


Fig. 2. Axial profiles of temperature and  $O_2$  in the conical FBC when co-firing PRH and MRH at EA  $\approx 40\%$ , using different co-firing options for (a) EF<sub>2</sub> = 0.15 and (b) EF<sub>2</sub> = 0.25, in comparison with the conventional combustion of PRH.

optimization analysis.

For given operating conditions, the mass fluxes of  $NO_x$  (as  $NO_2$ ), CO, and  $C_xH_y$  (as  $CH_4$ ) emissions in Eq. (1) were predicted by taking into account the feed rate (kg/s) of the co-fired fuels, as well as the actual emission concentrations (in cm<sup>3</sup> m<sup>-3</sup>), measured at the cyclone exit as:

$$\dot{m}_{\text{NO}_x} = 2.05 \times 10^{-6} (\dot{m}_{\text{fl}} + \dot{m}_{\text{f2}}) \text{NO}_x V_{\text{dg,cf}}$$
 (2)

$$\dot{m}_{\rm CO} = 1.25 \times 10^{-6} (\dot{m}_{\rm f1} + \dot{m}_{\rm f2}) \text{COV}_{\rm dg,cf}$$
 (3)

$$\dot{m}_{C_x H_y} = 0.71 \times 10^{-6} (\dot{m}_{f1} + \dot{m}_{f2}) C_x H_y V_{dg,cf}$$
 (4)

where  $V_{\rm dg,cf}$  is the volume of dry combustion products from the cofiring of MRH and PRH at actual excess air (in m<sup>3</sup> kg<sup>-1</sup>, under standard conditions), determined according to Refs. [27,29] using the mass fractions of the two fuels.

Taking into account the selected specific "external" costs ( $P_{\rm NOx}$ ,  $P_{\rm CO}$ , and  $P_{\rm CH4}$ ) and differences in the density of NO<sub>x</sub> (as NO<sub>2</sub>), CO, and C<sub>x</sub>H<sub>y</sub> (as CH<sub>4</sub>), it can concluded that the contribution of NO<sub>x</sub> to the total "external" costs in Eq. (1) is predominant. For a given co-combustion technique and similar emission concentrations of the pollutants (at stack), the NO<sub>x</sub> emissions cost is about 10 times greater than for CO, and 20 times greater than for C<sub>x</sub>H<sub>y</sub>. Thus, the NO<sub>x</sub> reduction inside the reactor is a goal of great importance.

#### 3. Results and discussion

#### 3.1. Distribution of temperature and $O_2$ in the conical FBC

Fig. 2 shows the axial temperature and  $O_2$  profiles in the combustor for the selected co-combustion techniques, co-fired with PRH and MRH at EF $_2$  = 0.15 (Fig. 2a) and EF $_2$  = 0.25 (Fig. 2b), and EA  $\approx$  40% with different SA/TA (applied in the reburning tests), as compared with the conventional combustion of the base fuel (PRH) at the specified EA.

In all trials, the axial temperature profiles were rather uniform, particularly in the fluidized bed region (i.e., within the conical section of the combustor). There were some effects of EF $_2$  and SA/TA on the bed temperature, including its maximum. When burning the base fuel on its own, a maximum bed temperature of about 920 °C was observed in the vicinity of PRH injection (at  $Z=0.6\,\mathrm{m}$ ). However, during cocombustion of pre-mixed PRH and MRH, the bed temperature was lower than that for firing pure PRH: by 10 °C at EF $_2=0.15$  and by 35 °C at EF $_2=0.25$ , likely due to the increased moisture content in the fuel blend.

In the tests for fuel staging with bottom air injection, the temperature at all points in the bottom region was lower, compared to the other co-firing options. This was mainly due to the reduced feeding of PRH that resulted in an increased (local) excess air ratio at the primary combustion zone (i.e., in the fluidized bed). Because of the effects from secondary fuel injection, the maximum temperature for  $EF_2 = 0.15$ ,

P. Ninduangdee, V.I. Kuprianov Biomass and Bioenergy 112 (2018) 73-84

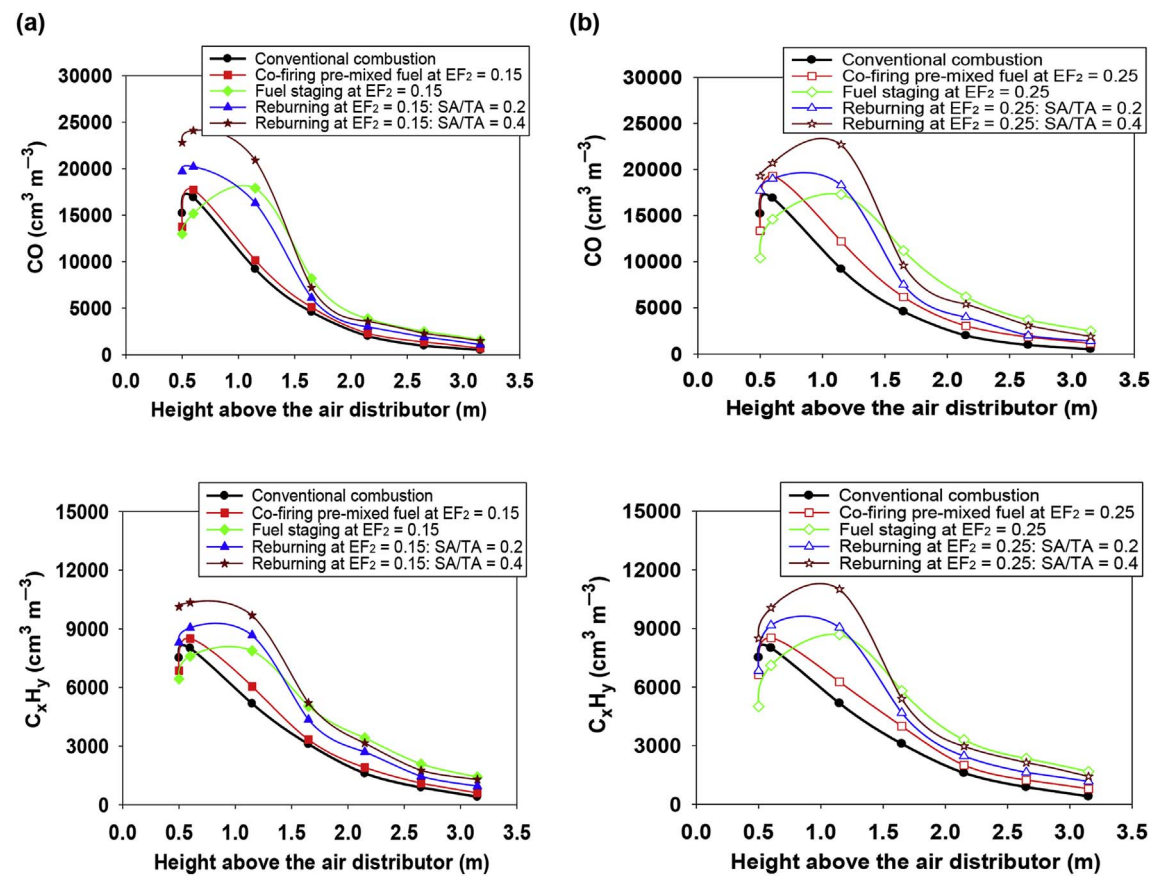


Fig. 3. Axial profiles of CO and  $C_xH_y$  (as  $CH_4$ ) in the conical FBC when co-firing PRH and MRH at  $EA \approx 40\%$ , using different co-firing options for (a)  $EF_2 = 0.15$  and (b)  $EF_2 = 0.25$ , in comparison with the conventional combustion of PRH.

910 °C, was observed at a higher level,  $Z=1.15\,\mathrm{m}$  (i.e., beyond the conical section), compared to burning pure PRH. However, during fuel-staged co-combustion at EF $_2=0.25$  (i.e., at a higher feed rate of MRH), the maximum temperature, 890 °C, was shifted to  $Z=1.6\,\mathrm{m}$  due to the strengthened effects from the secondary fuel.

It can be seen in Fig. 2 that during the reburning tests at SA/TA = 0.2 and SA/TA = 0.4, the temperatures inside the reactor were basically higher, as compared to the other two co-firing options for similar EF<sub>2</sub>. This is mainly due to the lowered (local) excess air ratio in the primary combustion zone. Injection of secondary air at  $Z=1.65\,\mathrm{m}$  resulted in the higher maximum temperature in the reburning tests, because of delayed oxidation of combustibles formed in the reburn zone and, therefore, shifting this temperature to a higher level (Z). Note that the maximum temperature in the reburning tests was almost independent of EF<sub>2</sub>. However, it was noticeably affected by SA/TA: 915 °C for SA/TA = 0.2 and 930 °C for SA/TA = 0.4, observed at  $Z=1.15\,\mathrm{m}$  for EF<sub>2</sub> = 0.15 and at  $Z=1.6\,\mathrm{m}$  for EF<sub>2</sub> = 0.25.

In all the test runs, the temperature showed a gradual decrease in the upper part of the combustor, mainly because of the heat loss across the reactor walls, at nearly the same rate. Therefore, the difference between the axial temperature profiles for the selected (co-)combustion methods was primarily affected by the magnitude and location of the maximum temperature in each test run. As a result, in the reburning tests at  $\text{EF}_2 = 0.25$  and SA/TA = 0.4, the temperatures at similar points in the reactor top were higher, as compared to other test series.

From Fig. 2, the axial profiles of  $O_2$  in the tests for burning pure PRH, co-firing of premixed PRH and MRH, and fuel-staged co-combustion of the two fuels showed similar trends, with weak effects from EF<sub>2</sub>. In these three test series, a substantial axial gradient of  $O_2$  was observed in the lower part of the reactor ( $Z < 1.6 \,\mathrm{m}$ ), comprising primary and secondary combustion zones, whereas in the upper region

of the reactor,  $O_2$  consumption and, respectively, fuel oxidation occurred along the combustor height with an insignificant rate.

However, in the reburning tests (when air staging was used along with fuel staging), the  $O_2$  behavior was substantially different. In the primary and reburn zones,  $O_2$  was noticeably lower, compared to the other three test series, which likely caused the above-mentioned delay in oxidation of the secondary fuel. It should be noted that by  $Z\approx 1.7$  m,  $O_2$  regained to a level comparable with the other test series. At the reactor top (Z=3.2 m),  $O_2$  showed the concentration values that were similar to those for the other (co-)combustion techniques, which were correlated with the selected amount of EA (40%).

#### 3.2. Formation and oxidation of CO and $C_xH_y$ inside the conical FBC

Fig. 3 shows the axial profiles of CO and  $C_xH_y$  (as  $CH_4$ ) in the conical FBC for the same (co-)firing techniques and operating parameters, as in Fig. 2. In all the test runs, these profiles showed two specific regions: (i) rapid generation of CO and  $C_xH_y$  in the bottom region of the combustor and (ii) gradual oxidation of these pollutants in the upper region of the reactor.

The axial CO and  $C_x H_y$  profiles for burning pure PRH, as well as for the co-firing of pre-mixed PRH and MRH, showed similar shapes, with a concentration peak at  $Z \approx 0.6$  m, i.e., at the level of PRH (or PRH/MRH mixture) injection.

In the bottom region, CO and  $C_xH_y$  increased drastically along the combustor height in all test series, primarily due to rapid devolatilization of PRH and fuel-char oxidation (at a lesser extent), both contributing to CO formation. The two pollutants were oxidized in this region at low rates, compared to their formation rates. According to Turns [34], CO was generally oxidized to  $CO_2$  by O and OH radicals, whereas the  $C_xH_y$  oxidation involved two stages: (i) breakdown of  $C_xH_y$  to CO and (ii) further oxidation of CO to  $CO_2$ .

P. Ninduangdee, V.I. Kuprianov

Biomass and Bioenergy 112 (2018) 73-84

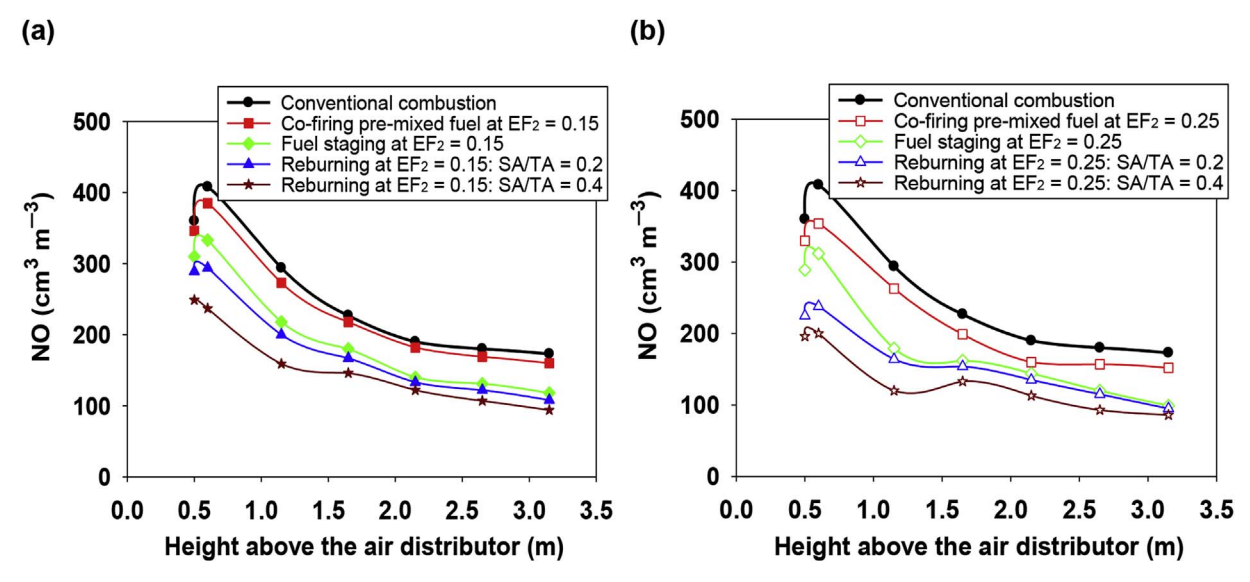


Fig. 4. Axial profiles of NO in the conical FBC when co-firing with PRH and MRH at EA  $\approx 40\%$ , using different co-firing options for (a) EF<sub>2</sub> = 0.15 and (b) EF<sub>2</sub> = 0.25, in comparison with the conventional combustion of PRH.

It can be seen in Fig. 3 that when co-firing premixed PRH and MRH, CO and  $C_xH_y$  at all points along the combustor height were somewhat higher, compared to burning pure PRH. This is mainly due to the reduced bed temperature (see Fig. 2), which led to the lower rates of CO and  $C_xH_y$  oxidation in the primary combustion zone.

From Fig. 3, the use of fuel staging with bottom air injection led to the lowest level of both CO and  $C_x H_y$  in the primary combustion zone (i.e., in the fluidized bed). This fact can be attributed to the reduced feed rate of the primary fuel (PRH) that resulted in the increased (local) excess air ratio at the reactor bottom. Both these factors enhanced the CO and  $C_x H_y$  oxidation rate in the primary combustion zone despite the reduced bed temperatures (as seen in Fig. 2). However, when using reburning, CO and  $C_x H_y$  in the primary combustion zone were highest, as compared to other test series. This is mainly due to the substantially decreased  $O_2$  at  $Z\,<\,1.5$  m, which resulted in a lowered rate of CO and  $C_x H_y$  oxidation at the combustor bottom.

Note that, in the trials for fuel staging and reburning, CO and  $C_xH_y$  in the secondary/reburn zone were substantially higher than those for the two other test series: for individual burning of PRH and co-firing of pre-mixed PRH and MRH. This result can be explained by the rapid devolatilization of the secondary fuel injected into the reactor at  $Z=1.15\,\mathrm{m}$ . Furthermore, when using reburning, the reduced  $O_2$  concentrations resulted in a lower rate of CO and  $C_xH_y$  oxidation in both the primary and reburn zones. The highest peaks of CO and  $C_xH_y$  were therefore observed in the reburning tests at SA/TA = 0.4 with weak effects from EF2. However, an increase of EF2 from 0.15 to 0.25 shifted the peaks of CO and  $C_xH_y$  from the primary combustion zone to a level close to MRH injection in the reburn zone, as can be seen in Fig. 3.

In the region above the secondary fuel injection, where oxidation reactions prevailed, both CO and  $C_xH_y$  decreased gradually along the reactor height to their minimum values at the reactor top. In the reburning tests, CO and  $C_xH_y$  rapidly decreased downstream from the point of injection of secondary air (particularly at SA/TA = 0.4), which enhanced their oxidation rates in the middle region of the reactor. As a result, a substantial amount of heat was released in the vicinity of secondary air injection, which resulted in the increased temperatures in the cylindrical section of the reactor during reburning tests, especially at highest EF2 and SA/TA (see Fig. 2).

#### 3.3. Formation and reduction of NO inside the reactor

During biomass combustion, NO is mainly formed from volatile matter in a fuel, via oxidation of volatile  $\mathrm{NH}_3$  and HCN in multiple

routes of the fuel-NO formation mechanism (with proportional effects of fuel-N, excess air, and temperature), whereas the contributions of thermal-NO and prompt-NO are reported to be minor [9,35]. However, due to secondary reactions, such as the catalytic reduction of NO by CO on the char/ash surfaces [36–38] and homogeneous reactions of NO with some radicals (such as CH<sub>i</sub>, NH<sub>2</sub>/NH, and HCCO) in a flame [21,35,39,40], NO formed in the primary reactions is reduced to a substantial extent.

Fig. 4 depicts the axial profiles of NO in the conical FBC for the same (co-)firing techniques and operating parameters, as in Figs. 2 and 3. Note that in all the trials, the contribution of  $\mathrm{NO}_2$  to  $\mathrm{NO}_x$  was negligible. In the analysis below,  $\mathrm{NO}_x$  is therefore represented only by NO.

It can be seen in Fig. 4 that at Z < 0.6 m, NO was rapidly formed from volatile nitrogenous species in PRH (or PRH/MRH mixture), according to the above-mentioned fuel-NO formation mechanism, attaining a peak in the vicinity of fuel injection in all the test runs.

During co-firing of the pre-mixed fuels at any selected EF<sub>2</sub>, NO at all points inside the combustor was lower, compared to burning PRH alone. An increase in EF<sub>2</sub> from 0.15 to 0.25 led to an insignificant reduction of NO at each point, generally because of the higher CO and  $C_xH_y$ , both being a source of  $CH_i$  and HCCO radicals, enhancing the NO reduction reactions [39,40].

From Fig. 4, during experiments for fuel staging at  $\mathrm{EF_2}=0.15$  and  $\mathrm{EF_2}=0.25$ , NO (including the peak values) was noticeable lower than in the test series for burning pure PRH and co-firing premixed PRH and MRH at similar EA. The reduced NO peaks can be explained by the lowered bed temperatures for both  $\mathrm{EF_2}$  (see Fig. 2), despite that the local excess air ratio in the primary combustion zone increased because of the reduced feeding of PRH. When  $\mathrm{EF_2}$  increased from 0.15 to 0.25, a significant reduction of NO was observed at 0.6 m  $< Z < 1.15\,\mathrm{m}$ . This fact can be attributed to the higher concentrations of CO and  $\mathrm{C_xH_y}$  in the vicinity of secondary fuel injection, which enhanced the homogeneous reduction reactions of NO in the secondary combustion zone with higher feeding of the MRH. Apart from this, at greater  $\mathrm{EF_2}$ , the concentration of fuel chars in the secondary combustion zone was higher, which facilitated the catalytic reduction of NO in this zone.

In the reburning tests, the NO concentrations in the reactor bottom (at  $Z < 0.6\,\mathrm{m}$ ), and consequently, the NO peak were substantially lower than those in the other test series, mainly due to the higher concentration of reducing species, such as CO and  $C_xH_y$ , in this region. It should be noted that the axial NO profiles in the reburning tests exhibited the significant impacts of the secondary air. With increasing SA/TA at fixed EA and EF<sub>2</sub> (i.e., with decreasing the air-to-fuel ratio in both

Biomass and Bioenergy 112 (2018) 73–84

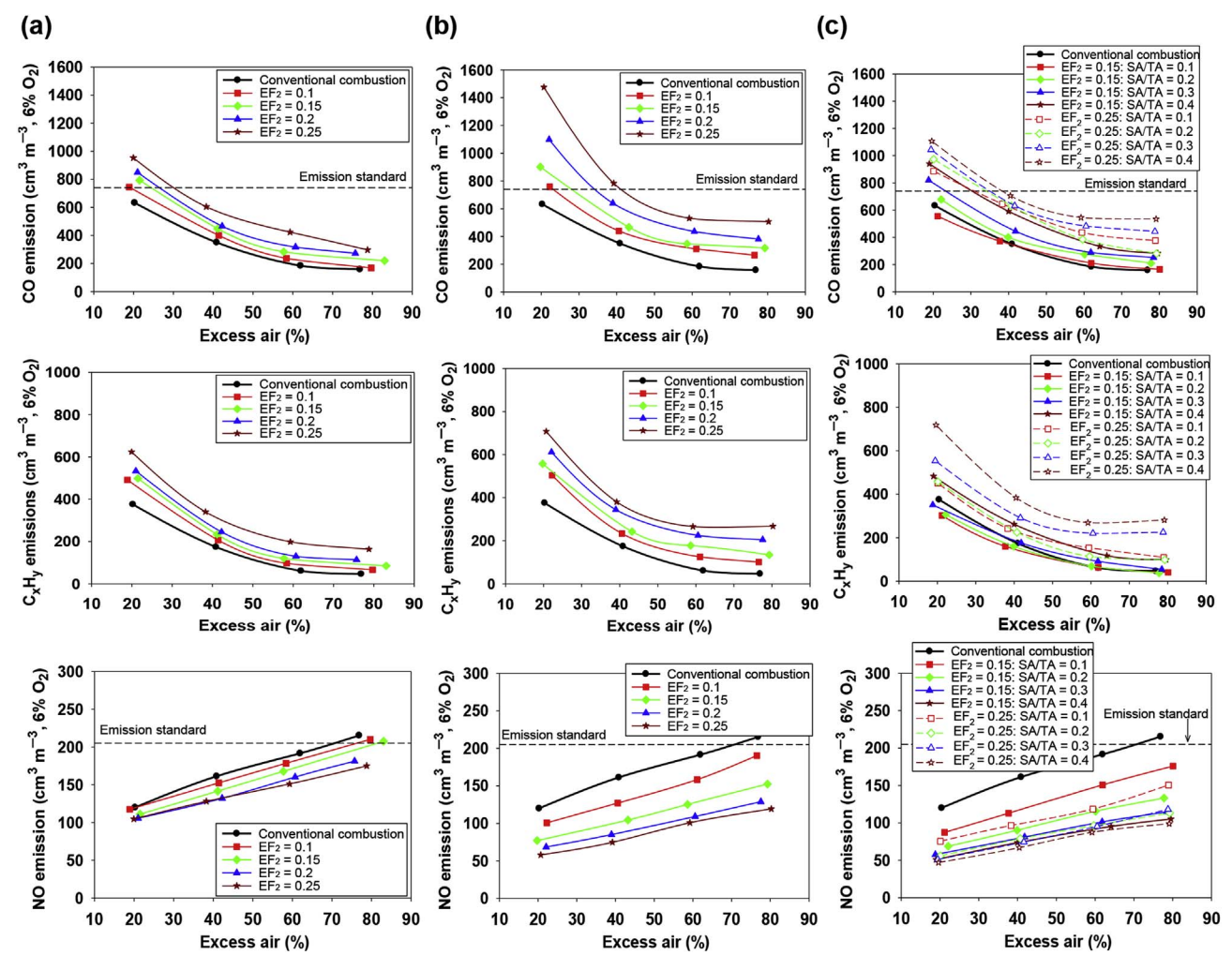


Fig. 5. Emissions of CO (upper), C<sub>x</sub>H<sub>y</sub> as CH<sub>4</sub> (middle), and NO (lower) from the conical FBC when co-firing PRH and MRH under variable operating conditions, using: (a) pre-mixed fuels, (b) fuel staging at bottom air injection, and (c) reburning.

the primary and reburn zones), NO in the primary combustion zone showed a noticeable decrease, mainly due to the lowered  $O_2$  (see Fig. 2). However, there was a substantial increase of both CO and  $C_xH_y$  in the two zones, which enhanced the rate of the secondary (reduction) reactions, particularly in the lower part of the combustor [41].

P. Ninduangdee, V.I. Kuprianov

In the upper regions of the combustor, NO showed a gradual decrease along the combustor height in all test series. The rate of NO reduction at each point was dependent on the NO formation/reduction history (in the primary combustion zone), as well as on the levels of CO and  $C_xH_y$  in the secondary/reburn zone. Note that, at  $EF_2=0.25$ , a low secondary peak of NO can be observed in Fig. 4b in the vicinity of the secondary air injection (at  $Z\approx1.65$  m), which was likely caused by the NO formed from oxidation of nitrogenous volatile species, released from MRH.

At a lowered level of  $O_2$ , the role of  $NH_2/NH$  (generated from volatile nitrogenous species in rice husk) for NO reduction in the two combustion zones was important in the reburning tests [24,39]. Taking into account the reduced formation of NO in the primary combustion zone and highest levels of CO and  $C_xH_y$  in the reburn zone, the reburning method showed the highest potential for the NO reduction among the co-firing techniques studied in this work.

Due to generation of substantial concentrations of CO and  $C_x H_y$  in the secondary combustion zone, the fuel-staged co-firing of PRH and MRH with bottom air injection also showed its effectiveness in terms of NO reduction, however, at a lesser extent compared to reburning.

#### 3.4. Effects of the co-firing options on gaseous emissions

Fig. 5 depicts the CO,  $C_xH_y$  (as  $CH_4$ ), and NO emissions (all represented on a dry gas basis and at 6%  $O_2$ ) from the conical FBC (co-) fired with PRH and MRH under variable operating parameters using the proposed co-firing methods. For comparison, the national emission limits of CO (740 cm<sup>3</sup> m<sup>-3</sup>) and NO (205 cm<sup>3</sup> m<sup>-3</sup>), both represented on a dry gas basis and at 6%  $O_2$ , are shown in Fig. 5 as well [42].

It can be seen in Fig. 5 that, in all the co-firing tests, the CO and  $C_xH_y$  emissions from the combustor were higher than in the tests for burning PRH alone, following the formation and oxidation of these pollutants in different regions inside the reactor. However, an increase in the CO and  $C_xH_y$  emissions during the co-firing of pre-mixed PRH and MRH (see Fig. 5a) was less important, compared to the fuel-staged and reburning tests.

With increasing EA within the range (at fixed  $EF_2$  and SA/TA), both CO and  $C_xH_y$  emissions decreased in all the test runs, mainly due to the enhanced oxidation reactions in all regions inside the reactor. At higher values (60–80%), EA showed its weak influence on these emissions. However, an increase of the two emissions was observed with higher  $EF_2$  and SA/TA (at fixed EA), mainly due to strengthening effects from CO and  $C_xH_y$  at the lower part of the reactor (see Fig. 3).

From Fig. 5, the minimal NO emission (about  $50\,\mathrm{cm^3\,m^{-3}}$ ) was achieved when using reburning at the lowest EA, highest EF<sub>2</sub>, and highest SA/TA. Note that under these conditions, CO and  $C_xH_y$  in the reburn zone (and, consequently, the CO and  $C_xH_y$  emissions) attained

Biomass and Bioenergy 112 (2018) 73-84

Table 3

Combustion-related heat losses and combustion efficiency of the conical FBC (co-)fired with PRH and MRH at actual operating variables using the selected (co-)combustion techniques.

Energy fraction of secondary fuel	Secondary to total air ratio (SA/TA)	Excess air at stack (%)	O <sub>2</sub> at stack	CO at stack <sup>b</sup> (cm <sup>3</sup>	C <sub>x</sub> H <sub>y</sub> at stack <sup>b</sup> (cm <sup>3</sup>	Unburned carbon in PM	Heat loss (%)		Combustion —efficiency (%)
(EF <sub>2</sub> )	aii 1440 (612) 113)	at states (70)	(%) <sup>a</sup>	m <sup>-3</sup> )	m <sup>-3</sup> )	(%) <sup>c</sup>	Due to unburned carbon	Due to incomplete combustion	emercinely (70)
Conventional combus	tion of PRH								
0	0	21	3.7	742	440	3.63	0.81	0.82	98.4
		41	6.2	350	174	3.15	0.70	0.41	98.9
		62	8.1	160	53	2.09	0.46	0.17	99.4
		77	9.1	126	37	1.98	0.44	0.14	99.4
Co-combustion of pre	mixed PRH and MRH								
0.15	0	22	3.9	923	580	1.62	0.41	1.06	98.5
		41	6.2	448	233	1.59	0.40	0.53	99.1
		58	7.7	253	107	1.77	0.45	0.30	99.3
		83	9.6	169	65	1.52	0.38	0.22	99.4
0.25	0	20	3.7	1100	720	1.28	0.35	1.27	98.4
		38	5.9	604	340	1.55	0.43	0.73	98.8
		59	7.9	367	172	1.09	0.30	0.46	99.2
		79	9.3	229	126	1.07	0.29	0.35	99.4
Co-combustion of PR	H and MRH using fuel	staging							
0.15	0	20	3.7	1080	668	2.12	0.54	1.45	98.0
		43	6.4	467	242	2.49	0.64	0.56	98.8
		59	7.8	313	160	2.51	0.64	0.37	99.0
		79	9.3	253	107	2.30	0.59	0.27	99.1
0.25	0	20	3.7	1704	817	2.09	0.78	1.51	97.7
0.20		39	6.0	783	380	1.96	0.63	0.76	98.6
		59	7.9	464	232	2.13	0.65	0.44	98.9
		80	9.4	391	206	2.33	0.61	0.35	99.0
Co-combustion of PR	H and MRH using a re	hurning technia	ue						
0.15	0.2	22	3.9	778	352	1.94	0.49	0.74	98.8
		40	6.0	400	160	2.17	0.55	0.41	99.0
		60	7.9	240	60	2.05	0.52	0.22	99.3
		78	9.2	165	30	2.44	0.62	0.15	99.2
	0.4	19	3.5	1108	569	2.27	0.58	1.05	98.4
	- * *	40	6.1	591	262	2.50	0.64	0.60	98.8
		64	8.2	284	100	2.68	0.69	0.30	99.0
		80	9.3	220	77	1.81	0.46	0.26	99.3
0.25	0.2	20	3.7	1142	537	2.57	0.72	1.13	98.2
V.=0	V.=	41	6.2	632	225	2.35	0.65	0.63	98.7
		60	7.9	339	100	3.33	0.94	0.35	98.7
		79	9.3	220	82	2.89	0.81	0.28	98.9
	0.4	20	3.7	1300	844	2.47	0.69	1.48	97.8
	0.1	40	6.2	705	384	2.74	0.77	0.85	98.4
		59	7.9	480	237	3.26	0.92	0.62	98.5
		J 2	/.7	700	43/	J.20	0.54	0.02	JU.J

<sup>&</sup>lt;sup>a</sup> As a volume fraction.

their maximum, pointing at the important roles of CO and  $C_xH_y$  in the NO reduction reactions. As compared to individual firing of PRH at fixed EA, all the co-firing options resulted in lower NO emission, and the NO emission reduction became more significant for increasing EF2 and/or SA/TA. This result can be attributed to the substantial contribution of elevated CO and  $C_xH_y$  to the NO reduction in secondary (reduction) reactions at different regions inside the reactor. Note that the fuel staging and reburning techniques provided better results for the NO emission reduction, mainly due to the higher CO and  $C_xH_y$  in the secondary/reburn zone, as compared to burning PRH on its own and cofiring of pre-mixed PRH and MRH. However, with increasing EA, the NO emission increased in all test runs, following the fuel-NO formation mechanism [9,34,35] and because of the lowered CO and  $C_xH_y$ .

It can be concluded from the analysis of data in Fig. 5 that EA, EF<sub>2</sub>, and/or SA/TA had the opposite impacts on the NO and  $\text{CO/C}_x\text{H}_y$  emissions. Indeed, with decreasing EA, as well as with increasing EF<sub>2</sub> and/or SA/TA, the CO and  $\text{C}_x\text{H}_y$  emissions showed their substantial increase, whereas the NO emission showed a decreasing trend. Therefore, there is a need to optimize the selected operating parameters, with

an objective to minimize the environmental impacts by the combustor (as discussed below).

#### 3.5. Combustion efficiency

Table 3 shows the predicted combustion-related heat losses (due to unburned carbon and incomplete combustion) and the combustion efficiency of the conical FBC, co-fired with PRH and MRH using the proposed co-combustion methods, along with the results for burning pure PRH. Data required for determining the actual amount of excess air and the heat losses, such as unburned carbon content in the PM and actual  $O_2$ , CO, and  $C_xH_y$  (as  $CH_4$ ) at stack, are also included in Table 3 for all the test series and runs.

An analysis of the heat losses and combustion efficiency of the conical FBC showed the weak influence of the co-firing methods, but important effects of operating conditions on these characteristics. When burning PRH alone (i.e., at  $\mathrm{EF_2}=0$ ), the heat loss due to unburned carbon decreased from 0.81% to 0.44%, whereas the heat loss due to incomplete combustion diminished from 0.82% to 0.14%, as EA ranged

b At actual O2 at stack.

<sup>&</sup>lt;sup>c</sup> As a mass fraction.

P. Ninduangdee, V.I. Kuprianov

Biomass and Bioenergy 112 (2018) 73-84

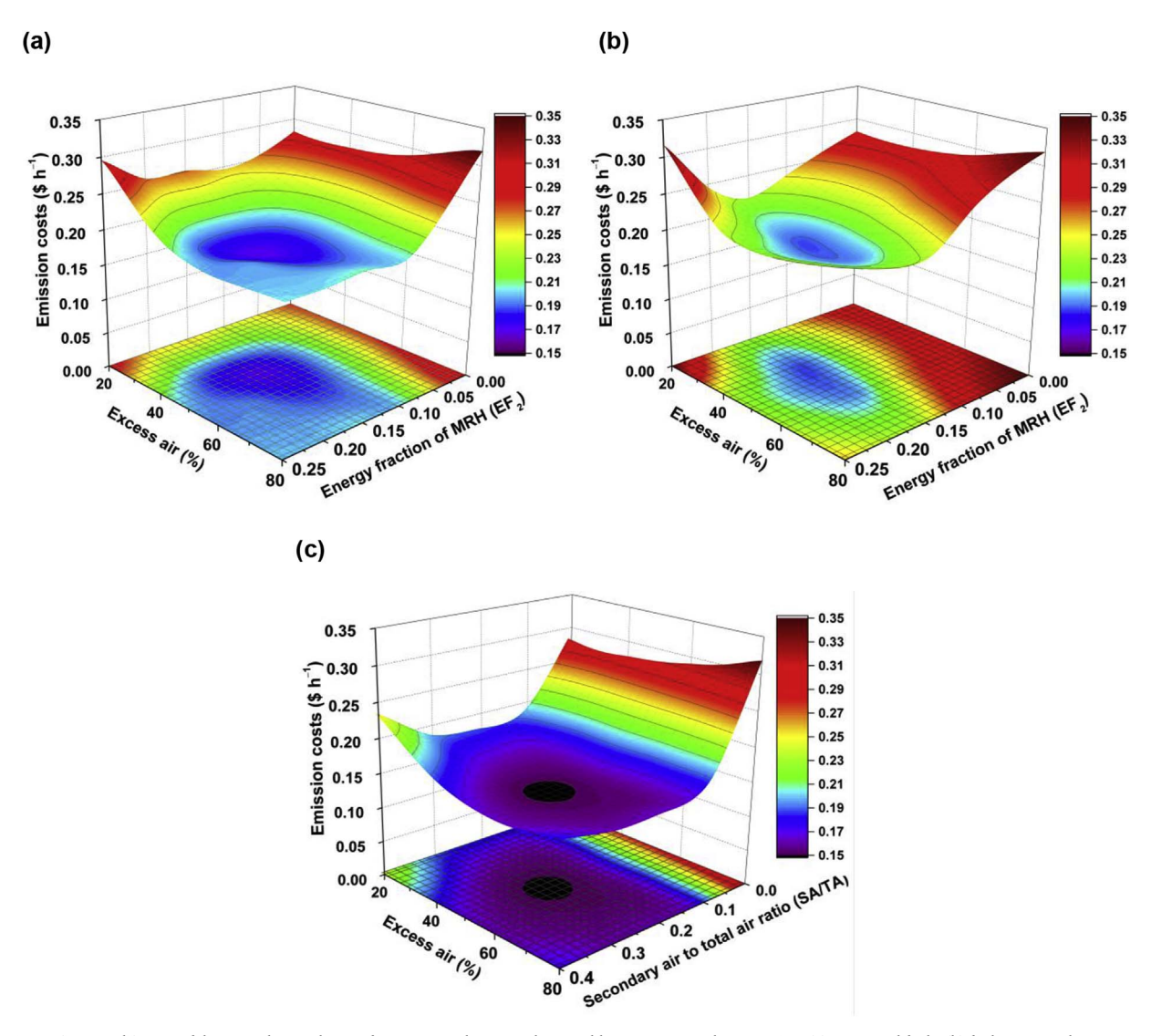


Fig. 6. Emission ("external") costs of the conical FBC when co-firing PRH and MRH under variable operating conditions, using: (a) pre-mixed fuels, (b) fuel staging at bottom air injection, and (c) reburning at  $EF_2 = 0.15$ .

Table 4
Major gaseous emissions from the conical FBC co-fired with PRH and MRH at optimal operating parameters when using the selected co-combustion methods, as compared with burning pure PRH at similar excess air.

(Co-)combustion	Operating	Emissi	on <sup>a</sup> (cm <sup>3</sup> m	n <sup>-3</sup> )	NO —emission
method	parameters	CO	$C_xH_y$	NO	reduction
Conventional	EA = 45%	320	150	167	
combustion of a base fuel (PRH)	EA = 50%	270	120	176	
Co-firing premixed fuels	$EF_2 = 0.15,$ EA = 45%	410	220	145	13%
Co-firing using fuel staging	$EF_2 = 0.15\%,$ EA = 45%	450	235	106	37%
Co-firing using reburning	$EF_2 = 0.15\%,$ EA = 50%, SA/ TA = 0.25	380	170	82	53%

 $<sup>^{\</sup>rm a}$  At 6%  ${\rm O_2}$  on a dry gas basis.

from about 20% to 80%. As a result, with increasing EA within the range, the combustion efficiency of the reactor fired with pure PRH showed some improvement, from 98.4% to 99.4%.

Note that, in the tests for co-firing premixed PRH and MRH in

different proportions (EF $_2$  = 0.15 and EF $_2$  = 0.25), the combustion efficiencies were close to those for firing pure PRH at similar amounts of EA. However, when using fuel staging with bottom air injection, the combustion efficiency of the conical FBC was lower (by 0.3–0.5%), compared to co-firing premixed PRH and MRH at similar operating conditions (EF $_2$  and EA). This result was mainly due to an insignificant increase of the two heat losses (both were slightly higher at greater EF $_2$ ) caused by the secondary fuel injection. In the reburning tests, the combustion efficiency was affected by the three operating parameters (EF $_2$ , EA, and SA/TA). Because of the effects from both fuel and air staging, the minimal combustion efficiencies, 97.8–98.8%, were observed at highest EF $_2$  and SA/TA for EA from 20 to 80%.

#### 3.6. Optimal operating conditions

Fig. 6 depicts the 3-D surfaces representing the emission costs of the co-firing of PRH and MRH with the selected co-combustion methods, which were obtained using Eqs. (1)–(4) and the above-reported CO,  $C_xH_y$ , and NO emissions, as well as other relevant parameters, all quantified for the ranges of EF<sub>2</sub>, EA, and SA/TA. From Fig. 6, the operating conditions showed the substantial effects on the emission costs. At relatively low EA, but elevated EF<sub>2</sub> and/or SA/TA, the emission costs for all the co-firing methods were generally high, mainly due to

P. Ninduangdee, V.I. Kuprianov

Biomass and Bioenergy 112 (2018) 73-84

important contributions of the CO and  $C_xH_y$  emissions. The effects of the NO emissions on the "external" costs were significant when cofiring PRH/MRH with high EA at relatively low EF<sub>2</sub> and/or SA/TA.

As seen in Fig. 6a and b,  $EF_2 = 0.15$  and EA = 45% were optimal for the co-combustion of pre-mixed PRH and MRH, as well as for their co-firing using fuel staging with bottom air injection. Under these operating conditions, the "external" costs of the conical FBC were minimal for both co-combustion methods. For the reburning technique, EA and SA/TA were optimized for  $EF_2 = 0.15$  that (as mentioned above) was optimal for the first and second co-firing techniques. From Fig. 6c, EA = 50% and SA/TA = 0.25 were optimal for the co-firing using reburning at  $EF_2 = 0.15$ .

It can be seen in Table 3 that under optimal operating parameters, the combustor ensured high (about 99%) combustion efficiency, which was close for the selected co-firing methods.

Table 4 compares the CO,  $C_x H_y$ , and NO emissions (all on a dry gas basis and at 6%  $O_2$ ), as well as the NO emission reduction, for the cocombustion techniques at the optimal operating parameters. For comparability, Table 4 presents the corresponding emission values for burning pure PRH at excess air of 45% and 50%. Through the co-firing of PRH and MRH under optimal operating conditions, a noticeable/substantial reduction of the NO emission from the combustor can be achieved, as compared to burning PRH alone: by 13% (145 cm³ m $^{-3}$  against 167 cm³ m $^{-3}$ ) when co-firing the pre-mixed fuels, by 37% (106 cm³ m $^{-3}$  against 167 cm³ m $^{-3}$ ) for fuel-staged co-combustion of PRH and MRH at bottom air injection, and by 53% (82 cm³ m $^{-3}$  against 176 cm³ m $^{-3}$ ) when using the reburning technique.

However, under these operating conditions, the CO emission may increase by  $90\text{--}130\,\mathrm{cm^3\,m^{-3}}$ , as compared with burning pure PRH, to a level of  $380\text{--}450\,\mathrm{cm^3\,m^{-3}}$  (depending on the co-combustion method), which is substantially lower than the national emission limit for CO (740 cm³ m<sup>-3</sup>). From Table 4, during co-combustion of PRH and MRH, the  $C_xH_y$  emissions may increase by  $50\text{--}85\,\mathrm{cm^3\,m^{-3}}$ , as compared to firing PRH on its own, to  $170\text{--}235\,\mathrm{cm^3\,m^{-3}}$  in different co-firing techniques.

#### 4. Conclusions

The effects of co-firing methods and operating parameters on the emissions and combustion efficiency of a conical fluidized-bed combustor co-fired with pelletized rice husk (base fuel) and moisturized rice husk (secondary fuel) have been investigated for a variable energy fraction of moisturized rice husk (in total fuel supply), excess air, and secondary-to-total air ratio. The proposed co-combustion methods and the operating parameters have noticeable effects on the major gaseous emissions and combustion efficiency of the combustor. The selected cofiring techniques create reducing conditions for NO (due to substantial CO and C<sub>v</sub>H<sub>v</sub>) in the primary and secondary/reburn zones. To minimize the emission costs of the combustor,  $EF_2 = 0.15$  and EA = 45% are optimal for co-combustion of the pre-mixed fuels, as well as for their cofiring using fuel staging with bottom air injection, while  $EF_2 = 0.15$ , EA = 50%, and SA/TA = 0.25 are most appropriate when co-firing the fuels using a reburning method. When operated optimally, the conical FBC can ensure high (~99%) combustion efficiency at a noticeable reduction of the NO emission: (i) by 13% when co-firing the pre-mixed fuels, (ii) by 37% for fuel-staged co-combustion with bottom air injection, and (iii) by 53% when using a reburning technique, as compared to the NO emission of 167-176 cm<sup>3</sup> m<sup>-3</sup> from burning PRH alone. However, the CO emission may show some increase, by  $90\text{--}130\,\text{cm}^3\,\text{m}^{-3}$  depending on the co-firing technique, to a level of  $380\text{--}450\,\text{cm}^3\,\text{m}^{-3}$  (which is substantially lower than the national CO emission standard), whereas the CxHv emissions can be maintained within  $170-235 \text{ cm}^3 \text{ m}^{-3}$ .

#### Acknowledgement

The authors wish to acknowledge the financial support from the Thailand Research Fund (Contract No. BRG 5980005).

#### Appendix A. Determining excess air for individual test runs

Prior to determining EA for a test run, the excess air ratio ( $\alpha$ ) was predicted using the actual volume fractions of  $O_2$ , CO, and  $C_xH_y$  (as  $CH_4$ ) measured at stack (all represented as the percentages on a dry gas basis), by neglecting  $H_2$  and assuming 79%  $N_2$  in the "dry" flue gas, as:

$$\alpha = \frac{21}{21 - (O_2 - 0.5CO - 2CH_4)} \tag{A.1}$$

The percentage of EA at stack was then determined as:

$$EA = 100(\alpha - 1) \tag{A.2}$$

#### Appendix B. Heat losses and combustion efficiency for co-combustion tests

For each test run, the heat loss due to unburned carbon ( $q_{uc,cf}$  as the percentage of LHV<sub>cf</sub>) was predicted by using the mass fraction of unburned carbon in the sampled fly ash ( $C_{fa}$ , %) determined in the laboratory analysis and the lower heating value and ash content of the "equivalent fuel" as:

$$q_{\text{uc,cf}} = \frac{32,866C_{\text{fa}}}{100 - C_{\text{fa}}} \times \frac{A_{\text{cf}}}{LHV_{\text{cf}}}$$
(B.1)

The heat loss due to incomplete combustion ( $q_{ic,cf}$ , as the percentage of LHV<sub>cf</sub>) was quantified, based on the actual CO and C<sub>x</sub>H<sub>y</sub> (as CH<sub>4</sub>) emissions (both in units of cm<sup>3</sup> m<sup>-3</sup> on a dry gas basis), using  $V_{dg,cf}$ , LHV<sub>cf</sub>, and the above-estimated  $q_{uc,cf}$  as:

$$q_{\rm ic,cf} = (126.4 \text{CO} + 358.2 \text{C}_{\rm x} \text{H}_{\rm y}) \times 10^{-4} V_{\rm dg,cf} \frac{(100 - q_{\rm uc,cf})}{\text{LHV}_{\rm cf}}$$
(B.2)

The combustion efficiency of the reactor ( $\eta_c$ , as the percentage of LHV<sub>cf</sub>) was predicted as:

$$\eta_{\rm c} = 100 - (q_{\rm uc,cf} + q_{\rm ic,cf})$$
(B.3)

#### References

- [1] Department of Alternative Energy Development and Efficiency, Ministry of Energy, Thailand. Thailand Alternative Energy Situation 2015 (accessed December 22, 2017). Available from: http://www.dede.go.th/download/state\_59/Thailand %20alternative%20energy%202015.pdf.
- [2] E. Natarajan, A. Nordin, A.N. Rao, Overview of combustion and gasification of rice husk in fluidized bed reactors, Biomass Bioenergy 14 (5–6) (1998) 533–546.
- [3] L. Armesto, A. Bahillo, K. Veijonen, A. Cabanillas, J. Otero, Combustion behaviour of rice husk in a bubbling fluidised bed, Biomass Bioenergy 23 (3) (2002) 171–179.
- [4] M. Fang, L. Yang, G. Chen, Z. Shi, Z. Luo, K. Cen, Experimental study on rice husk combustion in a circulating fluidized bed, Fuel Process. Technol. 85 (11) (2004) 1273–1282.
- [5] C.S. Chyang, K.T. Wu, C.S. Lin, Emission of nitrogen oxides in a vortexing fluidized bed combustor, Fuel 86 (1–2) (2007) 234–243.
- [6] V.I. Kuprianov, R. Kaewklum, S. Chakritthakul, Effects of operating conditions and fuel properties on emission performance and combustion efficiency of a swirling fluidized-bed combustor fired with a biomass fuel, Energy 36 (4) (2011) 2038–2048.
- [7] F. Duan, C.S. Chyang, C.W. Lin, J. Tso, Experimental study on rice husk combustion in a vortexing fluidized-bed with flue gas recirculation (FGR), Bioresour. Technol. 134 (2013) 204–211.
- [8] T. Madhiyanon, A. Lapirattanakun, P. Sathitruangsak, S. Soponronnarit, A novel cyclonic fluidized-bed combustor (ψ-FBC): combustion and thermal efficiency, temperature distributions, combustion intensity, and emission of pollutants, Combust. Flame 146 (1–2) (2006) 232–245.
- [9] J. Werther, M. Saenger, E.-U. Hartge, T. Ogada, Z. Siagi, Combustion of agricultural residues, Prog. Energy Combust. Sci. 26 (1) (2000) 1–27.
- [10] T. Nussbaumer, Combustion and co-combustion of biomass: Fundamentals, technologies, and primary measures for emission reduction, Energy Fuels 17 (6) (2003) 1510–1521
- [11] S.G. Sahu, N. Chakraborty, P. Sarkar, Coal-biomass co-combustion: an overview, Renew. Sustain. Energy Rev. 39 (2014) 575–586.
- [12] M. Sami, K. Annamalai, M. Wooldridge, Co-firing of coal and biomass fuel blends, Prog. Energy Combust. Sci. 27 (2) (2001) 171–214.
- [13] S.Q. Turn, B.M. Jenkins, L.A. Jakeway, L.G. Blevins, R.B. Williams, G. Rubenstein, C.M. Kinoshita, Test results from sugar cane bagasse and high fiber cane co-fired with fossil fuels. Biomass Bioenergy 30 (6) (2006) 565–574.
- [14] K.V. Narayanan, E. Natarajan, Experimental studies on cofiring of coal and biomass blends in India, Renew. Energy 32 (15) (2007) 2548–2558.
- [15] F. Al-Mansour, J. Zuwala, An evaluation of biomass co-firing in Europe, Biomass Bioenergy 34 (5) (2010) 620–629.
- [16] A. Lüschen, R. Madlener, Economic viability of biomass cofiring in new hard-coal power plants in Germany, Biomass Bioenergy 57 (2013) 33–47.
- [17] V.I. Kuprianov, K. Janvijitsakul, W. Permchart, Co-firing of sugar cane bagasse with rice husk in a conical fluidized-bed combustor, Fuel 85 (4) (2006) 434–442.
- [18] S. Chakritthakul, V.I. Kuprianov, Co-firing of eucalyptus bark and rubberwood sawdust in a swirling fluidized-bed combustor using an axial flow swirler, Bioresour. Technol. 102 (17) (2011) 8268–8278.
- [19] C.E. Baukal Jr., The John Zink Combustion Handbook, CRC Press, New York, 2001.
- [20] P. Suheri, V.I. Kuprianov, Co-firing of oil palm empty fruit bunch and kernel shell in a fluidized-bed combustor: optimization of operating variables, Energy Procedia 79 (2015) 956–962.

- [21] L.D. Smoot, S.C. Hill, H. Xu, NO<sub>x</sub> control through reburning, Prog. Energy Combust. Sci. 24 (5) (1998) 385–408.
- [22] N.T. Carlin, K. Annamalai, W.L. Harman, J.M. Sweeten, The economics of reburning with cattle manure-based biomass in existing coal-fired power plants for NO<sub>x</sub> and CO<sub>2</sub> emissions control, Biomass Bioenergy 33 (9) (2009) 1139–1157.
- [23] N.S. Harding, B.R. Adams, Biomass as a reburning fuel: a specialized cofiring application, Biomass Bioenergy 19 (6) (2000) 429–445.
- [24] R. Salzmann, T. Nussbaumer, Fuel staging for NO<sub>x</sub> reduction in biomass combustion: Experiments and modeling, Energy Fuels 15 (3) (2001) 575–582.
- [25] P. Ninduangdee, V.I. Kuprianov, A study on combustion of oil palm empty fruit bunch in a fluidized bed using alternative bed materials: performance, emissions, and time-domain changes in the bed condition, Appl. Energy 176 (2016) 34–48.
- [26] P. Ninduangdee, V.I. Kuprianov, Combustion of an oil palm residue with elevated potassium content in a fluidized-bed combustor using alternative bed materials for preventing bed agglomeration, Bioresour. Technol. 182 (2015) 272–281.
- [27] K. Sirisomboon, V.I. Kuprianov, Effects of fuel staging on the NO emission reduction during biomass–biomass co-combustion in a fluidized-bed combustor, Energy Fuels 31 (1) (2017) 659–671.
- [28] H.J.M. Visser, S.C. Van Lith, J.H.A. Kiel, Biomass ash-bed material interactions leading to agglomeration in FBC, J. Energy Resour. Technol. 130 (1) (2008) 011801.
- [29] P. Basu, K.F. Cen, L. Jestin, Boilers and Burners, Springer, New York, 2000.
- [30] P. Ninduangdee, V.I. Kuprianov, Combustion of palm kernel shell in a fluidized bed: optimization of biomass particle size and operating conditions, Energy Convers. Manag. 85 (2014) 800–808.
- [31] ESCAP-UN, Energy Efficiency, United Nations, New York, 1995.
- [32] X. Wei, L. Zhang, H. Zhou, Evaluating the environmental value of pollutants in China power industry, Proceedings of the International Conference on Energy and the Environment, 2003 Shanghai, China.
- [33] L. Czarnowska, C.A. Frangopoulos, Dispersion of pollutants, environmental externalities due to a pulverized coal power plant and their effect on the cost of electricity, Energy 41 (2012) 212–219.
- [34] S.R. Turns, An Introduction to Combustion: Concepts and Applications, second ed., McGraw-Hill series in mechanical engineering, Singapore, 2006 international ed..
- [35] F. Winter, C. Wartha, H. Hofbauer, NO and N<sub>2</sub>O formation during the combustion of wood, straw, malt waste and peat, Bioresour. Technol. 70 (1) (1999) 39–49.
- [36] P. Lu, S.-R. Xu, X.-M. Zhu, Study on NO heterogeneous reduction with coal in an entrained flow reactor, Fuel 88 (1) (2009) 110–115.
- [37] B.J. Zhong, W.W. Shi, W.B. Fu, Effects of fuel characteristics on the NO reduction during the reburning with coals, Fuel Process. Technol. 79 (2) (2002) 93–106.
- [38] O. Karlström, M. Perander, N. DeMartini, A. Brink, M. Hupa, Role of ash on the NO formation during char oxidation of biomass, Fuel 190 (2017) 274–280.
- [39] C. Casaca, M. Costa, NO<sub>x</sub> control through reburning using biomass in a laboratory
- furnace: effect of particle size, Proc. Combust. Inst. 32 (2) (2009) 2641–2648.

  [40] J. Ballester, R. Ichaso, A. Pina, M.A. González, S. Jiménez, Experimental evaluation and detailed characterisation of biomass reburning, Biomass Bioenergy 32 (10)
- [41] Y. Shu, F. Zhang, H. Wang, J. Zhu, G. Tian, C. Zhang, An experimental study of NO reduction by biomass reburning and the characterization of its pyrolysis gases, Fuel 139 (2015) 321–327.

(2008) 959-970.

[42] Pollution Control Department, Ministry of Natural Resources and Environment, Thailand. Air Pollution Standards for Industrial Sources (accessed December 22, 2017). Available from: http://www.pcd.go.th/info\_serv/reg\_std\_airsnd03.html.



# Songklanakarin J. Sci. Technol. 40 (5), 1081-1089, Sep. - Oct. 2018



#### Original Article

## Co-combustion of rice husk pellets and moisturized rice husk in a fluidized-bed combustor using fuel staging at a conventional air supply

Pichet Ninduangdee<sup>1\*</sup> and Vladimir I. Kuprianov<sup>2</sup>

<sup>1</sup> Division of Mechanical Engineering, Faculty of Engineering and Industrial Technology, Phetchaburi Rajabhat University, Mueang, Phetchaburi, 76000 Thailand

<sup>2</sup> School of Manufacturing Systems and Mechanical Engineering, Sirindhorn International Institute of Technology, Thammasat University, Khlong Luang, Pathum Thani, 12121 Thailand

Received: 31 July 2016; Revised: 27 June 2017; Accepted: 30 June 2017

#### **Abstract**

This paper presents an experimental study on co-combustion of two types of rice husk with substantially different properties in a fluidized-bed combustor using fuel staging for lowering NO emission. Rice husk pellets were burned as a base (or primary) fuel, whereas moisturized rice husk was injected downstream from the primary combustion zone as a secondary fuel. The experiments were conducted at 200 kWth heat input to this reactor with a bottom air supply, while the energy fraction of the secondary fuel in the total heat input ranged from 0 to 0.25, and excess air was within 20–80% for each co-firing option. The study revealed significant effects of the operating parameters on combustion and emission performance of the combustor. Compared to burning of the base fuel, a nearly 40% NO emission reduction is achievable with fuel staging, while controlling the CO and  $C_xH_y$  emissions from the combustor to acceptable levels. However, fuel staging causes some deterioration in the combustion efficiency.

Keywords: fluidized bed, rice husk, co-combustion, fuel staging, NO reduction

#### 1. Introduction

For many years, rice husk has been an important resource of bioenergy in Thailand. In 2014, some 8 million tons of rice husk were produced in this country, which is equivalent to 2,840 ktoe (or about 120 PJ) energy potential (Department of Alternative Energy Development and Efficiency [DEDE], 2014).

Due to its excellent combustion properties, rice husk has shown high potential and suitability as a fuel in the direct combustion systems at heat and power plants. A number of studies have reported high effectiveness of fluidized-bed combustion systems converting rice husk into energy (Fang *et al.*, 2004; Janvijitsakul & Kuprianov, 2008; Kuprianov *et al.*,

2010). When using conventional bed materials (silica/quartz sand), these systems are commonly free of the operational problem known as bed agglomeration (Duan *et al.*, 2013; Janvijitsakul & Kuprianov, 2008). This fact can be attributed to the favorable composition of rice husk ash (with a predominant content of Si and a rather low proportion of K), which prevents "coating-induced" and/or "melt-induced" bed agglomeration when burning rice husk (Visser *et al.*, 2008).

However, fluidized-bed combustion of rice husk is generally accompanied by elevated/ high  $NO_x$  emissions, whose level is dependent on fuel-N, operating conditions, and combustion method/technique used (Madhiyanon *et al.*, 2010; Sirisomboon *et al.*, 2010; Werther *et al.*, 2000). Having an insignificant fuel-N content, 0.2–0.5% (by wt., on an asreceived basis), rice husk, nevertheless, can generate elevated and, in some cases, high  $NO_x$  emissions: up to 180 ppm (on a dry gas basis, and at 6%  $O_2$ ) when fired in conventional fluidized-bed combustion systems (Chyang *et al.*, 2007; Fang

et al., 2004; Kuprianov et al., 2010), and up to 425 ppm when burning this biomass in fluidized-bed combustion systems with alternative hydrodynamics and/ or high combustion intensity (Madhiyanon et al., 2004, 2006, 2010).

Co-firing of two or more fuels seems to be an effective technique to remedy this deficiency. The most important advantage of co-firing is its flexibility with regard to fuel type and combustion method, as established in studies on grate-firing, pulverized fuel-firing, and fluidized-bed combustion techniques (Areeprasert et al., 2016; Nussbaumer, 2003; Sami et al., 2001). A large number of studies have addressed various aspects of co-firing coal and biomass, commonly combusted as a blended feedstock in modified pulverized coal-fired boilers. In most co-firing tests on these boilers, a lowered net production of CO2 and a substantial reduction in NOx and SO2 emissions have been achieved with a more stable combustion process and reduced costs of heat/power generation compared to burning coal on its own (Narayanan & Natarajan, 2007; Sahu et al., 2014; Sami et al., 2001;).

However, not much information regarding biomass –biomass co-firing in fluidized-bed combustion systems is available in literature. The recent studies on (i) co-combustion of rice husk premixed with sugar cane bagasse and (ii) co-combustion of rubberwood sawdust blended with eucalyptus bark have revealed that problematic fuels (e.g., with rather low calorific value and/ or elevated emissions) can be effectively utilized by co-firing in a fluidized-bed combustor (Chakritthakul & Kuprianov, 2011; Kuprianov *et al.*, 2006). From these two studies, co-combustion of a biomass with a relatively high calorific value and a different one of higher fuel-moisture and/ or lower fuel-N can lead to a substantial reduction of NO<sub>x</sub> emissions, whose level is dependent on the energy proportions of the blended fuels and on the amount of excess air.

Fuel staging has been proven an effective technique for reducing  $NO_x$  in a combustion system (co-) fired with coal/biomass. In fuel-staged combustion, a base fuel is fed into the bottom region of the reactor together with combustion air and therefore fired with excess air. Meantime, the rest of the fuel (or a different fuel with dedicated properties) is delivered into the above zone with no air supply to create preferable conditions for  $NO_x$  reduction (Baukal, 2001). This technique can be readily applied in a co-firing system with the aim to ensure fuel staging (biasing) along the reactor height.

In a combination with the air-staged injection into a combustion system, the fuel staging can ensure a significant reduction in  $NO_x$  emissions, as shown in studies on the cofiring of two woody residues in a laboratory scale grate-fired system (Salzmann & Nussbaumer, 2001, 2003). Apparently, such a system requires a more complicated configuration of a furnace/combustor (and so is more expensive) and a rather difficult control of primary air injection compared to that with a conventional (bottom) air supply. However, the literature sources lack information on biomass—biomass co-firing in fluidized-bed combustion systems using fuel staging (i. e., separate injection of primary and secondary fuels into a system) with a single-flow air injection through the air distributor fixed at the reactor bottom.

This work was therefore aimed at studying the effects of fuel staging (i.e., mass/energy fraction of the cofired fuels in the total heat input) and excess air on the

combustion and emission performance of a fluidized-bed combustor co-fired with rice husk pellets and moisturized rice husk using a conventional (bottom) air injection system. An assessment of the NO emission reduction for specified operating parameters of the proposed combustor using fuel staging was the main focus of this work.

#### 2. Materials and Methods

#### 2.1 Experimental setup

Figure 1 shows a schematic diagram of the experimental setup with the cone-shaped fluidized-bed combustor (referred to as 'conical FBC') used in this work. The setup included the combustor (equipped with a nineteen bubble-cap air distributor) and auxiliary facilities, such as an air blower, two screw-type fuel feeders, a cyclone for collecting particulate matter, and a diesel-fired start up burner.

The conical FBC has been previously employed in studies on individual burning of some problematic biomass fuels, as reported by Ninduangdee and Kuprianov (2015 and 2016). However, compared to the previous configuration with a single fuel supply, the combustor was modified for the current study (equipped with an additional fuel feeder) to conduct co-firing tests for fuel staging. During the experiments, primary and secondary biomass fuels were delivered separately into the conical FBC by the two screw-type fuel feeders, as shown in Figure 1. The primary fuel was injected into the fluidized bed at 0.65 m level above the air distributor, whereas the secondary fuel was introduced into the cylindrical section 0.5 m higher, thus ensuring co-firing of the two biomass fuels using fuel staging with bottom air supply.

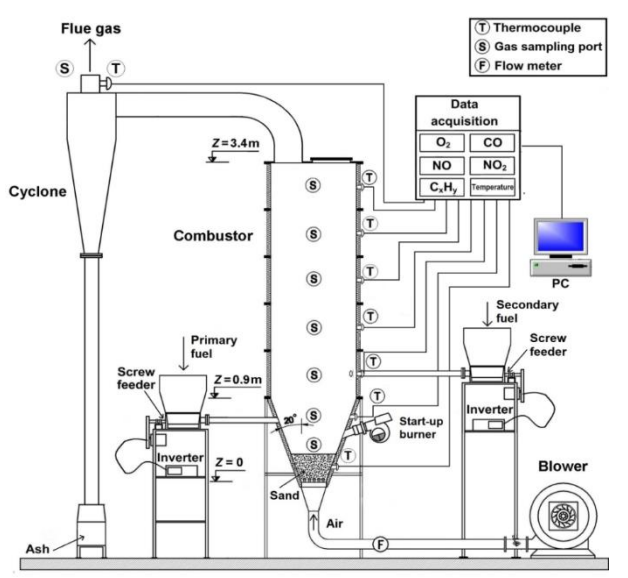


Figure 1. Schematic diagram of the experimental setup for fuelstaged co-firing of two biomass fuels.

#### 2.2 The fuels and bed material

In co-combustion tests, pelletized rice husk (PRH) was used as the base (or primary) fuel, whereas moisturized rice husk (MRH) was injected downstream from the primary combustion zone as the secondary fuel.

PRH was supplied by a local company manufacturing pelletized biomass fuels. Prior to the pelleting process using a flat die fuel pellet machine, as-received rice husk was conveyed to a sieving system (to remove solid impurities) and then ground in a grinding mill to the specified particle size. Afterwards, the ground rice husk was fed together with some amount of water into the 100-hp pelletizer, which pressed the ground biomass into cylindrical pellets with a diameter of 6 mm and a variable length (between 5 and 15 mm). At the final stage, the pellets were spread onto a wire screen for cooling and drying, and, afterwards, were packed in fabric super sacks to keep up the fuel quality.

However, the secondary fuel was prepared by adding a specified amount of water to "as-received" rice husk supplied from a local rice mill. The average dimensions of MRH particles were 2-mm width, 0.5-mm thickness, and 10-mm length. Compared to burning "as-received" rice husk, the use of MRH with rather low calorific value prevented intensive formation of fuel-NO in the secondary combustion zone (mainly by low fuel-N content in MRH and reduced local temperature) and increased CO and C<sub>x</sub>H<sub>y</sub> levels, which enhances NO reduction reactions in this zone (Nussbaumer, 2003; Sirisomboon & Kuprianov, 2017).

Typically, rice husk contains about 40% C, 30% O, 5% H, up to 20% ash, and up to 10% moisture (all by weight, on as-received basis), whereas N and S contribute only small weight percentages (Fernandes *et al.*, 2016; Kuprianov *et al.*, 2011; Wannapeera *et al.*, 2008). However, during fuel processing (pelletizing and moisturizing), the fuel properties are subject to significant changes.

Table 1 presents the proximate and ultimate analyses, and the lower heating value of PRH and MRH (all presented on an "as-fired" basis) used in co-combustion experiments. From Table 1, the two types of rice husk had substantial contents of volatile matter making them highly reactive. Due to the higher moisture content in MRH, the lower heating value of this secondary fuel, LHV $_{12}=10.6$  MJ/kg, was noticeably lower than that of PRH, LHV $_{11}=15.1$  MJ/kg. It can be concluded that with its higher content of volatiles and high calorific value, PRH burned in the primary combustion zone (in effect, in the fluidized bed) and was more reactive than the MRH injected over the fluidized bed. Because of the insignificant S contents of both fuels, this work disregarded all issues related to formation and emission of SO<sub>2</sub> during co-firing of the selected fuels.

Silica sand (SiO<sub>2</sub>  $\approx$  88 wt.%), with 0.3–0.5 mm particle size and solid density of 2500 kg/m³, was used as the bed material in this combustor when co-firing PRH and MRH. In all experiments the bed height was 30 cm (in a static state).

Table 1. Ultimate and proximate analyses, and the lower heating value (all on an as-fired basis) of the selected fuels used in (co-)combustion experiments.

Bio-	Ult	imate	analysi	s (wt.	%)	Proxir	LHV (kJ/			
mass	С	Н	0	N	S	W	VM	FC	A	kg)
PRH MRH	43.27 29.94									15,100 10,600

#### 2.3 Experimental methods for co-firing tests

In this work, the energy fraction of secondary fuel (EF<sub>2</sub>) and the excess air (EA) were selected as independent operating parameters, while the total heat input to the reactor was constant (~200 kW<sub>th</sub>) across all the experimental tests. To ensure this heat input, PRH and MRH were delivered into the reactor at respective mass flow rates ( $\dot{m}_{\rm fl}$  and  $\dot{m}_{\rm f2}$ ) for each (fixed) EF<sub>2</sub>, quantified as the ratio of energy contribution by MRH ( $\dot{m}_{\rm f2}$  LHV<sub>f2</sub>) to the total heat input to the combustor by both fuels ( $\dot{m}_{\rm f1}$  LHV<sub>f1</sub> +  $\dot{m}_{\rm f2}$  LHV<sub>f2</sub>).

In the first stage of this study, PRH was co-fired with MRH at different values of EF<sub>2</sub> (0, 0.1, 0.15, 0.2, and 0.25) while maintaining excess air constant (~40%), with the aim to investigate the effects of fuel staging on formation and oxidation/ reduction of major gaseous pollutants inside the conical FBC. During a test run at fixed operating parameters (EF<sub>2</sub> and EA), temperature, O<sub>2</sub>, CO, C<sub>x</sub>H<sub>y</sub> (as CH<sub>4</sub>), and NO were measured along the reactor axial distance on centerline, as well as at the cyclone gas exit, using a new model "Testo-350" gas analyzer.

To investigate the effects of the operating parameters on emissions and combustion efficiency of the conical FBC, another test series was performed for the selected range of EF $_2$  while EA was varied from 20% to 80% for each fuel option. In this experimental series, only CO,  $C_xH_y$  (as CH $_4$ ), and NO emission concentrations were measured along with  $O_2$  at the cyclone gas exit.

In each individual test run (at fixed  $EF_2$  and EA) of the two experimental series, the actual amount of EA was quantified according to Basu *et al.* (2000), by using  $O_2$ , CO, and  $C_xH_y$  (as  $CH_4$ ) measured at the cyclone exit.

# 2.4 Heat losses and combustion efficiency of the conical FBC for the co-firing tests

For each co-firing test, the heat loss due to unburned carbon and that due to incomplete combustion in the combustor were predicted according to Basu *et al.* (2000) using the 'equivalent fuel' concept, whose properties were determined as a weighted average from the corresponding properties and mass fractions (as the weights) of PRH and MRH (Sirisomboon & Kuprianov, 2017).

The heat loss due to unburned carbon ( $q_{uc,cf}$ , % LHV $_{cf}$ ) was predicted by using the carbon content in particulate matter (PM) emitted from the combustor ( $C_{PM}$ , wt.%) and the properties of the 'equivalent fuel', such as ash content ( $A_{cf}$ , wt.%) and lower heating value (LHV $_{cf}$ , kJ/kg), as:

$$q_{\text{uc,cf}} = \frac{32,866C_{\text{PM}}}{(100 - C_{\text{PM}})} \frac{A_{\text{cf}}}{\text{LHV}_{\text{cf}}}$$
(1)

Afterwards, the heat loss due to incomplete combustion ( $q_{uc,cf}$ , % LHV $_{cf}$ ) was quantified based on the CO and C $_x$ H $_y$  (as CH $_4$ ) concentrations at stack (both in ppm, at 6% O $_2$  and on a dry gas basis) and by taking into account the volume of dry combustion products originated from the combustion of the 'equivalent fuel' ( $V_{dg,cf}$ ), as well as the LHV $_{cf}$  (kJ/kg) and the above-calculated  $q_{uc,cf}$  (%LHV $_{cf}$ ), as:

$$q_{\text{ic,cf}} = (126.4\text{CO} + 358.2\text{C}_{\text{x}}\text{H}_{\text{y}})_{@6\%\text{O}_{2}}$$
$$\cdot 10^{-4}V_{\text{dg,cf}} \frac{(100 - q_{\text{uc,cf}})}{\text{LHV}_{\text{cf}}}$$
(2)

The combustion efficiency of the conical FBC (%LHV  $_{\!cf})$  was then quantified as:

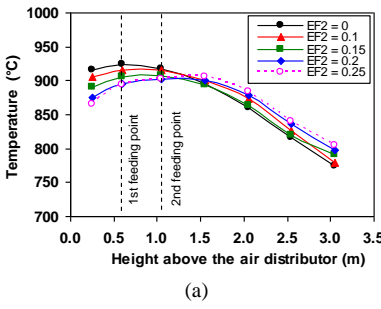
$$\eta_{\rm cf} = 100 - (q_{\rm uc,cf} + q_{\rm ic,cf})$$
(3)

#### 3. Results and Discussion

# 3.1 Effects of fuel staging on the axial temperature and O<sub>2</sub> profiles in the reactor

Figure 2 depicts the major combustion characteristics – the axial distribution of temperature and  $O_2$  – in the conical FBC (co-) fired with PRH and MRH in various proportions at constant excess air. It can be seen in Figure 2 that the energy fraction of the secondary fuel (MRH), or fuel biasing, had noticeable effects on profiles of both temperature and  $O_2$  inside the combustor.

In each trial (at fixed EF<sub>2</sub>), the axial temperature profile was fairly uniform, exhibiting, however, a slight positive gradient in the bottom region of the combustor and a negative gradient in its upper region. The positive gradient was likely due to the impacts from (i) combustion air injected through the air distributor and (ii) endothermic devolatilization of PRH (occurred in the vicinity of fuel injection), whereas the negative gradient was mainly caused by the heat loss through combustor walls. These two regions met above the air distributor level at location of the peak temperature inside the reactor.



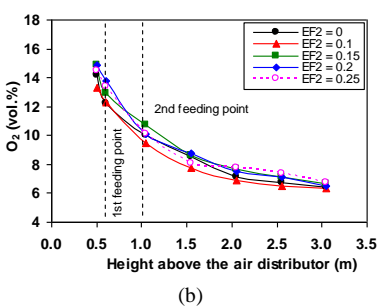


Figure 2. Effects of the energy fraction of secondary fuel (EF<sub>2</sub>) on the axial profiles of (a) temperature and (b)  $O_2$  in the conical FBC (co-)fired with PRH and MRH in different proportions at constant excess air ( $\sim 40\%$ ).

From Figure 2a, with increasing EF<sub>2</sub> (at fixed EA), temperature at all points in the bottom region (including the peak temperature) was lower, mainly due to the reduced supply of the primary fuel (PRH), which increased the excess of air in this region. In the meantime, an increase of EF<sub>2</sub> from 0 to 0.25 shifted the peak temperature location from Z = 0.6 m (the level of PRH injection above the air distributor) to Z = 1.6 m, which was somewhat above the level of MRH injection.

It can be seen in Figure 2b that, in all the test runs,  $O_2$  decreased along the reactor height, however with a weakening rate. A substantial axial gradient of  $O_2$  was observed in the lower part of the reactor (Z < 1.6 m), comprising primary and secondary combustion zones, whereas in the upper part, the  $O_2$  consumption (and, accordingly, fuel oxidation) along the combustor height occurred at an insignificant rate. However, unlike with temperature,  $O_2$  did not show apparent effects from  $EF_2$  in the fluidized-bed (bottom) region.

# 3.2 Formation and oxidation/reduction of gaseous pollutants in the conical FBC

Figure 3 shows the axial profiles of CO,  $C_xH_y$  (as CH<sub>4</sub>), and NO in the conical FBC for the same operating parameters as in Figure 2. In all experiments, these profiles showed two specific regions (with an opposite behavior of the profiles) pointing at: (1) rapid (net) formation of the pollutants at the bottom part of the conical FBC and (2) highly-intensive secondary reactions in the reactor freeboard, such as oxidation of CO and  $C_xH_y$ , and reduction of NO. The shape of these profiles was mainly determined by the difference between the rate of primary (formation) processes/reactions and that of the secondary reactions in these two regions.

In the primary combustion zone (i.e., in effect, in the conical section with primary fuel injection), CO and  $C_xH_y$  originated from the fuel volatile matter and drastically increased along the combustor height, primarily due to the prompt devolatilization of PRH, followed/accompanied by oxidation of CO and  $C_xH_y$ , and fuel chars. While the CO oxidation occurred via its reactions with  $O_2$  and OH, the  $C_xH_y$  oxidation reactions involved a breakdown of  $C_xH_y$  to CO, followed by oxidation of CO to  $CO_2$  (Turns, 2006). It can be seen in Figure 3 (a and b) that in all the test runs, CO at different points inside the combustor was noticeably higher than  $C_xH_y$ , mainly due to the breakdown of  $C_xH_y$  to CO at high-temperature conditions.

At a rather low contribution of the secondary fuel (EF<sub>2</sub> = 0–0.15), the peaks of  $C_xH_y$  and CO were observed at the level of PRH injection ( $Z\approx 0.6$  m), whereas at a greater heat input by MRH (EF<sub>2</sub> = 0.20–0.25), these peaks shifted to the secondary combustion zone (to the level of secondary fuel injection,  $Z\approx 1.15$  m), as can be seen in Figure 3 (a and b). With increasing EF<sub>2</sub> within the specified range (at fixed EA of the reactor), the maximum values of CO and  $C_xH_y$  in the primary zone ( $Z\approx 0.6$  m) decreased, mainly due to the reduced PRH feed rate and the corresponding increase (local) in excess air at this zone, which enhanced the oxidation of CO and  $C_xH_y$  in spite of the decreased bed temperature (Figure 2). However, CO and  $C_xH_y$  measured at  $Z\approx 1.15$  m showed the opposite trend, generally due to the rapid devolatilization of MRH in the vicinity of its injection into the combustor.

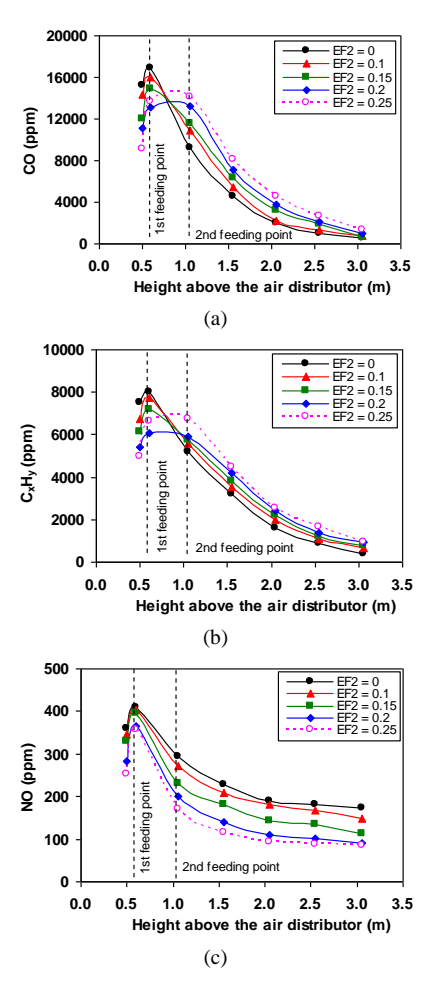


Figure 3. Effects of the energy fraction of secondary fuel (EF<sub>2</sub>) on the axial profiles of (a) CO, (b)  $C_xH_y$  (as  $CH_4$ ), and (c) NO in the conical FBC (co-) fired with PRH and MRH in different proportions at constant excess air ( $\sim 40\%$ ).

With increasing EF<sub>2</sub> within the specified range (at fixed EA of the reactor), the maximum values of CO and  $C_xH_y$  in the primary zone ( $Z\approx0.6$  m) decreased, mainly due to the reduced PRH feed rate and the corresponding increase (local) in excess air at this zone, which enhanced the oxidation of CO and  $C_xH_y$  in spite of the decreased bed temperature (Figure 2). However, CO and  $C_xH_y$  measured at  $Z\approx1.15$  m showed the opposite trend, generally due to the rapid devolatilization of MRH in the vicinity of its injection into the combustor.

In the region above the secondary fuel injection, where the rate of the secondary (oxidation) reactions prevailed over the primary (formation) processes and reactions, both CO and  $C_xH_y$  gradually decreased along the reactor height to their minima (at the reactor top), showing the same effects from EF<sub>2</sub> as at  $Z\approx 1.15$  m.

Like CO and C<sub>x</sub>H<sub>y</sub>, NO originated from the biomass volatile matter, via oxidation of volatile NH<sub>3</sub> and HCN by the numerous routes of the fuel-NO formation mechanism, including the proportional effects from fuel-N, excess air and temperature (Winter *et al.*, 1999; Werther *et al.*, 2000). However, due to some secondary reactions, such as heterogeneous

reduction of NO by CO (mainly on the surface of fuel char particles) and homogeneous reactions of NO with light  $C_xH_y$  and NH<sub>2</sub>/NH radicals, NO generated in the primary reactions was likely reduced to a substantial extent (Winter *et al.*, 1999; Werther *et al.*, 2000). It can be seen in Figure 3 (a and b) that the fuel staging extended the region with high concentrations of CO and  $C_xH_y$ , covering the secondary combustion zone, thus creating conditions for reducing a part of NO (formed during combustion of PRH in the bottom region) to N<sub>2</sub> in the secondary combustion zone.

Like with CO and  $C_xH_y$ , all axial NO profiles showed two specific regions in the combustor, as seen in Figure 3c. In the first (lower) region (Z < 0.6 m), where the rate of the NO formation reactions was significantly higher than that of the NO reduction reactions, NO increased rapidly along the combustor height, attaining the NO peak at Z = 0.6 m (at the level of primary fuel feeding) in all the test runs. With increasing EF<sub>2</sub>, the NO peak at this point somewhat decreased, despite the increased excess air ratio at the primary combustion zone. This result can be likely attributed to the lowered bed temperature (Figure 2) and increased concentrations of CO and  $C_xH_y$  in this zone.

In the upper region of the axial NO profiles ( $Z>0.6\,$  m), the rate of the reactions responsible for NO reduction prevailed over NO formation, which led to a gradual decrease of NO along the reactor height. However, as seen in Figure 3c, with increasing EF2, the NO reduction rate at  $0.6\,$  m <  $Z<1.5\,$  m was much higher than that at the combustor top, particularly at EF2 = 0.25. This fact can be explained by the highest concentrations of both CO and  $C_xH_y$  in the vicinity of secondary fuel injection (when testing at the highest feeding of MRH), which enhanced the catalytic reduction of NO at the secondary combustion zone. Therefore, in the test at EF2 = 0.25, NO at all points inside the combustor was at a minimal level, compared to the other tests.

# 3.3 Effects of operating parameters on the major gaseous emissions

Figure 4 depicts the CO,  $C_xH_y$  (as  $CH_4$ ), and NO emissions from the conical FBC (all on a dry gas basis and at 6%  $O_2$ ) when co-firing PRH and MRH at variable  $EF_2$  and EA.

It can be seen in Figure 4 (a and b) that in all test runs with fuel staging, the CO and  $C_x H_y$  emissions from the combustor were increased compared to burning pure PRH. On increasing EA from about 20% to 40% (at fixed EF2), these two emissions decreased significantly, showing however a rather weak effect of this operating parameter at its high values (60–80%). According to the domestic environmental legislation regarding biomass-fueled industrial applications (PCD, 2017), in order to meet the national emission limit for CO (740 ppm, as corrected to 6% O2 on a dry gas basis), PRH and MRH should be co-fired at EF2 not higher than 0.2 and EA = 40–80%.

In contrast, at fixed EA the fuel staging (via injecting MRH downstream from the primary combustion zone) gave lower NO emissions than individual burning of PRH (delivered through the lower fuel pipe), and the NO emission reduction became more significant as  $EF_2$  was increased. This result can be generally attributed to the increased CO and

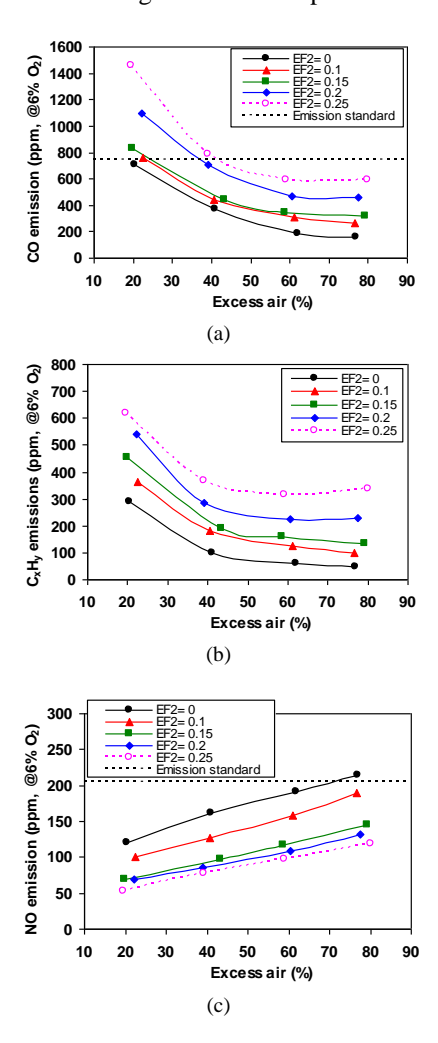


Figure 4. Emissions of (a) CO, (b)  $C_xH_y$  (as  $CH_4$ ), and (c) NO from the conical FBC (co-)fired with PRH and MRH in different proportions at various air excess levels.

 $C_xH_y$  in the secondary combustion zone, which enhanced the catalytic reduction of NO in this zone. However, with increasing EA (for each fuel option), the NO emission was observed to increase, following the fuel-NO formation mechanism.

Note that, in all the tests with fuel staging, the NO emission was noticeably below the national emission limit for this pollutant (205 ppm, as corrected to 6% O<sub>2</sub> on a dry gas basis), as regulated by PCD (2017).

Figure 5 shows the NO emission reduction, as a function of  $EF_2$  and EA. It can be seen in Figure 5 that this index was substantially affected by  $EF_2$  but exhibited a weak effect from EA. At  $EF_2=0.1$ , the reduction efficiency was rather low, 12-22%, for the specified range of EA. However, as seen in Figure 5, the NO emission reduction can be increased to about 40% by switching  $EF_2$  to 0.2-0.25 (regardless of EA).

Thus, fuel-staged co-firing of PRH and MRH with bottom air injection shows an apparent potential to reduce the NO emission from the conical FBC despite the elevated  $O_2$  levels in the primary combustion zone.

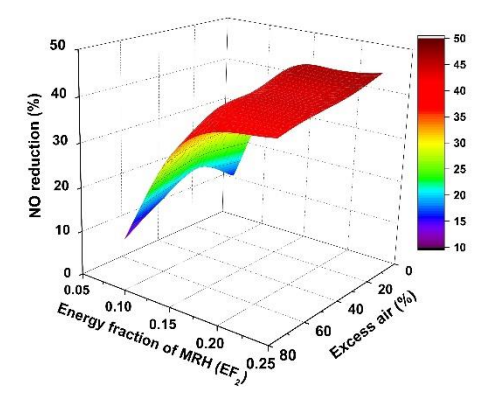


Figure 5. Effects of the energy fraction of secondary fuel (EF<sub>2</sub>) and excess air on the NO emission reduction of the conical FBC when using fuel staging, relative to baseline use of only the primary fuel.

#### 3.4 Heat losses and combustion efficiency of the conical FBC in test runs

Table 2 presents the predicted heat loss due to unburned carbon and that due to incomplete combustion together with the combustion efficiency of the proposed combustion technique co-fired with PRH and MRH at actual EF<sub>2</sub> and EA (or  $O_2$  at stack) . Some supporting variables required in Equations (1)–(3), such as the content of unburned carbon in PM and the CO and  $C_xH_y$  emission concentrations, are included in Table 2 as well.

As seen in Table 2, the two heat losses had important effects on the combustion efficiency of the conical FBC. When firing pure PRH (EF $_2$  = 0), the unburned carbon content in PM decreased from 3.63% to 1.98% as EA was increased from 21% to 77%, thus pointing at an increased rate of the char-C burnout with higher airflow rate. When using fuel staging, the impact of EA on unburned carbon in PM was minor. At EF $_2$  = 0.1–0.25, the carbon content in PM changed insignificantly when varying EA.

However, the CO and  $C_xH_y$  emissions, and consequently, the heat loss due to incomplete combustion showed quite strong influences of both EF2 and EA. With increasing EA within the range (at any fixed EF2), this heat loss decreased substantially. This result was generally due to the enhanced rates of CO and  $C_xH_y$  oxidation reactions. In contrast, with increasing EF2 (at fixed EA), the heat loss due to incomplete combustion somewhat increased, which slightly reduced the combustion efficiency.

# 3.5 Operating conditions recommended for fuel-staged co-firing PRH and MRH

To reduce the environmental impact of NO emission, a more harmful pollutant than CO and  $C_xH_y$ , it is suggested that, at a fixed energy fraction of secondary fuel (EF2), the excess air (EA) in the combustor be controlled to its least possible value, controlling however the CO emission to a level somewhat below the national limit for this pollutant. Based on this approach and aiming at the maximum reduction in NO emission, EF2  $\approx$  0.2 and EA  $\approx$  40% can be regarded as the best option for the operating parameters when co-firing PRH and MRH in the conical FBC using fuel staging.

Table 2. Heat losses and combustion efficiency in the conical FBC when co-firing PRH and MRH at various combinations of EF2 and EA.

Excess air (%)	O <sub>2</sub> at the cyclone exit (vol.%)	Unburned carbon in PM (wt.%)	CO <sup>a</sup> (ppm)	$C_xH_y^a$ (ppm)	Heat loss (%) due to:		Combustion
					Unburned carbon	Incomplete combustion	efficiency (%)
		Ind	ividual firing	of PRH (EF $_2$ = 0	))		
21	3.7	3.63	709	290	0.81	0.74	98.4
41	6.2	3.15	373	98	0.70	0.31	99.0
62	8.1	2.09	184	61	0.46	0.17	99.4
77	9.1	1.98	158	46	0.44	0.14	99.4
		Co-fir	ing of PRH an	d MRH at EF <sub>2</sub> =	= 0.1		
22	4.0	1.47	759	364	0.36	0.86	98.8
41	6.1	2.89	440	180	0.71	0.45	98.8
61	8.0	3.02	311	125	0.74	0.32	98.9
77	9.1	2.89	265	101	0.71	0.26	99.0
		Co-firi	ng of PRH and	d MRH at EF <sub>2</sub> =	0.15		
20	3.7	2.12	835	455	0.54	1.03	98.4
43	6.4	2.49	440	192	0.64	0.48	98.9
59	7.8	2.51	347	160	0.64	0.39	99.0
79	9.3	2.30	317	134	0.59	0.34	99.1
		Co-fir	ing of PRH an	d MRH at EF <sub>2</sub> =	= 0.2		
22	4.0	2.93	1099	542	0.78	1.24	98.0
39	6.0	2.36	704	285	0.63	0.71	98.7
61	8.0	2.45	473	225	0.65	0.52	98.8
77	9.2	2.29	460	228	0.61	0.52	98.9
		Co-firi	ng of PRH and	d MRH at EF <sub>2</sub> =	0.25		
20	3.7	2.09	1463	618	0.58	1.51	97.9
39	6.0	1.96	783	368	0.54	0.86	98.6
59	7.9	2.13	595	317	0.59	0.70	98.7
80	9.4	2.33	593	337	0.65	0.73	98.6

<sup>&</sup>lt;sup>a</sup>At 6% O<sub>2</sub> on dry gas basis

Under these conditions, an NO emission reduction by about 40% can be achieved from that with individual firing of the base fuel (PRH), while operating the combustor with quite high (~99%) combustion efficiency and controlling the CO emission within the national emission limit.

#### 4. Conclusions

The effects of fuel staging on the emissions and combustion efficiency of a conical fluidized-bed combustor co-fired with pelletized rice husk (primary fuel) and moisturized rice husk (secondary fuel) have been investigated across a range of energy fractions of moisturized rice husk (in the total fuel supply) and a range of excess air. These two operating parameters have substantial effects on the formation and the oxidation/reduction of the major gaseous pollutants (CO, C<sub>x</sub>H<sub>y</sub>, and NO) in the primary and secondary combustion zones, as well as in the freeboard, and, consequently, on the emissions and combustion efficiency of the proposed combustion technique. With increasing the energy contribution of the secondary fuel to the reactor heat input and/or on lowering excess air, CO and CxHy in the secondary combustion zone increase, thus facilitating a noticeable decrease in NO in this zone and lowering the NO emission from this combustor using fuel staging with bottom air injection. The proposed co-firing method may insignificantly deteriorate the combustion efficiency. However, the co-firing of rice husk pellets and moisturized rice husk at 20% energy contribution by the secondary fuel (to the reactor heat input) and with about 40% excess air can ensure ~99% combustion efficiency and result in NO emission reduction by 60% from that when burning pelletized rice husk on its own.

#### Acknowledgements

The authors gratefully acknowledge the National Research Council of Thailand (NRCT), Phetchaburi Rajabhat University, as well as Thammasat University for supporting this research.

#### References

Areeprasert, C., Scala, F., Coppola, A., Urciuolo, M., Chirone, R., Chanyavanich, P., & Yoshikawa, K. (2016). Fluidized bed co-combustion of hydrothermally treated paper sludge with two coals of different rank. Fuel Processing Technology, 144, 230–238. doi:10.1016/j.fuproc.2015.12.033

- Basu, P., Cen, K. F., & Jestin, L. (2000). *Boilers and burners*. New York, NY: Springer.
- Baukal, C. E. Jr. (2001). *The john zink combustion handbook*. New York, NY: CRC Press.
- Chakritthakul, S., & Kuprianov, V. I. (2011). Co-firing of eucalyptus bark and rubberwood sawdust in a swirling fluidized-bed combustor using an axial flow swirler. *Bioresource Technology*, 102(17). 8268–8278. doi:10.1016/j.biortech.2011.06.056
- Chyang, C. S., Qian, F. P., Lin, Y. C., & Yang, S. H. (2008). NO and N<sub>2</sub>O emission characteristics from a pilot scale vortexing fluidized bed combustor firing different fuels. *Energy and Fuels*, 22(2). 1004–1011. doi:10.1021/ef7005595
- Department of Alternative Energy Development and Efficiency, Ministry of Energy, Thailand. (2014). *Thailand alternative energy situation 2014*. Retrieved from http://www.dede.go.th/download/state\_58/sit\_57\_58/Thailand%20Alternative%20Energy%20 Situation.pdf
- Duan, F., Chyang, C. S., Lin, C. W., & Tso, J. (2013). Experimental study on rice husk combustion in a vortexing fluidized-bed with flue gas recirculation (FGR). Bioresource Technology, 134, 204–211. doi:10.1016/j.biortech.2013.01.125
- Fang, M., Yang, L., Chen, G., Shi, Z., Luo, Z., & Cen, K. (2004). Experimental study on rice husk combustion in a circulating fluidized bed. *Fuel Processing Tech*nology, 85(11), 1273–1282. doi:10.1016/j.fuproc. 2003.08.002
- Fernandes, I. J., Calheiro, D., Kieling, A. G., Moraes, C. A. M., Rocha, T. L. A. C., Brehm, F. A., & Modolo, R. C. E. (2016). Characterization of rice husk ash produced using different biomass combustion techniques for energy. *Fuel*, 165, 351–359. doi:10.1016/j.fuel.2015.10.086
- Janvijitsakul, K., & Kuprianov, V. I. (2008). Major gaseous and PAH emissions from a fluidized-bed combustor firing rice husk with high combustion efficiency. Fuel Processing Technology, 89(8), 777–787. doi: 10.1016/j.fuproc.2008.01.013
- Kuprianov, V. I., Janvijitsakul, K., & Permchart, W. (2006). Co-firing of sugar cane bagasse with rice husk in a conical fluidized-bed combustor. *Fuel*, 85(4), 434–442. doi:10.1016/j.fuel.2005.08.013
- Kuprianov, V. I., Kaewklum, R., & Chakritthakul, S. (2011). Effects of operating conditions and fuel properties on emission performance and combustion efficiency of a swirling fluidized-bed combustor fired with a biomass fuel. *Energy*, *36*(4), 2038–2048. doi: 10. 1016/j.energy.2010.05.026
- Kuprianov, V. I., Kaewklum, R., Sirisomboon, K., Arromdee, P., & Chakritthakul, S. (2010). Combustion and emission characteristics of a swirling fluidized-bed combustor burning moisturized rice husk. *Applied Energy*, 87(9), 2899–2906. doi:10.1016/j.apenergy. 2009.09.009

- Madhiyanon, T., Lapirattanakun, A., Sathitruangsak, P., & Soponronnarit, S. (2006). A novel cyclonic fluidized-bed combustor (ψ-FBC): Combustion and thermal efficiency, temperature distributions, combustion intensity, and emission of pollutants. *Combustion and Flame, 146*(1–2), 232–245. doi:10. 1016/j.combustflame.2006.03.008
- Madhiyanon, T., Piriyarungroj, N., & Soponronnarit, S. (2004). A novel vortex-fluidized bed combustor with two combustion chambers for rice-husk fuel. Songklanakarin Journal of Science and Technology, 26(6), 875–893.
- Madhiyanon, T., Sathitruangsak, P., & Soponronnarit, S. (2010). Combustion characteristics of rice-husk in a short-combustion-chamber fluidized-bed combustor (SFBC). *Applied Thermal Engineering*, *30*(4), 347–353. doi:10.1016/j.applthermaleng.2009.09.014
- Narayanan, K. V., & Natarajan, E. (2007). Experimental studies on cofiring of coal and biomass blends in India. *Renewable Energy*, *32*(15), 2548–2558. doi: 10.1016/j.renene.2006.12.018
- Ninduangdee, P., & Kuprianov, V. I. (2015). Combustion of an oil palm residue with elevated potassium content in a fluidized-bed combustor using alternative bed materials for preventing bed agglomeration. *Bio*resource Technology, 182, 272–281. doi:10.1016/j. biortech.2015.01.128
- Ninduangdee, P., & Kuprianov, V. I. (2016). A study on combustion of oil palm empty fruit bunch in a fluidized bed using alternative bed materials: Performance, emissions, and time-domain changes in the bed condition. *Applied Energy*, 176, 34–48. doi:10.1016/j.apenergy.2016.05.063
- Nussbaumer, T. (2003). Combustion and co-combustion of biomass: Fundamentals, technologies, and primary measures for emission reduction. *Energy and Fuels*, 17(6), 1510–1521. doi:10.1021/ef030031q
- Pollution Control Department, Ministry of Natural Resources and Environment, Thailand. (2017). *Air pollution standards for industrial sources*. Retrieved from http://www.pcd.go.th/info\_serv/reg\_std\_airsnd03.ht ml
- Sahu, S. G., Chakraborty, N., & Sarkar, P. (2014). Coalbiomass co-combustion: An overview. *Renewable* and Sustainable Energy Reviews, 39, 575–586. doi:10.1016/j.rser.2014.07.106
- Salzmann, R., & Nussbaumer, T. (2001). Fuel staging for NO<sub>x</sub> reduction in biomass combustion: Experiments and modeling. *Energy and Fuels*, 15(3), 575–582. doi:10.1021/ef0001383
- Sami, M., Annamalai, K., & Wooldridge, M. (2001). Cofiring of coal and biomass fuel blends. *Progress in Energy and Combustion Science*, 27(2), 171–214. doi:10.1016/S0360-1285(00)00020-4
- Sirisomboon, K., & Kuprianov, V. I. (2017). Effects of fuel staging on the NO emission reduction during biomass—biomass co-combustion in a fluidized-bed combustor. *Energy and Fuels*, 31(1) 659–671. doi:10.1021/acs.energyfuels.6b02622

- Turns, S. (2006). *An introduction to combustion*. Boston, MA: McGraw-Hill.
- Visser, H. J. M., Van Lith, S. C., & Kiel, J. H. A. (2008). Biomass ash-bed material interactions leading to agglomeration in FBC. *Journal of Energy Resources Technology, Transactions of the ASME, 130*(1), No. 0118011–0118015. doi:10.1115/1.2824247
- Wannapeera, J., Worasuwannarak, N., & Pipatmanomai, S. (2008). Product yields and characteristics of rice husk, rice straw and corncob during fast pyrolysis in a drop-tube/ fixed-bed reactor. *Songklanakarin Journal of Science and Technology*, 30(3), 393–404.
- Werther, J., Saenger, M., Hartge, E. U., Ogada, T., & Siagi, Z. (2000). Combustion of agricultural residues. *Progress in Energy and Combustion Science*, 26(1), 1–27. doi:10.1016/S0360-1285(99)00005-2
- Winter, F., Wartha, C., & Hofbauer, H. (1999). NO and N<sub>2</sub>O formation during the combustion of wood, straw, malt waste and peat. *Bioresource Technology*, 70(1), 39–49. doi:10.1016/S0960-8524(99)00019-X